UNIVERSITÀ
DEGLI STUDI
DI PADOVA

Sede Amministrativa: Università degli Studi di Padova

Dipartimento di Scienze Chimiche

SCUOLA DI DOTTORATO DI RICERCA IN SCIENZA ED INGEGNERIA DEI MATERIALI

CICLO XXVIII

Graphene and beyond: development of new two-dimensional materials

Direttore della Scuola : Ch.mo Prof. Gaetano Granozzi

Supervisore : Prof. Stefano Agnoli

Dottorando : Mattia Cattelan

Contents

Abstract (English version)

During the three years of my PhD project, I explored part of the world of two-dimensional materials. My activity has been focused on the growth and analysis of two-dimensional materials by means of Surface Science techniques. For the growth both chemical methods, such as decomposition of gaseous precursors, as well as physical methods, such as evaporation of metals under ultra-high vacuum conditions, were used. The main method for studying the properties of these materials was photoemission spectroscopy from core levels and valence band.

The materials were mostly grown and analysed directly *in-situ*, avoiding air exposure, which is known to alter their properties. Taking the cue from the results on single materials, I further widened my investigation toward complex heterostructures, i.e. artificial architectures of two-dimensional materials. Systems stemming from different combinations among graphene, hexagonal boron nitride and two-dimensional chalcogenides were produced and investigated with the aim to unravel the structure-activity relationships in heterostructures.

The thesis is divided into four main chapters.

The first is an introduction to the world of two-dimensional materials and summarized the main themes and the general structure of the thesis.

The second chapter is dedicated to the growth and study of graphene, which is the archetype of this class of materials. After an introduction on its electrical properties and on its growth on conventional metal single crystals, the chapter is divided into four sections that cover specific issues. Paragraphs 2.1.1 and 2.1.2 examine the properties of graphene and nitrogen doped graphene in contact with ultra-thin layers of iron. The section 2.2 studies the reaction of water with graphene grown on nickel single crystal, for the production of hydrogen. The paragraph 2.3 describes the growth of graphene on an unconventional substrate: platinum nickel alloy (Pt_3Ni).

The third chapter is devoted to the study of other two-dimensional materials firstly introducing the studied materials: hexagonal boron nitride, transition metals dichalcogenides, other layered chalcogenides and heterostructures. Afterward, this chapter continues with three specific sections: paragraphs 3.1.1 and 3.1.2 are dedicated to two innovative methods for preparing heterostructures under ultra-high vacuum conditions. The section 3.1.1 presents a new strategy to synthesize monolayer *in-plane* heterostructure composed by graphene and hexagonal boron nitride, the 3.1.2 discusses a versatile route to create vertically stacked heterostructures of various two-dimensional materials. The last paragraph, 3.2, reports a detailed investigation of the electronic and chemical properties of a bulk layered chalcogenide, indium selenide.

The fourth chapter summarizes the main conclusions of the work.

Abstract (Italian version)

In questi tre anni di progetto di dottorato ho esplorato parte del mondo dei materiali bidimensionali. Il mio lavoro si è concentrato sull'analisi e la crescita di materiali bidimensionali con tecniche della Scienza delle Superfici. Per la crescita sono stati utilizzati sia metodi chimici, come la decomposizione di precursori gassosi, che fisici, come l'evaporazione di metalli in condizioni di ultra alto vuoto. Il metodo principale usato per studiare le proprietà di questi materiali è stata la fotoemissione da livelli di core e dalla banda di valenza.

I materiali sono stati in gran parte cresciuti e analizzati direttamente *in-situ*, cioè evitando l'esposizione all'aria che ne altera le loro proprietà. Prendendo spunto dai risultati sui singoli materiali ho ulteriormente ampliato le mia ricerca verso complesse eterostrutture, ossia delle architetture artificiali di materiali bidimensionali. I sistemi derivanti da diverse combinazioni di grafene, nitruro di boro esagonale e calcogenuri bidimensionali sono stati prodotti e analizzati con lo scopo di rivelare la relazioni tra struttura e attività nelle eterostrutture.

La tesi è divisa in quattro capitoli principali.

Il primo è un'introduzione al mondo dei materiali bidimensionali e riassume i temi principali e la struttura generale della tesi.

Il secondo capitolo è dedicato alla crescita e allo studio del grafene, archetipo di questa classe di materiali. Dopo un'introduzione sulle sue proprietà elettriche e sulla sua crescita su monocristalli metallici convenzionali il capitolo si suddivide in quattro sezioni che trattano tematiche specifiche. I paragrafi 2.1.1 e 2.1.2 esaminano le proprietà di grafene e grafene drogato azoto in contatto con strati ultrasottili di ferro. La sezione 2.2 studia la reazione dell'acqua con grafene cresciuto su monocristallo di nickel, per la produzione di idrogeno. Il paragrafo 2.3 descrive la crescita di grafene su un substrato non convenzionale: una lega di platino e nickel (Pt_3Ni).

Il terzo capitolo è rivolto allo studio di altri materiali bidimensionali, innanzitutto introduce i materiali trattati: nitruro di boro esagonale, dicalcogenuri di metalli di transizione, altri calcogenuri stratificati e le eterostrutture. Poi prosegue con tre sezioni specifiche; i paragrafi 3.1.1 e 3.1.2 sono dedicati a due metodi innovativi per formare eterostrutture in condizioni di ultra alto vuoto. La sezione 3.1.1 presenta un nuovo metodo per sintetizzare l'eterostruttura nel piano composta da grafene e nitruro di boro esagonale, la 3.1.2 propone un metodo versatile per creare eterostrutture impilate verticalmente di vari materiali bidimensionali. L'ultimo paragrafo, 3.2, riporta una ricerca dettagliata sulle proprietà elettroniche e chimiche di un calcogenuro stratificato massivo, l'indio seleniuro.

Il quarto capitolo riassume le conclusioni del lavoro.

1. Introduction

Graphene (G), a single layer of hybridized sp^2 carbon atoms, has attracted the world attention after its re-discovery in 2004 by A. K. Geim and K. Novosëlov who were awarded the 2010 Nobel Prize in Physics *"for groundbreaking experiments regarding the two-dimensional material graphene"*.[1]

Its exceptional properties such as: room temperature (RT) electron mobility of 2.5×10^5 cm^2/Vs,[2] Young's modulus of 1 TPa, intrinsic strength of 130 GPa,[3] very high thermal conductivity,[4] optical absorption of exactly $\pi\alpha \approx 2.3$ % (in the infrared limit, where α is the fine structure constant),[5] ability to sustain extremely high densities of electric current (a million times larger than copper),[6] and the possibility to be chemically functionalized,[7,8,9,10] make G one of the most studied materials nowadays. A real research "boom" approximately started in 2006-2007, and only in 2014, more than 11000 publications in international journals present the word "graphene" in their title (Figure 1).

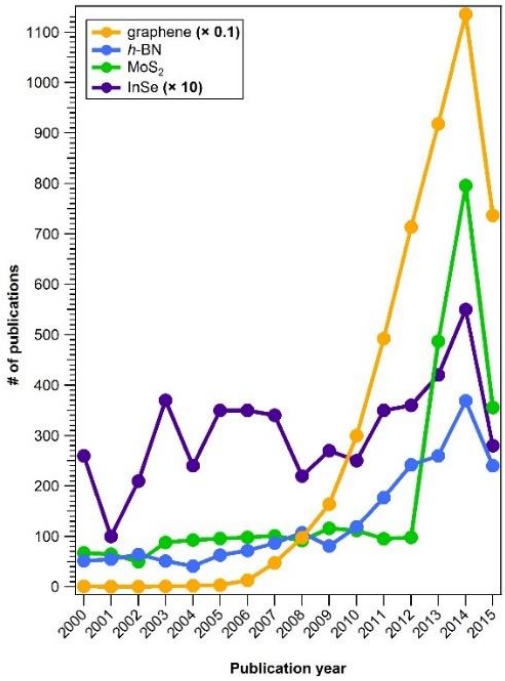

Figure 1. Number of publications with "graphene" (multiply by a factor 0.1), "h-BN", "MoS_2" and InSe (multiply by a factor of 10) contained in their title. Survey conducted using www.scopus.com .

Because of this huge publication number, this introduction is not thought as a comprehensive overview of the "graphene world", but it is focusing only on selected aspects relevant for the understanding of the present work. In the present thesis not only G but also other two-dimensional (2D) materials have been investigated. Therefore each section starts with a small introductive paragraph dealing with the specific topic pertaining to a selected material.

The aim of this chapter is to explain why scientists are moving from the study of G to the investigation of other 2D materials. Moreover, at the end there is a brief description summarizing the different sections that constitute this thesis.

Graphene is not alone

G has been applied in several science and technology fields ranging from electronics to energetics, from catalyst to optoelectronics, from medicine to sensors etc.[11]The first studies on G were aimed to exploit its unique electronic properties as substitute for silicon in electronic devices.[12] The main problem however is to open a sufficiently large band gap in the semimetallic band structure of G, in order to obtain a good on/off ratio for field effect transistors. In this context great efforts have been made by introducing chemical doping or exploiting metal interactions, but these methods proved to be inadequate to open energy gaps large enough for practical applications. Therefore, researchers in this field are moving principally in three different ways:

- the first is to exploit strong chemical modification of G by hydrogenation in graphane[7] (band gap ≈ 3.5 eV)[13] or fluorination in fluorographene (band gap ≈ 3 eV);[9]
- the second is downsizing G, from 2D to 1D, in G nanoribbons, which have an intrinsic band gap;[14]
- the third is to exploit other G properties to invent completely new devices without the need to induce band gap in the electronic structure, e.g. the multinational Samsun studied a device based on triode setup, called barristore, that uses the shift of G Fermi level position by an external potential.[15]

However, soon after the G discovery, the necessity to find efficient materials for electronics pushed scientists "off the graphene road". Indeed, probably one of the most important contribution to Science given by G it is not about G itself, but is to have opened the "Science eyes" to the 2D materials world. Researchers have turned their attention to other materials with intrinsic band gap and other interesting properties to create new devices.

In its illuminating "Van der Waals heterostructure"[16] perspective paper published in 2013, the Nobel prize Prof. Geim tried to summarize the "2D material library" in the following Table 1.

Table 1. Monolayers proved to be stable under ambient conditions (RT in air) are shaded blue; those probably stable in air are shaded green; and those unstable in air but that may be stable in inert atmosphere are shaded pink. Grey shading indicates 3D compounds that have been successfully exfoliated down to monolayers. 'Others' indicates that many other 2D crystals, including borides, carbides, nitrides and so on, have probably been or can be isolated. BCN and BSCCO stands for boron carbon nitride and bismuth strontium calcium copper oxide, respectively. Reprinted from Ref. [16] © 2013 NPG.

<table>
<tr><td>Graphene family</td><td>Graphene</td><td colspan="2">hBN
'white graphene'</td><td>BCN</td><td>Fluorographene</td><td>Graphene oxide</td></tr>
<tr><td rowspan="2">2D chalcogenides</td><td colspan="2" rowspan="2">MoS_2, WS_2, $MoSe_2$, WSe_2</td><td colspan="2" rowspan="2">Semiconducting dichalcogenides:
$MoTe_2$, WTe_2,
ZrS_2, $ZrSe_2$ and so on</td><td colspan="2">Metallic dichalcogenides:
$NbSe_2$, NbS_2, TaS_2, TiS_2, $NiSe_2$ and so on</td></tr>
<tr><td colspan="2">Layered semiconductors:
GaSe, GaTe, InSe, Bi_2Se_3 and so on</td></tr>
<tr><td rowspan="2">2D oxides</td><td>Micas, BSCCO</td><td colspan="2">MoO_3, WO_3</td><td colspan="2" rowspan="2">Perovskite-type:
$LaNb_2O_7$, $(Ca,Sr)_2Nb_3O_{10}$,
$Bi_4Ti_3O_{12}$, $Ca_2Ta_2TiO_{10}$ and so on</td><td>Hydroxides:
$Ni(OH)_2$, $Eu(OH)_2$ and so on</td></tr>
<tr><td>Layered Cu oxides</td><td colspan="2">TiO_2, MnO_2, V_2O_5,
TaO_3, RuO_2 and so on</td><td>Others</td></tr>
</table>

It is interesting to note that in Table 1 phosphorene, a single layer of black phosphorus, which is currently a hot-topic 2D material,[17] is not even reported nor mentioned in the text, as, on the contrary, is done for silicene (a single layer of silicon atoms arranged in a honeycomb lattice).[18] This notable absence, observed in a paper only two years old, can be understood by the incredibly fast pace of this new exciting field research where new materials are explored every day.

One of the first 2D material that has been re-discovered after G, is hexagonal boron nitride (*h*-BN)[19], which is the insulating counterpart of G constitute by boron and nitrogen atoms arranged in hexagonal lattice. In Figure 1 is clearly visible an increase in publications number with *h*-BN in their title in 2010-2011, about four years later of the "graphene boom". Another example of "old material" that has been brought of the world attention in its monolayer form is the molybdenite, MoS_2,[20] the increase of the publication number is more recent, about 2012 (Figure 1), and it is only the most notable first transition metal dichalcogenides (TMDs) that are studied nowadays.

As for G, in the beginning they have been investigated for their electronic properties: monolayer *h*-BN is an insulator with band gap of 5.97 eV,[21] whereas monolayer MoS_2 in its trigonal prismatic phase (called 2H) is a direct gap semiconductor with a band gap of 1.8 eV.[20] In addition, these materials exhibit also several other interesting properties, e.g. monolayer MoS_2 shows remarkable photoluminescence (PL) properties[22] and is a good catalyst for the hydrogen evolution reaction (HER).[23]

The link of these two materials to G is clear; their bulk counterparts are layered crystals with planes kept together by van der Waals forces. For initial studies they have been isolated in monolayer form, using the same method developed by Novosëlov and Geim for graphite some years ago i.e. by mechanical exfoliation (Scotch-tape method). Mechanical exfoliation has a pivotal role in fundamental science on exfoliable layered materials because, at the moment, it allows producing flakes with the highest quality. Therefore, all fundamental characterizations (Raman spectroscopy, photoemission spectra, electrical measurements, etc.…) can be carried out in sub-micrometric areas using *state-of-art* technology. Interestingly, uncomplete exfoliation (i.e. the formation of variably stacked systems) is not always a problem but an opportunity to study how properties change as function of the number of layers. An example of a typical micro Raman characterization of mechanically exfoliated MoS_2 is reported in Figure 2.

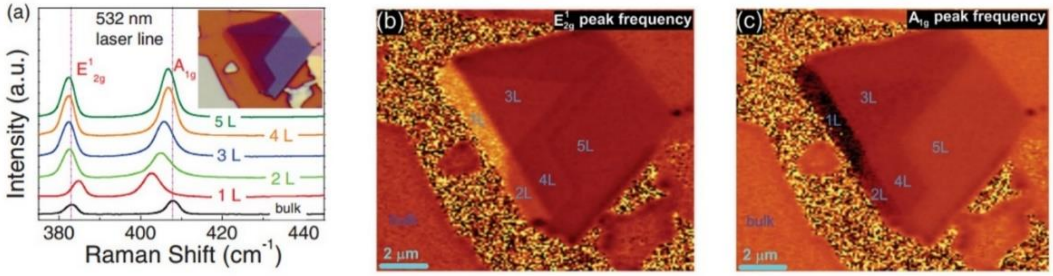

Figure 2. Raman characterizations of mechanically exfoliated MoS_2 using 532 nm line. a) The Raman spectra of different locations with various thicknesses. Inset: optical image of sample S2. The left and right dashed lines indicate the positions of the E^1_{2g} and A_{1g} peaks in bulk MoS_2, respectively. Raman mapping image with (b) the E^1_{2g} peak frequency and (c) the A_{1g} peak frequency. The scale bars represent 2 μm. "1 L", "2 L", "3 L", "4 L", and "5 L" indicate monolayer, bilayer, trilayer, quadrilayer, and quinquelayer, respectively. Adapted from Ref. [24] © 2012 Wiley.

However, nowadays the "low hanging fruits" of the "2D material tree", i.e. layered bulk materials with a good oxidation resistance, have already been harvested, and researchers have now started paying more attention to other 2D materials and the mechanical exfoliation method is showing all its limit in this new mission.

For example some materials, e.g. phosphorene, are becoming more and more popular even if they oxidize very easily in air.[25] Various techniques have been used to stabilize these materials, for example oxidizable layers can be protected by stable 2D sheets not permeable to gases, such as G or *h*-BN.[26] This method implies the access of advanced equipment such as clean-rooms, vacuum annealing chambers to remove the carbon contamination, (which is usually thicker than the studied 2D sheets themselves[27]), alignment systems and, most importantly, all these processes require a lot of experience and therefore are very operator-dependent. Moreover, other 2D materials that are not naturally found as layered material, such as silicene, unfortunately are not achievable by mechanical exfoliation.

All these problems are solved by bottom-up syntheses, such as chemical vapour deposition (CVD) and molecular beam epitaxy (MBE), which can be carried out in controlled atmosphere, e.g. ultra-high vacuum (UHV) conditions. These techniques allow producing several types of materials by a careful assembly of isolated atoms, and has the great advantage of being industrially scalable methods. Two main drawbacks however affect CVD and MBE: typically the flakes are smaller than those obtained mechanical exfoliation and the growth process required a catalytic substrate, which is often a metal substrate but also oxides have recently emerged. Often, the supporting catalyst must be removed in order to transfer 2D sheets on arbitrary low interacting substrates. This process is usually carried out by complex transfer procedures[28] that can eliminate completely the advantages connected to a clean bottom-up synthesis.[29]

A larger and larger research field is addressing the realization of 2D heterostructures.[16] These can be built by stacking 2D materials on top of each other, not only to protect easy oxidizable materials,[25,26] but also to create innovative junctions with unique properties. An example is reported in Figure 3, where the PL of WSe_2/MoS_2 heterojunction can be opportunely tuned introducing *h*-BN spacers in between the two layers.[30] 2D heterojunctions can be formed also by stitching together the nanosheets forming seamless *in-plane* boundaries in order to form flat heterostructures.

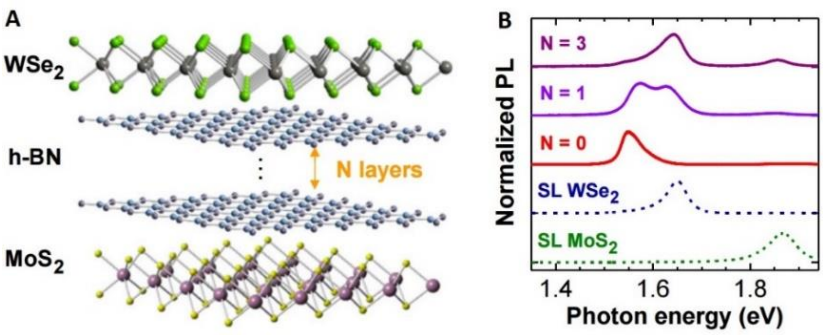

Figure 3. (A) An atomistic illustration of the heterostructure of WSe_2/ MoS_2 with few-layer h-BN spacer in the van der Walls gap. (B) Normalized PL spectra from WSe_2/ MoS_2 heterostructure with n layers of h-BN (n = 0, 1, and 3). Adapted from Ref. [30] © 2014 PNAS.

Bottom-up syntheses allow creating these innovative stacked structures based on van der Waals epitaxy where different 2D layers relate each other with precise stacking orientation and with sharp and clean interfaces, i.e. without impurities as water or hydrocarbons, by using this kind of syntheses *in-plane* junctions are also attainable. On the contrary, mechanical exfoliation method allows only stacking different materials without precise orientation and *in-plane* junctions are not feasible. This significant difference is due to the different concepts behind the two methodologies. In bottom-up methods single atoms (or small group of atoms) can diffuse on a surface and arrange to form stable structures, and synthesis can be stopped in any moment controlling defectivity or island size. The versatility of the methods is granted by the control of several parameters, such as temperature, reactant pressures, substrates, etc. On the contrary, mechanical exfoliation method implies to use of pre-formed micrometric sheets that can be only stacked or post processed, e.g. by deposition of metallic contacts or functionalization.

A representative sketch of possible heterostructures formed by two TMDs via CVD is reported in Figure 4.

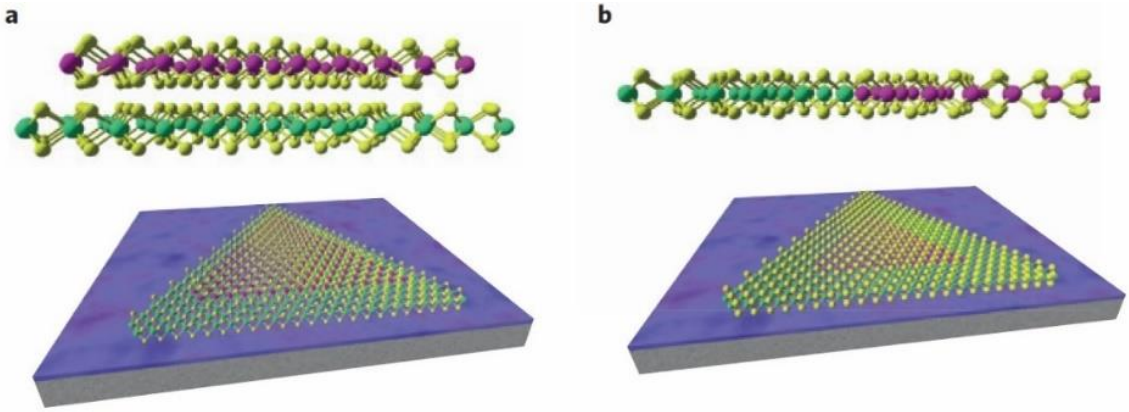

Figure 4. Schematic representation of heterojunctions between two different transition metal dichalcogenides, for example, between MoS_2 and WS_2. Mo, W and S atoms are represented by green, pink and yellow spheres, respectively. WS_2 can grow on top of (a) or laterally from (b) a MoS_2 monolayer by changing the growth parameters during chemical vapour deposition (bottom). Cross sections of the heterojunctions are also shown (top). Reprinted from Ref. [31] © 2014 NPG.

The vast possibility of parameters for bottom-up syntheses on the other hand can represent disadvantage in this extremely dynamic field research because they require a lot of time to optimize the growth of every single different 2D materials. However bottom-up approaches, even if are more complex, are essential for the future large scale production of these materials.

The principal pros and cons of mechanical exfoliation methods and bottom-up syntheses are summarized in Table 2.

Table 2. List of principal advantages or disadvantages of mechanical exfoliation and bottom-up production of 2D materials.

	Mechanical exfoliation method	**Bottom-up syntheses**
Advantages	Highest quality, easy to operate, easy to change material, optimal for fundamental science.	Scalable method, controllable orientation, *in-plane* and stacked junctions, controllable atmosphere, almost infinite possibilities of materials
Disadvantages	Exposed to air contaminants and oxidation, not scalable, only stacked junctions without controllable orientation, limited to bulk layered materials.	Lower quality, smaller grains, catalytic substrate usually required, time-consuming to optimize growth and layer quality, difficult to change materials.

Research line of the Surface Science and Catalysis group

The huge number of publications in the 2D materials field research (see Figure 1) means also a fierce competition that is the principal driving force that is pushing researchers to study constantly new unexplored materials, looking for the "new graphene".

A logic consequence of being a Surface Science group equipped with facilities for fundamental studies of ultra-thin layers and a consolidate experience in advanced synchrotron characterization, is to use our expertise in synthesis and characterization of surfaces in this new field where materials themselves are surfaces.

Since having the possibility to operate under UHV conditions, we performed almost exclusively *in-situ* experiments, i.e. we carried out materials synthesis and characterization in UHV chambers maintaining the samples at pressure below $<10^{-8}$ mbar. Experiments have been usually repeated also in various synchrotron facilities in order to performed *state-of-art* characterization. By working in such controlled atmosphere we avoid two important problems: first materials do not oxidize and second there is no carbon contamination from the environment. This allows us to investigate the pristine properties of materials.

Because of the intrinsic disadvantage of bottom-up syntheses (see Table 2) such as long time for experiment optimization, and to get access to synchrotron facilities (each proposal takes about six months to be evaluated by synchrotron committees and scheduled), we had to make a compromise between to study effectively well-known materials, e.g. G and *h*-BN, and to explore new ones, such as WS_2, WSe_2 and InSe.

The latter were chosen in the prospective to study most innovative 2D materials. Tungsten disulphide and diseleneide were selected from the TMDs family for their good electrochemical[32] and optoelectronical properties.[33] Indium selenide is a layered material that is currently studied for its good electrical and optical properties.[34] Actually a detailed investigation of some of its bulk properties was still

missing in the literature, which is pivotal to pave the way for new applications. From a methodological point of view, this material represents an exception in this thesis, we decided to study vacuum exfoliated bulk crystals instead to synthetized it via bottom-up synthesis.

We also explore both *in-plane* and stacked heterostructures composed by different 2D materials exploiting the great advantage offered by the bottom-up syntheses (Table 2). Our idea was to couple different materials to obtain possible interesting heterostructures as ideally reported in the Venn diagram in Figure 5.

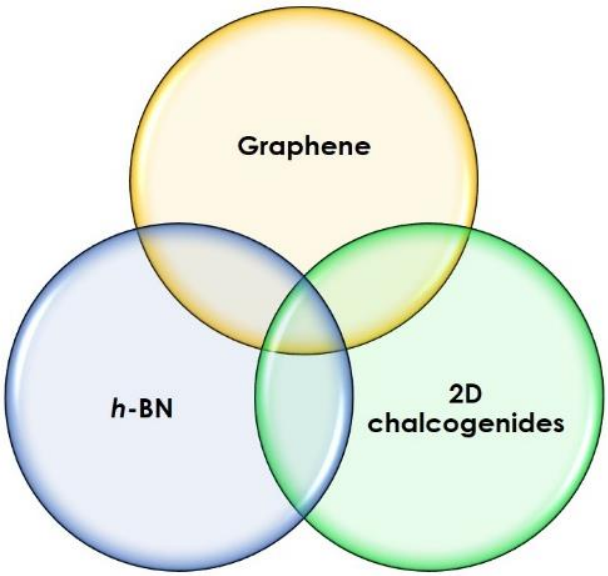

Figure 5. Scheme to represent the possible heterostructures create by different 2D materials.

Thesis structure

This thesis is divided in two main sections called "Graphene" and "Other 2D materials and heterostructures". Every chapter contains paragraphs where a single topic on a precise material or heterostructure is taken into account.

We put a great deal of effort into the study of G in contact with different metals. Simple syntheses of well-known 2D material on classic substrates, e.g. growth of G and *h*-BN on Pt(111) and Ni(111) single crystals, are well-known in the literature, therefore we turned our attention on more specific subjects. In sections 2.1.1 and 2.1.2 are reported studies of the interaction of G and nitrogen doped G (N-G) grown on Pt(111) with an ultra-thin layer of iron. In section 2.2 G grown on Ni(111) has been studied for its reaction with water, and only section 2.3 is focused on the synthesis of G because it has been carried out on an unconventional substrate, a bulk alloy $Pt_3Ni(111)$.

In sections 3.1.1 and 3.1.2 *h*-BN and G were used as a constituent of innovative 2D heterostructures. Finally in section 3.2 we exploited our acquired knowledge of the chemical and electronical properties of 2D materials to study one of the most innovative layered material, InSe.

In Figure 6 is reported a Venn scheme representative of this thesis.

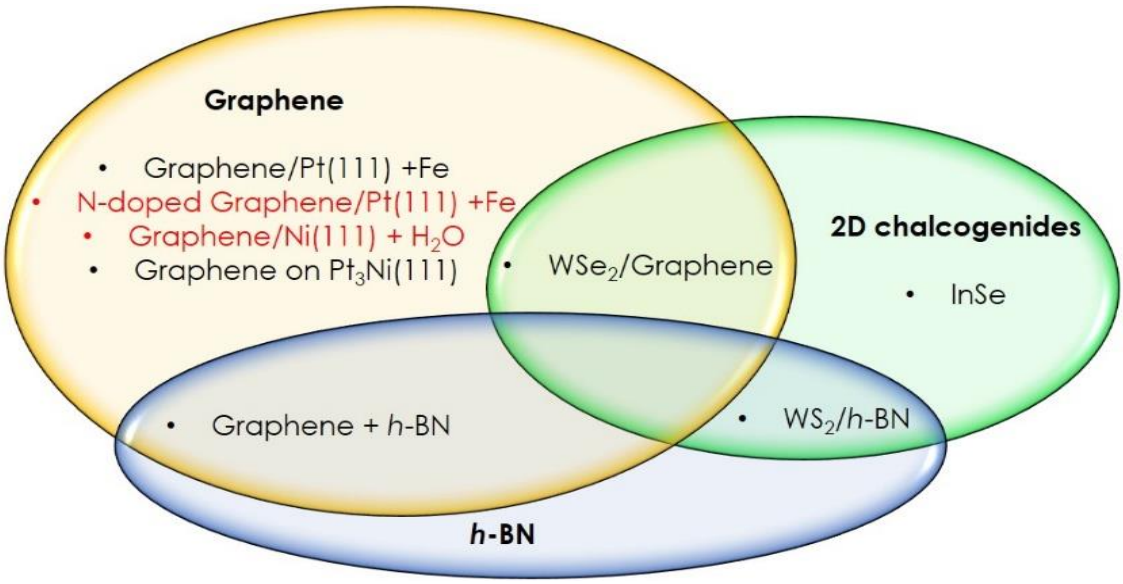

Figure 6. Representative scheme of this thesis, the section related to catalysis are reported in red.

References

1 Geim, A. K.; Nobel Lecture: Random walk to graphene. *Rev. Mod. Phys.* **2011**, *83*, 851

2 Mayorov, A. S.; Gorbachev, R. V.; Morozov, S. V.; Britnell, L.; Jalil, R.; Ponomarenko, L. A.; Blake, P.; Novoselov, K. S.; Watanabe, K.; Taniguchi, T.; Geim, A. K. Micrometer-scale ballistic transport in encapsulated graphene at room temperature. *Nano Lett.* **2011**, *11*, 2396.

3 Lee, C.; Wei, X. D.; Kysar, J. W.; Hone, J. Measurement of the elastic properties and intrinsic strength of monolayer graphene. *Science* **2008**, *321*, 385.

4 Balandin, A. A. Thermal properties of graphene and nanostructured carbon materials. *Nature Mater.* **2011**, *10*, 569.

5 Nair, R. R.; Grigorenko, A. N.; Novoselov, K. S.; Booth, T. J.; Stauber, T.; Peres, N. M. R.; Geim, A. K. Fine structure constant defines visual transparency of graphene. *Science* **2008**, *320*, 1308.

6 Moser, J., Barreiro, A. & Bachtold, A. Current-induced cleaning of graphene. *Appl. Phys. Lett.* **2007**, *91*, 163513.

7 Elias, D. C.; Nair, R. R.; Mohiuddin, T. M. G.; Morozov, S. V.; Blake, P.; Halsall, M. P.; Ferrari, A. C.; Boukhvalov, D. W.; Katsnelson, M. I.; Geim, A. K.; Novoselov, K. S. Control of graphene's properties by reversible hydrogenation: evidence for graphane. *Science*, **2009**, *323*, 610.

8 Loh, K. P.; Bao, Q. L.; Ang, P. K.; Yang, J. X. The chemistry of graphene. *J. Mater. Chem.* **2010,** *20*, 2277.

9 Nair, R. R.; Ren, W.; Jalil, R.; Riaz, I.; kravets, V. G.; Britnell, L.; Blake. P.; Schedin, F.; Mayorov, A. S.; Yuan, S.; Katsnelson, M. I.; Cheng, H.-M.; Strupinski, W.; Bulusheva, L. G.; Okotrub, A. V.; Grigorieva, I. V.; Grigorenko, A. N.; Novoselov, K. S.; Geim, A. K. Fluorographene: a two-dimensional counterpart of Teflon. *Small* **2010**, *6*, 2877.

10 Dreyer, D. R.; Park, S.; Bielawski, C. W.; Ruoff, R. S. The chemistry of graphene oxide. *Chem. Soc. Rev.* **2012**, *39*, 228.

11 Novoselov, K. S.; Fal'ko, V. S.; Colombo, L.; Gellert, P. R.; Schwab, M. G.; Kim, K. A roadmap for graphene. *Nature* **2012**, *490*, 192.

12 Schwierz, F. Graphene transistors. *Nat. Nanotech.* **2010**, *5*, 487.

13 Sofo, J. O.; Chaudhari, A. S.; Barber. G. D. Graphane: A two-dimensional hydrocarbon. *Phys. Rev. B* **2007**, *75*, 153401.

14 Li, X.; Wang, X.; Zhang, L.; Lee, S.; Dai, H.; Chemically derived, ultrasmooth graphene nanoribbon semiconductors. *Science* **2008**, *319*, 1229.

15 Yang, H.; Heo, J.; Seongjun, P.; Song, H. J.; Seo, S. H.; Byun, K.-H.; Kim, P.; yoo, I; Chung, H.-J.; Kim, K.; Graphene barristor, a triode device with a gate-controlled schottky barrier. *Science* **2012**, *336*, 1140.

16 Geim, A. K.; Grigorieva, I. V. Van der Waals heterostructures. *Nature* **2013**, *499*, 419.

[17] Reich, R. S. Phosphorene excites materials scientists. *Nature* **2014**, *506,*19.

[18] Vogt, P.; De Padova, P.; Quaresima, C.; Avila, J.; Frantzeskakis, E.; Asensio, M. C.; Resta, A.; Ealet, B.; Le Lay, G. Silicene: Compelling experimental evidence for graphenelike two-dimensional silicon. *Phys. Rev. Lett.* **2012**, *108*, 155501.

[19] Pakdel, A.; Bando, Y.; Golberg, D. Nano boron nitride flatland. *Chem. Soc. Rev.*, **2014**, *43*, 934.

[20] B. Radisavljevic, A. Radenovic, J. Brivio, V. Giacometti, A. Kis Single-layer MoS_2 transistors. Nat. Nanotech. **2011**, *6*, 147.

[21] Kubota, Y.; Watanabe, K.; Tsuda, O.; Taniguchi, T. Deep ultraviolet light-emitting hexagonal boron nitride synthesized at atmospheric pressure. *Science* **2007**, *317*, 932.

[22] Splendiani, A.; Sun, L.; Zhang, Y.; Li, T.; Kim, J.; Chim, C.-Y.; Galli, G.; Wang, F. Emerging photoluminescence in monolayer MoS_2. *Nano Lett.*, **2010**, *10*, 1271.

[23] Lukowski, M. A.; Daniel, A. S.; Meng, F.; Forticaux, A.; Li, L.; Jin, S. Enhanced Hydrogen Evolution Catalysis from Chemically Exfoliated Metallic MoS_2 Nanosheets. *J. Am. Chem. Soc*. **2013**, *135*, 10274.

[24] Li, H.; Zhang, Q.; Yap, C. C. R.; Tay, B. K.; Edwin, T. H. T.; Olivier, A.; Baillargeat, D. From bulk to monolayer MoS_2: evolution of Raman scattering. *Adv. Funct. Mater.* **2012**, *22*, 1385.

[25] Cao, Y.; Mishchenko, A.; Yu, G. L.; Khestanova, E.; Rooney, A. P.; Prestat, E.; Kretinin, A. V., Blake, P.; Shalom, M. B.; Woods, C.; Chapman, J.; Balakrishanan, Grigorieva, I. V.; Novoselov, K.; Piot, B. A.; Potemski, M.; Watanabe, K.; Taniguchi, T.; Haigh, S. J.; Geim, A. K.; Gorbachev, R. V. Quality heterostructures from two-dimensional crystals unstable in air by their assembly in inert atmosphere. *Nano Lett.,* **2015**, *15*, 4914.

[26] Gillgren, N.; Wickramaratne, D.; Shi, Y.; Espiritu, T.; Yang, J.; Hu, J.; Wei, J.; Liu, X.; Mao, Z.; Watanabe, K.; Taniguchi, T.; Bockrath, M.; Barlas, Y.; Lake, R. K.; Lau, C. N. Gate tunable quantum oscillations in air-stable and high mobility few-layer phosphorene heterostructures. *2D Mater*, **2015**, *2*, 011001.

[27] Haigh, S. J.; Gholinia, A.; Jalil, R.; Romani, S.; Britnell, L.; Elias, D. C.; Novoselov, K. S.; Ponomarenko, L. A.; Geim, A. K.; Gorbachev, R. Cross-sectional imaging of individual layers and buried interfaces of graphene-based heterostructures and superlattices. *Nat. Mater*. **2012**, *11*, 764.

[28] Levendorf, M. P.; Ruiz-Vargas, C. S.; Garg, S.; Park, J. Transfer-free batch fabrication of single layer graphene transistors. *Nano Lett.,* **2009**, *9*, 4479.

[29] Ambrosi, A.; Pumera, M. The CVD graphene transfer procedure introduces metallic impurities which alter the graphene electrochemical properties. *Nanoscale* **2014**, *6*, 472.

[30] Fang, H.; Battaglia, C.; Carraro, C.; Nemsak, S.; Ozdol, B.; Kang, J. S.; Bechtel, H. A.; Desai, S. B.; Kronast, F.; Unal, A. A. M.; Conti, G.; Conlon, C.; Palsson, G. K.; Martin, M. C.; Minor, A. M.; Fadley, C. S.; Yablonovitch, E.; Maboudian, R.; Javey, A. Strong interlayer coupling in van der Waals heterostructures built from single-layer chalcogenides. *Proc. Natl. Acad. Sci. U S A.*, **2014**, *111*, 6198.

[31] Duesberg, G. S. Heterojunctions in 2D semiconductors. A perfect match. *Nat. Mater.*, **2014**, *13*, 1075.

[32] Voiry, D.; Yamaguchi, H.; Li, J.; Silva, R.; Alves, D. C. B.; Fujita, T.; Chen, M.; Asefa, T.; Shenoy, V. B.; Eda, G.; Chhowalla, M. Enhanced catalytic activity in strained chemically exfoliated WS_2 nanosheets for hydrogen evolution. *Nat. Mater.* **2013**, *12*, 850.

[33] Koperski, M.; Nogajewski, K.; Arora, A.; Cherkez, V.; Mallet, P.; Veuillen, J.-Y.; Marcus, J.; Kossacki, P.; Potemski, M. Single photon emitters in exfoliated WSe_2 structures. *Nat. Nanotech.* **2015**, *10*, 503.

[34] Sucharitakul, S.; Goble, N. J.; Kumar, U. R.; Sankar, R.; Bogorad, Z. A.; Chou, F.-C.; Chen, Y.-T.; Gao, X. P. A. Intrinsic electron mobility exceeding 10^3 $cm^2/(V\ s)$ in multilayer InSe FETs. *Nano Lett.*, **2015**, *15*, 3815.

2. Graphene

Graphene electronic properties in brief

A. K. Geim and K. Novosëlov focused their attention on G because of its peculiar electronic structure predicted already by P. R. Wallace[1] in 1947. This first study was followed by several other theoretical predictions[2] of the special properties of G and graphite. For example J. W. McClure emphasized the presence of Dirac-like quasiparticles,[3] which was re-iterated several years later by G. Semenoff.[4]

These studies indicate that G is a semi-metal, i.e. it has zero bandgap, with linear dispersion of the energy vs momentum around the chemical potential, which determines the formation of cones in the two-dimensional reciprocal space. This results is quite surprising because most of the matter waves exhibit quadratic dispersions following the Schrödinger equation, which is first order in time and second order in space. In the simplest model (e.g. free electrons), it leads to the following dispersion for the conduction and valence bands, respectively:

$$E_S(k)=E_{C,V}+\frac{\hbar^2|k|^2}{2m_{C,V}} \quad (1)$$

where $E_{C,V}$ are the conduction and valence band (VB) edges and $m_{C,V}$ are the effective masses of electrons in the conduction band and holes in the VB, respectively (m_V is negative, S subscript is for Schrödinger). One gets zero band gap for $E_C = E_V$; however, the E vs k dispersion still remains quadratic.

In contrast to the Schrödinger equation, the dispersion for the Dirac equation is

$$E_D(k)=\pm\sqrt{m^2c^4+\hbar^2c^2|k|^2} \quad (2)$$

where c is the speed of light and m is the relativistic mass (D subscript is for Dirac).

The positive and negative dispersion plots are shown in Figure 1, which shows a mass-dependent gap of $2mc^2$ between the positive energy of matter (electron in this case) and the negative energy of anti-matter (positron; the mc^2 product for an electron is about 0.512 MeV). In the limiting case of m=0, clearly the gap becomes zero. Furthermore, equation 2, becomes:

$$E_D(k)=\pm\hbar c|k| \quad (3)$$

which is plotted in Figure 1, where it can be noticed the linear E vs k dispersion with zero bandgap.

As a reference, the band structure of G is shown in Figure 1, which follows the following equation based on tight-binding description:[5]

$$E_G(k)=\pm t\sqrt{1+4\cos\left(\frac{3k_xa_{cc}}{2}\right)\cos\left(\frac{\sqrt{3}k_ya_{cc}}{2}\right)+4\cos^2\left(\frac{\sqrt{3}k_ya_{cc}}{2}\right)} \quad (4)$$

where a_{cc}=1.42 Å is the C–C bond length and t is the first nearest-neighbour tight-binding parameter. The band gap is zero and the dispersion is linear around the points where conduction and valence bands meet with a renormalized velocity v resulting in:

$$E_G(k)=\pm\hbar v|k| \quad (5)$$

which is similar to the dispersion of Dirac's in formula 3.

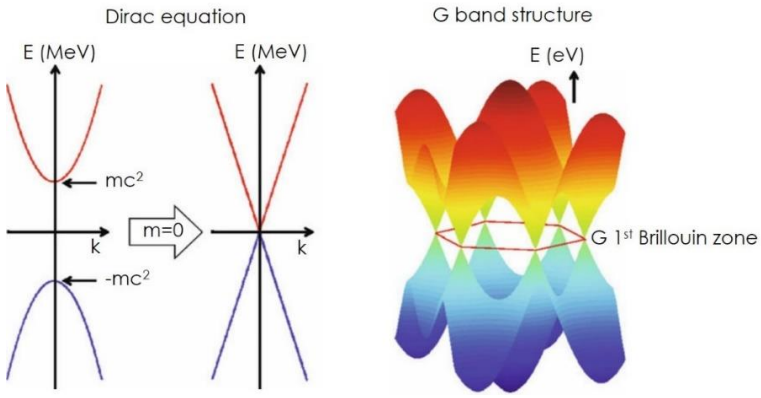

Figure 1. Sketches of G band structure. Dirac dispersions with $2mc^2$ gap are shown. In the limit of m=0, the gap becomes zero with a linear dispersion, where the energy scale is of the order of MeV. Similarly, the G band structure has a linear dispersion with zero gap around the Dirac point, although the energy is in the eV range.

This analogy suggests that in G electrons and holes act like Dirac fermions with zero mass and hence zero gap. In other words, charge carriers are mass-less relativistic Dirac fermions with points of intersection between conduction and valence bands labelled as Dirac point. The E vs k dispersion curves of electron and holes therefore form two-dimensional cones around the Dirac points, which are usually referred to as "Dirac cones". Furthermore, there are six points inside the first Brillouin zone where the conduction and the valence bands meet as shown in Figure 1. Although, one may think that there are six Dirac points, with careful analysis, one concludes that only two points are inequivalent. Interestingly, these two points are related by the time-inversion symmetry.

What in 1947[1] was only a calculation, after 57 years was experimentally verified, using advanced spectroscopy techniques, such as angle resolved photoemission spectroscopy (ARPES), and the G band structure with the six Dirac cones could be directly visualized.

The first calculations were carried out on a perfect infinite freestanding layer of sp^2 carbons, but this is only an idealization of G. In the real life, G is in contact with other substances, it has intrinsic defectivity and a definite size, and therefore much more detailed and precise calculations must be used to predict its practical properties. Density functional theory (DFT) has been used in section 2.1.1 to simulate G band hybridization in contact with Pt(111) and Fe ultrathin layers.

In the following paragraphs is presented a short review on the preparation methods of G with special focus on the bottom-up synthesis on transition metals used in this thesis.

Preparation methods

The outstanding properties of G have kindled the interest of a significant number of researchers to look into methods of producing high purity G layers in a large scale.

As mentioned in "Introduction" section, in 2004 A. K. Geim and K. Novosëlov developed the mechanical exfoliation method to isolate G starting from highly ordered pyrolytic graphite (HOPG).[6] This method produces G with a perfect crystal structure, as predefined in HOPG, however it is not a scalable process to produce large-area G sheets. Furthermore, the size of the G produced by this method is usually of the order of micrometres and incomplete exfoliation (i.e. formation of stacked layers) is very common.

Wet chemical exfoliation of G can be performed through an ultrasonication treatment of graphite powders using polymer–organic solvents[7] or organic solvents[8] with a surface energy that matches that of G. This approach produces G with a bigger size, but prolonged exposure to sonication may cause structural damage.

G can be chemically derived from graphite using as intermediate G oxide (GO), which can be prepared by the Hummers[9] method. GO is dispersible in water because of the interaction between water and oxygen-containing functionalities introduced in its basal plane. These species make GO hydrophilic, which causes water to readily intercalate between the G sheets and disperse them as individual sheets under mild sonication.[10] Various methods have been reported to reduce GO to G,[11] as example via thermal annealing,[12] or using different type of chemical agents like hydrazine, $NaBH_4$, ascorbic acid etc. However, it is difficult for GO to be reduced to a perfect G sheet because the reduction process introduces structural defects into the sp^2 layer.

Two different bottom up approaches are widely used to grow wafer-scale G, namely, the epitaxial growth of G from SiC and the catalytic growth on transition metals by decomposition of carbon precursors.

The advantages of epitaxial SiC growth reside on the ability to produce monolayers of G in a controllable manner by the thermal decomposition of the substrate. When SiC is heated the in vacuum or in inter atmosphere, only the silicon atoms leave the surface due to the difference in the vapour pressures of silicon and carbon, and the remaining carbon atoms form epitaxial G spontaneously on the surface.[13] However, this method has some important drawbacks, such as the need for an atomically flat surface covered by a single layer of G, which requires advances in SiC substrate preparation and a detailed knowledge of G nucleation and growth.[14] In addition, the transfer of G to another substrate is complicate[15] and the substrates are relatively expensive.

Comparatively, the growth of G on transition metals, by decomposition of controlled quantity of carbon sources or by chemical vapour deposition (CVD), are a rather easy approach to obtain G with desired features. Furthermore, the transfer of G to other arbitrary substrates is a well-known procedure.[16]

Various transition metals, such as Cu, Ni, Pt, Ru, Rh, Co and Ir, have been proven to catalyse the growth of G.[17] The number of G layers from single to multilayers, can be

controlled by the type and thickness of the catalyst used, whereas the dimensions of the films corresponds to the size of the catalyst.[16] Using these growth strategies also chemically modified G are relatively easy to synthesize, indeed the doping of G has developed as one of the most interesting research fields after the synthesis of pure G sheets. The desire for the controlled addition of defects, such as nitrogen[18] and boron[19] atoms, in the G sheet was driven by the need to open a band gap in G band structure[20] and also to study the catalytic properties of chemically modified G.[21,22]

All the section 2 is focused on the preparation of pure G layers, an exception is represented by the chapter 2.1.2 that is dedicated to N-doped G (N-G) synthesized under UHV conditions on Pt(111), I refer to that section for a detailed introduction on syntheses and properties of N-G.

Brief introduction on graphene/transition metal interfaces

G can be synthesized on transition metal by two main mechanisms: via carbon segregation or surface limited reaction. Both of these possible growth strategies can be schematized in multiple elementary steps.

Carbon segregation growth starts from the dilution or incorporation of carbon into the bulk of a metal substrate at high temperature. In a second step G is formed by surface segregation/precipitation. Figure 2 shows the typical G formation by this process: the hydrocarbons (or other simple molecules e.g. alchenes, chetones, aromatics etc.) that chemisorb on the metal surface (step 1), dissociate through dehydrogenation (step 2), and carbon atoms diffuse into the bulk of the metal (step 3). The chemisorption is facilitated by the empty *d*-shell of the transition metals, which serves as an electron acceptor. The segregation process begins when the concentration of carbon atoms in the bulk metal has achieved the threshold for nucleation or during the cooling process, when the carbon solubility in the metal decreases. The supersaturated carbon atoms in the bulk diffuse to the surface (step 4), and then the segregation process for G formation occurs (step 5). The segregation does not stop until the concentration of carbon in the bulk metal has decreased to equilibrium, even though the supply of hydrocarbons has been switched off.[23] Both the nucleation and equilibrium concentrations change under different operating conditions.

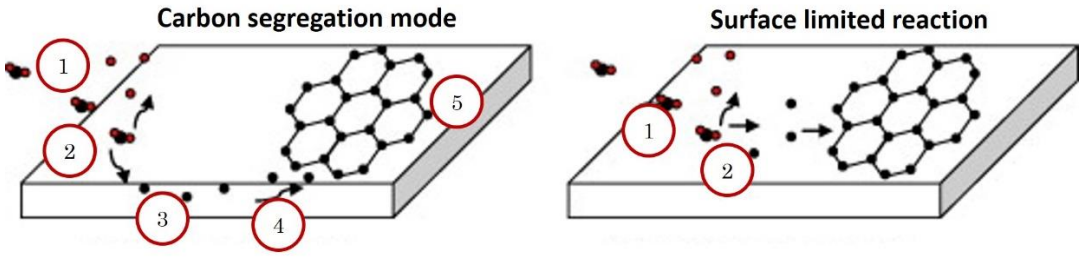

Figure 2. Sketch of G formation steps for carbon segregation mode and surface limited reaction. Adapted from Ref. [24] © 2014 Elsevier.

When the carbon solubility is very low the surface limited reaction explains better the formation mechanism of G. A simplified model is presented in Figure 2, the hydrocarbons dissociate on the surface (step 1), and then the carbon adatoms or cluster diffuse and nucleate on the surface to form G islands (step 2). The growth of G

starts right after the hydrocarbon dissociation and stop immediately when the supply of hydrocarbons is cut off.

Prototypical examples of these two different growth processes are the CVD synthesis of G on Cu and Ni. Ruoff's group investigated their mechanism dosing alternatively isotope labelled methane, $^{13}CH_4$ and $^{12}CH_4$, on Cu and Ni foils,[25] as sketched in Figure 3a and b. Experimentally micro Raman spectroscopy, which is one of the most powerful tools to analyse G layers,[26] can discriminate the vibrational mode of G composed by ^{13}C and ^{12}C. The Raman map of the G E_{2g} mode of the films grown on Cu (Figure 3c) shows well-defined islands composed by ^{13}C as well as borders formed by ^{12}C. These regions composed by different carbon isotopes were obtained by the sequential gas dosing (Figure 3b). The Raman map can therefore be explained by a surface limited reaction (Figure 2) that is due by the low carbon solubility in copper. On the contrary, G layer on Ni are formed via carbon segregation, whereby during the hydrocarbon exposure at high temperature there was a mixing of ^{13}C and ^{12}C inside the substrate, when the Ni foil was cooled down the not isotope-sensitive precipitation started. Consequently, the Raman map (Figure 3d) shows randomly distributed carbon isotopes into G layer as sketched in Figure 3a.

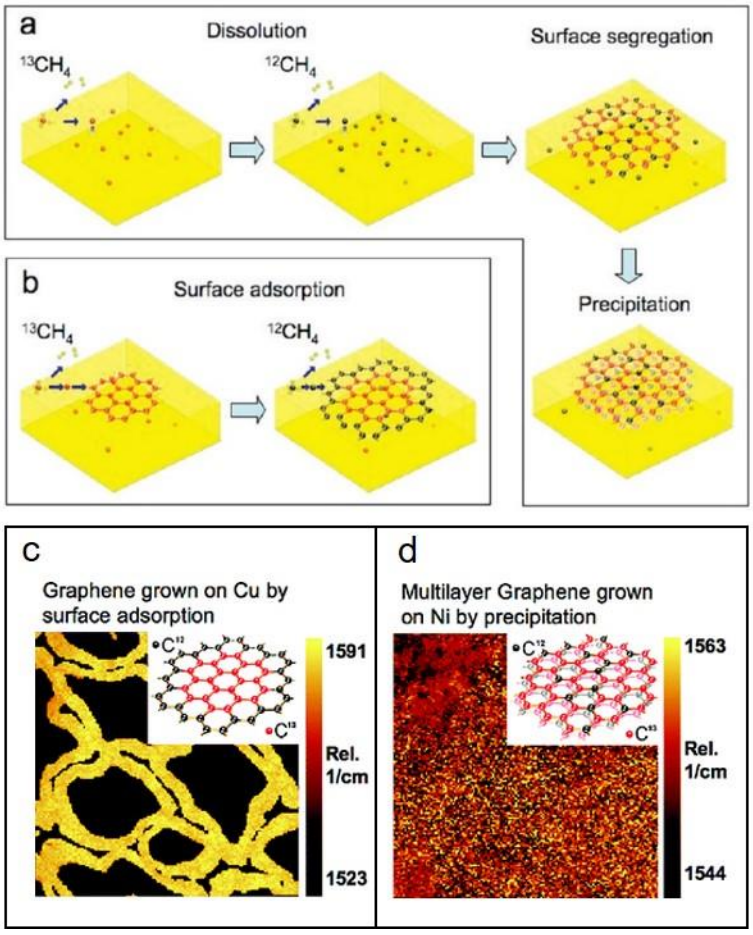

Figure 3. Schematic diagrams of the possible distribution of C isotopes in graphene films based on different growth mechanisms for sequential input of C isotopes. (a) Graphene with randomly mixed isotopes such as might occur from surface segregation and/ or precipitation. (b) Graphene with separated isotopes such as might occur by surface adsorption. (c) Raman map of E_{2g} mode of G grown on Cu and (d) on Ni. Adapted from Ref. [25] © 2009 ACS.

As it will be explained later in detail for Ni(111) and Pt(111), it is worth to mention that substrates where G grows by carbon segregation, if exposed to a small controlled quantity of carbon sources, e.g. during experiments under UHV conditions, it can be also synthesized by surface limited reactions. In that case the temperature must be finely tuned to avoid carbon dissolution inside the crystal structure and formation of carbide phases, as will be explain later in "Graphene on Ni(111)" paragraph.

In the quest for synthesizing G over transition metal substrates, a great deal of effort has been spent in the attempt to understand the fundamental growth processes involved in the formation of high quality G sheets. As mentioned above several different substrates can be used as catalysts for G, but the G/metal interaction is not always the same. Usually substrates are divided into strongly and weakly interacting materials. Surface scientists tried to rationalize this classification by considering the position of the *d*-bands of the metal surface, since the *d*-band electrons are primarily responsible for the bonding with G. This can give some guidance to justify the differences in the interaction.

In Table 1 the position of the centre of the *d*-band of the transition metal is compared to the values for the G-metal bond length,[17] typically obtained by low energy electron diffraction (LEED) I-V studies. Obviously the interplanar distance between G and the metal substrate provide a direct indication of the strength of the interaction between the two. From this comparison one may reach an empirical rule to characterized materials. Metals with their *d*-band centroid centred at binding energy (BE) lower than ~2 eV below the Fermi level are strongly interacting, on the contrary if the *d*-band centre is above ~2 eV the metal is considered weakly interacting . It is also interesting to note that weakly interacting metals have a G-metal separation of about 3.3 Å, similar to the interlayer spacing of graphite that is 3.36 Å, whereas for strongly interacting metals the interfacial distance is much less, typically in the range of 2.1 Å.

Table 1. Comparison between d-band centre of the transition metal surfaces and the reported values for G–metal separation (for strongly corrugated moiré-structures the area with the smallest separation was chosen as this represents the areas with strongest adsorption). From Ref. [17]

Metals	**BE of *d*-band centre relative to Fermi energy (eV)**	**G–metal separation (Å)**
Co(0001)	−1.17	2.1
Ni(111)	−1.29	2.1
Cu(111)	−2.67	3.3
Ru(0001)	−1.41	2.1
Rh(111)	−1.73	2.2
Pd(111)	−1.83	2.5
Ag(111)	−4.30	3.3
Re(0001)	−0.51	2.1
Ir(111)	−2.11	3.4
Pt(111)	−2.25	3.3
Au(111)	−3.56	3.3

However, the lattice-mismatch and ensuing moiré-pattern complicates the situation as the carbon atoms are forced away from the most stable adsorption configuration. Therefore more detailed electronic structure calculations are required to understand the G-metal bonding.

From the experimental point of view the interaction between G and underlying metal substrates can be studied by photoemission spectroscopy, both using C 1*s* core-level and VB mapping, which is performed by means of ARPES. The shift of the C 1*s* photoemission line can be also exploited to visualize indirectly the G corrugation on the metal surfaces, as in the case of G/Ru(0001).[27]

The VB mapping gives a straightforward evidence of G band hybridization induced by the contact with different metals. Strongly interacting metals induce shift, hybridization and band gap opening of G π band; on the contrary, weakly interacting metals induce only doping of G, i.e. a rigid shift of the G band structure upward and downward for the depletion or donation of electrons, respectively. An example of ARPES of G in contact with strongly and weakly interacting metals is reported later in "Graphene on Ni(111)" in Figure 5.

In this thesis both C 1*s* photoemission line separated into single chemically shifted components and ARPES have been used to study the interaction between G and ferromagnetic metals in 2.1.1 and 3.1.2.

Most fundamental surface science studies about the growth of G have been reported for Pt, Ru, Ir and Ni. These studies are facilitated by the fact that G can be grown in UHV, i.e. by exposure to hydrocarbons at fairly low pressure. The choice of the substrate to study G is influenced by several factors such as epitaxial matching, e.g. G/Ni(111) has almost a perfect (1×1) epitaxy, desired moiré structures, e.g. G corrugation can template the size and shape of nanoparticles (NPs),[28] electronic interaction, e.g. quasi-freestanding G vs strongly hybridized bands, and last but not least also the acquired knowledge in the preparation of optimal surface.

In this thesis we choose Pt(111) as the prototypical weakly interacting metal principally because on this substrate polycrystalline G can be easily grown using a very low hydrocarbon pressure. As a representative of strongly interacting metals, we chose Ni(111), for its ability to grow G layer with a very well defined morphology. We also explore the alloy of these two metals in the section 2.3 where G is grown on the Pt skin of the bulk $Pt_3Ni(111)$ alloy. In the following two paragraphs the growth and principal features of G on Pt(111) and Ni(111) are discussed. The preparation of G on $Pt_3Ni(111)$ was absent in the literature, therefore the synthesis and characterization on this novel substrate is presented in a dedicate paragraph 2.3.

Graphene on Pt(111)

G can be grown on platinum by carbon segregation from the bulk or by a surface limited decomposition of hydrocarbons. Comparison of specular beam LEED I(V) measurements with simulated I(V) spectra showed the best Pendry R-factor for G-Pt separation of 3.3 Å.[29] This is similar to the interplanar (0002) distance in graphite (i.e. 3.36 Å) and is in excellent agreement with DFT simulations for G on Pt(111), which demonstrates a low interaction between G and the substrate. This weak interaction

causes the formation of many rotational domains; see scanning tunneling microscopy (STM) images in 2.1.1 and 2.1.2.

An accurate investigation[29] of G/Pt(111) has been carried out by the Sutter's group using low energy electron microscopy (LEEM) and photoemission electron microscopy (PEEM), this instrument is able to characterize materials locally on the single G grain. By LEEM studies they have identified a huge variety of domains with small (3×3), $(\sqrt{6}\times\sqrt{6})R2_G$, and $(2\times2)R4_G$ or large unit cells $(\sqrt{44}\times\sqrt{44})R15_G$, $(\sqrt{52}\times\sqrt{52})R14_G$ and $(8\times8)_G$. To explain the multitude of different rotation angles between G and Pt(111) a simple geometrical model has been proposed.[30] In this model the mismatch of the moiré-superstructure unit cell with respect to Pt atoms are considered. Moiré structures with rotation angles that result in a small mismatch are considered more favourable and thus expected to occur more frequently. This simple model is able to provide a satisfying agreement with experimental observations.

G films grown by direct decomposition of ethylene at high temperature showed the best quality at growth temperatures around 800-1000 K.[31] This optimum growth temperature was associated with a sparse nucleation of G. From the experimental point of view, carbon segregation method requires high dose (>10000 L) of carbon precursors at very high temperature (~1300 K), that are usually very demanding conditions for UHV preparation chambers. Whereas, surface limited reactions require much less carbon precursors and moderate temperature (150 L at 1000 K)[31] that are much less challenging requirements, for this reason this growth strategy is used by most experimenters. Notably, DFT calculations show that different orientations of G with respect to the Pt(111) surface, and consequently different moiré superstructure, have not strong influence on the G/Pt interaction.[32] Therefore, results coming from experiments where G/Pt(111) has been grown by different methodology or when signals are mediated on differently oriented G rotational angles can be safely compared. Micro ARPES on different G domains showed that the band structure of Pt support G is very similar to free-standing layers, with well-defined linear π band dispersion at the K-point. The G monolayer was p-doped with the Dirac point, the exactly estimation of the Dirac cone position of G/Pt(111) is still debated in the literature but can be safely ranged from about 0.06-0.3 eV above the Fermi-level[29,35,36] in good agreement with DFT calculations.[31,33]

As stated above the carbon segregation mode is experimentally challenging using UHV equipment, but it is standard procedure in CVD where high precursor pressure and high temperature are easily obtainable. G has been synthesized via CVD on Pt foils obtaining single grains with lateral size up to millimetre, moreover it has been developed an electrochemical bubbling method to transfer G films to arbitrary substrate, which is non-destructive not only for G, but also for the Pt substrate, that can be reused for several growth cycles. [34]

Recently, it has been demonstrated by two papers that is possible to obtain an almost completely covering $(\sqrt{3}\times\sqrt{3})R30_G$ superstructure on Pt(111). In the first paper[35] propylene (about 280 L at 1200 K) was dosed on the surface, this represents an intermediate case between carbon segregation from the bulk and self-limiting reactions. In the second one[36] G was grown by surface limited reaction thus G/Pt(111) was annealed at ~1800 K to ordered the G patches. These papers are interesting

because they are the only two cases found in the literature where G/Pt(111) has almost only one orientation on Pt(111).

Epitaxial G/Pt(111) with a single orientation, $(\sqrt{3}\times\sqrt{3})R30_G$, has been analysed by spin polarized ARPES.[36] The structural homogeneity of G on the whole Pt surface is crucial for these measurements because the low efficiency of spin-resolved electron detector. Indeed, using nowadays technology, spin polarized photoemission can be carry out only on polycrystalline G only if all domains have the same orientation, because measurements cannot be carried out on single G grains without suppressing great part of the signal. By spin polarized ARPES a small gap opening, 80-200 meV, in the G π band has been detected due to the hybridization between G bands and Pt *5d* orbitals, at about 1 eV below the Fermi level. This small hybridization is comparable to what is observed on G/Ir(111),[37,38] which is considered as well as weakly interacting substrate. However, this gap is much smaller than what is observed for G in contact with strongly interacting metals, e.g. for G/Co(0001)[39] two distinct Dirac cones with an energy split of 3.2 eV are observed. This is very similar to our results on 1 monolayer (ML) of Fe intercalated underneath G/Pt(111)[32] that is discussed in detail in the section 2.1.1.

Graphene on Ni(111)

The formation of G on Ni(111) is a thoroughly studied case in the literature for the good matching between G and Ni lattices that allows the growth of a commensurate G overlayer on Ni(111) with no superstructure spots in LEED and makes Ni a unique substrate for studying the G/metal interface.

LEED I(V) studies identified the adsorption structure of G with one carbon atom atop surface Ni atom and the second carbon on fcc-hollow sites, Figure 4a. The G–Ni separation was determined to be 2.11 and 2.16 Å for carbon atoms sitting on fcc-hollow and atop carbon sites, respectively.[40] Adsorption of the over hcp-hollow sites instead of the fcc-hollow site is only slightly less favoured, see Figure 4a, this indicates the possibility that under certain growth conditions both adsorption geometries are present in different domains.[41] The domain boundaries resulting from such two domains, which have a registry offset relative to the Ni-substrate, have been investigated by STM.[42,43] If the two domains meet, the G sheets do not match, consequently the interface has to reconstruct into a pair of pentagons and an octagon as demonstrated by the STM images shown in Figure 4a,b. More recent DFT calculations and STM measurements on G/Ni(111) showed that also a third component top-bridge structure can be found.[43]

Similarly to Pt(111), G can grow on Ni(111) via carbon segregation or by surface-limited reaction, but the scenario is slightly more complicate with respect to G/Pt(111) due to the presence of a stable carbide phase.

The growth of single layer and multiple layer[44] of G by carbon segregation has been studied by LEEM.[45] The first layer G shows low nucleation density and single G grains as large as 100 μm can be obtained then it was found that a second layer may nucleate and grow underneath the first layer upon its completion.[45]

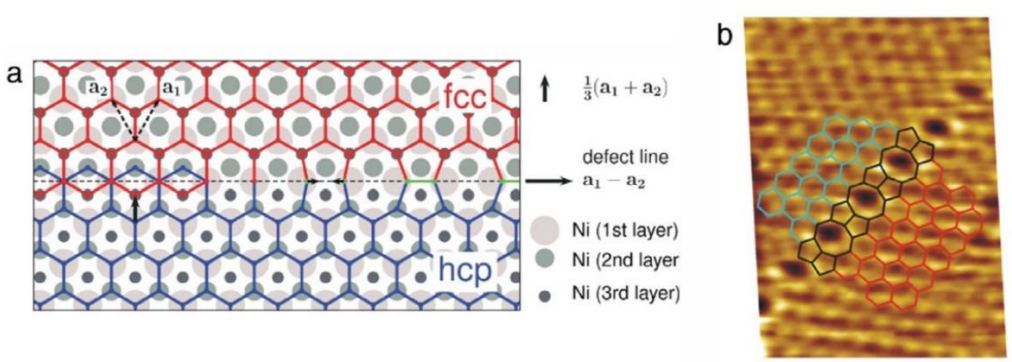

Figure 4. (a) The two half-lattices can be joined along the a_1–a_2 direction, indicated by the horizontal vector, without any unsaturated dangling bonds, by restructuring the G lattice. The domain boundary can be constructed as shown, by joining two carbon atoms, indicated by the two arrows, along the domain boundary line. This reconstructed domain boundary forms a periodic structure consisting of octagonal and pentagonal carbon rings. The underlying Ni(111) structure illustrates how the extended defect is formed by anchoring two graphene sheets to a Ni(111) substrate at slightly different adsorption sites. If one G domain has every second carbon atom located over a fcc-hollow site (red) and the other domain over a hcp-hollow site (blue), then the two domains are translated by 1/3(a_1 + a_2) relative to one another. (b)STM image show the structure of the domain boundary. Adapted from Ref. [42] © 2010 NPG.

X-ray photoemission spectroscopy (XPS) studies of G growth under UHV conditions on a thin Ni(111) epitaxial film on W(110) substrates showed that G growth is self-limiting after the completion of the first monolayer.[46] It is important to point out that these studies were performed at low hydrocarbon pressures (2.7×10^{-7} mbar of propylene) and on a clean metal, i.e. without significant amount of carbon dissolved into the Ni crystal. Upon exposure to propylene a C 1s photoemission signal at 283 eV BE was observed and the G signal at ~284.7 eV BE started to grow after around 100 s time delay. However, the 283 eV carbon peak was only observed for growth temperatures below 600 °C. In early works,[46] this peak was associated with hydrocarbon fragments, but now it has been demonstrated that is related to nickel carbide phase, which is another possible carbon/nickel phase, i.e. carbon can form a third phase in addition to the carbon diffused into the Ni lattice and G overlayer.[47] As the G film grows, the 283 eV carbon species decreases and the C 1s peak at 284.7 eV related to G, saturates at completion of one monolayer. We also verified this trend in the paragraph "Interaction between graphene and water". At higher growth temperatures (669 °C) G exists only on the surface as long as carbon is supplied. Once the hydrocarbon is shut off, the G peak decreases and disappears after ~400 s. This indicates that carbon dissolves back into the bulk at high temperature.[46] This temperature is lower compared to the temperature found for a carbon saturated Ni crystal where G was found to be stable up to ~900 °C.[48] These findings indicate that the stability and growth of G on Ni is related to the subsurface carbon concentration, which in many experiments, e. g. CVD process, is difficult to control.

In general a much lower hydrocarbon exposure is required for the G growth on ultrathin Ni-films (e.g. Ni/W(110)) than on bulk Ni(111) samples, further indicating a significant loss of carbon into the bulk during growth on bulk samples. Importantly, in UHV growth studies, the growth temperature is adjusted below the thermodynamic stability G on Ni, which is only ~650–700 °C and this enables monolayer growth at the surface.

As mentioned above, Ni-C phase diagram exhibits a phase that is an ordered surface carbide, i.e. a carbide confined to the surface layer. Its structure has been described as a quasi-squared Ni_2C overlayer on the hexagonal Ni(111).[49] G is stable to 650 °C while the carbide is stable only up to 460 °C, and above this temperature carbon dissolves into the bulk. Consequently, between 460 °C and 650 °C G grows on pure Ni without forming a carbide. The lower temperature stability of the carbide compared to the formation of a G layer, has the consequence that if G is grown by carbon segregation from the bulk upon sample cooling, the G film forms on the surface before the carbide can form and thus under these conditions G is grown in the absence of a carbide.

Below 460 °C, a carbide is forming on the surface with a kinetics that is faster compared to the growth of G. The carbide phase once formed may prevent the nucleation of the carbon-denser G phase by carbon segregation from the bulk. Once eventually G nucleates within the surface carbide the G sheet can grow differently from the growth of G in the absence of the carbide.[47] In this case G grows at the boundary with the carbide phase presumably by replacing Ni-atoms by carbon, a consequence of this kind of growth is that not the Ni(111)-substrate but the carbide boundary, which is rotated by 3° relative to the ⟨1–10⟩ direction of the Ni(111) substrate, determines the orientation of G. The rotation of the G with respect to the substrate causes the formation of a moiré superstructure, which is not observed if G grows in the absence of the carbide at elevated temperatures.

To summarize, on Ni, three different growth scenarios can be observed. Below 460 °C a Ni_2C surface phase forms readily and later on G growth proceeds by the *in-plane* transformation of the carbide along a one-dimensional G-Ni_2C phase boundary. At temperatures between 460 and 650 °C on pure Ni the growth mechanisms does not differ much from that on other transition metals. Above 650–700 °C carbon dissolves into the bulk and G is formed only during the cooling of the sample by carbon segregation on the surface.

Several ARPES studies of the electronic structure of G on Ni have been performed. They all show a large downward shift of the π states by about 2 eV[50,51] and the opening of a bandgap at the K-point indicating a strong interaction between Ni and G. A pivotal work on G/Ni(111) has been performed by Varykhalov et al.[51] where G/Ni(111) has been intercalated by gold, which is a weakly interacting metal (Table 1),to form a quasi-freestanding G, they visualized this transition by ARPES reported in Figure 5. The intercalation of only 1 ML of metal dramatically changes the band structure of G, as we observed in 2.1.1.[32] Is also worth to mention the complete study carried out by Voloshina et al. [52] on the intercalation of G/Ni(111) by a non *d*-metal, aluminium, to avoid any hybridization between G π band and *d* electrons.

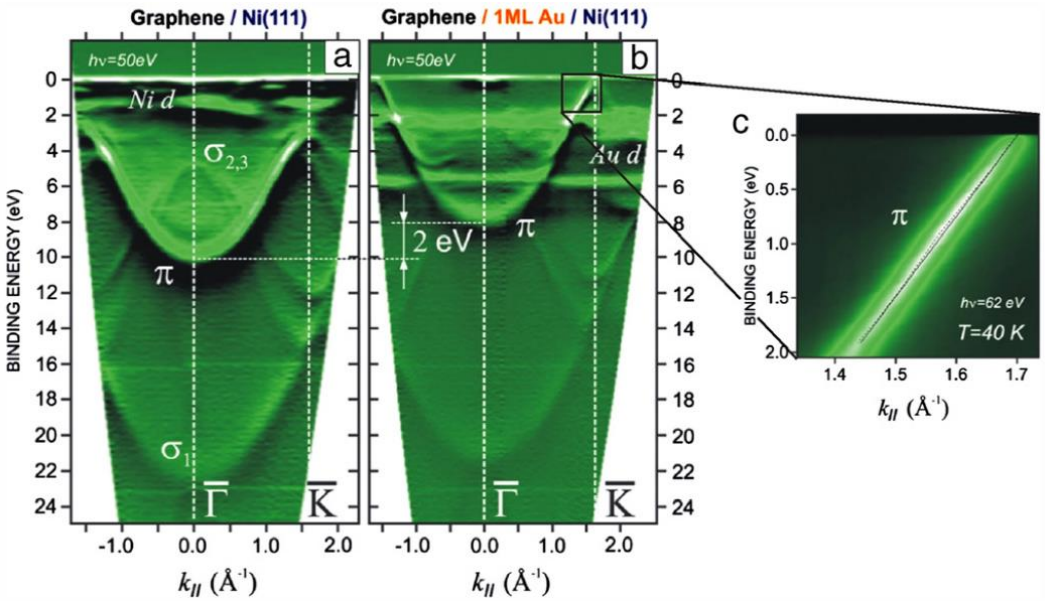

Figure 5. ARPES measurement of G grown on Ni(111)(a) and after intercalation of a monolayer of Au (b). The linear band dispersion at the Dirac point after Au intercalation is highlighted in (c). For G on Ni the π band is downshifted by ~2 eV. Intercalation of Au decouples G from the Ni-substrate and forms electronically quasi-freestanding G. Adapted from Ref. [51] © 2008 APS.

Indeed metal intercalation underneath G is a versatile a powerful technique to modulate G properties, a variety of different metal elements can intercalate G. Elements, which interact with carbon strongly, are supposed to produce transient atomic-scale defects at the G lattice, and the intercalant atoms can penetrate through the carbon G lattice. On the other hand, those elements and molecules which are not able to activate C-C bonds need to diffuse under G through extended defects, such as domain boundaries and island edges.[53] It is also interesting to note that gases do not easily intercalate underneath G, in section 2.1.2 is reported the case of Fe intercalation but also the G impermeability to CO. Also other 2D material can be intercalated by metal atoms as we show in 3.1.2 with the intercalation of *h*-BN/Ni(111) by few layer of Au.[54]

G grown on Ni(111) was the first example of the possibility to induce magnetism in G by contact with ferromagnetic metals. X-ray magnetic circular dichroism (XMCD) experiments on the C K edge revealed an induced magnetic moment on the π-electrons of carbon atoms. This magnetic moment of 0.05-0.1 μ_b per atom, is due to the strong hybridization between C π and Ni 3*d* VB states.[52,55,56] On G/Ni(111) system after the intercalation of 1 ML of Fe beneath G, the magnetic moment of carbon was enhanced up to 0.25 μ_b.[57] These studies of the magnetism in G are essential for future spintronic and magnetic applications of G.

References

1 Wallace, P. R. The band theory of graphite *Phys. Rev.* **1947**, *71*, 622.

2 Johnston, D. F. The structure of the π-band of graphite *Proc. R. Soc. A*, **1955**, *227*, 349 (1955).

3 McClure, J. W. Band structure of graphite and de Haas-van Alphen effect *Phys. Rev.* **1957**, *108*, 612.

4 Semenoff, G. W. Condensed-matter simulation of a three-dimensional anomaly *Phys. Rev. Lett.* **1984**, *53*, 2449.

[5] Saito, R.; Dresselhaus, G.; Dresselhaus, M. S. *Physical Properties of Carbon Nanotubes*, (Imperial College Press, London, UK, 1998).

[6] Novoselov, K. S.; Geim, A. K.; Morozov, S. V.; Jiang, D.; Zhang, Y.; Dubonos, S. V.; Grigorieva, I. V.; Firsov, A. A. Electric field effect in atomically thin carbon films *Science*, **2004**, *306*, 666.

[7] Liang, Y. T.; Hersam, M. C.Highly concentrated graphene solutions via polymer enhanced solvent exfoliation and iterative solvent exchange *J. Am. Chem. Soc.*, **2010**, *132*, 17661.

[8] Zhu, Y.; Murali, S.; Cai, W.; Li, X.; Suk, J. W.; Potts, J. R.; Ruoff, R. S. Graphene and Graphene Oxide: synthesis, properties, and applications *Adv Mater*, **2010**, *22*, 3906.

[9] Hummers, W. S.; Offeman, R. E. Preparation of graphitic oxide *J. Am. Chem. Soc.*, **1958**, *80*, 1339

[10] Allen, M. J.; Tung, V. C.; Kaner, R. B. Honeycomb carbon: a review of graphene *Chem. Rev.*, **2009**, *110*, 132.

[11] Pei, S.; Cheng, H.-M. The reduction of graphene oxide, *Carbon*, **2012**, *50*, 3210.

[12] Favaro, M.; Leonardi, S.; Valero-Vidal, C.; Nappini, S.; Hanzlik, M.; Agnoli, S.; Kunze-Liebhäuser, J.; Granozzi, G. In-situ carbon doping of TiO_2 nanotubes via anodization in graphene oxide quantum dot containing electrolyte and carburization to TiO_xC_y nanotubes *Adv. Mater. Interfaces* **2015**, *2*, 1400462.

[13] Norimatsu W.; Kusunoki, M. Epitaxial graphene on SiC{0001}: advances and perspectives Phys. Chem. Chem. Phys., 2014, 16, 3501.

[14] Robinson, J.; Weng, X.; Trumbull, K.; Cavalero, R.; Wetherington, M.; Frantz, E.; LaBella, M.; Hughes, Z.; Fanon, M.; Snydert, D. Nucleation of epitaxial graphene on SiC(0001) *ACS Nano*, **2009**, *4*, 153.

[15] Kim, J.; Park, H.; Hannon, J. B.; Bedell, S. W.; Fogel, K.; Sadana, D. K.; Dimitrakopoulos, C.; Layer-resolved graphene transfer via engineered strain layers *Science*, **2013**, *342*, 833.

[16] Bae, S.; Kim, H.; Lee, Y.; Xu, X.; Park, J.-S.; Zheng, Y.; Balakrishnan, J.; Lei, T.; Kim, H. R.; Song, Y. I.; Kim, Y.-J.; Kim, K. S.; Özyilmaz, B.; Ahn, J.-H.; Hong, B. H.; Iijima, S. Roll-to-roll production of 30-inch graphene films for transparent electrodes *Nat. Nanotechnol. 2010*, **5**, 574.

[17] Batzill, M. The surface science of graphene: Metal interfaces, CVD synthesis, nanoribbons, chemical modifications, and defects *Surf. Sci. Rep*. **2012**, *67*, 83.

[18] Cattelan, M.; Cavaliere, E.; Artiglia, L.; Gavioli, L.; Agnoli, S.; Granozzi, G. The dynamics of Fe intercalation on pure and nitrogen doped graphene grown on Pt(111) probed by CO adsorption, *Surf. Sci.* **2015**, *634*, 49.

[19] Cattelan, M.; Agnoli, S.; Favaro, M.; Garoli, D.; Romanato, F.; Meneghetti, M.; Barinov, A.; Pavel Dudin, P.; Granozzi, G. Microscopic view on a chemical vapor deposition route to boron-doped graphene nanostructure *Chem. Mater.*, **2013**, *25*, 1490.

[20] Wei, D; Liu, Y.; Wang, Y.; Zhang. H.; Huang, L.; Yu, G. Synthesis of N-doped graphene by chemical vapor deposition and its electrical properties *Nano Lett.*, **2009**, *9*,1752.

[21] Favaro, M.; Ferrighi, L.; Fazio, G.; Colazzo, L.; Di Valentin, C.; Durante, C.; Sedona, F.; Gennaro, A.; Agnoli, S.; Granozzi, G. Single and multiple doping in graphene quantum dots: unraveling the origin of selectivity in the oxygen reduction reaction *ACS Catal.*, **2015**, *5*, 129

[22] Duan, J.; Chen, S.; Jaroniec, M.; Qiao S. Z. Heteroatom-doped graphene-based materials for energy-relevant electrocatalytic processes *ACS Catal.*, **2015**, *5*, 5207.

[23] Loginova, E.; Bartelt, N. C.; Feibelmarr, P. J.; McCarty, K. F. Factors influencing graphene growth on metal surfaces *New Journal of Physics*, **2009**, *11*, 063046.

[24] Seah, C.-M.; Chai, S.-P.; Mohamed, A. R.; Mechanisms of graphene growth by chemical vapour deposition on transition metals *Carbon*, **2014**, 70, 1.

[25] Li, X.; Cai, W.; Colombo, L.; Ruoff, R. S. Evolution of graphene growth on Ni and Cu by carbon isotope labelling. *Nano Lett.* **2009**, *9*, 4268.

[26] Ferrari, A. C.; Meyer, J. C.; Scardaci, V.; Casiraghi, C.; Lazzeri, M.; Mauri, F.; Piscanec, S.; Jiang, D.; Novoselov, K. S.; Roth, S.; Geim, A. K. Raman spectrum of graphene and graphene layers *Phys. Rev. Lett.* **2006**, *97*, 187401.

[27] Preobrajenski, A. B.; Ng, M. L.; Vinogradov, A. S.; Mårtensson, N. Controlling Graphene Corrugation on Lattice-Mismatched Substrates. *Phys. Rev. B* **2008**, *78*, 073401.

[28] Sicot, M.; Leicht, P.; Zusan, A.; Bouvron, S.; Zander, O.; Weser, M.; Dedkov, Y. S.; Horn, K.; Fonin, M. Size-Selected Epitaxial Nanoislands Underneath Graphene Moiré on Rh(111), *ACS Nano* **2012**, 6, 151.

[29] Sutter, P.; Sadowski, J. T.; Sutter, E; Graphene on Pt(111): Growth and substrate interaction, *Phys. Rev. B* **2009**, *80*, 245411.

[30] Merino, P.; Svec, M.; Pinnardi, A. L.; Otero, G.; Martin-Gago, J. A. Strain-driven moiré superstructures of epitaxial graphene on transition metal surfaces. *ACS Nano* **2011**, *5*, 5627.

[31] Gao, M.; Pan, Y.; Huang, L.; Hu, H.; Zhang, L. Z.; Guo, H. M.; Du, S. X.; Gao, H.-J. Epitaxial growth and structural property of graphene on Pt(111). *Appl. Phys. Lett.* **2011**, *98*, 033101.

[32] Cattelan, M.; Peng, G. W.; Cavaliere, E.; Artiglia, L.; Barinov, A.; Roling, L. T.; Favaro, M.; Píš, I.; Nappini, S.; Magnano, E.; Bondino, F.; Gavioli, L.; Agnoli, S.; Mavrikakis, M.; Granozzi, G. The nature of the Fe–graphene interface at the nanometer level. *Nanoscale* **2015**, *7*, 2450.

[33] Giovannetti, G.; Khomyakov, P. A.; Brocks, G.; Karpan, V. M.; Van Den Brink, J.; Kelly, P. J. Doping Graphene with Metal Contacts *Phys. Rev. Lett.* **2008**, *101*, 026803.

[34] Gao, L.; Ren, W.; Xu. H.; Jin, L.;Wang, Z.; Ma, T.; Ma, L.-P.; Zhang, Z.; Fu, Q.; Peng, L.-M.; Bao, X.; Cheng, H.-M. Repeated growth and bubbling transfer of graphene with millimetre-size single-crystal grains using platinum. *Nat. Comm.* **2012**, *3*, *699*.

[35] Klimovskikh, I. I.; Tsirkin, S. S.; Rybkin, A. G.; Rybkina, A. A.; Filianina, M.V.; Zhizhin, E. V.; Chulkov, E. V.; Shikin, A. M. Nontrivial spin structure of graphene on Pt(111) at the Fermi level due to spin-dependent hybridization. *Phys. Rev. B* **2014**, *90*, 235431.

[36] Yao, W.; Wang, E.; Deng, K.; Yang, S.; Wu, W.; Fedorov, A. V.; Mo, S.-K.; Schwier, E. F.; Zheng, M.; Kojima, Y.; Iwasawa, H.; Shimada, K.; Jiang,K.; Yu, P.; Li, J.; Zhou, S. Monolayer charge-neutral graphene on platinum with extremely weak electron-phonon coupling *Phys. Rev. B* **2015**, *92*, 115421.

[37] Pletikosić, I.; Kralj, M.; Pervan, P.; Brako, R.; Coraux, J.; N'Diaye, A. T.; Busse, C.; Michely, T. Dirac Cones and Minigaps for Graphene on Ir(111) *Phys. Rev. Lett.* **2009**, *102*, 056808.

[38] Vita, H.; Böttcher, St.; Leicht, P.; Horn, K.; Shick, A. B.; Máca, F. Electronic structure and magnetic properties of cobalt intercalated in graphene on Ir(111) *Phys. Rev. B* **2015**, *90*, 165432.

[39] Usachov, D.; Fedorov, A.; Otrokov, M. M.; Chikina, A.; Vilkov, O.; Petukhov, A.; Rybkin, A. G.; Koroteev, Y. M.; Chulkov, E. V.; Adamchuk, V. K.; Grüneis, A.; Laubschat, C.; Vyalikh, D. V. Observation of Single-Spin Dirac Fermions at the Graphene/Ferromagnet Interface *Nano Lett.* **2015**, *15*, 2396.

[40] Gamo, Y.; Nagashima, A.; Wakabayashi, M.; Terai, M.; Oshima, C.; Atomic structure of monolayer graphite formed on Ni(111). *Surf. Sci.* **1997**, *374*, 61.

[41] Zhao, W.; Kozlov, S. M.; Höfert, O.; Gotterbarm, K.; Lorenz, M. P. A.; Viñes, F.; Papp, C.; Görling, A.; Steinrück, A.-P. Graphene on Ni(111): Coexistence of Different Surface Structures. *J. Phys. Chem. Lett.* **2011**, *2*, 759.

[42] Lahiri, J.; Lin, Y.; Bozkurt, P.; Oleynik, I. I.; Batzill, M. An extended defect in graphene as a metallic wire. *Nat. Nanotechnol.* **2010**, *5*, 326.

[43] Bianchini, F.; Patera, L. L.; Peressi, M.; Africh, C.; Comelli, G. Atomic scale identification of coexisting graphene structures on Ni(111). *J. Phys. Chem. Lett.* **2014**, *5*, 467.

[44] Chae, S. J.; Günes, F.; Kim, K. K.; Kim, E. S.; Han, G. H.; Kim, S. M.; Shin, H.-J.; Yoon, S.-M.; Choi, J.-Y.; Park, M. H.; Yang, C. W.; Pribat, D.; Lee, Y. H. Synthesis of large-area graphene layers on poly-nickel substrate by chemical vapor deposition: wrinkle formation. *Adv. Mater.* **2009**, *21*, 2328.

[45] Odahara, G.; Otani, S.; Oshima, C.; Suzuki, M.; Yasue, T.; Koshikawa, T. In-situ observation of graphene growth on Ni(111) *Surf. Sci.* **2011**, *605*, 1095.

[46] Grüneis, A.; Kummer, K.; Vyalikh, D. V. Dynamics of graphene growth on a metal surface: A time-dependent photoemission study. *New J. Phys.* **2009**, *11*, 073050.

[47] Lahiri, J.; Miller, T.; Adamska, L.; Oleynik, I. I.; Batzill, M. Graphene Growth on Ni(111) by transformation of a surface carbide *Nano Lett.* **2011**, *11*, 518.

[48] Shelton, J. C.; Patil, H. R.; Blakely, J. M. Equilibrium segregation of carbon to a nickel (111) surface: A surface phase transition. *Surf. Sci.* **1974**, *43*, 493.

[49] McCarroll, J. J.; Edmonds, T.; Pitkethly, R. C. Interpretation of a complex low energy electron diffraction pattern: carbonaceous and sulphur-containing structures on Ni(111). *Nature* **1969**, *223*, 1260.

[50] Nagashima, A.; Tejima, N.; Oshima C. Electronic states of the pristine and alkali-metal-intercalated monolayer graphite/Ni(111) systems. *Phys. Rev. B*, **1994**, *50*, 17487

[51] Varykhalov, A.; Sánchez-Barriga, J.; Shikin, A. M.; Biswas, C.; Vescovo, E.; Rybkin, A.; Marchenko, D.; Rader, O. Electronic and magnetic properties of quasifreestanding graphene on Ni. *Phys. Rev. Lett.* **2008**, *101*, 157601.

[52] Voloshina, E. N.; Generalov, A.; Weser, M.; Böttcher, S.; Horn K.; Dedkov, Y. S. Structural and electronic properties of the graphene/Al/Ni(111) intercalation system. *New J. Phys.* **2011**, *13*, 113028.

[53] Jin, L.; Fu, Q.; Yang, Y.; Bao, X. A comparative study of intercalation mechanism at graphene/Ru(0001) interface *Surf. Sci.* **2013**, *617*, 81.

[54] Cattelan, M.; Markman, B.; Lucchini, G.; Kumar Das, P.; Vobornik, I.; Robinson, J. A.; Agnoli, S.; Granozzi, G. New strategy for the growth of complex heterostructures based on different 2D materials *Chem. Mater.* **2015**, *27*, 4105.

[55] Weser, M.; Rehder, Y.; Horn, K.; Sicot, M.; Fonin, M.; Preobrajenski, A. B.; Voloshina, E. N.; Goering, E.; Dedkov, Y. S. Induced magnetism of carbon atoms at the graphene/Ni(111) interface. *Appl. Phys. Lett*. **2009**, 96, 012504.

[56] Dedkov, Y. S.; Fonin, M. Electronic and magnetic properties of the graphene–ferromagnet interface *New J. Phys.* **2010**, *12*, 125004.

[57] Weser, M.; Voloshina, E. N.; Horn K.; Dedkov, Y. S. Electronic structure and magnetic properties of the graphene/Fe/Ni(111) intercalation-like system *Phys. Chem. Chem. Phys.* **2011**, *13*, 7534.

2.1. Interaction between graphene and iron

In the following two sections, the interaction of iron with G and N-G has been studied.

G and N-G have been grown on Pt(111) single crystal. This substrate has the notable property to promote the growth of both controlled layer of G,[1] and ultrathin iron oxide layers.[2] Moreover, monolayer thick layers of iron on Pt(111) present peculiar magnetic properties.[3] Therefore, Pt(111) can be used as the perfect substrate to obtain G/iron junctions with tailored properties.

The work on G/Fe interface started with the aim of understanding how the reactivity of iron NPs is modified when they are placed in contact with G. By using temperature programmed desorption (TPD) experiments, we found out that Fe in proper conditions can intercalate quite easily underneath G.[4] We also verified that G can represent an impenetrable barrier for gases. This behaviour can be either helpful for practical applications in case air sensitive materials must be protected from oxidation, but it can be detrimental for catalytic applications since the metal catalytic sites underneath G result to be inaccessible. We, therefore, decided to address our attention to basic studies on iron and pure G interface using a variety of UHV techniques and several synchrotron based spectroscopies.[5]

In the section 2.1.1 is presented one of the most interesting system, which is composed by G/Pt(111) intercalated by 1 ML of Fe. By means of VB mapping and DFT calculations this interface emerged as a good candidate for "G spintronic"[6,7] studies and devices. With the aim to study more deeply its magnetic properties, cutting-edge synchrotron characterization, such as spin-resolved ARPES, is going to be undertaken in the near future.

On the other hand, because the catalysts formed by the combination of Fe and N-doped carbons are one of the most studied systems for oxygen reduction reaction (ORR) we decided to study the differences between the chemical reactivity of iron NPs on G as compared to N-G.[8] As explained in 2.1.2, we expected a surface stabilization of iron NPs due to chemical bonds with N functionalities, but unexpectedly, we found that iron intercalates faster underneath N-G than below pure G.[4]

To summarize the following chapters are:

- 2.1.1 on the investigation of iron and G for future spintronic applications;[5]
- 2.1.2 on the intercalation study of Fe underneath G and N-G performed by TPD.[4]

References

[1] Sutter, P.; Sadowski, J. T.; Sutter, E; Graphene on Pt(111): Growth and substrate interaction, *Phys. Rev. B* **2009**, *80*, 245411.

[2] Spiridis, N.; Wilgocka-Alęzak, D.; Freindl, K.; Figarska, B.; Giela, T.; Młyńczak, E.; Strzelczyk, B.; Zając, M.; Korecki, J. Growth and electronic and magnetic structure of iron oxide films on Pt(111), *Phys. Rev. B* **2012**, *85*, 075436.

[3] Moulas, G.; Lehnert, A.; Rusponi, S.; Zabloudil, J.; Etz, C.; Ouazi, S.; Etzkorn, M.; Bencok, P.; Gambardella, P.; Weinberger, P.; Brune, H. High magnetic moments and anisotropies for Fe_xCo_{1-x} monolayers on Pt(111), *Phys. Rev. B* **2006**, *78*, 214424.

[4] Cattelan, M.; Cavaliere, E.; Artiglia, L.; Gavioli, L.; Agnoli, S.; Granozzi, G. The dynamics of Fe intercalation on pure and nitrogen doped graphene grown on Pt(111) probed by CO adsorption, *Surf. Sci.* **2015**, *634*, 49.

[5] Cattelan, M.; Peng, G. W.; Cavaliere, E.; Artiglia, L.; Barinov, A.; Roling, L. T.; Favaro, M.; Píš, I.; Nappini, S.; Magnano, E.; Bondino, F.; Gavioli, L.; Agnoli, S.; Mavrikakis, M.; Granozzi, G. The nature of the Fe–graphene interface at the nanometer level. *Nanoscale* **2015**, *7*, 2450.

[6] Han, W.; Kawakami, R. K.; Gmitra, M., Fabian, J. Graphene spintronics, *Nat. Nanotechnol.* **2014**, *9*, 794.

[7] Seneor, P.; Dlubak, B.; Martin, M.; Anane, A.; Jaffres H.; Fert, A. Spintronic with graphene, *Mrs Bulletin* **2012**, *37*, 1245.

[8] Morozan, A.; Campidelli, S.; Filoramo, A.; Jousselme, B.; Palacin S. Catalytic activity of cobalt and iron phthalocyanines or porphyrins supported on different carbon nanotubes towards oxygen reduction reaction, *Carbon* **2011**, *49*, 4839.

2.1.1. Pure graphene and iron

Introduction

Almost all G-based electronic devices,[1,2] such as high frequency transistors, touch screens, foldable electronics etc., have in common a massive exploitation of G/metal junctions[3]. The detailed investigation of the G/metal interface at the nanoscale is crucial for technological advancement and it is expected to inspire the development of novel devices.

G is also emerging as an ideal platform for future spintronics, which is the study of intrinsic spin of the electron in addition to its fundamental charge for applications in solid-state devices. In this research field, a major challenge is the development of suitable spin transport channels with long spin lifetime and spin propagation on long-distance. G is a very promising spin channel material owing to RT spin transport with long spin-diffusion lengths of several micrometres, gate-tuneable carrier concentration, and high electronic mobility.[4]

In order to implement G in spintronic devices, a careful study of the G/ferromagnetic metal interface must be undertaken and several factors must be kept into account such as the electronic, structural and interfacial properties. For example, a critical issue still to be addressed for the realization of practical spintronic devices is the effective injection of the spin-polarized electrons in conductive channels.[5,6] Moreover, G and graphite are predicted[7] to be perfect spin filters between ferromagnetic surfaces such as Ni(111) or Co(0001) because their lattice constants match almost perfectly and their electronic structures overlap in reciprocal space in one spin direction only.

As mentioned in the section "Graphene", a versatile approach to tailor G properties relies on modifying the G/substrate interface by intercalation with other species.[8,9,10,11] For example, G grown on transition metal single crystals was successfully intercalated by alkali,[12] noble[8,13] and transition[14] metals or semimetals.[15] The role of the intercalated species is to tune the hybridization between the electronic states of G and the underlying substrate, either to restore the electronic structure of freestanding G or to induce doping and hybridizations. An important example for this section and for spintronic application is the intercalation of low interactive metals to prevent formation of a chemical bond between G and the open *d*-shell transition metals that might complicate or even prevent spin injection.[7,13]

Few studies in the literature have focused on spectroscopic measurements of the structural, electronic and magnetic properties of G in contact with ferromagnetic metals; one of the most studied cases is G/Ni(111). For this system a magnetic moment of 0.05-0.1 μ_b per atom, determined by XMCD on C K edge, is induced on G because of the hybridization of C π band with Ni 3*d* states.[16,17,18] Another study of G/Ni(111) revealed that after intercalation of 1 ML of Fe, the magnetic moment of carbon was enhanced up to 0.25 μ_b,[19] but it was difficult to distinguish exactly the magnetic contribution due to the Ni substrate from the component coming from the Fe intercalated film. Bilayer G films grown on SiC and intercalated with Fe were studied by ARPES;[20] however, the experimental ARPES data after iron intercalation were not

conclusive to assess the effect of the intercalation layer on the electronic structure, and theoretical studies indicate that the modifications due to the intercalation of a magnetic layer are minimal for multilayer G, whereas in the case of single layer G the band structure is expected to change dramatically.[21] For G grown on Co(0001) single crystal a spin-resolved ARPES study[22] shows that a perfectly oriented G on Co(0001) has two separated Dirac cones at the G K point with a difference of ~3.2 eV induced by the lifting of spin degeneracy induced by Co. Recently, G grown on Fe(110) has been intercalated by 1 ML of Au to suppress the interaction between the G π band and the Fe 3*d* states, this system has been studied by spin resolved ARPES and revealed an interesting "hedgehog spin texture".[13]

The choice of the catalyst substrates for the growth of long range ordered single layer G is critical. Some substrates, such as Ni or Co, are ferromagnetic on their own, while others, such as Rh[23] or Pd[24] (see Table 1 of section 2) are strongly interacting metals. A weakly interacting substrate is more desirable to highlight the effects of a further deposited and intercalated ferromagnetic metal, especially when the G VB is directly mapped by means of ARPES, as reported in this section.

The use of low interactive metals, such as Pt(111)and Ir(111), do not exclude small changes, such as hybridization between their *d* bands with G π band, and presence of doping.[25] For example, both Pt(111) and Ir(111) induce some small effects on the G π band via the interaction with *5d* orbitals such as minigaps opening for Ir(111)[26] and small (~80 meV) spin degeneracy lifting of Dirac cone for Pt(111).[27] However, the hybridization caused by ferromagnetic metal G is much stronger: the separation between spin polarized Dirac cones is ~3.2 eV for G/Co(0001)[22] and, as show later in this section, ~2.4 eV for G/Fe(1 ML)/Pt(111).

As mentioned above in the section 2, the choice of Pt(111) as a non-ferromagnetic catalytic substrate to grow large quasi-freestanding G flakes[28,29] is motivated by its possible application on a large scale for the production of G thanks to the possibility to reuse the metal substrate for several growths cycles.[30] We refer to the "Graphene on Pt(111)" paragraph of the section 2 for more detail about the growth of G on this metal.

We decided to use Fe as intercalant because of its peculiar electrical and magnetic properties and the large knowledge accumulated by surface science studies on the Fe/Pt(111) interface, whose structural and magnetic properties has been thoroughly investigated.[31,32,33,34] Moreover, the Curie temperature of Fe(1 ML)/Pt(111) is high enough (about 300 K)[34] to have a realistic use in practical devices at RT. For other system such as Co(1 ML)/Ir(111) the Curie temperature is much lower (about 90 K) posing serious limits in future applications.[35]

Advanced investigation tools have been used to study the electronic interactions induced by Fe on G. This section deals with a variety of experimental data based on photoemission from core-level, x-ray absorption spectroscopy (XAS), XMCD and ARPES that have been carried at different synchrotron radiation facilities. The results were interpreted with the assistance of DFT calculations. STM has been also performed in order to obtain a precise picture of the morphology of the G lattice at the atomic scale. All these characterizations have been carried out in order to disentangle intrinsic effects (electronic hybridization) from the role of structural defects, which may

be present at the G/Fe interface. Interestingly, the structure of the G layer is not modified by intercalation thanks to the epitaxial matching between Fe(1 ML)/Pt(111).[36]

In this section we investigate the Fe interaction with the G/Pt(111) system after *in-situ* UHV deposition, either at RT or at high (T=600 K) temperature. In this manner, two different systems are obtained: supported Fe NPs (hereafter Fe/G/Pt(111)) and intercalated Fe layers (hereafter G/Fe/Pt(111)), respectively. In both cases, experimental and theoretical data indicate a strong hybridization between the Fe layer and G, which lifts the G π band spin degeneracy. Moreover, a study of the oxidation at RT of these interfaces is presented, a reversible hybridization of G in sp^3 carbon occurs in the case of Fe/G/Pt(111), whereas intercalated Fe in G/Fe/Pt(111) is unaffected by the exposure to oxygen.[37] A separate paragraph is dedicated to XMCD on the Fe $L_{2,3}$ edge used to study the magnetization direction of Fe/Pt(111) and G/Fe/Pt(111).

These data suggest that the G/Fe/Pt(111) system can be a good platform to grow intercalated ferromagnetic metallic films that could be protected from air oxidation.

Experimental section

The sample was prepared in a UHV chamber with a base pressure of 3×10^{-10} mbar. The Pt(111) single crystal) by repeated cycles of sputtering (1.5 kV, 1×10^{-6} mbar of Ar), annealing at 925 K in 2×10^{-7} mbar O_2 partial pressure and flash annealing to 1100 K in UHV. The surface cleanness was checked by photoemission and the morphology by LEED and STM.

Iron was deposited by *in-situ* physical vapour deposition (PVD). The Fe evaporator was calibrated based on the reconstructions of Fe_xO_y ultrathin films grown on Pt(111), at increasing Fe coverage. The Fe film was deposited at RT in UHV and post-oxidized in 1×10^{-6} mbar of O_2 at 900 K.[38] The film growth was monitored by LEED and STM: the transition of LEED patterns between FeO and multi-layer Fe_3O_4 ultrathin films occurs at 2 ML nominal FeO coverage, when STM also shows the onset of the growth of Fe_3O_4 islands.[39,40] One ML of FeO corresponds to 2.16×10^{15} Fe atoms/cm^2. 1 ML Fe is defined as 2.60×10^{15} Fe atoms/cm^2 considering a pseudomorphic growth on Pt(111).[41]

Methods

The electronic structure in the VB band of structurally different iron/G systems supported on Pt, were investigated by ARPES at the Spectromicroscopy beamline at synchrotron Elettra (Trieste, Italy). The data were measured by using 74 eV photons, pass energy (PE) 20 eV and with an energy resolution of 125 meV. The ARPES data were acquired using a hemispherical electron energy analyser with angular resolution of 0.33°. The Sample was mounted onto a scanning stage, which enables positioning and raster imaging with respect to the fixed photon beam. Photoelectron intensity distribution maps I (k_x, k_y, E) were taken from microscopic areas (the beam size was about 1 μm) by rotating the electron energy analyser with respect to the sample using a two-axis goniometer. ARPES analyses were focused on the dispersion of the G π and σ bands from the Γ to the K point of the first Brillouin zone. The investigated BE range was from 0 to 24 eV, which includes G π σ, Pt 5*d* and Fe 3*d* bands.

The STM measurements, carried out in Prof. L. Gavioli's group (University of Brescia), were performed in a UHV multiscan lab from Omicron equipped with LEED optics, and a photoelectron spectrometer. STM images were acquired in constant current mode at RT with Pt/Ir tips prepared by ac electro-chemical etching in saturated $CaCl_2$ deionized water solution and cleaned in UHV by electron bombardment.

XPS from core levels and XAS spectra were acquired at the CNR-BACH beamline at synchrotron Elettra (Trieste, Italy). Photoemission spectra from C 1*s* core levels were recorded with 550 eV photons, PE=20 eV and with an energy resolution of 130 meV.

For the XMCD measurements, a dedicated beamtime was performed at the BACH beamline. XAS spectra of the Fe $L_{2,3}$-edge were acquired in total electron yield with an energy resolution of 160 meV. XMCD spectra were obtained by recording and subtracting two XAS spectra with opposite x-ray circular polarization (helicity). Measurements were carried out at the liquid nitrogen temperature (≈100 K - 130 K), which is much lower than the Curie temperature of Fe(1 ML)/Pt(111) that is close to RT.[34] XMCD data have been acquired in normal incidence (NI) and grazing incidence (GI), with the sample surface at 90° and 10° with respect to the photon beam, respectively. The sample was magnetized by an external magnet (0.5 T) brought close to the crystal border for some seconds at 45° from the surface plane. All measurements were acquired in pure remanence without any magnetic fields applied.

Calculations were performed by Prof. M. Mavrikakis's group using spin-polarized DFT, as implemented in the VASP code.[42] A G-(2×2)/Pt(111)-(√3×√3)R30° surface unit cell, with eight carbon atoms and three Pt atoms per layer, was used. For Fe adsorption or intercalation, three Fe atoms were introduced, corresponding to a coverage of one monolayer (ML), Figure 1. For FeO adsorption, a larger unit cell, G-(4×2)/Pt(111)-(2√3×√3), was used to account for the antiferromagnetic behaviour of FeO. For details about calculations see Ref. [43].

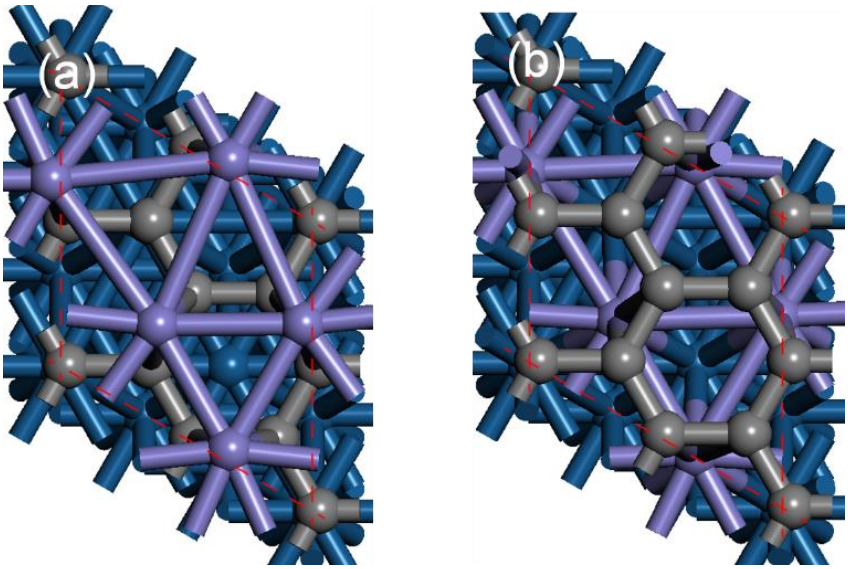

Figure 1. Optimized structure of G/Pt(111) with one monolayer Fe (a) adsorbed on top of G, and (b) intercalated between G and Pt(111) substrate. Grey, purple, and dark blue spheres indicate C, Fe, and Pt atoms, respectively. Reprinted from Ref. [43] © 2015 RSC.

Results and discussion

For XPS and STM measurements G was grown via surface limited reaction by dosing 150 L of C_2H_4 (6.5×10^{-7} mbar for 5 minutes) at 1000 K on Pt (111)[29] and cooling down the crystal at 30 K/min. Following this procedure, high quality films were obtained, which show the typical like R19° LEED superstructure (Figure 2.a),[29] whereas STM images indicate also the presence of other superstructures (the higher corrugated islands in Figure 2.b). In general, the mean size of rotationally different G domains is around 20-30 nm.

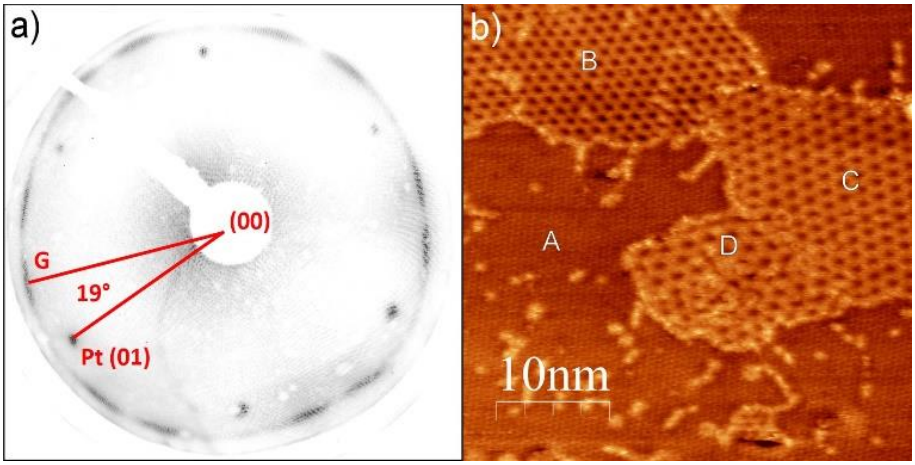

Figure 2. a) LEED pattern (E=55 eV) and b) different 'flakes' of bare G/Pt(111) as shown by STM (V=-27 mV; I=20.9 nA), with typical 20-30 nm average size. The G flakes in the figure above show some of the possible rotational domains observed on Pt(111): A-(3×3), B-(√37×√37)R21°, C-(√61×√61)R26°, D-(√67×√67)R12°. Reprinted from Ref. [43] © 2015 RSC.

For micro-ARPES measurements we tried to synthesize G by surface limited reaction, but the grains were too small to obtain a good quality of VB mapping. Therefore, we decided to use the carbon segregation mode in order to form micrometre size of G flakes dosing (>10000 L) of ethylene at very high temperature (~1300 K) and slowing cooling down the crystal. By this preparation the LEED pattern changes from the arcs features, reported in Figure 2a, in a variety of spots in the same position corresponding to the G lattice. This indicate that in the millimetre range we were sampling some tents of different grain orientation, which each one create six spots in the LEED pattern, and not a completely variety of orientation as represented by the arcs.

As mentioned in "Graphene on Pt(111)" paragraph of the section 2, the different G preparation, grown by carbon segregation mode or surface limited reaction, does not influence strongly the interaction with Pt(111). Moreover, spectroscopic investigations are not very sensitive to the type of G reconstruction, and DFT calculations for different G reconstructions lead to very similar results.

The G/Pt(111) system shows a sharp C 1s peak centred at a BE of 284.16 eV (Figure 3.a) that can be fitted by a single component characterized by a Doniach-Šunjić line shape.

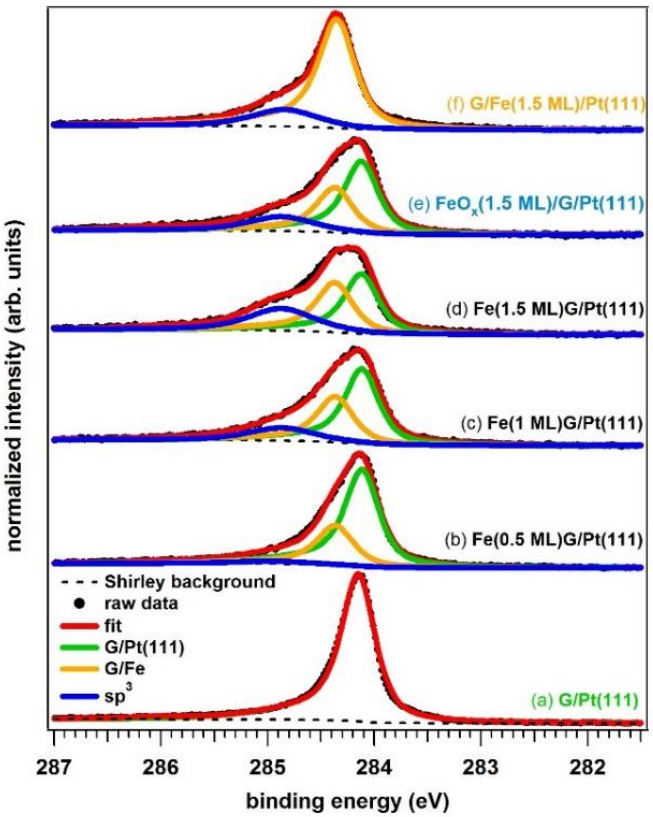

Figure 3. Normalized C 1s photoemission peaks (photon energy hv=550 eV) of (a) G/Pt(111), (b) Fe(0.5ML)/G/Pt(111), (c) Fe(1.0ML)/G/Pt(111), (d) Fe(1.5ML)/G/Pt(111), (e) FeO$_x$(1.5ML)/G/Pt(111) oxidized at RT, (f) G/Fe(1.5ML)/Pt(111) intercalated at 600 K. Reprinted from Ref. [43] © 2015 RSC.

The ARPES data (Figure 4.a) confirm the weak interaction between the π band of G and Pt 5*d* states; around the K point, the π bands of G have a linear dispersion as in quasi-freestanding layer.[44,45] The Dirac point energy, extrapolated from the crossing of a linear fit of the π band close to the K point (Figure 4.a), is slightly above the Fermi level, indicating that the G is slightly p-doped by the Pt contact.[28] Because of the limited resolution, it is impossible to resolve exactly the Dirac point position as done in Ref. [46,47].

Fe/G/Pt(111) and G/Fe/Pt(111)

Fe was deposited *in-situ* by PVD at RT on G/Pt(111) to obtain Fe/G/Pt(111). For XPS experiments, an increasing amount of Fe was evaporated on the surface (0.5, 1 and 1.5 ML), whereas for ARPES experiments only the 1 ML coverage was chosen to avoid a strong attenuation of the G spectroscopic features. Figure 3.b,c,d show the evolution of the C 1s photoemission line as a function of the Fe coverage.

After a least square fit analysis, three different components were clearly identified: the peak at BE 284.16 eV is due to the unperturbed sp^2 atoms, whereas the two new components at 284.40 eV and 285 eV are associated with the formation of the Fe/G interface, as confirmed by the intensity increase as a function of metal deposition. The component at 284.40 eV is likely connected to C sp^2 atoms underneath a metal island. The shift toward higher BE with respect to uncovered C atoms can be interpreted as an indication of the strong cohesive energy between G and Fe or as doping.[48] Analogous to similar results reported in the literature for other metals,[49,50] the small

component at 285 eV can be associated with a local rehybridization of G to sp^3 carbon, also driven by the strong Fe-C interaction. From the absence of C 1*s* peak components at ca 283.2 eV (Figure 3.b-f) and from the Fe $L_{2,3}$ XAS data (Figure 5.a,c), which indicate the zerovalent nature of Fe,[51] we can exclude the formation of iron carbides.

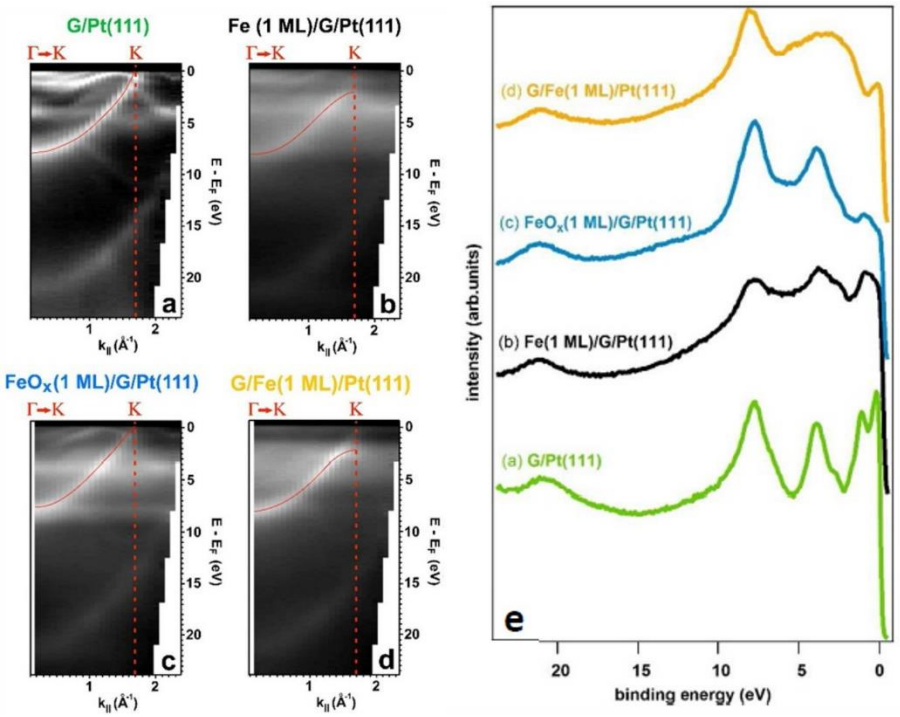

Figure 4. ARPES plot from Γ to K point of G first Brillouin zone obtained (photon energy hv=74 eV) for (a) G/Pt(111) (b) Fe(1ML)/G/Pt(111), (c) FeO_x(1ML)/G/Pt(111) oxidized at RT and (d) G/Fe(1ML)/Pt(111) intercalated at 600 K. Dashed red line are for the theoretical position of the K point in a freestanding G layer. (e) VB spectra acquired in Γ. Adapted from Ref. [43] © 2015 RSC.

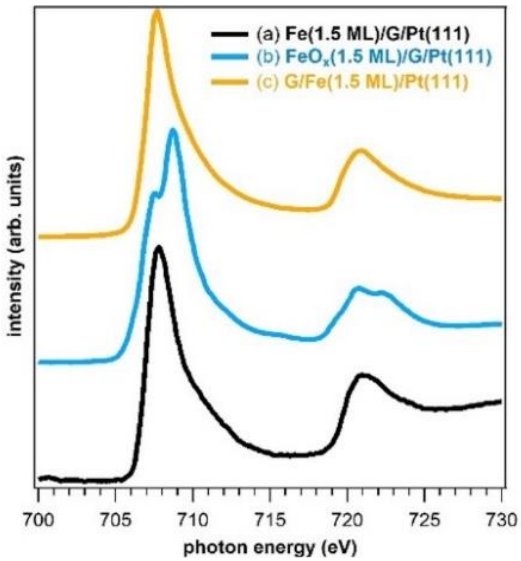

Figure 5. Fe $L_{2,3}$ XAS data for (a) Fe(1.5ML)/G/Pt(111), (b) FeO_x(1.5ML)/G/Pt(111) obtained after dosing 150 L of O_2 at RT and (c) G/Fe(1.5ML)/Pt(111) intercalated at 600 K.

A Volmer-Weber type 3D island growth mode characterizes the Fe NPs in the Fe/G/Pt(111) system at very low coverage (~0.1 ML) and RT. STM topographies

indicate a preferential nucleation at G domain boundaries and point defects (Figure 6.a,b,c).[10] The Fe NPs have a small size dispersion; they are typically round-shaped with a diameter of 2-3 nm (Figure 6.d) with an average thickness of several layers. This is very similar to previous results reported for the growth of Fe islands on G/Rh(111),[10] and other metal NPs on G/Ru(0001).[52] The Volmer-Weber-type 3D growth of Fe NPs on G is also confirmed by photoemission: the C 1s spectra (Figure 3.b,c,d) show that the component at 284.16 eV, pertaining to uncovered G on Pt(111), is visible even if the coverage exceeds 1 ML.

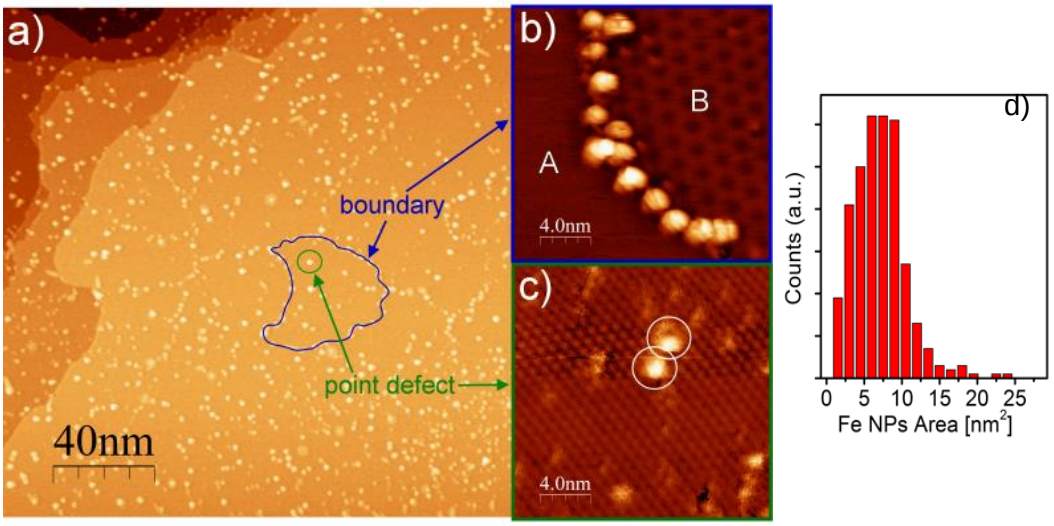

Figure 6. (a) Large area STM view of low coverage Fe(0.1 ML)/G/Pt(111) system (V=1.5V; I=0.3nA) outlines 3D Volmer-Weber type growth of Fe NPs at RT on pristine G/Pt(111) film, (b) STM (V=-0.69V I=0.63 nA) of Fe NPs nucleated at boundary of contiguous (3×3) (A) and (√67×√67)R12° (B) G flakes, c) STM (V=-65 mV I=40 nA) of Fe NPs pinned on point defects of a (√37×√37)R21° G flake, (d) histogram of the Fe NPs areas. Reprinted from Ref. [43] © 2015 RSC.

The intercalated system, G/Fe/Pt(111), was obtained at high temperature, by depositing Fe on the G/Pt(111) system directly at 600 K or by post-annealing the Fe/G/Pt(111) system at 700 K for 5 minutes.[53] The relatively high temperature was necessary to obtain a flat Fe layer[36] and to intercalate G completely. Temperature and time were tuned to avoid the formation of a Pt/Fe alloy, however the possibility that a minor amount Fe migrates into the Pt selvedge cannot be excluded.

Two strong experimental evidences from STM and ARPES data demonstrate the intercalation process of Fe beneath G. The STM data reported in Figure 7 indicate that, after 0.3 ML Fe deposition at 600 K, Fe monolayer islands are formed on the Pt surface, which are covered by a continuous unperturbed layer of G. This can be explained by the pseudomorphic growth of Fe islands on Pt(111),[41] which determines the same lattice mismatch at both G/Pt and G/Fe interfaces. Moreover, at particular tunneling conditions the moiré pattern visible on top of these islands is the same as that observed for G on Pt(111), however the bias dependence of the moiré corrugation of adislands is different from the main terraces, indicating the presence of compositionally distinct interfaces with G in the two cases.

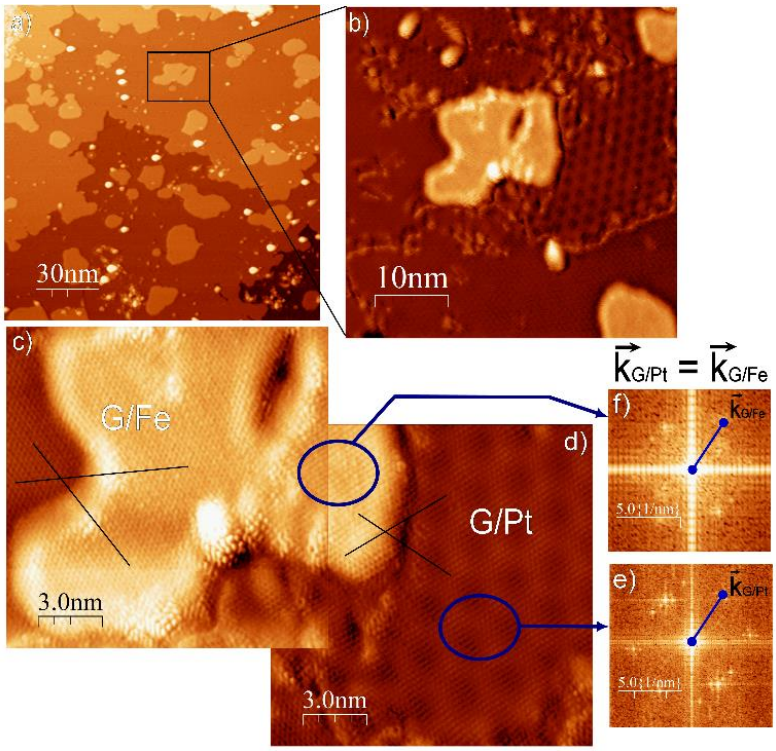

Figure 7. (a) Large area STM view (V=-1.5V I=0.3 nA) of the intercalated G/Fe(0.3 ML)/Pt(111) system. Buried and 1 ML-thick Fe islands are observed, (b) Higher resolution detail (V=-28 mV I=21.3 nA) on a Fe island decorated by two contiguous G flakes with different epitaxy. (c) and (d) (V=-28 mV I=34.6 nA) show atomic lattice of G lying on Fe and Pt. Black lines are used to outline that the G film continues as an unperturbed lattice stack both at Fe/Pt(111) and Pt(111) interfaces. Variation in electronic moirè contrast is observed in (d), when G is at the Fe interface. (e) is the fast Fourier transformation (FFT)-STM of the G/Pt(111) region of d), while (f) is the FFT of the G/Fe/Pt(111) region: reciprocal lattice vectors $\mathbf{k}_{G/Fe}$ *and* $\mathbf{k}_{G/Pt}$ *of G are actually the same (*$\mathbf{k}$*=4.13±0.01 nm^{-1}), corresponding to 2.42-2.43 Å. Reprinted from Ref. [43] © 2015 RSC.*

Differently from the growth of intercalated epitaxial islands underneath G grown on Rh(111) (G/Ni/Rh(111) and G/Fe/Rh(111)) where the local spatial variation of G-Rh(111) controls the size and shape of intercalated island,[10] the shape of the Fe NPs is random and there is not a significant size selection of the dimension. This is a further indication that the interaction between G and the Pt substrate is so weak that does not hinder the atom diffusion below the G layer.

Interestingly, whereas in the Fe/G/Pt(111) system 3D Fe islands are observed, the intercalated Fe islands are flat. This is evident from the STM images and is also confirmed by the XPS data. In the G/Fe(1.5 ML)/Pt(111) intercalated system, the peak at 284.16 eV, which is the fingerprint of G in contact with Pt(111), is completely suppressed (Figure 3.f). In the case of G/Fe/Pt(111), the residual presence of the 285 eV peak is probably due to the trapping of Fe into G defects. The photoemission data and STM therefore indicate that the intercalation is quantitative and leads to flat islands with an exclusive Fe/G interface.

Comparing the distribution of the Fe islands in Figure 6.a and Figure 7.a, we can deduce an easy diffusion of the Fe atoms underneath the G layer in order to form large islands. This was not observed in the case of Fe intercalated underneath G/Rh(111),[10] this is again related to the different strength of the G-substrate interaction, which is larger for Rh(111) than for Pt(111). (see Table 1 of section 2) In the

former, because of the presence of locally strong Rh-C bonds, the G layer limits atomic diffusion at the G/Rh interface, and the shape, orientation and size of the Fe islands are highly influenced. On the contrary, the carbon layer in G/Pt(111) is an adaptive cover that can be easily lifted to accommodate atom diffusion and the growth of large islands.

The relative intensity of the G bands and Fe 3*d* states in the ARPES spectra is very informative. In the case of Fe(1ML)/G/Pt(111) (Figure 4.b), the G π band (c.a. 8.1 eV) is strongly attenuated by Fe, and its intensity in Γ is almost as strong as the metallic features at about 3 eV (Figure 4.b). On G/Fe(1ML)/Pt(111) (Figure 4.d), the G π band has a much higher relative intensity, showing an intensity comparable to the G/Pt(111) system (Figure 4.a), confirming the presence of G on the surface.

ARPES data also show major differences in the G band dispersion between G/Pt(111) and G/Fe interfaces. As mentioned before, in the G/Pt(111) case (Figure 4.a), the G π band displays a linear dispersion close to the K point as in quasi-freestanding layer. On the contrary, when G is in contact with Fe, either because it supports Fe NPs (in Fe/G/Pt(111), Figure 4.b), or as a consequence of the intercalation (in G/Fe/Pt(111), Figure 4.d), a relevant hybridization of its π band with Fe 3*d* states can be observed.

The experimental data show that the G electronic structure is strongly modified by the Fe interface: from the Γ to K point of the BZ, the dispersion of the π band is very similar to the G/Pt(111) case until the band crosses the energy range of the Fe 3*d* levels (4 eV). Starting from this point, the band deviates from the linear dispersion typically observed around the K point, bending and remaining pinned at about 2.4 eV below the Fermi level. Moreover, at the Γ point, a small shift towards higher BE (about 0.2 eV with respect to G/Pt(111)) of both the π and σ bands (Figure 4.e) can be noticed, even if in this energy range there is not a direct overlap with the Fe 3*d* states. Similar features are reported in the literature for G interacting with other non-noble *d*-metals, such as Ni(111), and are connected to an overall n-doping of the G layer.[18,54,55,56]

To understand the electronic structures of the Fe/G/Pt(111) and G/Fe/Pt(111) systems, the calculation of Fe adsorption or intercalation on G/Pt(111) at Fe coverage of 1 ML has been undertaken. The spin-resolved band structures of Fe(1 ML)/G/Pt(111) due to the interaction with Fe states, the G π-bands are non-degenerate within two spin channels. Furthermore, the linear dispersion near the K point, found in the band structures of G/Pt(111) without Fe, is perturbed due to the hybridization between carbon $2p_z$ and Fe 3*d* orbitals. The Dirac point is roughly at 0.4 and 1.7 eV below the Fermi level for the majority and minority spin channels, respectively.

The calculated band structures of the intercalated system G/Fe(1ML)/Pt(111) are shown in Figure 8. The contributions of carbon $2p_z$ and Fe 3*d* states are highlighted in red and green, respectively. Similarly to the case of the adsorbed system, the G π-bands of the Fe intercalated system are non-degenerate within two spin channels: the Dirac point is roughly at 0.4 and 2.3 eV below the Fermi level in the majority and minority spin channels, respectively. We note that the downshift of the Dirac point at the minority spin channel (Figure 8.b) in the intercalated system is larger than the corresponding downshift in the adsorbed system.

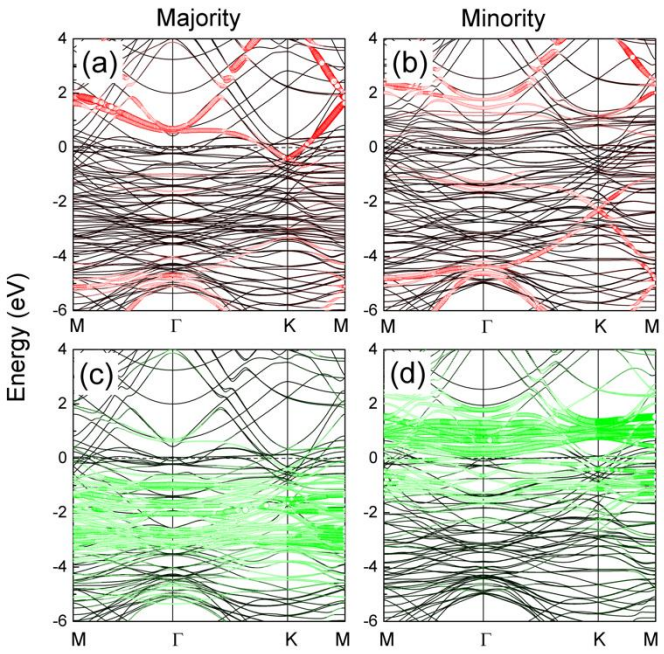

Figure 8. Band structures of the intercalated system G/Fe(1 ML)/Pt(111). (a) Majority spin and (b) minority spin band structures with the contributions of carbon $2p_z$ states are highlighted in red. The contributions of Fe 3d states to (c) majority and (d) minority spin band structures are highlighted in green. The Fermi level is set at zero. Reprinted from Ref. [43] © 2015 RSC.

To compare the ARPES map of the flat intercalated layer, Figure 4.d, with the calculated band structure, we show in Figure 9 an enlargement of the ARPES spectra of G/Fe(1ML)/Pt(111) close to the G K point. The band splits in two components at about 3 eV. One branch continues up to 0.6 eV and the other remains pinned at 2.4 eV. This is in excellent agreement with the calculated majority and minority spin band structures of G/Fe(1 ML)/Pt(111) shown in Figure 8.a and b.

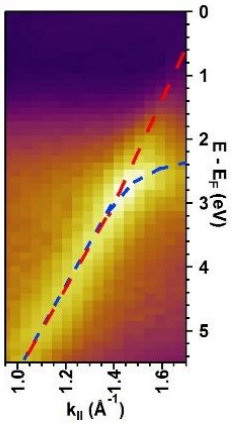

Figure 9. Enlarged view of ARPES of G/Fe(1 ML)/Pt(111) close to the G K point. Underlined with dashed red line spin majority band and in blue spin minority band. Reprinted from Ref. [43] © 2015 RSC.

It is worth mentioning that for the Fe/G/Pt(111) system, a direct comparison of the experimental data with the calculated band structures is rather difficult because 3D NPs are formed when 1 ML of Fe is deposited at RT. Some G/Pt(111) is likely not covered by Fe and can be sampled by photoemission, making the final ARPES map a combination of Fe/G/Pt(111) and G/Pt(111). Furthermore, the Fe band structures can

be modified by the size of the Fe NPs and consequently be different from one flat monolayer placed above G, as assumed in the calculations.

Interestingly, additional calculations for 1 ML Fe adsorbed on the Pt(111) surface, and for the incorporation of 1 ML of Fe atoms below the first and second Pt layer, all in the absence of G, provide formation energies of -4.89, -5.81, -5.61 eV, respectively. Although the models tested do not mix Pt and Fe within a given slab layer, these results indicate that Fe could easily alloy with the Pt substrate. Therefore, the most stable alloy was used, i.e. Pt(1 ML)/Fe(1 ML)/Pt(111), to support a G layer. It turns out that the G/Pt(1 ML)/Fe(1 ML)/Pt(111) system is 2.26 eV (i.e. -0.75 eV /Fe atoms) more stable than G/Fe(1 ML)/Pt(111). Interestingly, for this system (Figure 10), the calculated band structure of G is very similar to the simple G/Pt(111) interface: the Dirac energy is located at 0.3 eV above the Fermi level and the π band is spin degenerate and displays a linear dispersion around the K point. These results indicate that even a monolayer of Pt is sufficient to restore the weakly-interacting regime, as it has been also verified in section 2.3.

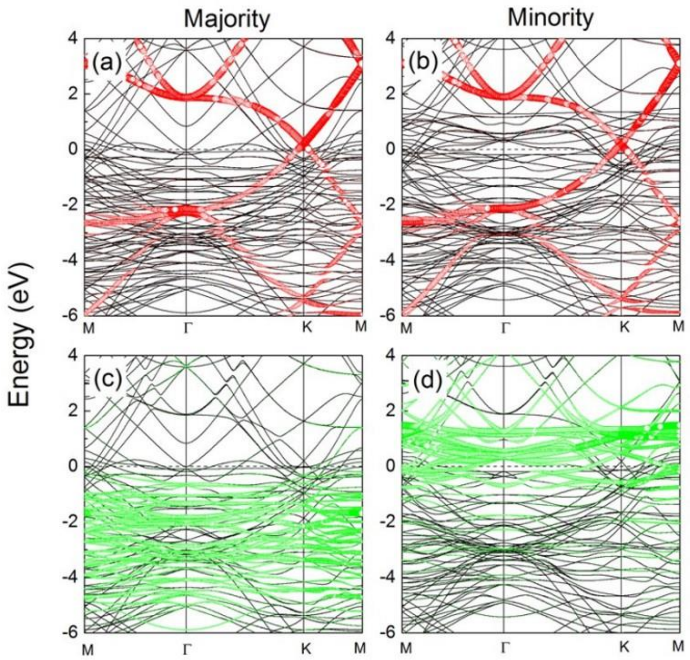

Figure 10. Band structures of the intercalated system G/Pt(1 ML)/Fe(1 ML)/Pt(111). (a) Majority spin and (b) minority spin band structures with the contributions of carbon $2p_z$ states are highlighted in red. The contributions of Fe 3d states to (c) majority and (d) minority spin band structures are highlighted in green. The Fermi level is set at zero. Reprinted from Ref. [43] © 2015 RSC.

Since the experimental ARPES data show a strong modification of the pristine G band structure and are compatible only with the features of G/Fe(1 ML)/Pt(111), we can conclude that the formation of the alloy, even if thermodynamically favoured, is prevented by kinetic factors.

X-ray circular magnetic dichroism

If we want apply Fe/G junctions as part of spintronic devices, the system spin orientation should be taken into account. The conventional ferromagnetic electrodes for G spintronic devices exploit *in-plane* magnetization,[4] however a recent work on G/Ni(111)[57] showed in that G layer trigger a transition of the magnetization orientation

of the substrate from *in-plane* to *out-of-plane* across the interface. Therefore, the magnetization orientation of the Fe layer deposited above and intercalated below G represents a crucial factor in order to provide a clear view for future magnetic and spintronic devices.[4,5] Notably, a system with a straightforward *out-of-plane* magnetization direction, e.g. Fe(< 1 ML)/Pt(111), can be used as prototypical case study to investigate G spin and magnetic texture for application in future devices.

The magnetic properties of Fe layers on Pt (111) have been thoroughly study in the literature;[32,33,34,58] for Fe(0.8 ML)/Pt(111) magnetization is oriented *out-of-plane* and therefore the XMCD signal is larger in NI geometry. This magnetic effect, as well its flat morphology on Pt(111) (Figure 7) are induced by an unusual face centred cubic (fcc) structure that is adopted by Fe in order to maintain a pseudomorphic growth on Pt(111).[41] When the Fe thickness is increased above one monolayer, the magnetization axis flips *in-plane* because of the Fe phase transition from epitaxially strained fcc to bulk-like body centred cubic (bcc), and the largest XMCD signal is observed in GI.

In order to visualize the magnetization orientation of Fe layer deposited above and below G and on Pt(111) the XMCD spectra were acquired in two different geometries, NI and GI. Theoretically, for a layer with a perfect *out-of-plane* magnetization the highest XMCD signal is observed in NI, meanwhile with a radiation perpendicular to the magnetic axis the XMCD should be zero. This principle is summarized in the formula

$$XMCD_{signal} = \mathbf{M}\cdot\mathbf{L} \quad (1)$$

with **M** and **L** the magnetic moment and circular x-ray polarization vector, respectively.[59,60]

Experimentally, it is not feasible to acquire XAS spectra with the sample surface parallel to synchrotron radiation; in our condition of GI (10° between sample surface and the beam) **L** can be separated in two components, one parallel and one perpendicular to the sample surface. Therefore the XMCD signal at GI, for a perfect *out-of-plane* magnetization, will be reduced by a factor

$$XMCD_{GI}/XMCD_{NI}=\sin(10°)=0.17 \quad (2).$$

The ratio between the two XMCD signals, acquired simply by rotating the sample, is a good indicator of magnetization orientation because it allows neglecting various unwanted experimental spurious effects such as uncompleted magnetization, temperature fluctuations, and non-complete radiation polarization.

Figure 11 reports the Fe $L_{2,3}$ XMCD spectra in NI and GI for Fe (0.8 ML)/Pt(111), G/Fe (0.8 ML)/Pt(111) and Fe (0.8 ML)/G/Pt(111).

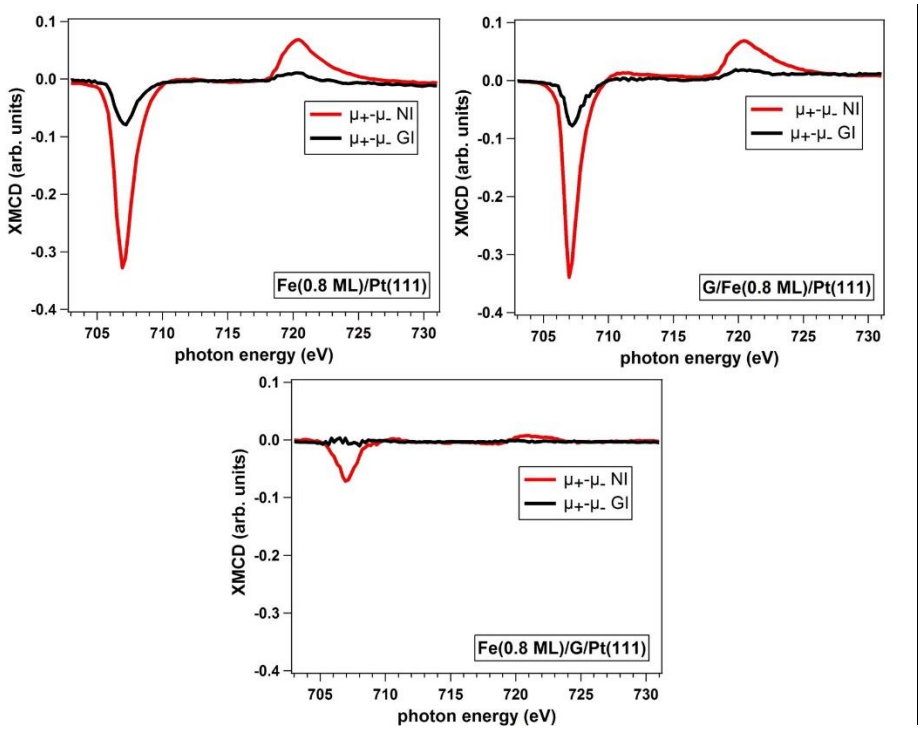

Figure 11. XMCD spectra of Fe(0.8 ML)/Pt(111), G/Fe(0.8 ML)/Pt(111) and Fe(0.8 ML)/G/Pt(111) in red NI and black GI.

For Fe(0.8 ML)/Pt(111) and G/Fe(0.8 ML)/Pt(111) the XMCD signals are much stronger in NI than in GI; the ratio between XMCD of L_3 edge ($XMCD_{GI}/XMCD_{NI}$) are 0.23 in both the cases that is in very good agreement with the theoretical value, reported in formula (2), for a perfect *out-of-the-plane* magnetization axis.

From XMCD and XAS spectra of G/Fe(0.8 ML)/Pt(111) acquired in NI, applying the XMCD sum rules,[61] the projection of the orbital *L* and effective spin $S_{eff}=S+7D$ magnetic moments onto the incidence light direction has been determined considering a number of holes in the 3*d* stated h_d=4.8, considering that in addition of the 3.4 e of Fe bulk sytem[61] other 1.44 e are donated by monolayer Fe intercalated, Pt accepts 0.84 e, and the remaining 0.6 e is donated to G.[43] L and S_{eff} resulted to be 0.14 and 2.80 μ_B/atom, respectively. These values are comparable with those reported for Fe (0.8 ML)/Pt(111) in Ref. [33], a small discrepancy can be traced to the missing consideration of the donation of electron from Fe to Pt substrate done by the authors of that paper.

Figure 11 shows that in our conditions the Fe(0.8 ML)/G/Pt(111) system shows a small amount of dichroism only in NI, whereas it is almost undetectable in GI. The strong reduction of XMCD signal for Fe(0.8 ML)/G/Pt(111) can be explained by the different morphology of Fe, which at low temperature forms NPs (Figure 6). In the literature some works indicate that the magnetism of Fe NPs deposited on G[62,63] and graphite depends on the cluster size,[64] moreover there is a strong temperature dependence.[65] It has been reported that residual magnetization of Fe NPs in remanence is very small also at temperature close to 6 K.[64] Anyway, it is not in the aim of this section to compare our results with previous papers that study Fe cluster deposited on graphitic substrate[64,65,66] because the measurements where acquired in total absence of

applied field during the measurements, without any NPs size or mass selection and for a fixed temperature of about ≈100-130 K.

When 2.4 ML Fe are deposited on Pt(111), the higher XMCD signal is observed in GI as expected for the flip magnetization axis orientation, the same effect is visible for Fe(2.4 ML)/G/Pt(111). On the contrary for G/Fe(2.4 ML)/Pt(111) the higher XMCD signal comes from NI incidence. An explanation for this behaviour can be envisaged in a not perfect intercalation of such big quantity of Fe, however it is difficult to obtain a precise morphologic investigation as done for submonolayer Fe coverage by STM.[43] Another explanation can be traced by the imposed *out-of-plane* magnetization of Ni(111) induce by G overlayer,[57] which can change the Fe magnetization direction for thicker layers. Further investigation by XMCD will be carried out in order to understand the reason this unexpected flipping of the magnetization for high Fe coverages.

Iron oxidation at room temperature

In order to investigate the oxidation of our systems a spectroscopic investigation of the Fe(1.5ML)/G/Pt(111) system after dosing molecular oxygen (6.5×10^{-7} mbar, 150 L at RT) was carried out. Oxygen reacts with the outer shell of the Fe islands forming a defective iron oxide (hereafter FeO_x(1.5 ML)/G/Pt(111)). The XAS measurements (Figure 5.b) indicate a clear modification of the Fe $L_{2,3}$-edges, which is characterized by a complex line shape that can be due to the overlap of two components, one coming from a residual metal phase and another one related to non-stoichiometric iron oxides.[67]

Because of the Fe oxidation, the 284.40 eV component of the C 1s photoemission line of the Fe(1.5 ML)/G/Pt(111) system decreases (Figure 3.e), whereas the peak at 284.16 eV, assigned to G/Pt(111), becomes more intense, reaching almost the same relative intensity observed for Fe(0.5ML)/G/Pt(111) (Figure 3.b). Surprisingly, the component related to sp^3 carbon, at c.a. 285 eV, is also strongly suppressed after oxidation, demonstrating that the local C sp^3 hybridization induced by Fe is reversible. The remaining peaks at 284.40 eV and 285 eV can be related to the metallic Fe/G interface, persisting in the lower inner portion of the islands.

The STM images of the oxidized surface are of low quality, likely due to the presence of residual mobile oxygen species (see Figure 12) and for the amorphous structure of FeO_x NPs synthetized at RT that probably also causes the broad features at about 4.5 and 8 eV in the VB spectrum (Figure 4.c), which do not show any energy dependence on **k** vector. Moreover, it can be seen that the morphology of the Fe NPs does not change significantly, and is characterized only by a small increment of the corrugation.

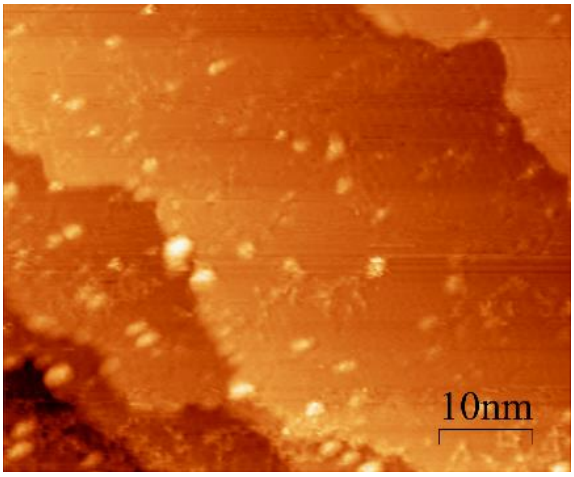

Figure 12. STM images of the Fe(1.5ML)/G/Pt(111) system after dosing molecular oxygen (6.5×10^{-7} mbar, 150 L at RT). Reprinted from Ref. [43] © 2015 RSC.

The ARPES measurements taken after dosing 150 L O_2 on Fe(1 ML)/G/Pt(111) confirm the absence of any interaction between the FeO_x layer and G, as evidenced by the complete recovery of the G π band, which is no longer hybridized with the Fe 3d states (Figure 4.c). The overall G electronic band structure is very similar to the G/Pt(111) case (Figure 4.a). Finally, at the Γ point also the small shift towards higher BE observed for G/Fe interface disappears.

Bader charge analysis shows that essentially no charge is transferred between FeO and G. This can be understood by the presence of the more electronegative O, which acts as an electron acceptor for the Fe donors and inhibits charge transfer from Fe to G. Considering the negligible interaction between FeO monolayer and G, the similarity of G band structures of FeO_x(1ML)/G/Pt(111) and that of G/Pt(111) observed in experimental ARPES is expected. Similar phenomenon has been observed for the reaction of Se atoms with Ni substrate in section 3.1.2.

Interestingly, any attempt to oxidize the G/Fe/Pt(111) system dosing the same amount of O_2 at RT was unsuccessful. Even when using a ten times higher oxygen dosage or direct air exposure we did not observe any iron oxidation. Further studies will be performed dosing oxygen at higher temperature to exploit the gas intercalation;[68] however, the observed oxidation protection[37] of the Fe intercalated islands is a crucial finding for the realisation and practical usage of future spintronic devices.

Conclusions

In this section the interaction between a quasi-freestanding G layer, grown on Pt(111), and iron was studied. We demonstrated that when iron is deposited on G at RT it forms NPs that aggregate on G grain boundaries and point defects. On the contrary, if Fe is deposited on the substrate Pt(111) at 600 K, it intercalates beneath G, creating monolayer flat islands. G displays an almost perfect carpeting mode on the Fe intercalated island, and the carbon sp^2 lattice goes continuously from above the Fe intercalated islands down to the Pt(111) substrate. Photoemission from C 1s core level shows that the C 1s peak shifts to higher BE when Fe is deposited atop or intercalated beneath G.

The hybridization between Fe 3*d* states and G π band was visualized experimentally using ARPES, and demonstrated theoretically using band structures predictions. We also demonstrated that Fe NPs deposited above G can be easily oxidized, and in the hybridization cease. On the contrary, Fe is well protected from the oxidation if it is intercalated beneath G.

Remarkably, DFT calculations show that the Fe contact lifts G spin degeneration, inducing a clear split in the C π band. Experimentally this is visible in the ARPES map of G/Fe(1 ML)/Pt(111), confirming the possibility to induce magnetism in monolayer G in contact with a monolayer of ferromagnetic material. Moreover, theoretical calculations indicate that the introduction a single Pt layer between G and Fe is sufficient to recover the electronic properties of self-standing G, situation experimentally verified for G/Pt_3Ni(111), see also section 2.3.

XMCD measurements of G/Fe(<1 ML)/Pt(111) confirmed the *out-of-plane* magnetization axis as it has been found for submonolayer of Fe/Pt(111) opening the way for this system application in spintronic devices where the spin direction is crucial.

To summarize, the system G/Fe/Pt(111) represents a quite interesting system with a very high structural versatility that can be used to study G magnetism in 2D devices for the following reasons:

1. G sp^2 lattice homogenously covers the Fe intercalated islands without inducing structural defects that could induce spurious magnetism;[69]
2. even if G is in contact with only one layer of ferromagnetic metal its spin degeneracy is removed;
3. intercalated Fe islands are efficiently protected by G from oxidation, which is a fundamental requirement for the development of practical devices.

References

1 Eda, G.; Fanchini, G.; Chhowalla, M. Large-area ultrathin films of reduced graphene oxide as a transparent and flexible electronic material, *Nat. Nanotechnol.* **2008**, *3*, 270.

2 Novoselov, K. S.; Fal'ko, V. I.; Colombo, L.; Gellert, P. R.; Schwab M. G.; Kim, K. A roadmap for graphene, *Nature* **2012**, *490*, 192.

3 Lee, E. J. H. ; Balasubramanian, K.; Weitz, R. T.; Burghard M.; Kern, K. Contact and edge effects in graphene devices, *Nat. Nanotechnol*. **2008**, *3*, 486.

4 Han, W.; Kawakami, R. K.; Gmitra, M., Fabian, J. Graphene spintronics, *Nat. Nanotechnol.* **2014**, 9, 794.

5 Tombros, N.; Jozsa, C.; Popinciuc, M.; Jonkman, H. T.; Van Wees, B. J. Electronic spin transport and spin precession in single graphene layers at room temperature, *Nature* **2007**, *448*, 571.

6 Seneor, P.; Dlubak, B.; Martin, M.; Anane, A.; Jaffres H.; Fert, A. Spintronic with graphene, *Mrs Bulletin*, **2012**, *37*, 1245.

7 Karpan, V. M.; Giovannetti, G.; Khomyakov, P. A.; Talanana, M.; Starikov, A. A.; Zwierzycki, M.; van den Brink, J.; Brocks, G.; Kelly P. J. Graphite and graphene as perfect spin filters, *Phys. Rev. Lett.* **2007**, *99*, 176602.

8 Shikin, A. M.; Prudnikova, G. V.; Adamchuk, V. K.; Moresco F.; Rieder, K. Surface intercalation of gold underneath a graphite monolayer on Ni(111) studied by angle-resolved photoemission and high-resolution electron-energy-loss spectroscopy, *Phys. Rev. B* **2000**, *62*, 13202.

9 Dedkov, Y. S.; Shikin, A. M.; Adamchuk, V. K.; Molodtsov, S. L.; Laubschat, C.; Bauer A.; Kaindl, G., Intercalation of copper underneath a monolayer of graphite on Ni(111), *Phys. Rev. B* **2001**, *64*, 035405.

[10] Sicot, M.; Leicht, P.; Zusan, A.; Bouvron, S.; Zander, O.; Weser, M.; Dedkov, Y. S.; Horn, K.; Fonin, M. Size-selected epitaxial nanoislands underneath graphene moiré on Rh(111), *ACS Nano* **2012**, *6*, 151.

[11] Addou, R.; Dahal, A.; Batzill, M. Graphene on ordered Ni-alloy surfaces formed by metal (Sn, Al) intercalation between graphene/Ni(111), *Surf. Sci.* **2012**, *606*, 1108.

[12] Nagashima, A.; Tejima N.; Oshima, C. Electronic states of the pristine and alkali-metal-intercalated monolayer graphite/Ni(111) systems, *Phys. Rev. B* **1994**, *50*, 17487.

[13] Varykhalov, A.; Sánchez-Barriga, J.; Marchenko, D.; Hlawenka, P.; Mandal, P. S.; Rader, O. Tunable Fermi level and hedgehog spin texture in gapped graphene *Nat. Commun.* **2015**, *6*, 7610.

[14] Gyamfi, M.; Eelbo, T.; Wasniowska, M.; Wiesendanger, R. Impact of intercalated cobalt on the electronic properties of graphene on Pt(111) *Phys. Rev. B* **2012**, *85*, 205434.

[15] Cui, Y.; Gao, J.; Jin, L.; Zhao, J.; Tan, D.; Fu Q.; Bao, X. An exchange intercalation mechanism for the formation of a two-dimensional Si structure underneath graphene *Nano Res.* **2012**, *5*, 352.

[16] Weser, M.; Rehder, Y.; Horn, K.; Sicot, M.; Fonin, M.; Preobrajenski, A. B.; Voloshina, E. N.; Goering, E.; Dedkov, Y. S. Induced magnetism of carbon atoms at the graphene/Ni(111) interface. *Appl. Phys. Lett*. **2009**, *96*, 012504.

[17] Dedkov, Y. S.; Fonin, M. Electronic and magnetic properties of the graphene–ferromagnet interface *New J. Phys.* **2010**, *12*, 125004.

[18] Voloshina, E. N.; Generalov, A.; Weser, M.; Böttcher, S.; Horn K.; Dedkov, Y. S. Structural and electronic properties of the graphene/Al/Ni(111) intercalation system *New J. Phys.* **2011**, *13*, 113028.

[19] Weser, M.; Voloshina, E. N.; Horn K.; Dedkov, Y. S. Electronic structure and magnetic properties of the graphene/Fe/Ni(111) intercalation-like system *Phys. Chem. Chem. Phys.* **2011**, *13*, 7534.

[20] Sung, S. J.; Yang, J. W.; Lee, P. R.; Kim, J. G.; Ryu, M. T.; Park, H. M.; Lee, G.; Hwang, C. C.; Kim, K. S.; Kim, J. S.; Chung, J. W. Spin-induced band modifications of graphene through intercalation of magnetic iron atoms *Nanoscale* **2014**, 6, 3824.

[21] Karpan, V. M.; Khomyakov, P. A.; Starikov, A. A.; Giovannetti, G.; Zwierzycki, M.; Talanana, M.; Brocks, G.; van den Brink, J.; Kelly, P. J. Theoretical prediction of perfect spin filtering at interfaces between close-packed surfaces of Ni or Co and graphite or graphene *Phys. Rev. B* **2008**, *78*, 195419.

[22] Usachov, D.; Fedorov, A.; Otrokov, M. M.; Chikina, A.; Vilkov, O.; Petukhov, A.; Rybkin, A. G.; Koroteev, Y. M.; Chulkov, E. V.; Adamchuk, V. K.; Grüneis, A.; Laubschat, C.; Vyalikh, D. V. Observation of Single-Spin Dirac Fermions at the Graphene/Ferromagnet Interface *Nano Lett.* **2015**, *15*, 2396.

[23] Gotterbarm, K.; Zhao, W.; Höfert, O.; Gleichweit, C.; Papp, C.; SteinrücK, H.-P. Growth and oxidation of graphene on Rh(111), Phys. *Chem. Chem. Phys.* **2013**, *15*, 19625.

[24] Murata, Y.; Starodub, E.; Kappes, B. B.; Ciobanu, C. V.; Bartelt, N. C.; McCarty K. F.; Kodambaka S. Orientation-dependent work function of graphene on Pd(111) *Appl. Phys. Lett* **2010**, *97*, 143114.

[25] Batzill, M. The surface science of graphene: Metal interfaces, CVD synthesis, nanoribbons, chemical modifications, and defects, *Surf. Sci. Rep*. **2012**, *67*, 83.

[26] Pletikosić, I.; Kralj, M.; Pervan, P.; Brako, R.; Coraux, J.; N'Diaye, A. T.; Busse, C.; Michely, T. Dirac Cones and Minigaps for Graphene on Ir(111) *Phys. Rev. Lett.* **2009**, *102*, 056808.

[27] Klimovskikh, I. I.; Tsirkin, S. S.; Rybkin, A. G.; Rybkina, A. A.; Filianina, M.V.; Zhizhin, E. V.; Chulkov, E. V.; Shikin, A. M. Nontrivial spin structure of graphene on Pt(111) at the Fermi level due to spin-dependent hybridization *Phys. Rev. B* **2014**, *90*, 235431.

[28] Sutter, P.; Sadowski, J. T.; Sutter, E; Graphene on Pt(111): Growth and substrate interaction, *Phys. Rev. B* **2009**, *80*, 245411.

[29] Gao, M.; Pan, Y.; Huang, L.; Hu, H.; Zhang, L. Z.; Guo, H. M.; Du, S. X.; Gao, H.-J. Epitaxial growth and structural property of graphene on Pt(111) *Appl. Phys. Lett.* **2011**, *98*, 033101.

[30] Gao, L.; Ren, W.; Xu. H.; Jin, L.;Wang, Z.; Ma, T.; Ma, L.-P.; Zhang, Z.; Fu, Q.; Peng, L.-M.; Bao, X.; Cheng, H.-M. Repeated growth and bubbling transfer of graphene with millimetre-size single-crystal grains using platinum *Nat. Commun.* **2012**, *3*, 699.

[31] del Castillo, E.; Cargnoni, F.; Achilli, S.; Tantardini, G. F.; Trioni, M. I. Spin asymmetric band gap opening in graphene by Fe adsorption. *Surf. Sci.* **2015**, *634*, 62.

[32] Repetto, D.; Lee, T. Y.; Rusponi, S.; Honolka, J.; Kuhnke, K.; Sessi, V.; Starke, U.; Brune, H.; Gambardella, P.; Carbone, C.; Enders, A.; Kern, K. Structure and magnetism of atomically thin Fe layers on flat and vicinal Pt surfaces. *Phys. Rev. B* **2006**, *74*, 054408.

[33] Moulas, G.; Lehnert, A.; Rusponi, S.; Zabloudil, J.; Etz, C.; Ouazi, S.; Etzkorn, M.; Bencok, P.; Gambardella, P.; Weinberger, P.; Brune, H. High magnetic moments and anisotropies for Fe_xCo_{1-x} monolayers on Pt(111). *Phys. Rev. B* **2008**, *78*, 214424.

[34] Chen, Y. –J.; Chang, C.-C.; HO, H.-Y.; Tsay, J.- S.; Effects of interfacial structure on the magnetic properties of ultrathin Fe/Pt(111) films with Ag buffer layer *Thin Solid Films* **2011**, 519, 8343.

[35] Vita, H.; Böttcher, St.; Leicht, P.; Horn, K.; Shick, A. B.; Máca, F. Electronic structure and magnetic properties of cobalt intercalated in graphene on Ir(111). *Phys. Rev. B* **2015**, *90*, 165432.

[36] Ma, T,.; Fu, Q.; Cui, Y.; Zhang, Z.; Wang, Z.; Tan D.; Bao, X. Controlled Transformation of the Structures of Surface Fe (FeO) and Subsurface Fe on Pt(111) *Chin. J. Catal.* **2010**, *31*, 24.

[37] Dedkov, Y. S.; Fonin, M.; Rüdiger, U.; Laubschat, C. Graphene-protected iron layer on Ni(111) *Appl. Phys. Lett.* **2008**, *93*, 022509.

[38] Spiridis, N.; Wilgocka-Alęzak, D.; Freindl, K.; Figarska, B.; Giela, T.; Młyńczak, E.; Strzelczyk, B.; Zając, M.; Korecki, J. Growth and electronic and magnetic structure of iron oxide films on Pt(111), *Phys. Rev. B* **2012**, *85*, 075436.

[39] Kim, Y. J.; Westphal, C.; Ynzunza, R. X.; Wang, Z.; Galloway, H. C.; Salmeron, M.; Van Hove, M. A.; Fadley, C. S. The growth of iron oxide films on Pt(111): a combined XPD, STM, and LEED study *Surf. Sci.* **1998**, *416*, 68.

[40] Ritter, M.; Ranke, W.; Weiss, W. Growth and structure of ultrathin FeO films on Pt(111) studied by STM and LEED *Phys. Rev. B* **1988**, *57*, 7240.

[41] Jerdev, D. I.; Koel, B. E. Fe deposition on Pt(1 1 1): a route to Fe-containing Pt–Fe alloy surfaces. Surf. Sci. **2002**, 513, L391.

[42] Kresse, G.; Furthmüller, J. Efficient iterative schemes for ab initio total-energy calculations using a plane-wave basis set Phys. Rev. B **1996**, 54, 11169.

[43] Cattelan, M.; Peng, G. W.; Cavaliere, E.; Artiglia, L.; Barinov, A.; Roling, L. T.; Favaro, M.; Píš, I.; Nappini, S.; Magnano, E.; Bondino, F.; Gavioli, L.; Agnoli, S.; Mavrikakis, M.; Granozzi, G. The nature of the Fe–graphene interface at the nanometer level. *Nanoscale* **2015**, *7*, 2450.

[44] Giovannetti, G.; Khomyakov, P. A.; Brocks, G.; Karpan, V. M.; Van Den Brink, J.; Kelly, P. J. Doping Graphene with Metal Contacts *Phys. Rev. Lett.* **2008**, *101*, 026803.

[45] Politano, A.; Marino, A. R.; Formoso, V.; Chiarello, G. Evidence of Kohn anomalies in quasi-freestanding graphene on Pt(111) *Carbon* **2012**, *50*, 734.

[46] Klimovskikh, I. I.; Tsirkin, S. S.; Rybkin, A. G.; Rybkina, A. A.; Filianina, M.V.; Zhizhin, E. V.; Chulkov, E. V.; Shikin, A. M. Nontrivial spin structure of graphene on Pt(111) at the Fermi level due to spin-dependent hybridization. *Phys. Rev. B* **2014**, *90*, 235431.

[47] Yao, W.; Wang, E.; Deng, K.; Yang, S.; Wu, W.; Fedorov, A. V.; Mo, S.-K.; Schwier, E. F.; Zheng, M.; Kojima, Y.; Iwasawa, H.; Shimada, K.; Jiang,K.; Yu, P.; Li, J.; Zhou, S. Monolayer charge-neutral graphene on platinum with extremely weak electron-phonon coupling *Phys. Rev. B* **2015**, *92*, 115421.

[48] Haberer, D.; Vyalikh, D. V.; Taioli, S.; Dora, B.; Farjam, M.; Fink, J.; Marchenko, D.; Pichler, T.; Ziegler, K.; Simonucci, S.; Dresselhaus, M. S.; Knupfer, M.; Büchner, B.; Grüneis, A. tunable band gap in hydrogenated quasi-free-standing graphene *Nano Lett.* **2010**, *10*, 3360.

[49] Knudsen, J.; Feibelman, P. J.; Gerber, T.; Grånäs, E.; Schulte, K.; Stratmann, P.; Andersen, J. N.; Michely, T. Clusters binding to the graphene moiré on Ir(111): X-ray photoemission compared to density functional calculations *Phys. Rev. B* **2012**, *85*, 035407.

[50] Feibelman, P. J.; Pinning of graphene to Ir(111) by flat Ir dots *Phys. Rev. B* **2008**, *77*, 165419.

[51] Gao, J.; Zhong, J.; Bai, L.; Liu, J.; Zhao, G.; Sun, X. Revealing the role of catalysts in carbon nanotubes and nanofibers by scanning transmission X-ray microscopy *Sci. Rep.* **2014**, *4*, 3606.

[52] Zhou, Z.; Gao, F.; Goodman, D. W. Deposition of metal clusters on single-layer graphene/Ru(0001): Factors that govern cluster growth *Surf. Sci.*, **2010**, *604*, L31.

[53] Cattelan, M.; Cavaliere, E.; Artiglia, L.; Gavioli, L.; Agnoli, S.; Granozzi, G. The dynamics of Fe intercalation on pure and nitrogen doped graphene grown on Pt(111) probed by CO adsorption, *Surf. Sci.* **2015**, *634*, 49.

[54] Dahal, A.; Batzill, M. Graphene-nickel interfaces: a review. *Nanoscale* **2014**, *6*, 2548.

[55] Varykhalov, A.; Sánchez-Barriga, J.; Shikin, A. M.; Biswas, C.; Vescovo, E.; Rybkin, A.; Marchenko, D.; Rader, O. Electronic and Magnetic Properties of Quasifreestanding Graphene on Ni. *Phys. Rev. Lett.* **2008**, *101*, 157601.

[56] Gong, C.; Lee, G.; Shan, B.; Vogel, E. M.; Wallace R. M.; Cho, K. First-principles study of metal–graphene interfaces *J. Appl. Phys.* **2010**, *108*, 123711.

[57] Matsumoto, Y.; Entani, S.; Koide, A.; Ohtomo, M.; Avramow, P. V.; Naramoto, H.; Amemiya, K.; Fujikawa, T.; Sakai, S. Spin orientation transition across the single-layer graphene/nickel thin film interface *J. Mater. Chem. C* **2013**, *1*, 5533.

[58] Kim, W.; Choi, J. H.; Nahm, T.-U.; Song, S. H.; Oh, S.-J. Magnetic Properties of Ultrathin Fe Films on Pt(111) and Pd(111): a Surface Magneto-Optic Kerr Effect Study, *J. Korean. Phys. Soc.* **2004** *44*, 722.

[59] Le Guyader, L.; Kleibert, A.; Fraile Rodríguez, A.; El Moussaoui, S.; Balana, A.; Buzzi, M.; Raabea, J.; Nolting, F. Studying nanomagnets and magnetic heterostructures with X-ray PEEM at the Swiss Light Source, *J. Electron. Spectrosc.* **2012**, *185*, 371.

[60] Beaurepaire, E.; Bulou, H.; Scheurer, F.; Jean-Paul, K. Magnetism and Synchrotron Radiation: New Trends, *Springer Proceedings in Physics* **2010**.

[61] Chen, C. T.; Idzerda, Y. U.; Lin, H. –J.; Smith, N. V.; Meigs, G.; Chaban, E.; Ho, G. H.; Pellegrin, E.; Sette F. Experimental confirmation of the x-ray magnetic circular dichroism sum rules for iron and cobalt. *Phys. Rev. Lett.***1995**, *75*, 152.

[62] Eelbo, T.; Waśniowska, M.; Thakur, P.; Gyamfi, M.; Sachs, B.; Wehling, T. O.; Forti, S.; Starke, U.; Tieg, C.; Lichtenstein, A. I.; Wiesendanger, R. Adatoms and clusters of 3d transition metals on graphene: Electronic and magnetic configuration. *Phys. Rev. Lett.* **2013**, *110*, 136804.

[63] Nguyen, H. D.; Ono T. Electronic Structures and Magnetic Anisotropy Energies of Graphene with Adsorbed Transition-Metal Adatoms *J. Phys. Soc. Jpn.* **2014**, *83*, 094716

[64] Binns, C.; Baker, S. H.; Maher, M. J.; Louch, S.; Thornton, S. C.; Edmonds, K. W.; Dhesi, S. S.; Brookes, N. B. Magnetism in Fe Nanoclusters — From Isolated Particles to Nanostructured Materials, *Phys. Status solidi A* **2002** *138*, 339.

[65] Edmonds, K. W.; Binns, C.; Baker, S.H.; Maher, M. J.; Thornton, S. C.; Tjernberg, O,; Brookes N. B: Size dependence of the magnetic moments of exposed nanoscale iron particles. *J. Magn. Magn. Mater.* **2011**, *231*,113.

[66] Lin, W.-C.; Lo, F.-Y.; Huang, Y.-Y.; Wang, C.-H.; Chern, M.-Y. Canted magnetization in Fe thin films on highly oriented pyrolytic graphite, *J. Appl. Phys*. **2011**, *110*, 083911.

[67] Monti, M.; Santos, B.; Mascaraque, A.; Rodríguez De La Fuente, O.; Niño, M. A.; Menteş, T. O.; Locatelli, A.; McCarty, K. F.; Marco J. F.; De La Figuera, J. Oxidation Pathways in Bicomponent Ultrathin Iron Oxide Films *J. Phys. Chem. C* **2012**, *116*, 11539.

[68] Addou, R.; Dahal, A.; Batzill, M. Growth of a two-dimensional dielectric monolayer on quasi-freestanding graphene *Nat. Nanotechnol.* **2013**, *8,* 41.

[69] Yazev, O. V.; Helm, L. Defect-induced magnetism in graphene *Phys. Rev. B* **2007**, *75*, 125408.

2.1.2. N-doped graphene and iron

Introduction

Chemically modified graphenes (CMGs) are G based compounds where carbon atoms are substituted by heteroatoms or by chemical functional groups.[1] CMGs and G represent a new frontier for catalysis, since they exhibit an exceptional chemical activity *per se*,[2,3,4] see section 2.2, but can also act as chemical promoters and boost the reactivity of supported metal NPs.[5,6,7]

A clear understanding of the real active sites involved in the different reactions has not been reached yet despite a large number of experimental works dealing with the preparation of complex materials and the characterization of their catalytic properties. One of the most studied materials is nitrogen doped graphene, N-G.[8,9] In the literature several practical and theoretical investigations about the use of N-G as catalyst for the oxygen reduction reaction (ORR) can be found.[3,10,11] However, the identification of the real active N centres and the microscopic comprehension of the reaction mechanism are still debated. Several different preparation routes have been proposed, such as CVD,[12,13] electrochemical and solution-based methods. In this section, a new method for the preparation of N-G films is proposed that employs a simple halogenated heterocyclic compound such as 3-bromopyridine. The use of this precursor is quite suited for UHV studies since the easy decomposition of the C-Br bonds on the catalytic surface[14] allows a fast growth of N-G films at relatively low pressure.

The structural complexity of these CMGs, together with the difficulties connected to the comprehension of a multi-step reaction, poses serious limits to a precise determination of structure-activity relationships. A way that we envisage as Surface Science group is to use advanced UHV techniques to perform extremely accurate studies on ideal systems prepared in controlled conditions. In the last few years this approach provided a full gamut of G based systems characterized by a high level of perfection, with tailored properties and controlled morphology, and offered a test field for the investigation of specific issues.[1]

As reported in the sections 2.1.1 and 2.3, surface science studies have also a pivotal role in the understanding G/metal interfaces.[15,16] For example interesting phenomena have been uncovered, such as the possibility to modify the electronic and magnetic properties of G.[17,18] Selective nucleation of nanoparticles on specific G sites in order to obtain templated growth[19] and the intercalation of metal atoms through the G layer.[20] As seen before, the metal interaction is one of the simplest ways to drastically change the G properties. However, the interaction between G and metals is even more complex when CMGs are considered, since different kinds of defects, as well as different types of interactions, can play a role. Both the chemical doping due to presence of heteroatoms in the G lattice and the hybridization between CMGs and metals must be kept in account. This complex interplay can eventually trigger a substantial modification of the chemical properties of the composite system.

In this section a typical surface science tool, i.e. TPD, was used to study the interaction of Fe with G/Pt(111) and N-G/Pt(111) films, in order to reveal the specific role played by nitrogen defects. The choice of Fe and N-G stems from the importance that these types of materials are quickly gaining as replacement of Pt in several electrochemical systems: actually, the catalysts formed by the combination of Fe and N-doped carbons are some of the most studied systems for applications in the ORR.[21,22,23,24] The idea is that Fe centres can be coordinated by two or four N functionalities (Fe-N_2-C and Fe-N_4-C), mimicking the active sites of natural porphyrines and enzymes.[25,26]

We also chose Fe because we wanted to exploit our large know-how on the Fe/G interaction,[27] see the section 2.1.1. In this section the intercalation dynamic has been studied. Metals can intercalate underneath graphenic layers using different paths. For example, metals that can interact strongly with carbon involves the formation of transient bonds between the metal and the carbon atoms. During this process, a hole can be opened in the C sp^2 network, making possible the passage of the metal through the G sheets.[28]

The intercalation through CMGs has not been well investigated in the literature for its complexity. Here it is reported[29] one of the first study about metal intercalation underneath a CMG. One question to be answered is if the defectivity introduced in the G layer by N defects inhibits intercalation by establishing a strong interaction between the N centres and the metal, or, on the contrary, if the defects represent sites for a facilitated mass transport through the G layer.

In order to answer these questions, carbon monoxide (CO) was used as a chemical probe to check that the whole Pt substrate was covered by the graphenic layer and to localize and quantify the Fe on the surface. By using TPD iteratively, interesting information on the dynamics of the Fe intercalation process were obtained. One advantage associated with TPD is its straightforward way to obtain an area-integrated information. STM was also used to visualize the defectivity of N-G and to understand how the N functionalities change the morphology of G. Surprisingly, it has been found that the N-doping boosts the rate of the intercalation process, indicating that the interaction between N centre and metal nanoparticles is not sufficient to pin the Fe NPs on the surface.

CO TPD data allow also an investigation of the electronic properties of the Fe NPs, since CO desorption temperature is very sensitive to the electronic structure of the adsorbing surface. Remarkably, in this work we did not observe any change in the NPs chemistry as a consequence of the interaction with N centres, probably for the low quantity of N functionalities with respect to Fe atoms.

Experimental section

Sample preparation

For preparation of Pt(111) crystal and Fe evaporator calibration see "Experimental section" of the section 2.1.1.

Ethylene was used to grow pure G, whereas N-G was synthesized dosing 3-bromopyridine vapours from a flanged test tube connected to a stainless steel gas

line. 3-bromopyridine is liquid at RT, before dosing it was purified by freeze-pump method.

Methods

TPD experiments were carried out by means of a Hiden quadrupole mass spectrometer. In order to analyse the desorption species coming only from the sample surface, the quadrupole filter, covered by a quartz shield holding a 8 mm hole in correspondence to the sample, was placed at 5 mm from the Pt(111) single crystal, which was suspended by two tantalum wires.

XPS measurements were carried out with conventional non-monochromatic Al K_α source with PE=20 eV; the BE scale was calibrated by normalizing the Au $4f_{7/2}$ BE position to 84.0 eV.

STM images were acquired by Prof. L. Gavioli's group. For details see "Experimental section" of the section 2.1.1.

Results and discussion

Graphene/Pt(111) and N-doped graphene/Pt(111) preparation and characterization

The G/Pt(111)system was prepared dosing 150 L (6.5×10^{-7} mbar for 5 minutes) of C_2H_4 at 900 K or 1000 K and cooling down the crystal at 30 K/min. The N-G/Pt(111) film was obtained dosing 300 L (1.3×10^{-6} mbar for 5 min) of 3-bromopyridine at 900 K or 1000 K, then the crystal was cooled down to RT at 30 K/min. The temperatures were chosen in order to vary the amount of N functionalities in the layer, the higher is the growth temperature and the lower is the incorporation of N atoms inside of the G layer.[30]

LEED was used to check the structure of both G/Pt(111) (Figure 1.a) and N-G/Pt(111) (Figure 1.b): a combination of R°19 and R°30 superstructures is visible,[31] but in the case of G the former is predominant.

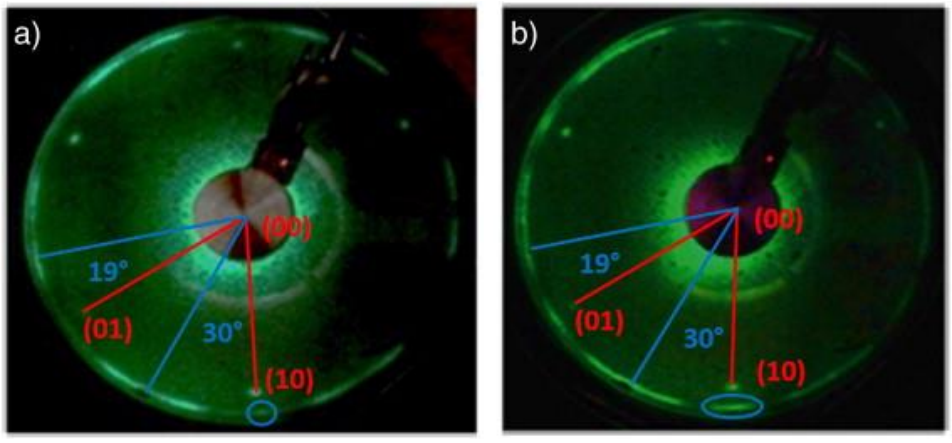

Figure 1. LEED pattern (62 eV) of (a) G/Pt(111) and (b) N-G/Pt(111) prepared at 900 K. Reprinted from Ref. [29] © 2015 Elsevier.

For the growth of N-G/Pt(111), TPD and XPS were used to confirm the absence of bromine into the layer. To individuate the desorption behaviour of the precursor, several layers of 3-bromopyridine were dosed at 130 K and desorption was followed using TPD, Figure 2.

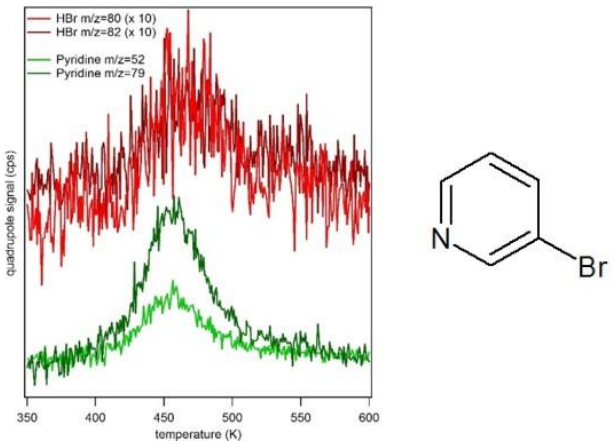

Figure 2. TPD data of multilayers of 3-bromopyridine, heating rate 0.5 K/sec, and sketch of the molecule. *Adapted from Ref. [29] © 2015 Elsevier.*

After the precursor desorption from physisorbed layer, two further components are desorbed at higher temperature from the sample surface, i.e. pyridine at 455 K, and HBr at about 466 K. This demonstrates that the C-Br bond is cracked at lower T than the growth ones, moreover no trace of bromine is detected by XPS after the synthesis of N-G. It also interesting to note that both pyridine and Br desorb as fully hydrogenated molecules and not without a hydrogen as expected for a simple fragmentation in Br^- and $pyridine^+$. This happens for the great quantity of hydrogen atoms that are produced by the partial dehydrogenation of the molecule. The hydrogen atoms diffuse and react with charged fragments of 3-bromopyridine forming HBr and pyridine.[32]

Figure 3 shows the C 1s photoemission lines for G/Pt(111) and N-G/Pt(111), acquired with PE 20 eV. The photoemission line of pure G exhibits a full width at half maximum (FWHM) of 1.1 eV with the maximum centred at 284.2 eV, which can be fitted by a single peak having a Doniach-Šunjić line shape. In the case of N-G the C 1s peak is broader due to the more complex structure induced by the introduction of the N functionalities: in total we can identify three components, the carbon sp^2 component (FWHM about 1.4 eV), and two further components at 285.7 eV and 283.5 eV associated to C-N bonds and carbon atoms defects (either C vacancies or Stone-Wales defects), respectively. The N 1s photoemission line for N-G/Pt(111), Figure 3, can be separated into three different peaks, assigned to pyridinic (398.7 eV), pyrrolic (400.2 eV) and substitutional (401.3 eV) defects into the G layer.[33,34,35]

The percentage of doping for the growth at 900 K, calculated as N/C atomic ratio, is about 8% (0.6% of N substitutional, 3.7 % of pyrrolic and 3.7 % of pyridinic functionalities). Similar results were obtained for the growth at 1000 K, not reported here.

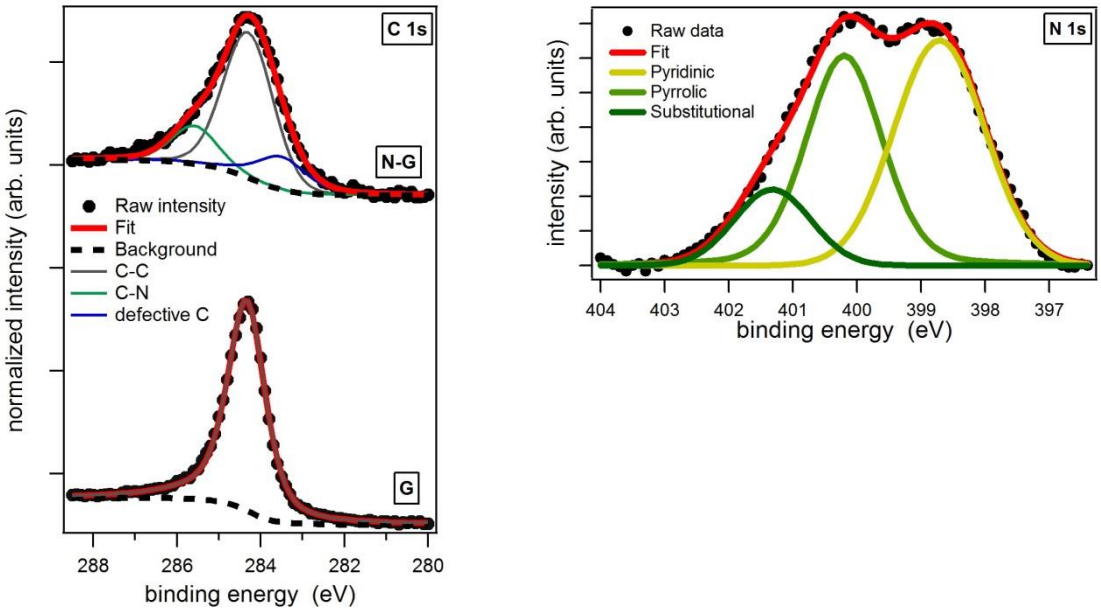

Figure 3. XPS C 1s and N 1s data for G and N-G films on Pt(111), after a subtraction of a linear background. The separation into single chemically shifted components is displayed. *Reprinted from Ref. [29] © 2015 Elsevier.*

TPD experiments using carbon monoxide (CO-TPD) as a probe were used to check the fraction of the Pt surface covered by G. 12 L (1 L=1.33×10^{-6} mbar×s) of CO (1.3×10^{-7} mbar for 2 minutes) were dosed at 130 K, then the temperature was linearly increased to 600 K using a 2 K/s heating rate. In our condition, the CO does not stick neither on G[36] nor on N-G. When the G coverage is partial, it is possible to observe a CO desorption peak centred at 381 K, due to Pt(111) uncovered areas. In our case, no CO desorption peaks were detected, indicating that the whole Pt surface was covered. This procedure has been used as routine method to determine the overall coverage of inert 2D system such as G or *h*-BN on metals (see the sections 2.2 and 3.1.1). Moreover, it must be pointed out that if 1 ML of Fe is intercalated, either below G or N-G, no CO desorption peaks are detected because the carbon layer can protect iron, thus preventing CO and O_2 adsorption.[37]

STM pictures, reported in Figure 4, show that film defectivity is much larger on N-G films than on pure G. Typical domain size is about 2-5 nm, whereas on pure G, the results are shown in Figure 2 of section 2.1.1, the extension of G single grain is about one order of magnitude larger.[27] In Ref. [38] the morphology of N-G film shows large prevalence of point-like N-induced defects, whereas in this case the defects are clustered and do not show the typical three-fold contrast of substitutional nitrogen defects (Figure 5.a,b). This supports the photoemission results that point to a prominent presence of pyridinic and pyrrolic groups. Also STM data show that these groups induce a different kind of electronic distortion in the graphenic lattice: such an example is outlined in the up-right inset of Figure 5.a. However, in analogy to the case of substitutional doping, long-range electronic ripples surrounding the defects, spreading to at least 2–3 nm from the defect centre, can be clearly observed. Interestingly it is possible to identify a bright square motif that characterizes several defects (black circles in Figure 4.b).

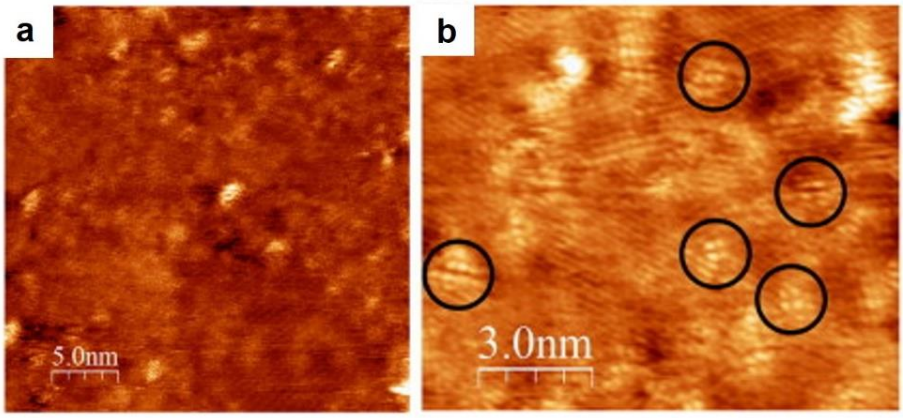

Figure 4. (a) STM picture (V = − 125 mV I = 13.6 nA) of N-G/Pt(111) grown from 3-bromopyridine precursor. (b) Atomic resolution frame (V = − 0.078 V, I = 1.32 nA) shows that original moiré patterns of pure G/Pt(111) are actually disrupted. Black circles point to possible N functionalities in the G lattice. Adapted from Ref. [29] © 2015 Elsevier.

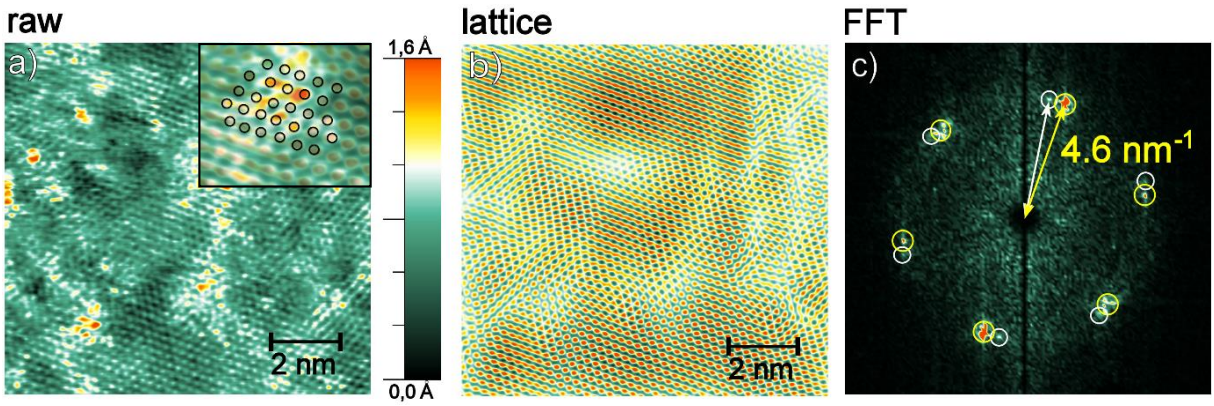

Figure 5. a) Atomically resolved frame of N-G/Pt(111) (V=-0.11V I=26.2 nA): defects are highlighted by yellow-red coloration. The inset displays a magnification of a nitrogen defect, the G lattice outlined by black circles. The following frames show the output of an FFT filter aimed to highlight G lattice and distortions, like in b), where red regions are related to most ordered regions and blue/white indicates less periodic lattice signal, and in c) FFT of frame a). *Reprinted from Ref. [29] © 2015 Elsevier.*

The reason for the smaller domains observed in the synthesis by 3-bromopyridine compared to ethylene can likely be connected to the different surface species formed in the two cases. At this relative low growth temperature, a pure surface limited reaction can be considered, see Figure 2 of section 2. Ethylene decomposes on the Pt surface by forming carbon monomers and dimers characterized by a fast surface diffusion, which facilitates the formation of few fast growing G nuclei. As widely reported in CVD studies, the use of relatively large organic molecules as carbon source induces the presence of a relevant number of defects, as confirmed by photoemission measurements and STM images. 3-bromopyridine when decomposed on Pt surface undergoes dehydrogenation, but forms bigger carbon clusters with respect to ethylene moieties, which are characterized by smaller mobility. This determines the formation of a larger number of slowly growing nuclei, explaining the observed morphology. Figure 5.a shows a high-resolution image of N-G where it is possible to observe that the lattice of the G becomes severely distorted. Using an FFT filter the periodicity of the carbon lattice can be outlined as reported in Figure 5.b. Interestingly the N defects can be found not only at boundaries but also inside

ordered patches (compare Figure 5.a vs Figure 5.b), however relevant local distortions of the lattice are observed around them, (see the inset of Figure 5.a). The FFT of the topographic image shows the presence of two distinct sets of hexagonal spots rotated by about 8°. This is in agreement with the macroscopic LEED patterns, which typically show ring shaped features. The presence of rather small domains, with different orientation likely indicates the facile nucleation of G nuclei.

Fe intercalation underneath G/Pt(111) and N-G/Pt(111)and CO-TPD data

Iron was deposited on G/Pt(111) and N-G/Pt(111) at 250 K (to avoid water condensation on the surface) and immediately cooled down to 130 K.

As mentioned in the previous section 2.1.1, Fe can be intercalated below the graphenic layer following two ways: annealing of the sample at high temperature (at about 600 K) immediately after low temperature iron deposition (explained in detailed below) or evaporating Fe while keeping the sample at 600 K. The amount of deposited Fe was monitored measuring the area of the first desorption peak by CO-TPD; moreover the Fe quantity was double checked using the area ratio between Fe 2*p*/Pt 4*f* and Fe 2*p*/C 1*s* with XPS; the estimated uncertainty in the Fe quantity was in the order of few %.

As mentioned above, several papers studied the Fe-N_2-C and Fe-N_4-C systems as possible catalysts for the ORR[21,22,23,24] as well as differently prepared N doped carbon materials. Even if an atomic scale characterization of these systems was not always provided a common point of these investigations is the indication that the interaction between iron NPs and N centres enhances the chemical activity and induces a strong interaction with the carbon substrate that increases the overall stability of the catalysts.

To understand the interaction between N-G and Fe NPs, CO-TPD was employed as a diagnostic tool in order to probe possible modifications of the electronic structure induced by the interaction with the N defects. Surprisingly, the comparison of CO desorption profiles of Fe/G/Pt(111) and Fe/N-G/Pt(111) does not show clear difference in the desorption temperature (Figure 7) and also the N 1s photoemission line does not change significantly after Fe deposition or intercalation, (not reported here).

The adsorption of CO on Fe NPs on HOPG has already been studied in Ref. [39]. In this work the CO desorption from Fe NPs with the diameter of 2−10 nm, displayed a low-temperature desorption peak at ca. 330 K. This temperature is significantly less, as much as about 20%, than the CO adsorption on Fe single crystal surfaces.[40,41,42] For Fe NPs with a 10−40 nm diameter, a lower temperature desorption peak was observed at ca. 250 K and the authors suggested that a transient carbonylation of Fe clusters ($Fe(CO)_x$, x = 1−5) operated by multiple CO adsorption takes place, leading to the formation of $Fe(CO)_x$ species that at 400 K decompose reforming Fe NPs and desorbing CO. They also proposed that the reduction of the CO adsorption energy and the carbonylation were originated by the interface interaction between Fe NPs and the graphite surface.

By CO-TPD also the dynamic of the Fe intercalation underneath G/Pt(111) and N-G/Pt(111) is studied using the desorption of CO from Fe NPs. At the best of our knowledge this was the first time[29] that TPD is used to analyse such phenomenon. In order to do that, two different sets of TPD experiments were carried out.

CO-TPD experiment #1

In the first experiment, five cycles of TPD (from 130 to 500 K with a heating rate of 2 K/s), were acquired after a 12 L dose of CO (1.3×10^{-7} for 2 minutes). At the end of each cycle, the sample was kept for five seconds at 500 K, (the temperature profile of such experiment is represented in Figure 6) to anneal shortly the system and to allow Fe intercalation.

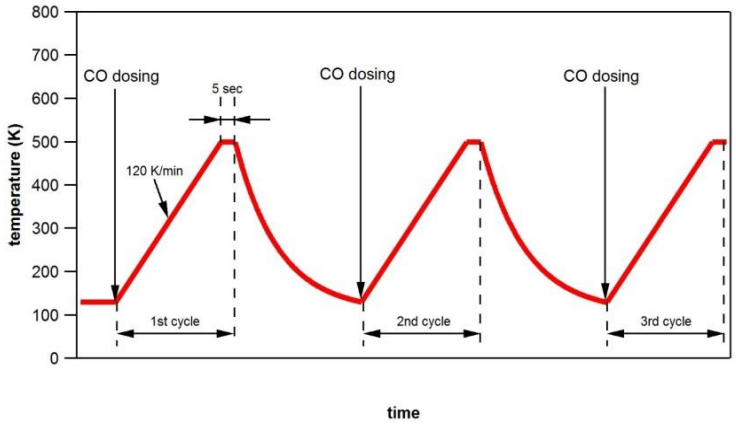

Figure 6. Representation of temperature profile vs time (not in scale) for the first type of CO-TPD experiment. Adapted from Ref. [29] © 2015 Elsevier.

The CO-TPD results of G/Pt(111) and N-G/Pt(111), both grew at 900 K, are reported in Figure 7.

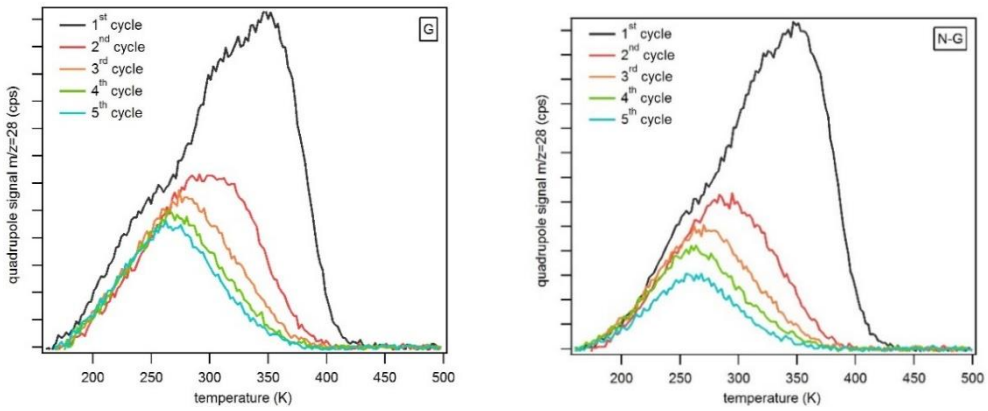

Figure 7. Five consecutive cycles of CO-TPD on 1 ML of Fe deposited on G/Pt(111) and N-G/Pt(111). The temperature profile of these experiments is sketched in Figure 6*. Adapted from Ref. [29] © 2015 Elsevier.*

The interaction of Fe NPs with the graphenic layer leads to a shift of the CO desorption peaks to lower temperature than bulk Fe, similarly to the Fe/HOPG system.[39] A clear change of the CO desorption peak shape as well as an overall decrease of its area are observed after the first cycle.

These findings can be explained by different phenomena taking place during the annealing. In first place, Fe NPs have enough energy to agglomerate and form bigger NPs with a consequent decrease of the amount of undercoordinated sites. Because of this morphological change, the shape of the CO desorption peak changes after the first desorption cycle. At the beginning the desorption peak contains three different components, whose maxima can be located at 270, 321 and 351 K. After the first TPD cycle, the two high temperature peaks are strongly suppressed, and completely disappear in the third cycle. Therefore, these components (321 and 351 K) can be related to highly uncoordinated atoms that after thermal treatment agglomerate more compact structures. In second place, the intercalation phenomenon must be kept in account. During the heating ramp, Fe atoms start to intercalate below the graphenic layer and are not anymore available for CO adsorption. The decrease of the CO desorption peak area observed after the second TPD cycle can be mainly ascribed to this phenomenon.

Also the formation of elemental carbon species could contribute to the reduction of the active sites number by poisoning the Fe NPs. It can be hypothesized through the reaction [43]

$$CO + CO \rightarrow CO_2 + C$$

that has already been observed on Fe single crystal. However, this reaction can be neglected because neither the C 1s photoemission line shows a larger signal after CO-TPD experiments, nor CO_2 desorption was observed.

As mentioned above, there are no relevant differences between Fe NPs supported either on G/Pt(111) and N-G/Pt(111), based on the desorption temperature peaks shape and maxima. What changes is the rate of Fe intercalation below the graphenic layer. To better visualize such a difference, the CO desorption peak areas corresponding to five consecutive cycles have been normalized to the first cycle and reported in Figure 8.

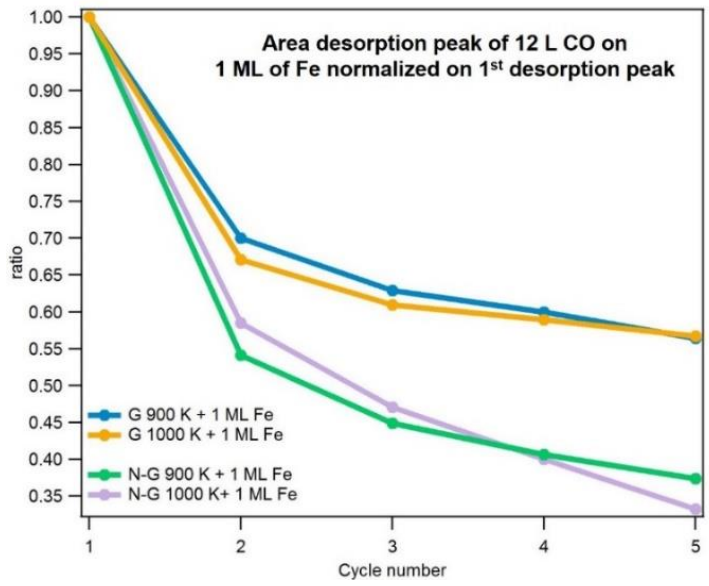

Figure 8. CO desorption peak area normalized to the first TPD cycle for the first type of CO-TPD experiment. The temperature profile of these experiments is sketched in Figure 6. Two different preparation for G and N-G have been used in order to form layers with different morphologies.

Figure 8 shows that in the case of Fe/N-G/Pt(111) the decrease of the normalized area is faster than on Fe/G/Pt(111), after five cycles, the desorption peak area decreases to 37 % and 56 % of its initial value for G and N-G layers, respectively.

It is possible to hypothesize three different mechanisms allowing the intercalation of Fe NPs:

1. by the diffusion of Fe atoms through the pristine G layer, according to a mechanism involving the transient disruption and subsequent recovery of C-C [28,30] and C-N bonds;
2. through N defects in the N-G layer;
3. through the G intrinsic defectivity (grain boundaries and point defects).

The first two mechanisms should favour the intercalation in N-G. Iron can exploit the *nanoholes* created pyridinic and pyrrolic heteroatoms in the graphenic layer, which from the structural point of view can be considered more open systems with respect to a perfect C sp^2 honeycomb layer. Furthermore, the intercalation on N-G can be faster because C-N species have a lower bond energy (305 kJ/mol), with respect to C-C bonds (346 kJ/mol),[44] and therefore can be broken easier by the Fe atoms.

It is interesting to point out that *nanoholes* do not behave as preferential CO diffusion paths, because CO-TPD experiments carried out on both N-G/Pt(111) and N-G/Fe(1 ML)/Pt(111) did not show any CO-TPD signal coming either from uncovered Pt(111) or completely intercalated Fe. This means that Fe is able to diffuse through the N-G layer and, afterwards, allows a complete recovery of the layer, as already observed for Si and Ni on G/Ru(0001).[45]

The third mechanism is common to both G and N-G, however being the defectivity in the N-G higher, a faster intercalation can be expected. In order to confirm that the different intercalation behaviour is not only due to morphology difference, exactly the same experiment carried out for G and N-G grew at 900 K, was also performed for layers synthesized at 1000 K. As reported in Ref. [31] G/Pt(111) with different morphology can be produced tuning the growth temperature. The CO-TPD results on G and N-G grown at 1000 K, reported in Figure 8, have a very similar trend of the one obtained at 900 K. This confirms that the N functionalities have an effective role in the Fe intercalation and it is not a pure morphologic effect.

CO-TPD experiment #2

The second set of TPD experiments further confirms the differences in the Fe intercalation behaviour on G/Pt(111) and N-G/Pt(111). The TPD cycles were performed as in first experiment, but, after each consecutive desorption cycle, the sample was annealed at a constant temperature for five minutes, with a different temperatures depending on the cycle (with 100 K steps, see Figure 9): in the first cycle is 500 K and reaches 800 K after the 4th cycle. At this point, no CO desorption peak was observed as a consequence of the complete Fe intercalation.

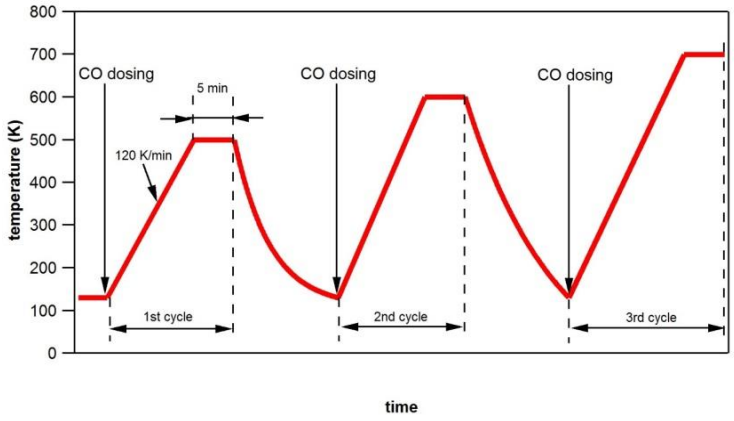

Figure 9. Representation of temperature profile vs. time (not in scale) of the second type of CO-TPD experiment. Adapted from Ref. [29] © 2015 Elsevier.

The CO desorption peaks from Fe/G and Fe/N-G synthesized at 900 K are reported in Figure 10.

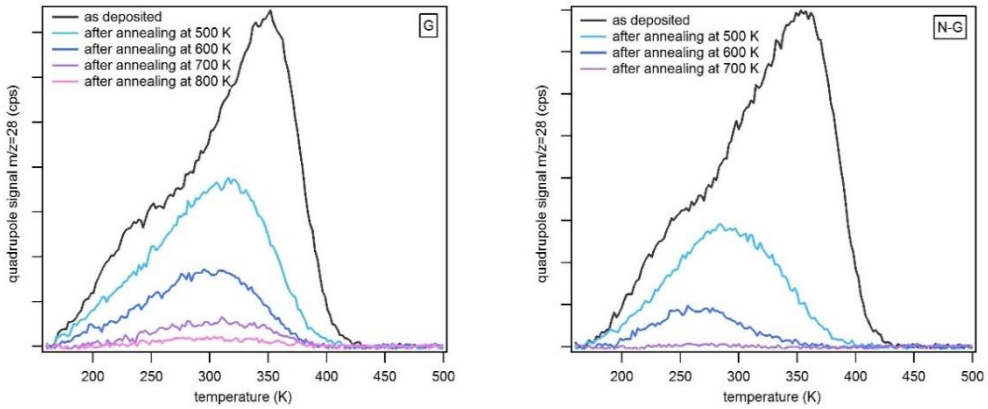

Figure 10. Consecutive cycles of TPD on1 ML of Fe deposited on G and N-G of 12 L of CO, the temperature profile of these experiments is sketched in Figure 9. Adapted from Ref. [29] © 2015 Elsevier.

The 4th CO desorption cycle on Fe/N-G/Pt(111), acquired after thermal treatment at 700 K for 5 minutes, shows a complete suppression of the CO desorption peak, whereas for Fe/G/Pt(111), the sample must be annealed up to 800 K to allow a complete Fe intercalation. Therefore, also the second TPD experiment suggests that Fe intercalation is easier on N-G than on pure G.

Surprisingly, comparing the two set of experiments the CO desorption peak area calculated after the 2nd desorption cycle (after 5 minutes of annealing at 500 K) during the second TPD experiment shows a decrease of 67% and 51% with respect to the first desorption peak area for G and N-G, respectively. These values are only slightly different than those after the 2nd TPD cycle of the first TPD experiment (76 % for G and 54 % for N-G) obtained with only 5 second annealing at 500 K. This can indicate that the carbonilation process of Fe NPs has a crucial role in this intercalation dynamics analysis.

Conclusions

In this section CO-TPD experiments from Fe NPs deposited on G/Pt(111) and N-G/Pt(111) were carried out to understand the dynamics of the Fe intercalation underneath the graphenic layer.

The N functionalities of N-G do not stabilize the Fe NPs on the surface; on the contrary, the intercalation process is faster than in G/Pt(111). The higher intercalation rate can be probably related to the presence of *nanoholes*, created by pyridinic and pyrrolic defects, which offer an additional intercalation channel, and/or to the lower bond energy of C-N, which can be broken and self-healed by Fe NPs easier than C-C.

No significant shift of the CO desorption temperature from the Fe NPs deposited on G or N-G was observed, indicating that the N-G/Fe interaction does not affect significantly the chemical properties of the Fe NPs, probably for the too low N/Fe atoms ratio.

These two experimental findings point therefore to a new hypothesis for the explanation of the high activity of N-G/Fe system. It is well known that one of the possible factors of the extreme activity of nanocatalysts is fluxionality that is an extreme mobility of the structural properties of catalytic centres, which can provide low energy reaction paths by adapting their structure to transient intermediates.[46] It is possible to envisage that the ability of Fe centre to crawl in and out the G layer could play an important role in catalysis. Actually, also for the ORR reaction it has been proposed that the catalytic cycle involves the ring opening of a cyclic C-N bond.[10] This structural change could be promoted by the iron NPs or maybe an enhanced mobility of the Fe centres around the nitrogen defects, which is demonstrated by the easy intercalation, could favour a dynamic rearrangement of the catalytic centre during the different reaction steps.

References

1 Agnoli, S.; Granozzi, G. Second generation graphene: Opportunities and challenges for surface science, *Surf. Sci.* **2013**, *609*,1.

2 Jeon, I.-Y.; Choi, H.-J.; Choi, M.; Seo, J.-M.; Jung, S.-M.; Kim, M.-J.; Zhang, S.; Zhang, L.; Xia, Z.; Dai, L.; Park, N.; Baek, J.-B. Facile, scalable synthesis of edge-halogenated graphene nanoplatelets as efficient metal-free eletrocatalysts for oxygen reduction reaction *Sci. Rep.* **2013**, *3*, 1810.

3 Jiao, Y.; Zheng, Y.; Jaroniec, M.; Qiao, S. Z. Origin of the electrocatalytic oxygen reduction activity of graphene-based catalysts: a roadmap to achieve the best performance *J. Am. Chem. Soc.* 136 (2014) 4394.

4 Su, C.; Acik, M.; Takai, K.; Lu, J.; Hao, S.-J.; Zheng, Y.; Wu, P.; Bao, Q.; Enoki, T.; Chabal, Y. J.; Loh, K. P. Probing the catalytic activity of porous graphene oxide and the origin of this behavior *Nat. Commun.* **2012**, *3*, 1298.

5 Sahoo, M.; Vinayan, B. P.; Ramaprabhu, S. Platinum-decorated chemically modified reduced graphene oxide–multiwalled carbon nanotube sandwich composite as cathode catalyst for a proton exchange membrane fuel cell *RSC Adv.* **2014**, *4*, 26140.

6 Guo, S.; Zhang, S.; Wu, L.; Sun, S. Co/CoO nanoparticles assembled on graphene for electrochemical reduction of oxygen *Angew. Chem.* **2012**, *47*, 11770.

7 Yang, S.; Dong, J.; Yao, Z.; Shen, C.; Shi, X.; Tian, Y.; Lin, S.; Zhang, X. One-Pot Synthesis of Graphene-Supported Monodisperse Pd Nanoparticles as Catalyst for Formic Acid Electro-oxidation *Sci. Rep.* **2014**, *4*, 4501.

[8] Wang, H.; Maiyalagan, T.; Wang, X. Review on Recent Progress in Nitrogen-Doped Graphene: Synthesis, Characterization, and Its Potential Applications *ACS Catal.* **2012**, *2*, 781.
[9] Genga, D.; Yanga, S.; Zhang, Y.; Yang, J.; Liu, J.; Li, R.; Sham, T.-K.; Sun, X.; Ye, S.; Knights, S. Nitrogen doping effects on the structure of graphene *Appl. Surf. Sci.* **2011**, *257*, 9193.
[10] Kim, H.; Lee, K.; Woo, S. I.; Jung, Y. On the mechanism of enhanced oxygen reduction reaction in nitrogen-doped graphene nanoribbons *Phys. Chem. Chem. Phys.* **2011**, *13*, 17505.
[11] Zhang, L.; Xia, Z, Mechanisms of oxygen reduction reaction on nitrogen-doped graphene for fuel cells *Phys. Chem. C* **2011**, *115*, 11170.
[12] Xue, Y.; Wu, B.; Jiang, L.; Guo, Y.; Huang, L.; Chen, J.; Tan, J.; Geng, D.; Luo, B.; Hu, W.; Yu, G.; Liu, Y. Low Temperature Growth of Highly Nitrogen-Doped Single Crystal Graphene Arrays by Chemical Vapor Deposition *J. Am. Chem. Soc.* **2012**, *134*, 11060.
[13] Usachov, D.; Vilkov, O.; Grüneis, A.; Haberer, D.; Fedorov, A.; Adamchuk, V. K.; Preobrajenski, A. B.; Dudin, P.; Barinov, A.; Oehzelt, M.; Laubschat, C.; Vyalikh, D. V. Nitrogen-doped graphene: efficient growth, structure, and electronic properties, *Nano Lett.* **2011**,*11*, 5401.
[14] Zhang, J.; Li, J.; Wang, Z.; Wang, X.; Feng, W.; Zheng, W.; Cao, W.; Hu, P. Low-temperature growth of large-area heteroatom-doped graphene film *Chem. Mater.* **2014**, *26*, 2460.
[15] Batzill, M. The surface science of graphene: Metal interfaces, CVD synthesis, nanoribbons, chemical modifications, and defects, *Surf. Sci. Rep*. **2012**, *67*, 83.
[16] Wintterlin, J.; Bocquet M. L. Graphene on metal surfaces *Surf. Sci.* **2009**, *603*, 1841.
[17] Tombros, N.; Jozsa, C.; Popinciuc, M.; Jonkman, H. T.; Van Wees, B. J. Electronic spin transport and spin precession in single graphene layers at room temperature, *Nature* **2007**, *448*, 571.
[18] Seneor, P.; Dlubak, B.; Martin, M.; Anane, A.; Jaffres H.; Fert, A. Spintronic with graphene, *Mrs Bulletin* **2012**, *37*, 1245.
[19] Zhou, Y. G.; Chen, J. J.; Wang, F.; Sheng, Z. H.; Xia, X. H. A facile approach to the synthesis of highly electroactive Pt nanoparticles on graphene as an anode catalyst for direct methanol fuel cells *Chem. Commun*. **2010**, *46*, 5951.
[20] Nagashima, A.; Tejima N.; Oshima, C. Electronic states of the pristine and alkali-metal-intercalated monolayer graphite/Ni(111) systems, *Phys. Rev. B* **1994**, *50*, 17487.
[21] Yang, J.; Liu, D.-J.; Kariuki, N. N.; Chen, L. X. Aligned carbon nanotubes with built-in FeN_4 active sites for electrocatalytic reduction of oxygen *Chem. Commun. (Camb.)* **2008**, *3*, 329.
[22] Morozan, A.; Campidelli, S.; Filoramo, A.; Jousselme, B.; Palacin S. Catalytic activity of cobalt and iron phthalocyanines or porphyrins supported on different carbon nanotubes towards oxygen reduction reaction**,** *Carbon* **2011**, *49*, 4839.
[23] Titov, A.; Zapol, P.; Král, P.; Liu, D.-J.; Iddir, H.; Baisha, K.; Curtiss, L. A. Catalytic Fe-xN Sites in Carbon Nanotubes *J. Phys. Chem. C* **2009**, *113*, 21629.
[24] Lefèvre, M., Doedelet, J.-P. Fe-based catalysts for the reduction of oxygen in polymer electrolyte membrane fuel cell conditions: determination of the amount of peroxide released during electroreduction and its influence on the stability of the catalysts *Electrochim. Acta* **2003**, *48*, 2749.
[25] Ramírez, G.; Trollund, E.; Isaacs, M.; Armijo, F.; Zagal, J.; Costamagna, J.; Aguirre, M. J. Electroreduction of Molecular Oxygen on Poly-Iron-Tetraaminophthalocyanine Modified Electrodes *Electroanal.* **2002**, *7-8*, 540.
[26] Baker, R.; Wilkinson, D. P.; Zhang, J.; Electrocatalytic activity and stability of substituted iron phthalocyanines towards oxygen reduction evaluated at different temperatures *Electrochim. Acta* **2008**, *53*, 6906.
[27] Cattelan, M.; Peng, G. W.; Cavaliere, E.; Artiglia, L.; Barinov, A.; Roling, L. T.; Favaro, M.; Píš, I.; Nappini, S.; Magnano, E.; Bondino, F.; Gavioli, L.; Agnoli, S.; Mavrikakis, M.; Granozzi, G. The nature of the Fe–graphene interface at the nanometer level. *Nanoscale* **2015**, *7*, 2450.
[28] Sicot, M.; Leicht, P.; Zusan, A.; Bouvron, S.; Zander, O.; Weser, M.; Dedkov, Y. S.; Horn, K.; Fonin, M. Size-Selected Epitaxial Nanoislands Underneath Graphene Moiré on Rh(111), *ACS Nano* **2012**, *6*, 151.
[29] Cattelan, M.; Cavaliere, E.; Artiglia, L.; Gavioli, L.; Agnoli, S.; Granozzi, G. The dynamics of Fe intercalation on pure and nitrogen doped graphene grown on Pt(111) probed by CO adsorption. *Surf. Sci.* **2015**, *634*, 49.
[30] Boukhvalov, D. W.; Katsnelson, M. I. Destruction of graphene by metal adatoms *Appl. Phys. Lett.* **2009**, *95*, 023109/1.
[31] Gao, M.; Pan, Y.; Huang, L.; Hu, H.; Zhang, L. Z.; Guo, H. M.; Du, S. X.; Gao, H.-J. Epitaxial growth and structural property of graphene on Pt(111) *Appl. Phys. Lett.* **2011**, *98*, 033101.

[32] Boukhvalov, D. W.; Katsnelson, M. I. Destruction of graphene by metal adatoms *Appl. Phys. Lett.* **2009**, *95*, 023109/1.

[33] Favaro, M.; Perini, L.; Agnoli, S.; Durante, C.; Granozzi, G.; Gennaro, A. Electrochemical behavior of N and Ar implanted highly oriented pyrolytic graphite substrates and activity toward oxygen reduction reaction *Electrochim. Acta* **2013**, *88*, 477.

[34] Ju, W.; Favaro, M.; Durante, C.; Perini, L.; Agnoli, S.; Schneider, O.; Stimming, U.; Granozzi, G. Pd Nanoparticles deposited on nitrogen-doped HOPG: New Insights into the Pd-catalyzed Oxygen Reduction Reaction *Electrochim. Acta* **2014**, *141*, 89.

[35] Imamura, G.; Saiki, K. Synthesis of Nitrogen-Doped Graphene on Pt(111) by Chemical Vapor Deposition *J. Phys. Chem. C* **2011**, *115*, 10000.

[36] Mu, R.; Fu, Q.; Jin, L.; Yu, L.; Fang, G.; Tan, D.; Bao X. Visualizing chemical reactions confined under graphene *Angew. Chem. Int. Ed.* **2012**, *51*, 4856.

[37] Dedkov, Y. S.; Fonin, M.; Rüdiger, U.; Laubschat, C. Graphene-protected iron layer on Ni(111) *Appl. Phys. Lett.* **2008**, *93*, 022509.

[38] Zhao, L.; He, R.; Rim, K. T.; Schiros, T.; Kim, K. S.; Zhou, H.; Gutiérrez, C.; Chockalingam, S. P.; Arguello, C. J.; Pálová, L.; Nordlund, D.; Hybertsen, M. S.; Reichman, D. R.; Heinz, T. F.; Kim, P.; Pinczuk, A.; Flynn, G. W.; Pasupathy, A. N. Visualizing individual nitrogen dopants in monolayer graphene *Science* **2011**, *333*, 999.

[39] Oh, J.; Kondo, T.; Hatake, D.; Arakawa, K.; Suzuki, T.; Sekiba, D.; Nakamura, J. Adsorption of CO on Iron Clusters on Graphite, *J. Phys. Chem. C* **2012**, *116*, 7741.

[40] Moon, D. W.; Dwyer, D. J.; Bernasek, S. L. Adsorption of CO on the clean and sulfur modified Fe(100) surface *Surf. Sci.* **1985**, *163*, 215.

[41] Gonzalez, L.; Miranda, R.; Ferrer, S. A thermal desorption study of the adsorption of CO on Fe(110); enhancement of dissociation by surface defects *Surf. Sci.* **1982**, *119*, 61.

[42] Seip, U.; Tsai, M. C.; Christmann, K.; Küppers, J.; Ertl, G. Interaction of Co with an Fe(111) surface *Surf. Sci.* **1984**, *139*, 29.

[43] Cameron, S. D.; Dwyer, D. J.; A study of pi-bonded carbon monoxide on iron(100), *Langmuir* **1988**, *4*, 282.

[44] Garey, A. A.; Sundber, R. J. Advanced Organic Chemistry. Part A: Structure and Mechanisms; *Plenum Press: New York* **1984**.

[45] Cui, Y.; Gao, J.; Jin, L.; Zhao, J.; Tan, D.; Fu Q.; Bao, X. An exchange intercalation mechanism for the formation of a two-dimensional Si structure underneath graphene *Nano Res.* **2012**, *5*, 352.

[46] Heiz, U.; Bullock, E. L. Fundamental aspects of catalysis on supported metal clusters *J. Mater. Chem.* **2004**, *14*, 564.

2.2. Interaction between graphene and water

Introduction

Hydrogen is considered a promising sustainable energy vector, but in order to use it in real life at least three important issues has to be solved, production, storage, and convenient conversion into energy services.[1,2] Currently, hydrogen is mainly produced from natural gas via steam reforming. Alternative routes include degradation of biomasses (biological or catalytic) and water splitting (electrochemical or photochemical). A lot of efforts still must be addressed in the sustainability of these processes, moreover, for a diffuse usage, advanced energy devices must be compact, combining both fuel production/storage and conversion of primary energy sources into the energy service.

A smart solution would be represented by a unique material active for both the production and the storage of hydrogen. An excellent candidate for this role is G. Indeed, carbon-based structures are particularly attractive for hydrogen storage because carbon is a light element, and G in particular has potentially the most favourable gravimetric density among the carbon-based materials. The storage of molecular hydrogen in G relies on the van der Waals forces, leading to theoretical estimates of gravimetric density of ~3.3%,[3] which is increased up to 8% in multi-layers spaced by pillar structures or carbon nanotubes at cryogenic temperatures and/or high pressure.[4] G therefore represents a competitive alternative to metal hydrides and metal-organic frameworks.[5] An important challenge is represented by the effective production of H_2 from G.[4]

Herein, it is demonstrated that G/transition metal interfaces can be exploited for the production and storage of hydrogen from water. The model system is G/Ni(111), advanced spectroscopic tools have been adopted to elucidate the various steps of the reactions leading to water dissociation at G/metals at RT and to the subsequent hydrogen production from water.

Unlike section 2.1.2 where G and N-G were used to support a catalyst, i.e. Fe NPs, in this section the chemical activity of G *per-se* are tested for the production of hydrogen from water.

Experimental section

Sample preparation

The sample was a single crystal of Ni(111) that was cleaned by repeated cycles of ion sputtering (1.5 kV, $1x10^{-6}$ mbar of Ar) and annealing at 1050 K. The surface cleanness was checked by photoemission and LEED.

Graphene growth

As previous explained in "Graphene on Ni(111)" paragraph of section 2, G can grow on Ni(111) by surface limited reaction. Figure 1 shows the real-time evolution of C 1s during the growth of G on Ni(111) by decomposition of ethylene at 790 K, which is a temperature where G growth is favoured with respect to Ni carbide phase (T<733 K)

and carbon dissolution into metal bulk (T> 923 K).[6] At higher exposure, the G phase appears, as evidenced by the emergence of a peak at 284.84 eV.

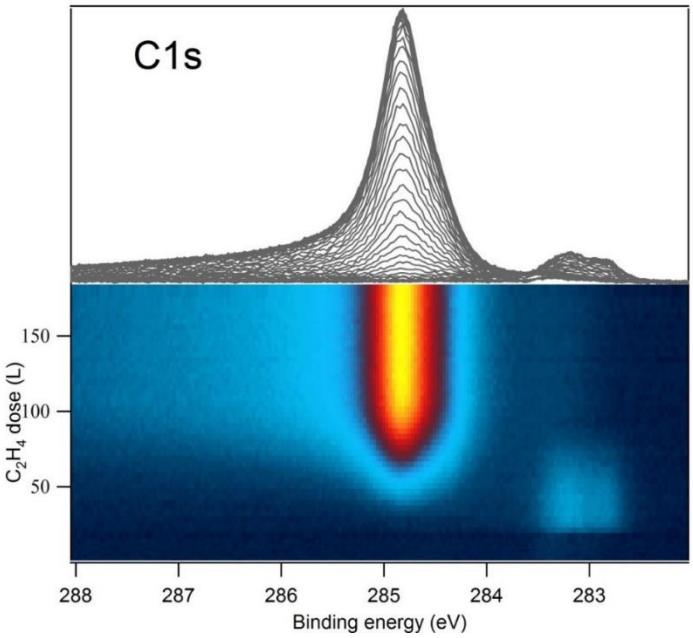

Figure 1. Real-time growth of G on Ni(111). Evolution of the C 1s signal during the exposure of the Ni(111) surface to ethylene at 790 K . The photon energy is 400 eV.

Exposure to water

Water (or deuterated water in the case of TPD experiments) was dosed at RT on a G/Ni(111) surface from a flanged test tube connected to a stainless steel gas line. Before dosing it was purified by freeze-pump method. The dosing pressure was of 10^{-4} mbar for about 2 hours to reach a total exposure of about 10^6 L.

Methods

TPD measurements were acquired with the same set up used for section 2.1.2, therefore for technical details, e.g. sample mounting and quadrupole features, of this experiment can be found in that section.

High-resolution XPS experiments were performed by Dr. R. Larciprete at the SuperESCA beamline at synchrotron Elettra (Trieste, Italy). High-resolution C 1s and O 1s core-level spectra were measured at a photon energy of 400 and 650 eV, respectively, with an overall energy resolution ranging from 40 to 150 meV. Valence-band spectra were acquired with a photon energy of 135 eV. For each spectrum, the BE was calibrated by measuring the Fermi level position of the Ni substrate. The measurements were performed with the photon beam impinging at GI (70°) while photoelectrons were collected at normal emission angle.

High-resolution electron energy loss spectroscopy (HREELS) experiments were performed by Dr. A. Politano using an electron energy loss spectrometer (Delta 0.5, SPECS). The energy resolution of the spectrometer is 5 meV. The primary electron beam energy is 4 eV. Each spectrum was normalized to the intensity of the elastic peak. HREELS spectra were acquired in specular conditions, with incident and scattering angles of 55° with respect to the surface normal.

Results and discussion

Water dosing at room temperature on graphene/Ni(111)

The overall chemical changes of the G/Ni(111) system after the exposure to water at RT were explored by means of high-resolution XPS. The C 1s photoemission lines deconvoluted into single chemically shifted components were fitted with Doniach-Šunjić functions convoluted with Gaussians, and a subtracted by a linear background. C 1s spectrum measured on pristine G/Ni(111) (Figure 2a, top spectrum) has two components at BE of 284.39 (C_1) and 284.84 eV (C_0) arising from the coexistence of different G/Ni(111) structures.[7,8,9]

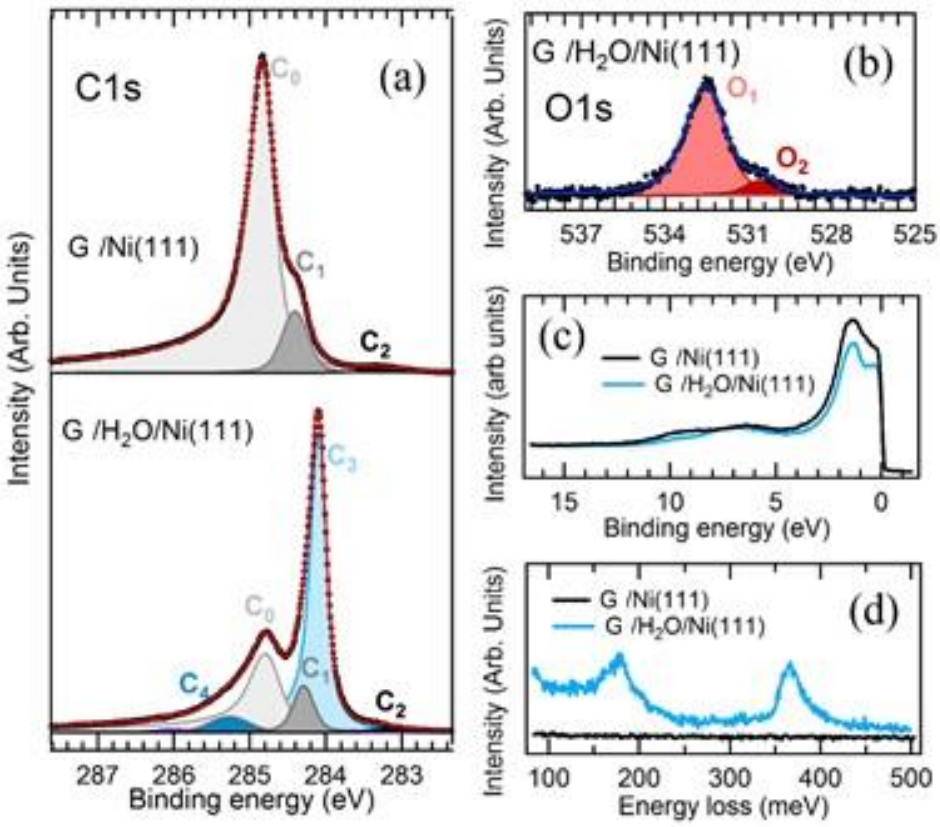

Figure 2. XPS and vibrational investigation of pristine and water-exposed G. (a) C 1s core level in pristine G/Ni(111) (top panel) and H_2O-exposed G/Ni(111) (bottom panel), measured with photon energy of 400 eV. The assignment of C_0, C_1, C_3, C_4 peaks is described in the main text. By contrast, C_2 is a residual carbide species.[6] (b) O 1s core level in H_2O-exposed G/Ni(111). The photon energy is 650 eV. (c) VB in pristine (black curve) and H_2O-expoxed G/Ni(111) (blue curve). The photon energy is 135 eV. (d) Vibrational spectrum, measured by HREELS in specular scattering conditions for pristine (black curve) and H_2O-expoxed G/Ni(111) (blue curve).

The exposure of G to 10^6 L of water at RT strongly modifies the C 1s line-shape (Figure 1a, bottom spectrum): the intensity of the originally dominant peak C_0 peak decreases and a new peak (C_3) emerges at 284.08 eV, which can be related to hydrogenated G[10] or to a quasi-freestanding G.[11] This suggests that water molecules decouple G from the Ni substrate by the hydrogenation process that leads to a buckling of the G sheet, with an increase of the G-Ni distance.[12] Upon water adsorption, the two components C_0 and C_1 shift by -0.1 eV, these components can

be related to patches of pristine G that were partially decoupled from the substrate as a consequence of the water-induced *p*-doping.[13]

Further information on the process were obtained by the analysis of the O 1*s* core levels (Figure 2b). The XPS spectrum in the region of O 1s shows two components at 532.51 and 530.54 eV, attributed to traces of H_2O and OH groups, respectively.[14] Water-induced effects are also evident in the VB. In comparison to the VB measured on the pristine G/Ni(111) (Figure 2c, black curve), the VB spectrum acquired after water exposure (Figure 2c, blue curve) shows that the intensity is attenuated by the intercalated species. Moreover, the band associated with the H_2O-$3a_1$ state appears at 6.5 eV.[15]

The investigation of surface vibrations by HREELS provide additional information on chemical reactions at the water-modified G/Ni(111) interface. The observation in the vibrational spectrum of H_2O-dosed G/Ni(111) of C-H bending and stretching modes at 179 and 367 meV[16] (Figure 2d) and the absence of C-OH and O-H vibrations at 50-70 and 410-460 meV,[17] respectively, ensure that –OH groups arising from water dissociation are not bound to G, which only forms bonds with H atoms. Unfortunately, HREELS cannot confirm the presence of NiOH or un-dissociated water molecules detected by XPS (Figure 2b), because these species are covered by G and their vibrational modes cannot be probed.[18]

In order to understand the dynamic of the production of H_2 in the case of water dosed on G/Ni(111) at RT, the evolution of the system was observed by time-resolved XPS spectra acquired during sample heating.

The curves in Figure 3a and b show that annealing at 350 K starts to convert C_3 into C_0 and that, above 440 K, the C 1*s* spectrum has fully recovered the line-shape and intensity of the pristine G on Ni(111) (inset of Figure 3b). This is a strong indication that the production of H_2 is reversible process. Moreover, these measurements indicate that the oxygen groups revealed by XPS (Figure 2b) must be only traces, e.g. due to G defects. This because if there is a big quantity of oxygen groups underneath G, e.g. NiO, NiOH or trapped water, the C 1*s* spectrum after annealing will be different to the pristine G/Ni(111). The latter is characteristic of G on strongly hybridizing metal, whereas oxygen groups are expected to strongly inhibit both hybridization and charge transfer from metal to G (see "Iron oxidation at room temperature" paragraph in section 2.1.1).

Likewise to XPS, the vibrational spectrum (Figure 3c) shows a similar evolution: above 440 K, C-H bending and stretching vibrational modes disappear, thus indicating dehydrogenation of G. This proves the reversibility of the process and makes G a suitable candidate for uptake/release processes of H.

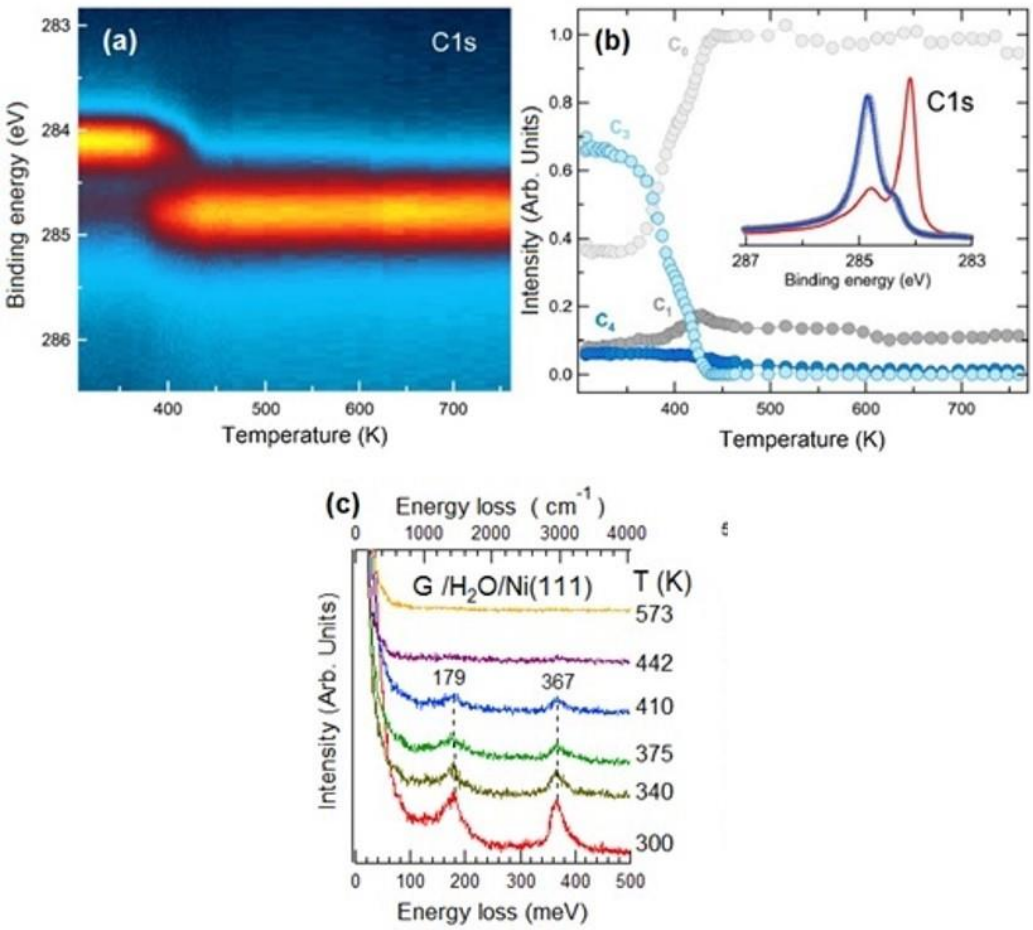

Figure 3. Desorption of water fragments from G and D_2 production from D_2O. (a) Real-time evolution of the C 1s signal in H_2O-exposed G/Ni(111) during the heating at a rate of 0.4 K/s. (b) Intensity of the various components of the C 1s core level. Each peak has been labelled as in Figure 2a. The inset shows the C 1s signal recorded for G/Ni(111) (grey circles), H_2O-dosed G/Ni(111) (red curve) and after heating to 450 K (blue curve) (c) Vibrational spectrum measured by HREELS for the H_2O-modified G/Ni(111) surface annealed to different values of temperature. The bottom axis reports vibrational energies in meV, while the corresponding values in cm^{-1} are shown in the top axis.

TPD experiments were used to check the desorption products from hydrogenated G, i.e. the production of hydrogen from water. To avoid any possible contribution due to background H_2 in the UHV chamber, these experiments were carried out dosing deuterated water (D_2O). TPD measurements were also performed on the bare Ni(111) exposing to a saturation dose of D_2O (12 L). Preliminary tests on G/Ni(111) were also carried out dosing H_2 at different pressure (from 10^{-8} to 10^{-4} mbar) at RT and 150 K, no desorption peaks related to chemical reactions, chemisorption, physisorption or intercalation were observed from 150 to 800 K.

The water desorption experiments were performed dosing about 10^6 L of D_2O on G/Ni(111) at RT. After waiting several hours (typically overnight), to decrease the chamber pressure, the manipulator was cooled down to liquid nitrogen temperature and the sample was thermalized at 200 K to avoid water condensation on the surface see the paragraph "Water dosing at low temperature on graphene/Ni(111)" below. Two principal reasons motivated the use of liquid nitrogen cooling: first the cooling coil at liquid nitrogen temperature traps water residues by condensation decreasing notably the pressure in the chamber; second in this experiment the range of interested

is from RT to 800 K, in order to perform a good linear ramp by TPD is necessary to start 50-100 K below the designed starting temperature.

The TPD profiles measured for G/Ni(111) (Figure 4b and Figure 6) show the D_2 desorption peak centred at 442 K corresponding to an activation energy of ~1.0 eV, followed by a secondary peak at 643 K corresponding to an activation energy of ~1.6 eV. These results are in agreement with TPD experiments carried out on atomic H dosed G/Ni(111).[10] The first desorption peak has been related in the literature[10] by the combination and desorption of two H atoms bonded with carbon atoms in meta position, whereas the second is related to H atoms that must diffuse on the G lattice before to desorb and therefore they require higher energy.

By contrast, D_2 cannot be produce from clean Ni(111) see Figure 4a. The small D_2 signal observable in Figure 4a, can be safely related to D_2 impurities from the D_2O dosing, indeed the temperature of this small desorption is comparable to H_2 dosed Ni(111), see Figure 5.

It is interesting to note that if water is dosed at lower pressure on G/Ni(111), i.e. 10, 100, 1000 or 10000 L in 10^{-8}, 10^{-7}, 10^{-6} and 10^{-5} mbar, no reactions are detected, this suggests that for the production of hydrogen, water molecules must have a relative high chemical potential.

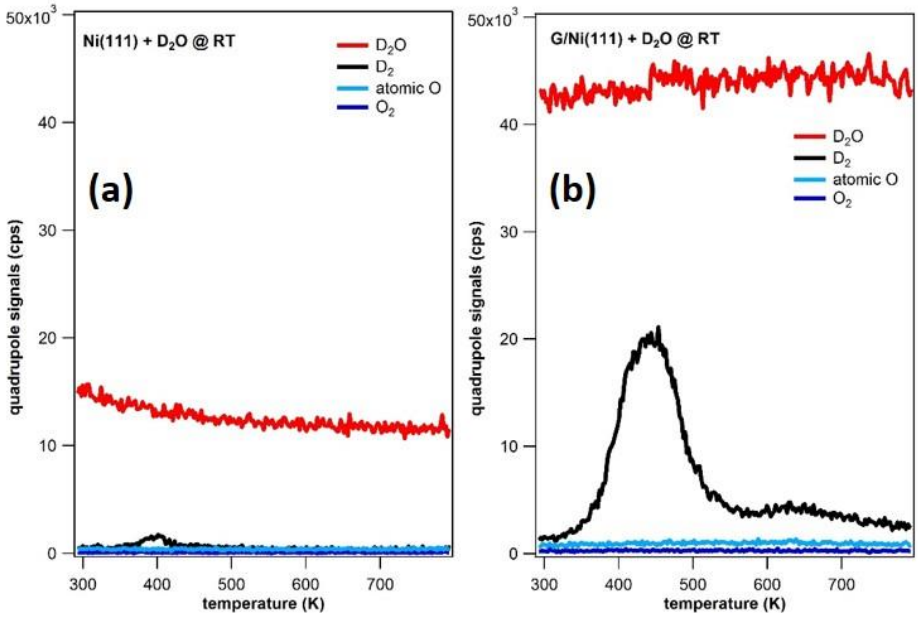

Figure 4. TPD spectra acquired for the D_2O-exposed (a) Ni(111) and (b) G/Ni(111) surfaces. The evolution of D_2O (red curve), D_2 (black curve), atomic O (green curve) and O_2 (blue curve) has been recorded. The weak D_2 desorption peak from Ni(111) is caused by residual deuterium in the water flask.

The determination of H coverage on water-exposed G/Ni(111) is calculated via other TPD experiments. Molecular hydrogen was dosed on the Ni(111) surface to saturate all β_2 sites, which correspond to 0.5 ML H on Ni(111).[19] In the TPD spectra measured after dosing 1000 L of H_2 on Ni(111) at 150 K, Figure 5, the area related to the β_2 sites is estimated by an heuristic deconvolution of the desorption peaks into two components, after subtraction of a liner background. The β_2 desorption peak is found at 367 K, whereas the one at lower temperature, 320 K, is related to the β_1 sites.

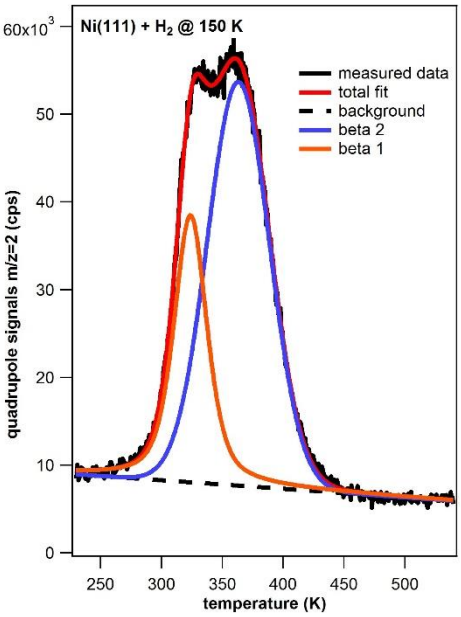

Figure 5. Desorption of H_2 from Ni(111). TPD spectra of the desorption of H_2 dosed on clean Ni(111) acquired using a 2 K/s heating rate. Measured data, linear background, total fit, desorption peak from β_2 sites and desorption peak from β_1 sites are represented with black dots, dashed black line, red line, purple line and orange line, respectively.

For the D_2O-dosed G/Ni(111) the amount of desorbed D_2 is estimated by summing the area of the two components obtained by deconvolution of the desorption profile after subtraction of a linear background, Figure 6.

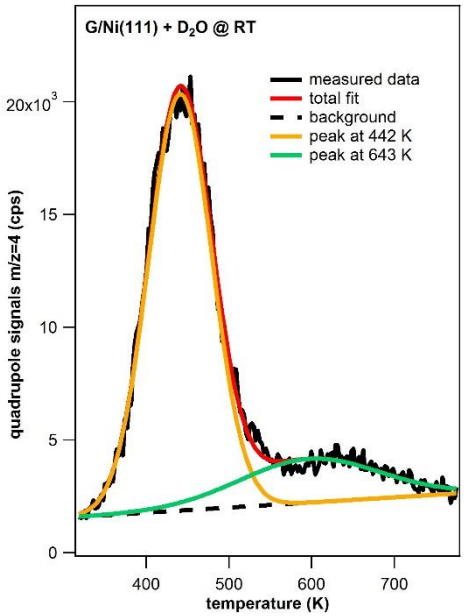

Figure 6. Desorption of D_2 from G/Ni(111). TPD spectra of the desorption of D_2 after exposure of 10^6 L of D_2O on G/Ni(111) acquired using a 2 K/s heating rate. Measured data, linear background, total fit, desorption peak at 442 K and desorption peak at 643 K are represented with black dots, dashed black line, red line, yellow line and green line, respectively.

Since the G coverage on Ni(111) is 2 ML (G forms a (1×1) on Ni, but the G lattice has a basis with two C atoms), the hydrogen coverage per carbon atom may be estimated as:

$$\text{Coverage}=\text{Area}\{D_2\}/\text{Area}\{[1\ \text{ML H/Ni(111)}*2]\}=0.17\ \text{ML} \quad (1)$$

The gravimetric density reachable is thus 1.4 wt.% at RT and under UHV conditions (with a storage pressure of ~10^{-13} bar). As a comparison, $LaNi_5$, a typical metal alloy forming hydrides, shows 1.37 wt. % [1] at RT and with a storage pressure of 2 bar. It is expected that decoration of G by Ca[20] or transition-metal atoms[21] and, moreover, the substitutional doping of G by N[21] or B[22] could further increase the gravimetric capacity. An additional increase is expected by storing H atoms at higher pressure.

From TPD spectra, a very small D_2O signal was observed at slightly higher temperature with respect to the first D_2 desorption. This signal may be related to intercalated water that is removed by annealing. Unfortunately, the high water background due to the several huge water dosing makes difficult to exactly estimate how much is the quantity of intercalated water, which has been detected by XPS and VB photoemission as well.(Figure 2a,b,c).

Combining only these experimental results it is difficult to have an absolute understanding of the reactions that occurs. What can be safely hypothesised is that water at RT, if dosed at relative high pressures, can dissociate on G to form hydrogenated G. The remaining oxygen atoms or OH groups from water molecules surprisingly do not stick on the surface. This can be confirmed form the absence of O_2 or atomic O desorption peaks when the sample is heated (Figure 4b). Moreover form TPD and XPS measurements it has been found that the process, i.e. dosing water at RT and production of H_2 at T>400 K, can be repeated successfully more than one time on the same G/Ni(111) sample. Therefore, also the formation of big quantities of NiO or NiOH groups, which should hinder or modify the catalytic process for subsequent dosing, can be safely excluded.

DFT calculations will be carried out to further shed light on this phenomenon.

Water dosing at low temperature on graphene/Ni(111).

If water is dosed at low temperature it physisorbs on G forming ice. The formation of ice on G/metals in the temperature range between ~80 and ~130 K has been reported by many groups.[23,24,25] Ice formation on epitaxial G is particularly interesting for the occurrence of metastable wetting bilayer of ice with hydrophobic properties.[23] The vibrational spectrum of ice grown on G (Figure 7a, red curve) may be divided into four major regions: frustrated translations around 30 meV; frustrated rotations, i.e. librations at 100-110 meV; H_2O deformations, i.e. the scissoring band centred around 200 meV; and O-H stretching modes around 400-460 meV. Instead, the vibrational band around 500 meV should be assigned to a combination mode of the O-H stretching and the libration modes.

By heating the sample to 180 K, ice completely desorbed from G, as indicated by the featureless vibrational spectrum (Figure 7a, black curve). Correspondingly, the TPD spectrum acquired after dosing few L of water at 150 K on G/Ni(111) (Figure 7b) and annealing the crystal up to 600 K with a linear heating ramp of 2 K/s, shows a desorption peak at 174 K, very similar to what observed for InSe, see section 3.2.

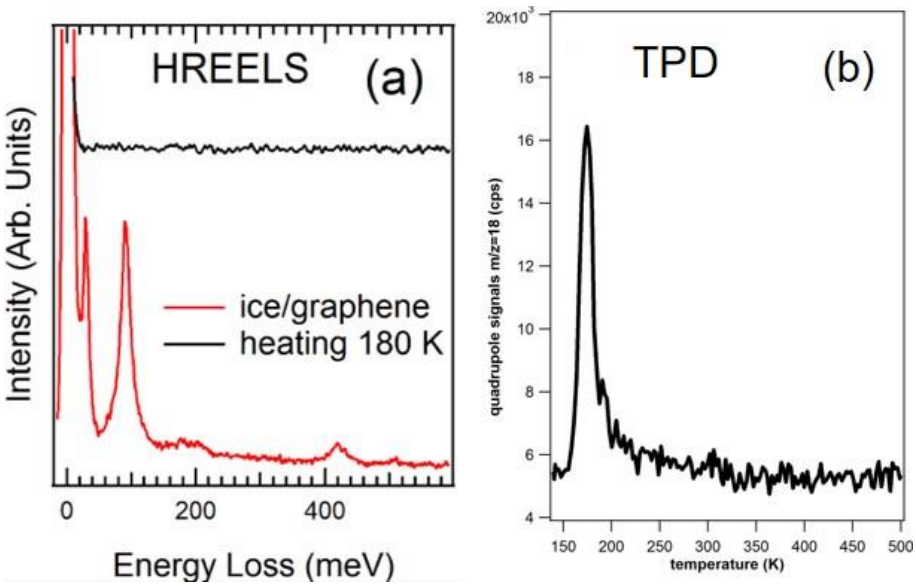

Figure 7. Ice formation and desorption on epitaxial G. (a) HREELS spectra for ice grown on epitaxial G, before (red curve) and after heating at 170 K (black curve). Both water exposures and HREELS experiments were carried out at 100 K. (b) TPD spectra acquired for G/Ni(111) exposed to water at 150 K. The ice desorption peak has a maximum at 174 K.

Conclusions

In conclusion, by means of a combination of spectroscopic techniques it has been demonstrated that water dissociates on G/Ni(111) at RT, resulting in hydrogenated G, with a gravimetric density competitive with current technology for H storage. Molecular hydrogen is produced by heating above 400 K. Even if the catalytic process has not been perfectly understood, the present results represent a crucial milestone in the technological road map for the use of G in catalysis and in energy-related applications.

References

1 Schlapbach, L.; Züttel, A. Hydrogen-storage materials for mobile applications. *Nature* **2001**, *414*, 353.

2 Satyapal, S.; Petrovic, J.; Read, C.; Thomas, G.; Ordaz, G. The U.S. Department of Energy's National Hydrogen Storage Project: Progress towards meeting hydrogen-powered vehicle requirements. *Catal. Today* **2007**, *120*, 246.

3 Patchkovskii, S.; Tse, J. S.; Yurchenko, S. N.; Zhechkov, L.; Heine, T.; Seifert, G. Graphene nanostructures as tunable storage media for molecular hydrogen. Proc. Natl. Acad. Sci. U.S.A. 102, 10439–10444 (2005).

4 Bonaccorso, F.; Colombo, L.; Yu, G.; Stoller, M.; Tozzini, V.; Ferrari, A. C.; Ruoff, R. S.; Pellegrini, V. Graphene, related two-dimensional crystals, and hybrid systems for energy conversion and storage. *Science* **2015**, *347*, 1246501.

5 Jena, P. Materials for hydrogen storage: past, present, and future *J. Phys. Chem. Lett.* **2011**, *2*, 206.

6 Grüneis, A.; Kummer, K.; Vyalikh, D. V. Dynamics of graphene growth on a metal surface: A time-dependent photoemission study. *New J. Phys.* **2009**, *11*, 073050.

7 Zhao, W.; Kozlov, S. M.; Höfert, O.; Gotterbarm, K.; Lorenz, M. P. A.; Viñes, F.; Papp, C.; Görling, A.; Steinrück, A.-P. Graphene on Ni(111): coexistence of different surface structures. *J. Phys. Chem. Lett.* **2011**, *2*, 759.

8 Lahiri, J.; Lin, Y.; Bozkurt, P.; Oleynik, I. I.; Batzill, M. An extended defect in graphene as a metallic wire. *Nat. Nanotechnol.* **2010**, *5*, 326.

[9] Bianchini, F.; Patera, L. L.; Peressi, M.; Africh, C.; Comelli, G. Atomic scale identification of coexisting graphene structures on Ni(111). *J. Phys. Chem. Lett.* **2014**, *5*, 467.

[10] Zhao, W.; Gebhardt, J.; Späth, F.; Gotterbarm, K.; Gleichweit, C.; Steinrück, H. P.; Görling, A.; Papp, C. Reversible hydrogenation of graphene on Ni(111)—synthesis of "graphone". *Chem.–Eur. J*. **2015**, 21, 3347.

[11] Haberer, D.; Vyalikh, D. V.; Taioli, S.; Dora, B.; Farjam, M.; Fink, J.; Marchenko, D.; Pichler, T.; Ziegler, K.; Simonucci, S.; Dresselhaus, M. S.; Knupfer, M.; Bu ̈chner, B.; Grüneis, A. tunable band gap in hydrogenated quasi-free-standing graphene *Nano Lett.* **2010**, *10*, 3360.

[12] Elias, D. C.; Nair, R. R.; Mohiuddin, T. M. G.; Morozov, S. V.; Blake, P.; Halsall, M. P.; Ferrari, A. C.; Boukhvalov, D. W.; Katsnelson, M. I.; Geim, A. K.; Novoselov, K. S. Control of graphene's properties by reversible hydrogenation: evidence for graphane. *Science*, **2009**, *323*, 610.

[13] Schedin, F.; Geim, A. K.; Morozov, S. V.; Hill, E. W.; Blake, P.; Katsnelson, M.; Novoselov, K. S. Detection of individual gas molecules adsorbed on graphene. *Nat. Mater.* **2007**, 6, 652.

[14] Yamamoto, S.; Bluhm, H.; Andersson, K.; Ketteler, G.; Ogasawara, H.; Salmeron, M.; Nilsson, A. In situ x-ray photoelectron spectroscopy studies of water on metals and oxides at ambient conditions. *J. Phys.: Condens. Matter* **2008**, *20*, 184025.

[15] Böttcher, S. *et al.* Graphene on ferromagnetic surfaces and its functionalization with water and ammonia. *Nanoscale Res. Lett.* **2011**, 6, 214.

[16] Kim, H., Balgar, T.; Hasselbrink, E. The stretching vibration of hydrogen adsorbed on epitaxial graphene studied by sum-frequency generation spectroscopy. *Chem. Phys. Lett.* **2011**, *508*, 1.

[17] Henderson, M. A. The interaction of water with solid surfaces: fundamental aspects revisited. *Surf. Sci. Rep.* **2002**, *46*, 1.

[18] Politano, A., Chiarello, G., Benedek, G., Chulkov, E. V.; Echenique, P. M. Vibrational measurements on alkali coadsorption systems: experiments and theory. *Surf. Sci. Rep.* **2013**, *68*, 305.

[19] Russell, J. N.; Gates, S. M.; Yates, J. T. Isotope effects in hydrogen adsorption on Ni(111): Direct observation of a molecular precursor state. *J. Chem. Phys.* **1986**, *85*, 6792.

[20] Lee, H., Ihm, J., Cohen, M. L.; Louie, S. G. Calcium-Decorated Graphene-Based Nanostructures for Hydrogen Storage. Nano Lett. **2010**, 10, 793.

[21] Parambhath, V. B., Nagar, R.; Ramaprabhu, S. Effect of Nitrogen Doping on Hydrogen Storage Capacity of Palladium Decorated Graphene. *Langmuir* **2012**, *28*, 7826.

[22] Beheshti, E., Nojeh, A.; Servati, P. A first-principles study of calcium-decorated, boron-doped graphene for high capacity hydrogen storage. *Carbon* **2011**, *49*, 1561.

[23] Kimmel, G. A.; Matthiesen, J.; Baer, M.; Mundy, C. J.; Petrik, N. G.; Smith, R. S.; Dohnálek, Z.; Kay, B. D. No confinement needed: Observation of a metastable hydrophobic wetting two-layer ice on graphene. *J. Am. Chem. Soc.* **2009**, *131*, 12838.

[24] Politano, A.; Chiarello, G. The nature of free O-H stretching in water adsorbed on carbon nanosystems. *J. Chem. Phys.* **2013**, *139*, 064704.

[25] Smith, R. S.; Matthiesen, J.; Kay, B. D. Desorption kinetics of methanol, ethanol, and water from graphene. *J. Phys. Chem. A* **2014**, *118*, 8242.

2.3. Graphene on $Pt_3Ni(111)$

Introduction

In this thesis, in the sections 2.1.1, 2.1.2 and 2.2 G grown on conventional substrates, i.e. weakly interacting Pt(111) and strongly interacting Ni(111), has been exploited to study its interaction with Fe and water. As mentioned in the section 2, this part is dedicated to the growth of G on a non-conventional substrate, i.e. $Pt_3Ni(111)$, which is composed by both weakly and strongly interactive metals.

The CVD growth of G on different alloys containing Ni has attracted considerable attention in recent years,[1,2,3,4,5,6] in consideration of the evidence that the presence of Ni in the alloy reduces the temperature for G formation.[5] Among the various metal-alloy substrates, Pt_3Ni would be particularly interesting since several studies have reported the great catalytic activity of the $Pt_3Ni(111)$ surface toward various surface chemical reactions.[7,8,9,10,11]

Previous studies on G growth on metal alloys have not been accompanied by a detailed knowledge of the electronic and geometric structure of the metal-alloy substrate, formed upon annealing a polycrystalline Ni film on top of noble-metal[5] surfaces or on Ni-Cu nanofibers.[12] Conversely, the electronic[13] and structural[14,15,16] properties of $Pt_3Ni(111)$ have been extensively investigated.

In particular, by annealing at 1000 K under UHV conditions the crystal, the outermost layer of the $Pt_3Ni(111)$ surface is entirely composed by Pt atoms (Pt-skin[14,15,16,17,18,19,20]), while the second layer is Ni-rich (52%), the third layer is again Pt-rich (87%) and from approximatively the 4th layer the stoichiometry is about 75 % of Pt and 25 %.[17] It has been also demonstrated both by experimentalists[8] and theoreticians[21] that in an oxygen environment the Ni atoms segregate toward the surface of $Pt_3Ni(111)$ to form a NiO skin. A more recent study has also put in evidence that Ni_2O_3 and NiO_x phases are also formed in strongly oxidizing conditions[22] on Pt_3Ni. G on Pt_3Ni thus allows studying the evolution of the electronic properties of G by changing the support from a metallic platinum skin to an insulator nickel-oxide skin.

Herein, spatially resolved ARPES and time-resolved XPS have been used to investigate the growth and the electronic properties of G supported on both platinum and nickel-oxide skins.

Experimental section

Sample preparation

The $Pt_3Ni(111)$ surface was cleaned by repeated cycles of sputtering (1.5 kV, 1×10^{-6} mbar of Ar) and annealing at 1400 K. Moreover prior to G deposition, the crystal underwent a series of oxidizing treatments (T_{max}=1000 K, $P_{O_2}=1\times10^{-7}$ mbar) to remove completely any traces of carbon. The cleanliness was checked by photoemission spectroscopy and LEED. The Pt-skin surface has been established before G growth by annealing the crystal at 1400 K.

Methods

XPS, and LEED experiments were carried out at the SuperESCA beamline at synchrotron Elettra (Trieste, Italy) by Dr. A. Politano. Time-dependent XPS experiments were carried out while dosing 5×10^{-7} mbar of C_2H_4. The C 1s spectra were recorded at hv=400 eV photon energy by using a Phoibos hemispherical electron analyser with 150 mm radius from SPECS. The total experimental resolution was ~40 meV. XPS measurements were performed with the photon beam impinging at GI (70°), while photoelectrons were collected at normal emission angle.

ARPES measurement have been acquired at the Spectromicroscopy beamline, for details see the methods paragraph in section 2.1.1.

Results and Discussion

Graphene growth

On Pt-skin $Pt_3Ni(111)$ alloy, G was grown through a surface limited reaction using ethylene as carbon precursor. In order to understand the chemical reaction of C_2H_4 with this surface the evolution in real time of C 1s photoemission line in ethylene environment was carried out as function of the substrate temperature (300-1000 K). For this set of experiments the $Pt_3Ni(111)$ sample has been heated by electron bombardment and its temperature has been monitored using a K-type thermocouple directly spot-welded on one side of the sample. The measurements are reported in Figure 1.

Selected spectra in the C 1s region acquired at 800, 650, and 350 K are reported in Figure 1 c,d,e, respectively. At RT, no C_2H_4 is found on the surface, as inferred by the absence of the component with BE 283.1 eV.[23] Conversely, the C 1s core level measured in the 300-400 K range in the ethylene-dosed surface is dominated by ethylidyne (CCH_3), whose component has BE 284.0 eV.[23] The shoulder at 283.6 eV is ascribed to C-H groups, [23] which have found to be the most stable hydrocarbon fragments on Pt(111).[24] The adsorption of ethylene at room temperature on $Pt_3Ni(111)$ is fully dissociative, resulting in CCH_3 e -CH fragments. For the sake of comparison, it should be noticed that the conversion of ethylene (C_2H_4) in ethylidyne on Pt(111) begins at 255 K,[25] but at RT well-defined islands of unreacted ethylene have been imaged by STM.[26] Time-resolved XPS by Fuhrmann et al. [23] reported that the conversion on Pt(111) is complete only at 320 K.

From the temperature evolution of C 1s core level for ethylene-dosed $Pt_3Ni(111)$ in the range between 438 and 715 K, we can assert that ethylidyne CCH_3 evolves into -CH groups, as evidenced by the relative increase of the component at 284.2 BE. The spectral weight of the peak at 283.6 eV changes with temperature and at 741 K it disappears.

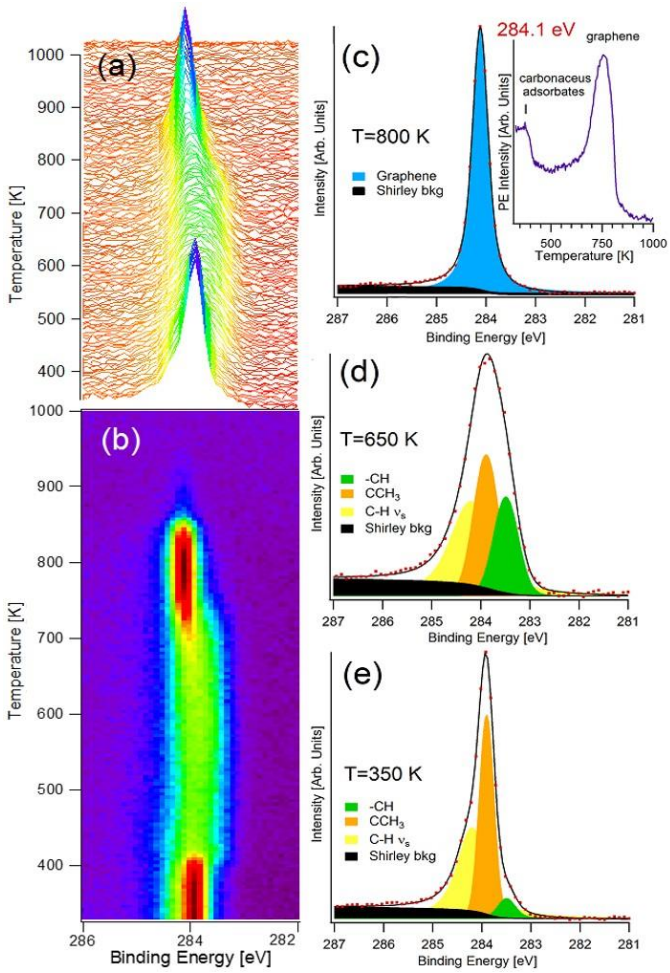

Figure 1. Panels (a) and (b) report the real-time evolution of the C 1s signal during the heating of the $Pt_3Ni(111)$ in an ethylene environment. Panels (c), (d), and (e) represent the C 1s core level measured with the sample kept at 350, 650, and 800 K, respectively. The black regions represent the Shirley background, which has been subtracted before fitting the resulting spectrum with Voigt line-shapes. The inset of panel (e) shows the behaviour of the photoemission intensity at a BE of 284.1 eV, corresponding to the G phase, as a function of temperature.

The C 1s signal for temperature in the range 777 - 823 K has a single narrow component at 284.1 eV. Both the sharpness of the line-shape and the BE suggest that a G phase is formed in this temperature range.

However, for temperature higher than 823 K, the intensity of the C 1s signal decreases (Figure 1, panels a and b). Above this temperature, carbon diffusion into the bulk limits the surface growth rate. The G layer starts to dissolves and the C 1s signal vanishes at T = 921 K. The reduced growth rate at higher temperatures can be described by the competition between carbon surface diffusion towards the G growth and the loss of surface carbon by diffusion into the bulk. Remarkably, this is a strong difference between G/Pt(111) and $G/Pt_3Ni(111)$. G can be grown by surface limited reaction on Pt(111) at higher temperature, such as 973-1000 K.[27,28] Moreover, in order to synthesized G by carbon segregation mode, it is possible to segregate carbon atoms from the bulk at 1137 K as shown by Sutter et al.[29] Noteworthy, G on Ni(111) is stable up to 923 K.[30] For the $G/Pt_3Ni(111)$, the lower temperature stability may indicate that Ni atoms allow an easier carbon dissolution into the bulk.

This experiment about the G growth on Pt_3Ni is a particular case where the presence of Ni atoms is not sufficient to reduce the temperature of G formation, such as it was observed for Ni/Au alloy[5]. For our system with Pt-skin the presence of Ni atoms underneath does not induce strong changes in the thermodynamics of the nucleation of G islands. Conversely, in the case of Ni/Au,[5] G nucleates on the residual Ni patches present on the surface and this explains why the growth temperature coincides with the cases of G/Ni(111)[30] and G/Ni(110).[31] Therefore, the mere presence of Ni atoms in a crystalline lattice of an alloy does not play any role in lowering the temperature for G formation, on the contrary from time-resolved XPS measurements it seems (Figure 1a,b) that the stability of G is lower at high temperature.

For G grown on $Pt_3Ni(111)$ dosing ethylene at 780 K, the LEED pattern exhibits incommensurate arcs like features at about 19° from the hexagonal lattice of $Pt_3Ni(111)$ similar to what is reported in Figure 1 of the section 2.1.2.

Both the C 1s BE (284.1 eV, Figure 1) and the LEED pattern indicate that G formed on the $Pt_3Ni(111)$ surface behaves as quasi-freestanding G sheet on the Pt-skin. In fact, the BE of the C 1s resembles that of G/Pt(111),[32,33] i.e. 284.1 eV see Figure 3 of the section 2.1.1, while for G/Ni(111) the C 1s has two components at 284 and 284.7 eV[30,34,35] because of the coexistence of top-fcc and bridge-fcc structures,[36,37] , see Figure 1 of the section 2.2.

It is noteworthy that no temperature-induced segregation of Ni has been observed during time-resolved XPS experiments in the region of Pt 4*f* and Ni 3*p* core levels. The ratio between the Pt 4*f* and the Ni 3*p* peaks remains unchanged during the heating.

ARPES with micrometric spatial resolution (micro-ARPES) was used to probe the G band structure to investigate further the electronic properties of $G/Pt_3Ni(111)$. In order to grow large enough grains, $Pt_3Ni(111)$ was heated up to about 1373 K and C_2H_4 was dosed (2×10^{-5} mbar per 20 minutes) to efficiently dissolve carbon inside the crystal. After cooling down very slowly the substrate to RT, G and multilayers G were obtained by carbon segregation. The LEED pattern observed after this kind of growth presents two superstructures: one hexagonal pattern with features at 30° with respect to the $Pt_3Ni(111)$ integer spots and another one rotated by 19°, which is similar to a well-known G reconstruction reported for Pt(111)[38]. A topographic map acquired with photoelectron close to Fermi edge at the Γ point, i.e. normal to the surface plane, and a G K point, are reported in Figure 2.

From the images four different zones can be identified and named as "Clean", "SLG", "BLG", "TLG" for clean substrate, single layer, bilayer and trilayer G, respectively. The contrast of Figure 2a is principally due to the attenuation of the metallic features, such as Pt 5*d* and Ni 3*d*, close to the Fermi edge. The contrast between SLG and "Clean" substrate is not strong at the Γ point for the absence of G features close to Fermi edge, therefore the "SLG" and "Clean" areas are difficult to distinguish. However, the attenuation of the metallic features is strong enough to clearly identify BLG and TLG. In Figure 2b the same map was acquired moving the analyser in coincidence of the position of a G Dirac cone. In this position, the contrast between "SLG" and "Clean" substrate is much stronger because of the presence of G Dirac cone that increase the photoemission intensity. In Figure 2b BLG and TLG are still visualized as darker areas for the attenuation of the metallic features.

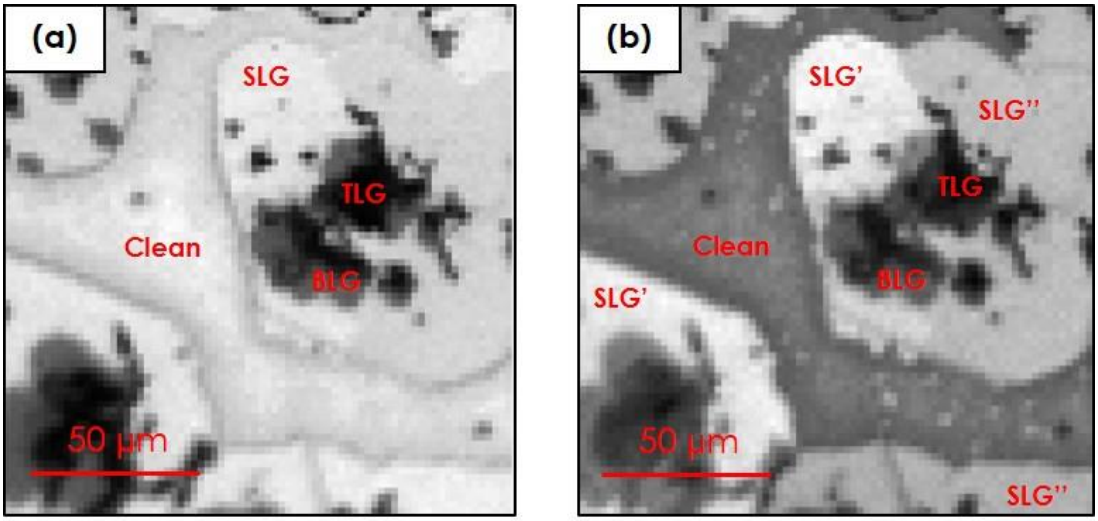

Figure 2. Topographic map of the photoemission signal of as-prepared G and multilayer G on $Pt_3Ni(111)$ (a) in Γ, (b) in a G K point.

Several information can be obtained from these real space topographic images:

- from Figure 2b two different G orientations called SLG' and SLG'' are distinguishable;
- SLG flakes are about 0.1 mm large, which is an outstanding result under UHV conditions;
- on the named "Clean" zone some small G grains may be present, which are visible in Figure 2b as bright spots;
- BLG and TLG islands seem to be randomly distributed on the surface, contradicting the previous investigation on multilayer growth of G on Pt(111) when it is stated that multilayer growth is triggered only on the border between misaligned SLG grains.[29]

K resolved VB maps of SLG', BLG and TLG were acquired. For SLG' an isoenergetic surface of the VB, and a Dirac cone acquisition are reported in Figure 3 a and b, respectively. We focused the measurement only on one SLG grain because calculations[33] and previous experimental investigations show that G weakly interacts with Pt(111)[29] and in a non-directional way.

The E vs K dispersion maps indicate that G is not hybridized with the Ni 3*d* states,[39] and overall the G electronic structure resembles the one of G/Pt(111):[29,33] along the Γ to K direction the π band has a liner dispersion close to the K point. The G doping results to be close to 0.0 ± 0.1 eV. These results confirm recent ARPES measurements on (√3×√3)R30 G/Pt(111) where small doping of 150-60 meV was observed.[40,41] and also the idea that one metal monolayer is enough to complete change the material VB, such as we have already found in the section 2.1.1.

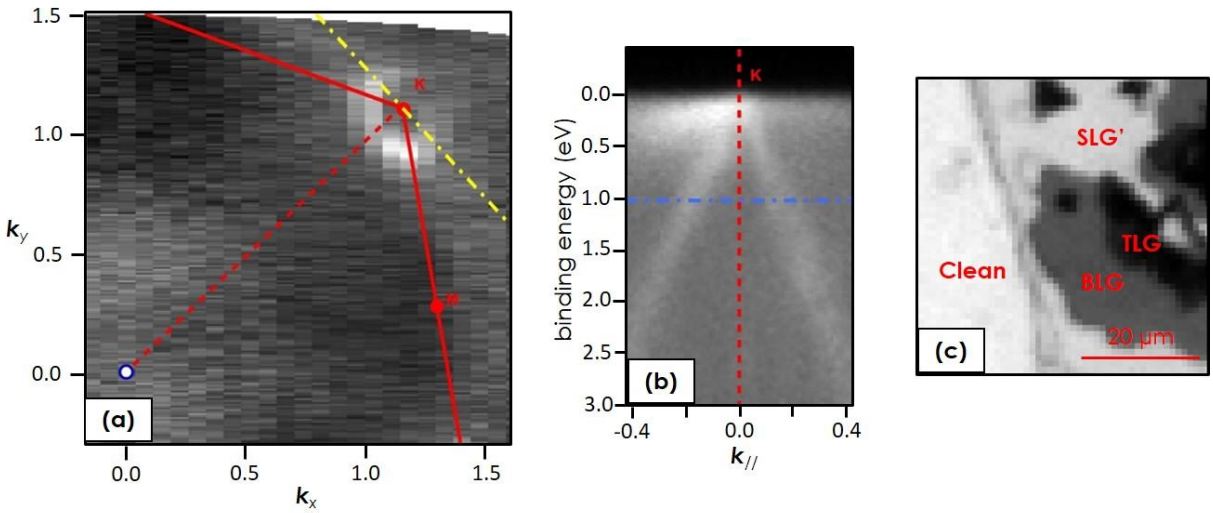

Figure 3. (a) Isoenergetic surface of SLG VB. The yellow dashed line in (a) represents the direction of the extracted profile in (b), which is perpendicular to Γ→K direction. The blue dashed line in (b) represents the energy cut of image (a). In (a) solid red lines indicate the border of the Brillouin zone of the SLG, red M and K mark the position of the maximum symmetry points, red dashed line indicates the Γ-K direction. In (b) red dashed line identify the position of the SLG Dirac cone. (c) Real space map with position marked where SLG', BLG and TLG valence maps were acquired.

A further insight on the multilayer growth can be obtained by VB analysis of BLG. We have found that BLG show two azimuthally disoriented Dirac cone, in Figure 4a is reported an isoenergetic surface of the VB of BLG (for the real space position see Figure 3c), where the two Dirac cones are visible.

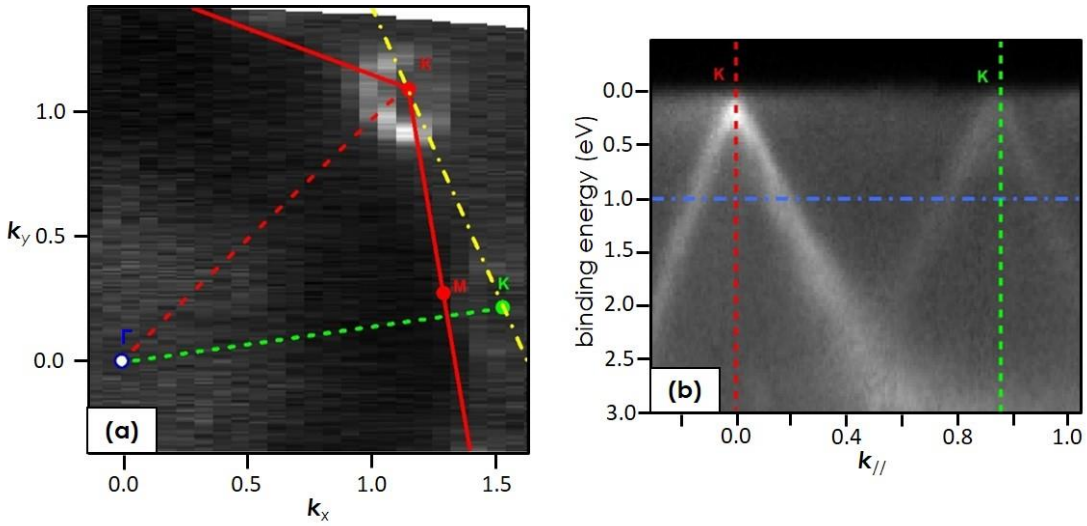

Figure 4. (a) Isoenergetic surface of BLG VB. The yellow dashed line in (a) represents the direction of the extracted profile in (b), which goes from the Dirac cones of the upper and lower G layer. The blue dashed line in (b) represents the energy cut of image (a). In (a) solid red lines indicate the border of the Brillouin zone of the upper G layer, red M and K mark the position of the maximum symmetry point of the upper G layer, red dashed line indicates the Γ-K direction of the upper G layer. Green dashed line and green K indicate the Γ-K direction of the lower G layer and the position of its K point, respectively. (b) Line profile between the two Dirac cones of the upper and lower G layers. The dashed red and green lines identify the position of the two Dirac cones.

The most intense Dirac cone, i.e. the upper G layer, has the same orientation of nearby SLG, see Figure 3a, therefore it can be inferred that is part of the same grain.

The photoemission intensity of the second Dirac cone (Figure 4a,b) is much lower due to photoelectron attenuation, indicating that the second layer grew underneath the first one, according to the typical surface carbon segregation mode,[42,43,44] as schematized in Figure 5. The orientation of the second layer can be calculated by the Dirac cone position of the second layer with respect to the first one; it has been found a rotation of about 37°, which is not a G symmetry direction.

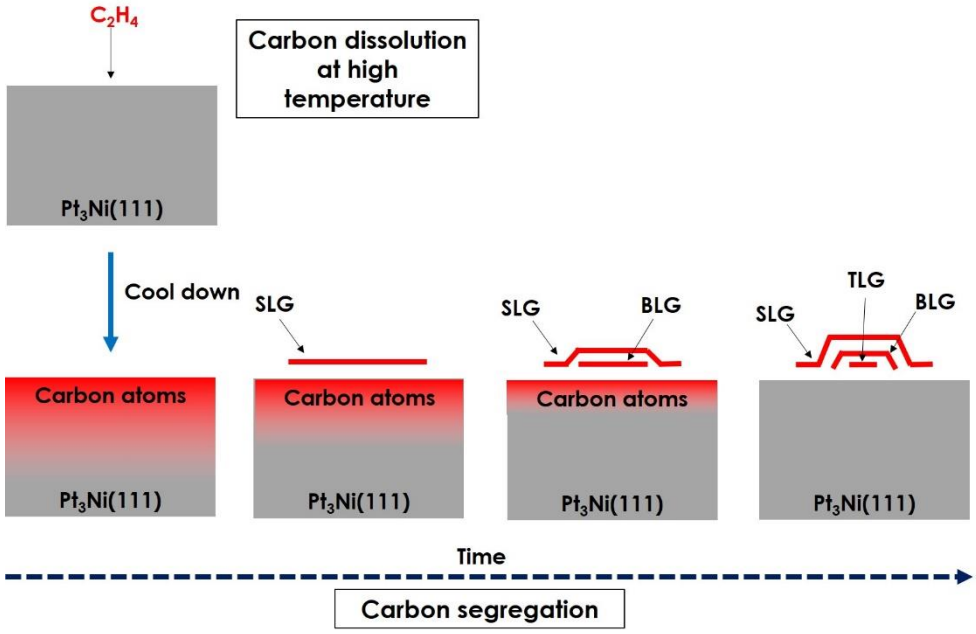

Figure 5. Growth scheme of G and multilayer G on $Pt_3Ni(111)$ through carbon segregation mode.

The same analyses were carried out for TL (not reported here), the rotation of the 3rd layer with the respect to the topmost one resulted to be 14°. The layers in contact with the substrates, i.e. SLG and the lowest sheets of the BLG and TLG, seem not to be affected by the multiple layer structure and a doping of about 0 eV is observed. On the contrary the second and third layers are slightly p-doped with a Dirac energy positioned at 0.18 eV below the Fermi level.

From these data, we can state that the synthesis by surface segregation mode allows the growth of BLG and TLG underneath the first G layer, however without a precise stacking. The formation of G layers underneath SLG has been observed for other weakly interactive transition metals such as Ir(111),[43] however on this metal only four different orientation of G can be formed[45] and multilayers can be quite easily found with a precise orientation with respect the topmost one.[43] As stated above $Pt_3Ni(111)$ with Pt skin resembles the Pt(111) surface where G has a variety of possible different orientation for its very weak interaction with G; [28,29,46] this characteristic increases notably the probability to form disoriented multilayers.

Reaction with oxygen

To probe phenomena occurring during oxidation, an XPS analysis of the G/$Pt_3Ni(111)$, obtained by surface limited reaction was undertaken. Oxygen was introduced in the UHV system through a doser, constituted by a molybdenum tube with a 6 mm diameter, placed almost in contact with the sample in order to enhance the local

pressure. In these conditions, a partial oxygen pressure of 10^{-4}-10^{-3} mbar was obtained on the sample surface. The sample was exposed to 10^6 L of O_2 at 520 and 620 K.

The analysis of the Ni $2p_{3/2}$ core level provides valuable information on the oxidation process (Figure 6a). The Ni $2p_{3/2}$ core level of the pristine $Pt_3Ni(111)$ surface is dominated by a peak at 852.2 eV, with a shoulder at 852.9 eV. The satellite at 858.0 eV instead is an indicator of Ni metallicity,[47] as well as the shoulder at 852.9 eV. The formation of G induces an attenuation of the Ni $2p_{3/2}$ photoemission signal without the emergence of spectral features. The heating in oxygen with the sample kept at 520 K only increases the intensity of the Ni $2p_{3/2}$ photoemission line, because of the onset of Ni segregation toward the outermost surface layer. Oxidation at 620 K induces the appearance of two well-distinct Ni $2p_{3/2}$ peaks at 853.6 and 856.0 eV, which are fingerprint of the formation of NiO and Ni_2O_3 oxides,[22,47] respectively. The satellite at 858 eV is strongly attenuated, thus signalling the insulating nature of the outermost layers underneath G.

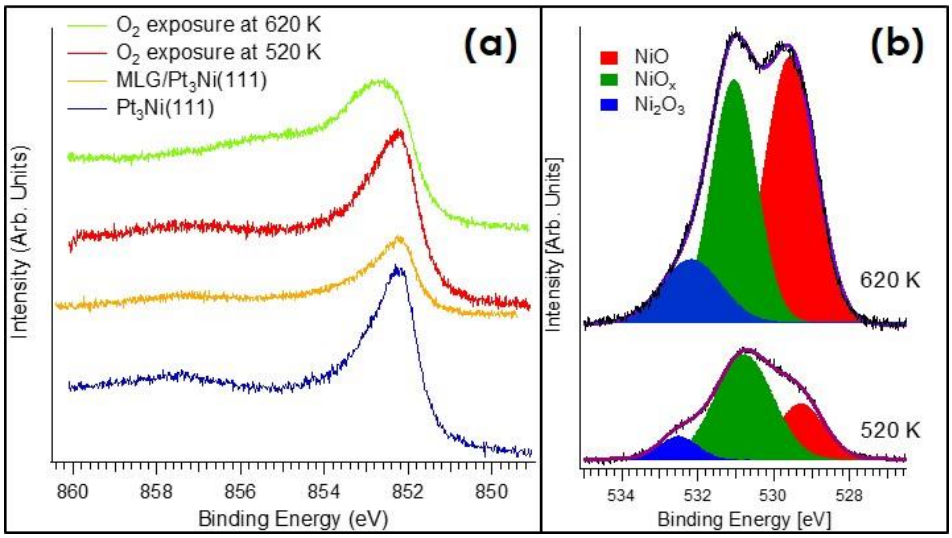

Figure 6. (a) Ni $2p_{3/2}$ and (b) O 1s photoemission lines before and after oxygen dosing.

However, we note that non-local core-hole screening should be considered in the interpretation of Ni $2p_{3/2}$ core-level spectra and Ni oxides have complex electronic structure.[48] Thus, in order to confirm the presence of oxides and resolve its chemical state, O 1s spectra have been measured (Figure 6b).

The analysis of the O 1s core level could shed the light on the formation of nickel oxide phases. Oxygen species at 529.4, 530.8, and 531.5 are identified as NiO, NiO_x and Ni_2O_3, respectively.[22] It should be taken into account that also Pt could form oxide phases, as found by ambient-pressure XPS by Miller et al. for O_2/Pt(111),[49] However, by inspecting the O 1s signal there are no components of possible platinum oxide species at 529.7 eV. As a matter of fact, the formation of platinum oxide is unlikely to form under present experimental conditions, also in consideration of the weakening of the adsorption energy of oxygen on $Pt_3Ni(111)$ compared to Pt(111).[13]

For oxidation at 520 K, the NiO_x phase is predominant on NiO and Ni_2O_3. Upon oxidation at 620 K, NiO becomes the more diffuse oxide phase on the interface.

In Ref. [21], it has been predicted that the Pt skin in $Pt_3Ni(111)$ is substituted by a NiO skin. Based on the results in Figure 6a, we can assert that the nickel oxide skin has more complex composition and it is characterized by the coexistence of NiO, NiO_x and Ni_2O_3 phases.

The evolution of the VB after the oxidation process was visualized by ARPES. At the ARPES facility no gas doser was available therefore O_2 (10^6 L) was dosed by a leak valve at 5×10^{-4} mbar at 620 K. The change from Pt skin to Ni-O skin has been checked by photoemission from the VB in normal emission, the comparison of the changes of SLG and bare substrate after oxygen exposure is reported in Figure 7a, the radiation was focused on the same positions identified in Figure 3c.

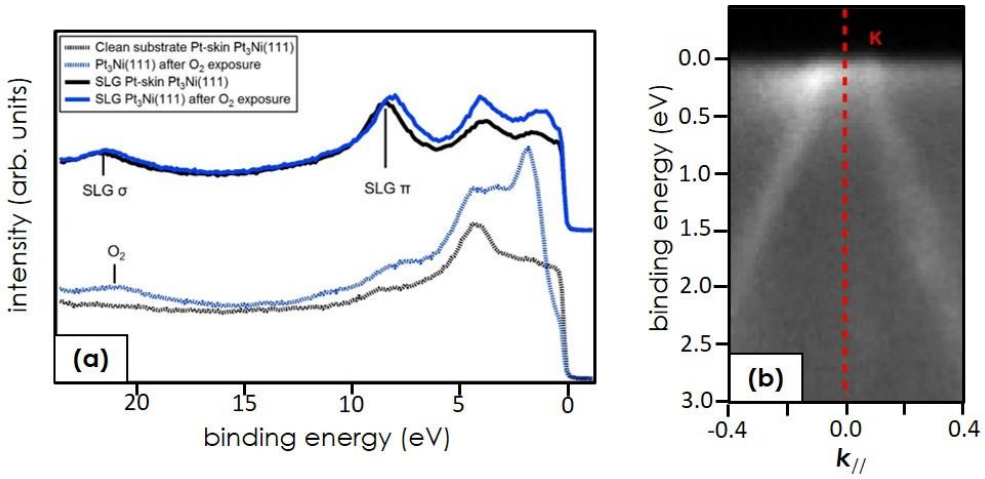

Figure 7. (a) VB acquisition in Γ, PE=5 eV for clean substrate (dashed lines) and SLG (solid lines). Black and blue lines are for pre- and post-oxidation, respectively. (b) VB acquired in perpendicular direction of the Γ-K direction, see yellow dashed line in Figure 3a, of SLG after O_2 exposure.

The VB modification of the clean substrate is strong, it is also detectable the signal coming from O 2*s* at 20.83 eV confirming the effective oxidation. The modification of the VB of SLG is much weaker, a p-doping of about 0.3 eV, i.e. the rigid shift to lower BEs, of the σ and π bands of SLG is visible. Figure 7b shows an ARPES acquisition of a Dirac cone of SLG after O_2 exposure, the p-doping is confirmed by the π band branches that cross at the K point at about 300 meV above Fermi energy. All the band structure resembles a quasi-freestanding G, no hybridization with Ni oxidized species is observable. Because of the overlap of O 2*s* and σ SLG band is impossible to visualize directly the intercalated oxygen.

From the complex shape of the of Ni $2p_{3/2}$, Figure 6a, and the VB acquisition reported in, Figure 7a, it can be inferred that the formed nickel oxide skin underneath G comprises different type of oxides and probably has a quite 3D structure.

Conclusions

This section deals with the growth of G and multilayer G on $Pt_3Ni(111)$. This crystal forms a monolayer Pt-skin by annealing under UHV conditions, this top most layer allows the growth of G in a very similar way to what happens on pure Pt(111) single crystals. It has demonstrated that G can grow by surface limited reaction and by surface segregation mode. Using this second approach, multilayers can grow underneath the

first layer. ARPES measurements indicate that G is not hybridized with Ni 3*d* orbitals, and has a quasi-freestanding band structure with almost no doping. At high partial pressure and relatively high temperature, oxygen can intercalate underneath the G layer and form a mixed Ni oxide layer. The G layer is in contact with this oxide, does not hybridize with metal oxide states but nonetheless it shows a small (0.3 eV) p-doping.

References

1 Addou, R.; Dahal, A.; Batzill, M., Graphene on ordered Ni-alloy surfaces formed by metal (Sn, Al) intercalation between graphene/Ni(111). *Surf. Sci.* **2012,** *606*, 1108-1112.

2 Chen, S.; Brown, L.; Levendorf, M.; Cai, W.; Ju, S.-Y.; Edgeworth, J.; Li, X.; Magnuson, C. W.; Velamakanni, A.; Piner, R. D.; Kang, J.; Park, J.; Ruoff, R. S., Oxidation resistance of graphene-coated Cu and Cu/Ni alloy. *ACS Nano* **2011,** *5*, 1321-1327.

3 Chen, S.; Cai, W.; Piner, R. D.; Suk, J. W.; Wu, Y.; Ren, Y.; Kang, J.; Ruoff, R. S., Synthesis and characterization of large-area graphene and graphite films on commercial Cu–Ni alloy foils. *Nano Lett.* **2011,** *11*, 3519-3525.

4 Liu, X.; Fu, L.; Liu, N.; Gao, T.; Zhang, Y.; Liao, L.; Liu, Z., Segregation growth of graphene on Cu–Ni alloy for precise layer control. *J. Phys. Chem. C* **2011,** *115*, 11976-11982.

5 Weatherup, R. S.; Bayer, B. C.; Blume, R.; Ducati, C.; Baehtz, C.; Schlögl, R.; Hofmann, S., In situ characterization of alloy catalysts for low-temperature graphene growth. *Nano Lett.* **2011,** *11*, 4154–4160.

6 Omiciuolo, L.; Hernández, E. R.; Miniussi, E.; Orlando, F.; Lacovig, P.; Lizzit, S.; Menteş, T. O.; Locatelli, A.; Larciprete, R.; Bianchi, M.; Ulstrup, S.; Hofmann, P.; Alfè, D.; Baraldi, A., Bottom-up approach for the low-cost synthesis of graphene-alumina nanosheet interfaces using bimetallic alloys. *Nat. Commun.* **2014,** *5*, 5062.

7 Chiarello, G.; Marino, A. R.; Formoso, V.; Politano, A., The adsorption and co-adsorption of oxygen and carbon monoxide on $Pt_3Ni(111)$: A vibrational study. *J. Chem. Phys.* **2011,** *134*, 224705.

8 Politano, A.; Caputo, M.; Goldoni, A.; Torelli, P.; Chiarello, G. Segregation and selective oxidation of Ni atoms in $Pt_3Ni(111)$ in low-pressure oxygen environment. *J. Phys. Chem. C* **2013,** *117*, 27007.

9 Politano, A.; Chiarello, G., The formation of HOCO in the coadsorption of water and carbon monoxide on $Pt_3Ni(111)$. *RSC Advances* **2014,** *4*, 45641-45646.

10 Stamenković, V. R.; Fowler, B.; Mun, B. S.; Wang, G.; Ross, P. N.; Lucas, C. A.; Marković, N. M., Improved oxygen reduction activity on $Pt_3Ni(111)$ via increased surface site availability. *Science* **2007,** *315*, 493-497.

11 Viswanathan, V.; Hansen, H. A.; Rossmeisl, J.; Jaramillo, T. F.; Pitsch, H.; Nørskov, J. K., Simulating Linear Sweep Voltammetry from First-Principles: Application to Electrochemical Oxidation of Water on Pt(111) and $Pt_3Ni(111)$. *J. Phys. Chem. C* **2012,** *116*, 4698-4704.

12 Liu, Z.-D.; Yin, Z.-Y.; Du, Z.-H.; Yang, Y.; Zhu, M.-M.; Xie, L.-H.; Huang, W., Low temperature growth of graphene on Cu-Ni alloy nanofibers for stable, flexible electrodes. *Nanoscale* **2014,** *6*, 5110-5115.

13 Kim, Y. S.; Jeon, S. H.; Bostwick, A.; Rotenberg, E.; Ross, P. N.; Stamenkovic, V. R.; Markovic, N. M.; Noh, T. W.; Han, S.; Mun, B. S., Role of transition metal in fast oxidation reaction on the Pt_3TM (111) (TM = Ni, Co) surfaces. *Adv. Energy Mater.* **2013,** *3*, 1257-1261.

14 Stamenković, V. R.; Mun, B. S.; Mayrhofer, K. J. J.; Ross, P. N.; Marković, N. M., Effect of surface composition on electronic structure, stability, and electrocatalytic properties of Pt-transition metal alloys: Pt-skin versus Pt-skeleton surfaces. *J. Am. Chem. Soc.* **2006,** *128*, 8813-8819.

15 van der Vliet, D. F.; Wang, C.; Li, D.; Paulikas, A. P.; Greeley, J.; Rankin, R. B.; Strmcnik, D.; Tripkovic, D.; Markovic, N. M.; Stamenkovic, V. R., Unique Electrochemical Adsorption Properties of Pt-Skin Surfaces. *Angew. Chem.* **2012,** *124*, 3193–3196.

16 Yang, Z.; Wang, J.; Yu, X., The adsorption, diffusion and dissociation of O_2 on Pt-skin $Pt_3Ni(111)$: A density functional theory study. *Chem. Phys. Lett.* **2010,** *499*, 83-88.

[17] Fowler, B.; Lucas, C. A.; Omer, A.; Wang, G.; Stamenković, V. R.; Marković, N. M., Segregation and stability at $Pt_3Ni(111)$ surfaces and $Pt_{75}Ni_{25}$ nanoparticles. *Electrochim. Acta* **2008,** *53*, 6076-6080.

[18] Ma, Y.; Balbuena, P. B., Surface properties and dissolution trends of Pt_3M alloys in the presence of adsorbates. *J. Phys. Chem. C* **2008,** *112*, 14520-14528.

[19] Ma, Y.; Balbuena, P. B., Pt surface segregation in bimetallic Pt_3M alloys: A density functional theory study. *Surf. Sci.* **2008,** *602*, 107-113.

[20] Stamenković, V.; Schmidt, T. J.; Ross, P. N.; Marković, N. M., Surface segregation effects in electrocatalysis: Kinetics of oxygen reduction reaction on polycrystalline Pt_3Ni alloy surfaces. *J. Electroanal. Chem.* **2003,** *554-555*, 191-199.

[21] Sun, D.; Zhao, Y.; Su, H.; Li, W., An atomistic thermodynamics study of the structural evolution of the Pt3Ni(111) surface in an oxygen environment. *Chin. J. Catal.* **2013,** *34*, 1434-1442.

[22] Lee, H. C.; Kim, B. M.; Jeong, C. K.; Toyoshima, R.; Kondoh, H.; Shimada, T.; Mase, K.; Mao, B.; Liu, Z.; Lee, H.; Huang, C.-Q.; Li, W. X.; Ross, P. N.; Mun, B. S., Surface segregation and oxidation of $Pt_3Ni(111)$ alloys under oxygen environment. *Catal. Today* **2015**, doi:10.1016/j.cattod.2015.05.003.

[23] Fuhrmann, T.; Kinne, M.; Tränkenschuh, B.; Papp, C.; Zhu, J. F.; Denecke, R.; Steinrück, H. P., Activated adsorption of methane on Pt(111) —an in situ XPS study. *New J. Phys.* **2005,** *7*, 107.

[24] Michaelides, A.; Hu, P., Insight into Microscopic Reaction Pathways in Heterogeneous Catalysis. *J. Am. Chem. Soc.* **2000,** *122*, 9866-9867.

[25] Cremer, P.; Stanners, C.; Niemantsverdriet, J. W.; Shen, Y. R.; Somorjai, G., The conversion of di-σ bonded ethylene to ethylidyne on Pt(111) monitored with sum frequency generation: evidence for an ethylidene (or ethyl) intermediate. *Surf. Sci.* **1995,** *328*, 111-118.

[26] Land, T. A.; Michely, T.; Behm, R. J.; Hemminger, J. C.; Comsa, G., Direct observation of surface reactions by scanning tunneling microscopy: Ethylene→ethylidyne→carbon particles→graphite on Pt(111). *J. Chem. Phys.* **1992,** *97*, 6774-6783.

[27] Gao, M.; Pan, Y.; Huang, L.; Hu, H.; Zhang, L. Z.; Guo, H. M.; Du, S. X.; Gao, H.-J. Epitaxial growth and structural property of graphene on Pt(111) *Appl. Phys. Lett.* **2011**, *98*, 033101.

[28] Cattelan, M.; Cavaliere, E.; Artiglia, L.; Gavioli, L.; Agnoli, S.; Granozzi, G. The dynamics of Fe intercalation on pure and nitrogen doped graphene grown on Pt(111) probed by CO adsorption, *Surf. Sci.* **2015**, *634*, 49.

[29] Sutter, P.; Sadowski, J. T.; Sutter, E; Graphene on Pt(111): Growth and substrate interaction, *Phys. Rev. B* **2009**, *80*, 245411.

[30] Grüneis, A.; Kummer, K.; Vyalikh, D. V., Dynamics of graphene growth on a metal surface: A time-dependent photoemission study. *New J. Phys.* **2009,** *11*, 073050.

[31] Ligato, N.; Cupolillo, A.; Sindona, A.; Riccardi, P.; Pisarra, M.; Caputi, L. S., A comparative study of the plasmonic properties of graphene on lattice-matched and lattice-mismatched Ni surfaces. *Surf. Sci.* **2014,** *626*, 40-43.

[32] Otero, G.; Gonzalez, C.; Pinardi, A. L.; Merino, P.; Gardonio, S.; Lizzit, S.; Blanco-Rey, M.; Van de Ruit, K.; Flipse, C. F. J.; Méndez, J.; de Andrés, P. L.; Martín-Gago, J. A., Ordered Vacancy Network Induced by the Growth of Epitaxial Graphene on Pt(111). *Phys. Rev. Lett.* **2010,** *105*, 216102.

[33] Cattelan, M.; Peng, G. W.; Cavaliere, E.; Artiglia, L.; Barinov, A.; Roling, L. T.; Favaro, M.; Pis, I.; Nappini, S.; Magnano, E.; Bondino, F.; Gavioli, L.; Agnoli, S.; Mavrikakis, M.; Granozzi, G., The nature of the Fe-graphene interface at the nanometer level. *Nanoscale* **2015,** *7*, 2450–2460.

[34] Ng, M. L.; Balog, R.; Hornekœr, L.; Preobrajenski, A. B.; Vinogradov, N. A.; Mårtensson, N.; Schulte, K., Controlling Hydrogenation of Graphene on Transition Metals. *J. Phys. Chem. C* **2010,** *114*, 18559-18565.

[35] Rusz, J.; Preobrajenski, A. B.; Ng, M. L.; Vinogradov, N. A.; Mårtensson, N.; Wessely, O.; Sanyal, B.; Eriksson, O., Dynamical effects in x-ray absorption spectra of graphene and monolayered *h*-BN on Ni(111). *Phys. Rev. B* **2010,** *81*, 073402.

[36] Zhao, W.; Kozlov, S. M.; Höfert, O.; Gotterbarm, K.; Lorenz, M. P. A.; Viñes, F.; Papp, C.; Görling, A.; Steinrück, H.-P., Graphene on Ni(111): Coexistence of Different Surface Structures. *J. Phys. Chem. Lett.* **2011,** *2*, 759-764.

[37] Lahiri, J.; Lin, Y.; Bozkurt, P.; Oleynik, I. I.; Batzill, M. An extended defect in graphene as a metallic wire. *Nat. Nanotechnol.* **2010**, *5*, 326.

[38] Gao, M.; Pan, Y.; Huang, L.; Hu, H.; Zhang, L. Z.; Guo, H. M.; Du, S. X.; Gao, H.-J. Epitaxial growth and structural property of graphene on Pt(111) *Appl. Phys. Lett.* **2011**, *98*, 033101.

[39] Voloshina, E. N.; Generalov, A.; Weser, M.; Böttcher, S.; Horn K.; Dedkov, Y. S. Structural and electronic properties of the graphene/Al/Ni(111) intercalation system. *New J. Phys.* **2011**, *13*, 113028.

[40] Klimovskikh, I. I.; Tsirkin, S. S.; Rybkin, A. G.; Rybkina, A. A.; Filianina, M.V.; Zhizhin, E. V.; Chulkov, E. V.; Shikin, A. M. Nontrivial spin structure of graphene on Pt(111) at the Fermi level due to spin-dependent hybridization. *Phys. Rev. B* **2014**, *90*, 235431.

[41] Yao, W.; Wang, E.; Deng, K.; Yang, S.; Wu, W.; Fedorov, A. V.; Mo, S.-K.; Schwier, E. F.; Zheng, M.; Kojima, Y.; Iwasawa, H.; Shimada, K.; Jiang,K.; Yu, P.; Li, J.; Zhou, S. Monolayer charge-neutral graphene on platinum with extremely weak electron-phonon coupling. *Phys. Rev. B* **2015**, *92*, 115421.

[42] Sun, J.; Nam, Y.; Lindvall, N.; Cole, M. T.; Teo, K. B. K.; Park, Y. W.; Yurgens, A. Growth mechanism of graphene on platinum: Surface catalysis and carbon segregation. *Appl. Phys. Lett.* **2014**, *104*, 152107.

[43] Nie, S.; Walter, A. L.; Bartelt, N. C.; Starodub, E.; Bostwick, A.; Rotenberg, E.; McCarty, K. F. Growth from below: graphene bilayers on Ir(111). *ACS Nano*, **2011**, *5*, 2298.

[44] Cui, Y.; Fu, Q.; Bao, X. Dynamic Observation of Layer-by-Layer Growth and Removal of Graphene on Ru(0001). *Phys. Chem. Chem. Phys.* **2010**, *12*, 5053.

[45] Loginova, E.; Nie, S.; Thürmer, K.; Bartelt, N. C.; McCarty, K. F. Defects of graphene on Ir(111): rotational domains and ridges. *Phys. Rev. B* **2009**, *80*, 085430

[46] Merino, P.; Svec, M.; Pinnardi, A. L.; Otero, G.; Martin-Gago, J. A. Strain-driven moiré superstructures of epitaxial graphene on transition metal surfaces. *ACS Nano* **2011**, *5*, 5627.

[47] Kim, K. S.; Winograd, N., X-ray photoelectron spectroscopic studies of nickel-oxygen surfaces using oxygen and argon ion-bombardment. *Surf. Sci.* **1974,** *43*, 625-643.

[48] Altieri, S.; Tjeng, L. H.; Tanaka, A.; Sawatzky, G. A., Core-level x-ray photoemission on NiO in the impurity limit. *Phys. Rev. B* **2000,** *61*, 13403-13409.

[49] Miller, D. J.; Öberg, H.; Kaya, S.; Sanchez Casalongue, H.; Friebel, D.; Anniyev, T.; Ogasawara, H.; Bluhm, H.; Pettersson, L. G. M.; Nilsson, A., Oxidation of Pt(111) under Near-Ambient Conditions. *Phys. Rev. Lett.* **2011,** *107*, 195502.

3. Other 2D materials and heterostructures

Hexagonal boron nitride

In 2004,[1] the rise of G and the subsequent research progress on single and multilayer graphitic nanosheets inspired curiosity about the existence and stability of other analogous 2D materials based on boron nitride (BN).[2] Actually, BN is isoelectronic with respect to C and presents similar polymorphism.

The most fundamental polymorph in the BN system is represented by *h*-BN: this may be depicted as a G layer, in which the C atoms have been fully substituted by alternating B and N atoms. Akin to G, within each *h*-BN layer, the atoms are bound together by strong covalent bonds, while weak van der Waals forces keep together the different layers. The crystallographic parameters of bulk *h*-BN and graphite are almost identical, the *in-plane* lattice parameter is slightly bigger (2.50 Å), whereas the interlayer spacing smaller (3.33 Å). The 3D staking however is different: in bulk *h*-BN the hexagons of neighbouring planes are superimposed, i.e. B and N atoms are in succession along the *c* axis (AA' stacking), while in graphite they are shifted by half a hexagon (AB stacking), as schematically depicted in Figure 1.

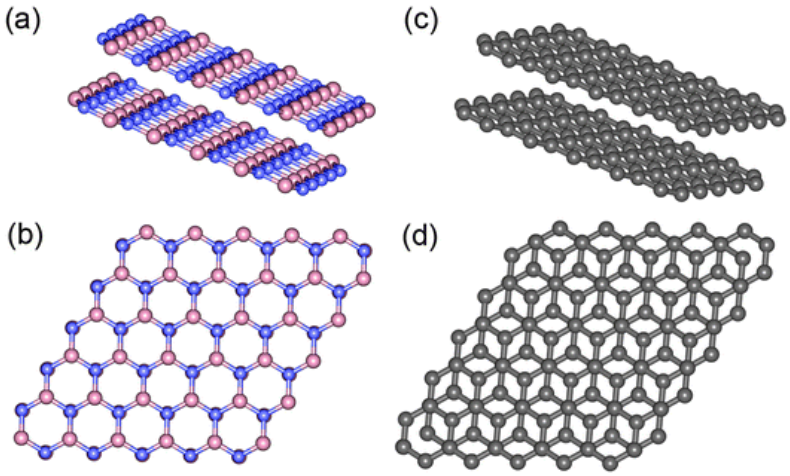

Figure 1. Structural models of (a and b) h-BN sheets and (c and d) graphite sheets displaying the difference in their stacking sequence. Highly-crystallized graphite possesses a Bernal (AB) stacking sequence, while h-BN is stacked with the B atoms on top of the N atoms and vice versa (AA' stacking). Adapted from Ref. [3] © 2014 RSC.

One important difference between G and *h*-BN is their electronic structure. As explained in the section 2, G is a semimetal with no band gap, on the contrary *h*-BN exhibits a bandgap of 5.97 eV[4] making it an attractive candidate for solar blind detectors, UV lasers, and low-k dielectric materials for 2D devices.[5,6,7,8]

Other three-dimensional (3D) BN allotropes are naturally found such as layered stacked structure in the rhombohedral form, cubic BN similar to diamond and a wurtzite like structure. Moreover *h*-BN can be shaped in nanoribbons,[9] nanotubes[10] and fullerenes (called fulborenes)[11] exactly as C based nanostructures.

In the following paragraphs is presented a short review on the preparation methods of *h*-BN with special focus on the bottom-up synthesis on transition metals.

Preparation methods

A variety of methods has been used to synthesize 2D BN nanostructures. Most of them are similar to the well-known techniques utilized for the growth of G sheets.

As mentioned in the section "Introduction", the mechanical exfoliation technique is the pioneering procedure to obtain atomic sheets of *h*-BN. This method was initially used to isolate G monolayers in 2004[1] and a few months later it was successfully applied to many other layered compounds such as *h*-BN and MoS_2.[12] BN sheets obtained by this method have a good combination of thickness and lateral size, making them suitable for fundamental studies in physics and optoelectronics.[13,14,15] However, in contrast to the G case, this technique has not been effective to produce few-layer and monolayer *h*-BN. This may be partially due to the stronger lip–lip interactions between BN basal planes, i.e. the formation of chemical bonds as bridges between the atoms of adjacent layers. This phenomenon contributes to a metastable energy minimum by decreasing the number of dangling bonds at the edges; therefore, the formation of multilayer *h*-BN stabilizes the whole structure.[16] Other approaches to the mechanical exfoliation of *h*-BN is the application of shear forces instead of direct pulling forces *via* peeling [17] or novel "vortex fluidic exfoliation".[18]

By a chemical-solution-derived method single and few layers *h*-BN sheets can be prepared,[19] BN nanoflakes have been synthesized *via* a catalyst-free CVD process using B_2O_3 and melamine powders as precursors,[20] or exploiting reaction between H_3BO_3 and urea under inert atmosphere.[21]

Similarly to G, a great deal of effort has been spent to realize high purity monolayer of *h*-BN in a large scale. Bottom-up syntheses, such as reaction of controlled quantity of precursors in controlled atmosphere or CVD on transition metals allow obtaining wafer-scale *h*-BN layers ideal for future electronic devices.

Epitaxial growth of h-BN monolayers

Deposition techniques have been applied to epitaxially grow BN thin films for several decades. M. Basche's patent on the thermal decomposition and reaction of ammonia with boron trichloride to deposit BN coatings onto a surface dates back to 1964.[22]

Under UHV conditions the synthesis of *h*-BN on transition metals is a catalytic surface limited reaction. To synthesize thin layers of *h*-BN the reaction between various reactants can be used, such as $BF_3 + NH_3$, $BCl_3 + NH_3$, $B_2H_6 + NH_3$ or it is possible to exploit the pyrolysis of a single precursor such as borazine ($B_3N_3H_6$), trichloroborazine ($B_3N_3H_3Cl_3$), hexachloroborazine ($B_3N_3Cl_6$) or borane-ammonia complex (BH_3–NH_3).[3]

The first *h*-BN monolayer film was grown by the adsorption and decomposition of borazine on transition metals such as Pt(111) and Ru(0001) in 1990.[23] Borazine is an analogue of benzene, in which the C atoms are substituted by alternate B and N atoms in a natural B:N stoichiometry of 1:1. The *h*-BN monolayer has been also successfully formed on a number of transition metal surfaces, such as Ni(111), Cu(111), Pt(111), Ru(001), Pd(111), Pd(110), Fe(110), Mo(110) and Cr(110).[3]

To achieve high-quality 2D *h*-BN layers on transition metal substrates low precursor pressures are required.[15,24] Figure 2 shows the decomposition of $B_3N_3H_6$ to form *h*-BN on Ru(0001) at 1×10^{-8} mbar. Initially, sparse arrays of *h*-BN nuclei form, followed by the growth of large islands, they then coalesce into a closed film covering the entire surface.

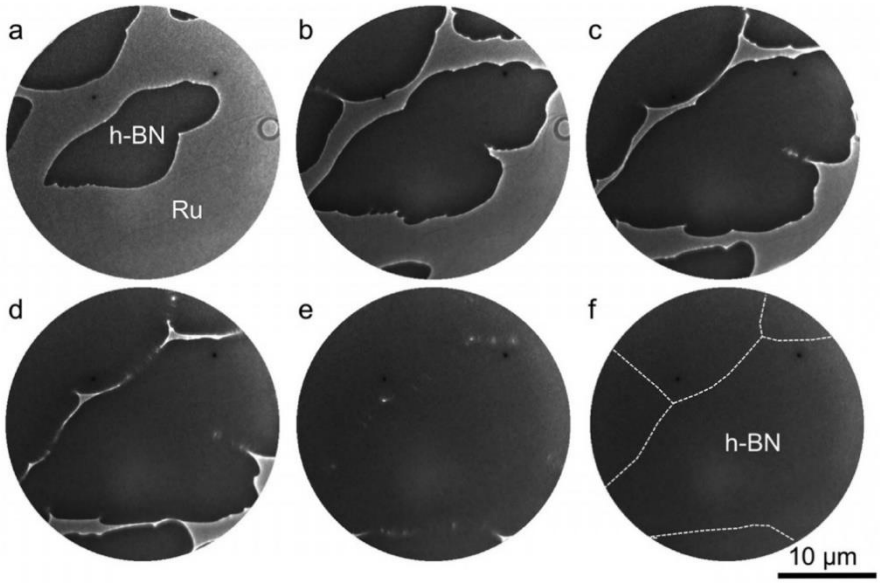

Figure 2. Macroscopic h-BN domains on Ru(0001) obtained by CVD growth from borazine. (a-f) LEEM images at different growth stages to the full coalescence of the h-BN monolayer. Temperature = 780 °C; borazine pressure = 1×10^{-8} mbar; elapsed time = (a) 0, (b) 300 s, (c) 600 s, (d) 900 s, I 1200 s, (f) 1350 s. (f) Complete coalescence is achieved. Dashed lines mark the final domain boundaries. Reprinted from Ref. [24] © 2011 ACS.

Ni(111) has been one of the most studied substrates for the growth of *h*-BN. The structure of monolayer *h*-BN/Ni(111), has been investigated by LEED I-V, these studies demonstrated that *h*-BN is not completely flat, but slightly buckled on Ni(111) with B atoms being closer to the surface than N atoms. This buckling was attributed to the small lattice mismatch between *h*-BN and Ni(111), which leads to a commensurate (1×1) system where h-BN is slightly compressed and thus buckled.[28] This structural model was confirmed further by X-ray photoelectron diffraction (XPD), STM, and also DFT studies.[25,26,27] HREELS,[28] core level spectroscopy and near-edge x-ray absorption fine structure (NEXAFS) investigations demonstrated a strong hybridization between Ni 3*d* and *h*-BN π states, indicating a strong interaction between *h*-BN and the metal surface.[29,30]

Similarly to G, the metal intercalation beneath the 2D overlayers is a useful and versatile strategy to tune the materials properties. Usachov et al.[31] demonstrate how to decouple a monolayer *h*-BN from Ni(111) surface by intercalation of Au layers underneath the 2D layer. This process has been systematically investigated using ARPES, XPS, and NEXAFS. It has been demonstrated that the transition of the *h*-BN layer from the buckled into the quasi-freestanding state is accompanied by a change of its lattice constant.

Similarly to G/Ni(111), (see Figure 5 in the section 2), the intercalation of Au underneath h-BN/Ni(111) leads to a rigid upshift of about 1.7 eV of the electronic band structure. Because of the insulating band structure of *h*-BN the hybridization of Ni 3*d* and *h*-BN

VB is not well visible by ARPES, as, on the contrary, is for G/Ni(111). For G the π band goes continuously from 8-10 eV (in the Γ point) of BE to the Fermi level (in the K point) crossing Ni 3*d* states at about 1.3 eV, whereas the *h*-BN π band goes from 8-10 eV (in the Γ point) and ends at 4 eV (in the K point) avoiding the Ni states. However, it has been predicted that the Ni states, which are not detectable in ARPES maps, interact with the conduction band of *h*-BN.[30]

The method to achieve a quasi-freestanding *h*-BN layer by intercalation of gold has been exploited in the section 3.1.2.

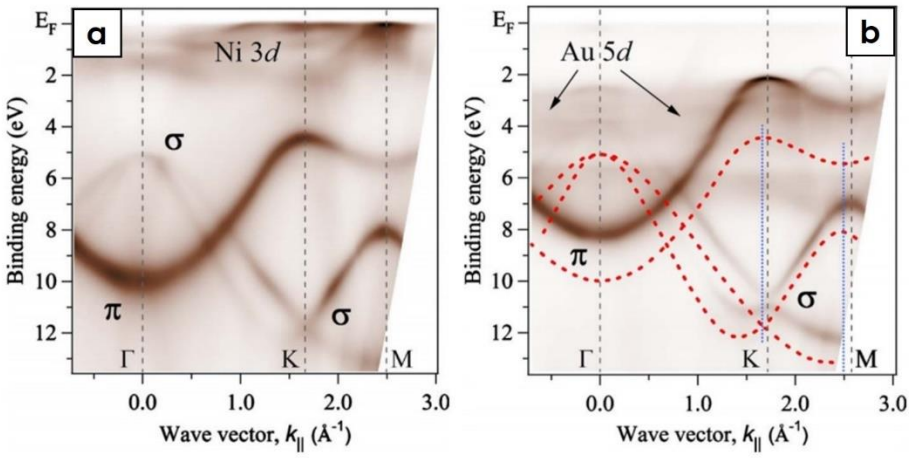

Figure 3. The electron-energy band structure of (a) h-BN/Ni(111)/W(110) system and (b) h-BN/Au(1 ML)/Ni(111)/W(110) system measured by ARPES. The vertical dashed and dotted lines indicate high-symmetry points in the BZ of h-BN/Au and h-BN/Ni, respectively. Adapted from Ref. [31] © 2010 APS.

Except for Ni(111), for all other hexagonal surfaces a coincidence superstructure between *h*-BN and the substrate is observed, whose size depends on the lattice mismatch with the underlying substrate, which varies between 7% and 10% depending on the specific metal. On Pt(111) *h*-BN grows with a well-defined moiré superstructure,[32] as shown by LEED pattern in Figure 4a. By measuring the ratio between the (01) Pt(111) and the (01) *h*-BN to 0.89 yields approximately 10 *h*-BN unit cells (0.247 nm) on 9 Pt(111) nearest neighbour distances (0.278 nm). The moiré pattern has been also confirmed by STM imaging, reported in Figure 4b. The well-defined orientation, and consequently characteristic LEED pattern, of *h*-BN/Pt(111) has been used to distinguish it from G in the section 3.1.1.

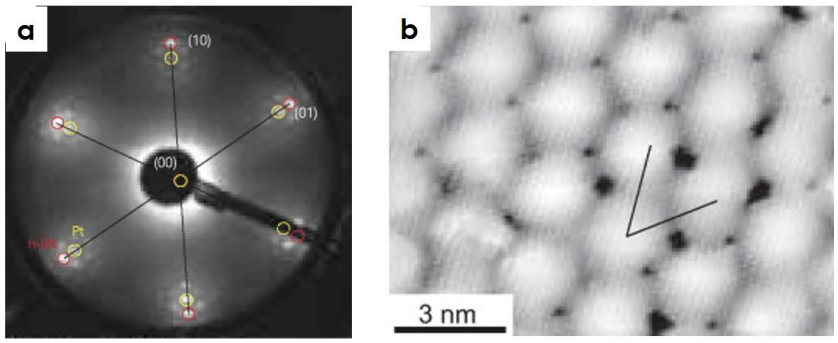

Figure 4. Pt(111) after exposure of 1×10^{-6} mbar at a sample temperature of 800 °C for 120 s. (a) LEED pattern displaying the coincidence between the h-BN layer and the Pt(111) surface (red h-BN, yellow Pt(111)). (b) STM image (V = 0.1 mV, I = 2 nA) displaying atomic resolution. Adapted from Ref. [32] © 2008 Elsevier.

Large area synthesis of few-layered *h*-BN films has been obtained on copper, platinum and nickel foils via CVD and then successful transfer process to different substrates have been optimized like in the case of G.[33,34,35] The growth of multilayers has not been well-explained in the literature. They seem to form on top of the first *h*-BN layer and probably are caused by defects on the surface. Multilayer growth is strongly hindered by the presence of the fist layer, which, being in direct contact with the catalytic metal surface, has a much higher growth rate. To trigger the multilayer formation high pressures of reactants (mbar range) are required, these are typically obtainable during CVD experiments, this also can explain why during UHV preparations multilayers of h-BN have been never observed.

As for G, a surface segregation mode of multilayer *h*-BN has been also reported in the literature for Fe-Cr-Ni alloy and for a purposely built sandwiched growth substrates,[36] in these cases, similarly to G, multilayers grow underneath the first *h*-BN layer.[37]

Transition metal dichalcogenides

Single-layered TMDs, whose general formula is MX_2, where M is a transition metal of groups from 4 to 10 and X is a chalcogen, exhibit interesting electrical and chemical properties. These materials offer opportunities for fundamental and technological research in a variety of fields including catalysis, energy storage, sensing, electronic and spintronic devices. More than forty different dichalcogenides are known as highlight in Figure 5a.

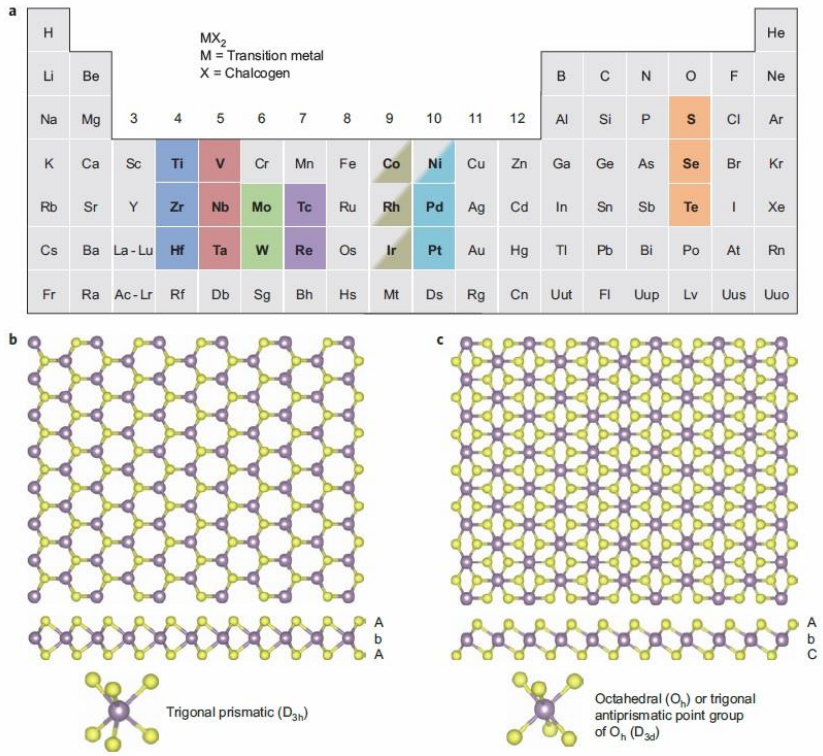

Figure 5. (a) The transition metals and the three chalcogen elements that predominantly crystallize in those layered structure are highlighted in the periodic table. Partial highlights for Co, Rh, Ir and Ni indicate that only some of the dichalcogenides form layered structures. (b,c) c-Axis and section view of single-layer TMD with trigonal prismatic (b) and octahedral (c) coordination. Atom colour code: purple, metal; yellow, chalcogen. The labels AbA and AbC represent the stacking sequence where the upper- and lower-case letters represent chalcogen and metal elements, respectively. Reprinted from Ref. [38] © 2013 NPG.

The electronic properties of bulk TMDs are diverse ranging from insulators such as HfS_2, semiconductors such as MoS_2 and WS_2, semimetals such as Wte_2 and $TiSe_2$, to true metals such as NbS_2 and VSe_2.[39,40,41] Exfoliation of these materials into mono- or few-layers leads to additional characteristics due to confinement effects.[42,43,44] The chemistry of MX_2 compounds thus offers opportunities for going beyond G and discovering new fundamental and technological applications based on inorganic 2D materials.

In layered structures TMDs, each layer typically has a thickness of ~6-7 Å, which consists of a hexagonally packed layer of metal atoms sandwiched between two layers of chalcogen atoms. The intra-layer M–X bonds are predominantly covalent in nature, whereas the sandwich layers are coupled by weak van der Waals forces, thus allowing the crystal to readily exfoliate along the layer surface. The metal atoms provide four electrons to fill the bonding states of TMDs such that the oxidation states of the metal (M) and chalcogen (X) atoms are +4 and –2, respectively. Bulk TMD crystals exhibit different polytypes, the most commonly encountered are 1T, 2H and 3R where the letters stand for octahedral, hexagonal and rhombohedral, respectively, and the digit indicates the number of X–M–X units in the unit cell (that is, the number of layers in the stacking sequence), see Figure 6. The monolayer TMDs, which itself contains three layers of atoms (X–M–X), exhibit only two polymorphs: trigonal prismatic and octahedral phases as shown in Figure 5b and Figure 5c, respectively. The former belongs to the D_{3h} point group whereas the latter belongs to the D_{3d} group. In the following discussion, they are referred to as monolayer 2H (or D_{3h}) and 1T (or D_{3d}) MX_2, respectively.

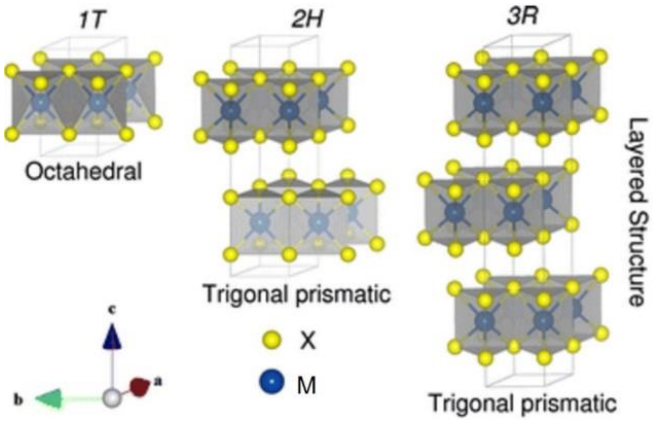

Figure 6. Structural representation of 1T, 2H and 3R TMD polytypes. Adapted from Ref. [45] © 2014 RSC.

The electronic structure of TMDs strongly depends on the coordination environment of the transition metal and its *d*-electron count. In both 2H and 1T phases, the non-bonding *d* bands of the TMDs are located within the gap between the bonding (σ) and antibonding (σ^*) bands of M–X bonds as illustrated in Figure 7a. Octahedrally coordinated transition metal centres (D_{3d}) of TMDs form degenerate d_{z^2,x^2-y^2} (e_g) and $d_{yz,xz,xy}$ (t_{2g}) orbitals that can together accommodate the TMDs *d* electrons (a maximum of 6, for group 10 TMDs). On the other hand, the *d* orbitals of transition metals with trigonal prismatic coordination (D_{3h}) split into three groups, d_{z^2} (a_1), $d_{x^2-y^2,xy}$, and $d_{xz,yz}$ (e'), with a sizeable gap (~1 eV) between the first two groups of orbitals.

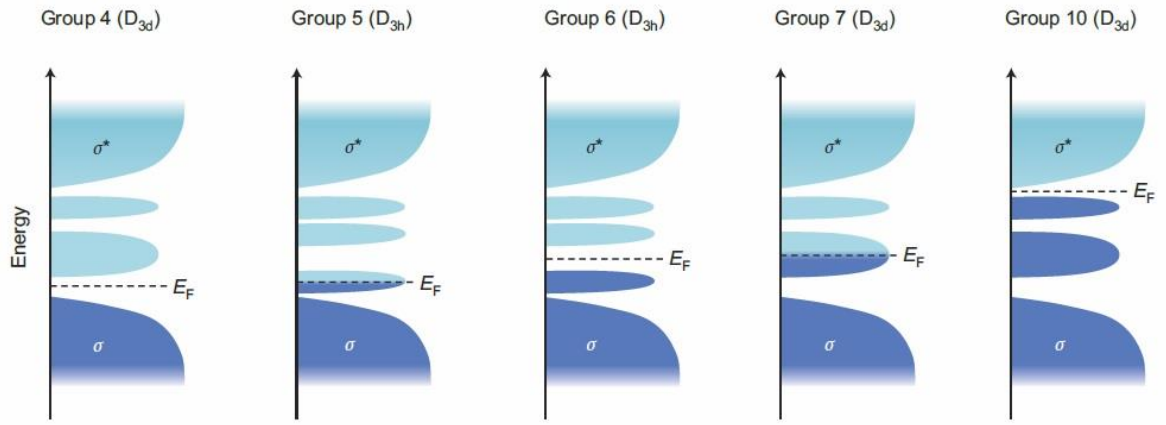

Figure 7. (a) Qualitative schematic illustration showing progressive filling of d orbitals that are located within the bandgap of bonding (σ) and anti-bonding states (σ) in group 4, 5, 6, 7 and 10 TMDs. D_{3h} and D_{3d} refer to the point group associated with the trigonal prismatic and the octahedral coordination of the transition metals. It should be noted that this simple model assumes ideal coordination; structural distortion often seen in many tellurides and group 7 TMDs lead to deviation in the electronic structure. The filled and unfilled states are shaded with dark and light blue, respectively. According to ligand field theory, D_{3d} compounds form two non-bonding d orbitals, $d_{yz,xz,xy}$ (bottom) and d_{z^2,x^2-y^2} (top), while D_{3h} compounds exhibit three d orbitals whose character is predominately d_{z^2}, $d_{x^2-y^2,xy}$,, and $d_{xz,yz}$ (from bottom to top). When an orbital is partially filled (such as in the case of group 5 and 7 TMDs), the Fermi level (E_F) is within the band and the compound exhibits a metallic character. When an orbital is fully filled (such as in group 6 TMDs), the Fermi level is in the energy gap and a semiconducting character is observed.* Reprinted from Ref. *[38]* © 2013 NPG.

The diverse electronic properties of TMDs arise from the progressive filling of the non-bonding *d* bands from group 4 to group 10 species. The effect of chalcogen atoms on the electronic structure is minor compared with that of the metal atoms, but a trend can still be observed: the broadening of the *d* bands and corresponding decrease in bandgap with increasing atomic number of the chalcogen. For example, the bandgap of 2H-MoS_2, 2H-$MoSe_2$ and 2H-$MoTe_2$ decreases gradually from 1.3 to 1.0 eV.[46]

The preferred phase adopted by a TMD depends primarily on the *d*-electron count of the transition metal. Group 4 TMDs (featuring d^0 transition metal centres) are all in the octahedral structure whereas both octahedral and trigonal prismatic phases are seen in group 5 TMDs (d^1). Group 6 TMDs (d^2) are primarily found in trigonal prismatic geometry and group 7 TMDs (d^3) are typically in a distorted octahedral structure. Group 10 TMDs (d^6) are all in an octahedral structure. Some strategies to induce phase changes are reported in the literature such as intercalation with alkali metals,[46,47] substitutional doping,[48] colloidal synthesis[49] or by irradiation with high-energy electrons, as in transmission electron microscopy (TEM).[50] Destabilization of the original phase may be attributed to the effective change in the *d*-electron count as well as the relative change in the free energy of the two phases.

The band structures of TDMs varies as a function of the number of layers, an example is reported in Figure 8b that shows the calculated band structures for bulk and few- to mono-layer MoS_2, a group 6 TMD in trigonal prismatic structure. The bulk material is an indirect-gap semiconductor having a bandgap of ~1 eV with a VB maximum (VBM) at the Γ point and a conduction band minimum at the midpoint along Γ–K symmetry lines. In contrast, an isolated monolayer of the same material is a direct-gap semiconductor with VBM and conduction band minimum coinciding at the K-point.

This indirect-to-direct bandgap transition on going from a bulk to a monolayer material arises from quantum confinement effects. The transition is manifested as enhanced PL in monolayers of MoS_2, $MoSe_2$, WS_2 and WSe_2, whereas only weak emission is observed in multilayer form[51,52,53,54] In the case of group 6 TMDs, the size of the monolayer bandgap is typically ~50% larger than that of bulk materials.[52,55]

Theoretical calculations have revealed intriguing physics of spin and valley coupling in monolayer group 6 TMDs.[55] A valley quantum number is a property of an electron inside a crystal that is associated with the electron momentum. Control of the valley degree of freedom allows manipulation of information, in a similar manner to spintronics and electronics, where the spin degree of freedom and the charge of an electron, respectively, are exploited. Broken inversion symmetry and spin–orbit coupling are properties of monolayer group 6 TMDs, for these materials there are two inequivalent momentum valleys (energy minima), K and K' (or –K), among the six found at the corners of the first Brillouin zone, Figure 7b. The VB at these valleys splits owing to strong spin–orbit coupling. For the monolayer MoS_2, time-reversal symmetry (a property in which motion is reversed when time is reversed) requires that the spin splitting at different valleys must be opposite, as shown in blue and red in Figure 7b, where *K* and *K'* show opposite situations, $[E(\mathbf{k},\uparrow)]=[E(-\mathbf{k},\downarrow)]$. On the contrary for bulk 2H-TMDs, such as 2H-MoS_2 and 2H-WSe_2, the inversion symmetry, i.e. $[E(\mathbf{k},\uparrow)]=[E(-\mathbf{k},\uparrow)]$, combined with the time-reversal symmetry ensures that electronic states are doubly spin-degenerate.

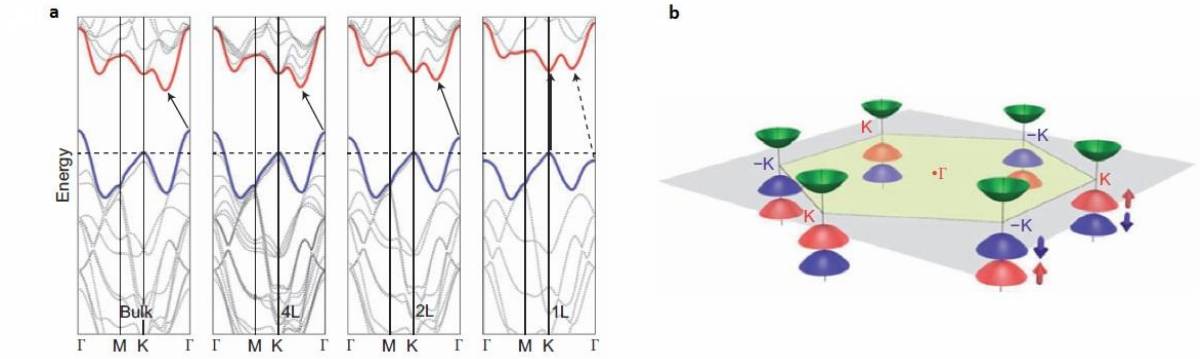

Figure 8. (a) Energy dispersion (energy versus wavevector k) in bulk, quadrilayer (4L), bilayer (2L) and monolayer (1L) MoS_2 from left to right. The horizontal dashed line represents the energy of a band maximum at the K point. The red and blue lines represent the conduction and VB edges, respectively. The lowest energy transition (indicated by the solid arrows) is direct (vertical) only in the case of a single layer. Indirect transition in monolayer (dashed arrow in 1L plot) is greater in energy than the direct band edge transition (solid arrow). Reprinted from Ref. [52] © 2010 ACS. (b) Band structure of MoS_2 showing six valleys and opposite spin–orbit splitting of the VB at the K and K' (-K) points. The red and blue surfaces represent spin–orbit-split VB maxima, each of which is associated with a particular electron spin. The green surfaces represent the conduction band minima or the valleys. Adapted from Ref. [55] © 2012 APS.

Experimentally, the existence of spin polarized features in the VB of group 6 TMDs has been verified by spin resolved ARPES studies that revealed spin polarized valence bands close to K and K' point in 3R-MoS_2 and not in 2H-MoS_2 bulk crystals. These two polytypes are composed by slabs of MoS_2 with D_{3h} symmetry, but only bulk 2H-MoS_2 is centrosymmetric, see Figure 6. The lack of this symmetry in 3R-MoS_2 bulk crystal allows the lifting of the spin degeneracy similar to what happen in monolayer 2H-MoS_2.[56] In another spin resolved ARPES study, bulk 2H-WSe_2 has been investigated.[57] In this case,

the bulk crystal inversion symmetry has been avoided using low energy photons sensitive only to the first layer WSe_2, which is intrinsically non-centrosymmetric.

Preparation methods

Similarly to the case of *h*-BN, the preparation of TMDs has been performed since the 1960s.[46] A focused effort on deposition and isolation of high-quality single-layer nanosheets was re-initiated after the discovery of G. Changes in interlayer coupling, degree of quantum confinement, and symmetry elements lead to dramatic differences in the electronic structure of single-layer TMDs compared with the bulk counterparts. The effect is particularly pronounced for semiconducting TMDs.[42,43,44,51,52,58,59,60]

Akin to G and *h*-BN, mechanical exfoliation yields the highest-quality monolayer samples, which are ideal for demonstration of high-performance devices and condensed-matter phenomena.[59] Large production of TMDs monolayers have been obtained by liquid exfoliation methods that are better suited for fundamental and proof-of-concept demonstrations in applications where large quantities of materials are required, such as electrochemical energy storage, catalysis, sensing or fillers for composites.[61,62,63] One of the most effective methods for mass production of fully exfoliated TMD nanosheets is the ultrasound-promoted hydration of lithium-intercalated compounds. The key advantage of the Li intercalation method is the ability to access the metallic 1T phase that is induced by the charge transfer from Li to the TMD,[59] however a disadvantage of the alkali metal intercalation is the partial damage of the TMDs layers by strain and reactions to form Li_2S.[64]

One of the most used bottom up synthesis for monolayer TMDs is CVD in hot-wall reactors.[58,65,66] A prototypical example is the growth of MoS_2, different strategies can be used for its synthesis such as: decomposition of metal and chalcogen single precursors (i.e. ammonium tetrathiomolybdate, $(NH_4)_2MoS_4$),[67] direct sulfurization of metallic molybdenum film,[68] or conversion of metal oxide (MoO_3) to MoS_2 by sulfurization. [69] Using these strategies, other TMDs have been successfully grown in their monolayer form such as $MoSe_2$,[70] WS_2,[71] WSe_2,[72] VSe_2,[73] TiS_2.[74] The sulfurization or selenization agents range from the elemental S and Se, to acid H_2S and H_2Se and organic compounds.

In this thesis monolayer WS_2 and WSe_2 have been grown using a strategy completely under UHV conditions, see the section 3.1.2. To synthesize a sulphide TMD in UHV reactors, the metals are deposited by evaporation, while depositing the metal the sulfurization agent can be introduced in the reaction chamber, e.g. dosing H_2S or exposing to elemental sulphur vapour pressure. The substrate must be annealed at moderate temperature (400 °C) during or after the deposition in order to trigger atoms diffusion and nucleation to form the desired TDM. This methodology has been extended also to selenides, but the lower vapour pressure of Se with respect to S makes necessary to use an evaporator for the chalcogenide sources. We decided to use this growth strategy because it allows studying the pristine properties of the materials without any contamination from air exposure or oxidation. The principal drawback is the typically nanometric dimension of the TMD islands. In the following, we report some example of TDMs obtained by UHV synthesis.

The Besenbacher's group has carried out a detailed work on MoS_2. They have studied the growth and the catalytic properties of small islands of MoS_2 (few nanometres wide) principally by STM and DFT, a review for this material can be found in Ref. [75] where the sulfurization agents, dopants and substrate roles has been investigated. For MoS_2, recent studies have demonstrated that larger islands (up to 50 nm) can be obtained on Au(111) tuning the growth temperature,[76] as reported in Figure 9. The same group has also investigated the deposition of WS_2 on Au(111)[77], inspired by this work we have also performed a detailed investigation of WS_2 growth on quasi-freestanding *h*-BN[78], see the section 3.1.2. Recently, direct selenization of Pt(111) single crystal has been suggested as a method to obtain well epitaxially oriented TMDs films, namely $PtSe_2$.[79] In addition, traditional MBE can be used to synthesize TDMs, as done for $HfSe_2$[80] Wse_2 e $MoSe_2$.[81]

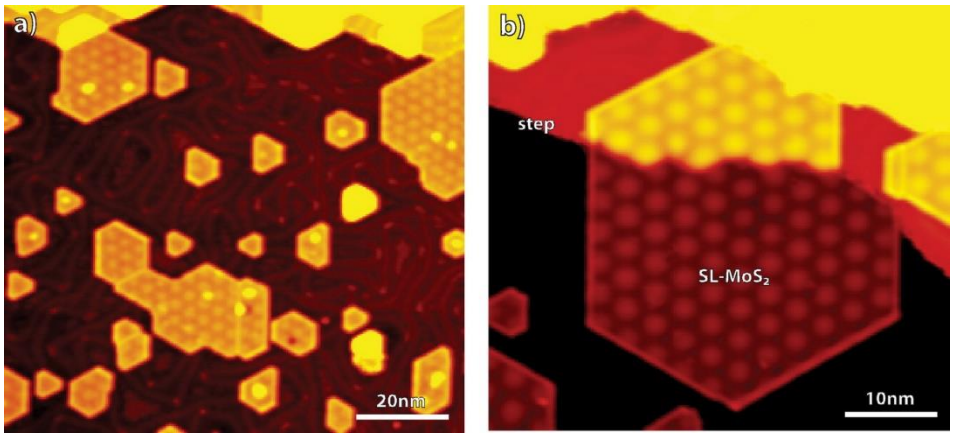

Figure 9. (a) Large-scale (100 × 100 nm) STM image of MoS_2 single-layer islands on the Au(111) surface corresponding to a surface coverage of 0.33 ML (b) 50 nm × 50 nm STM image of a single MoS_2 island with a hexagon shape crossing a single Au(111) step (V = −1250 mV, I_t = 0.61 nA). Reprinted from Ref. [76] © 2014 ACS.

Other layered chalcogenides

Other layered chalcogenide can be formed using metal of group 13-15. Their structures is usually more complex than the most common for layered TDMs, reported in Figure 5. Some of these structures are reported in Figure 10.

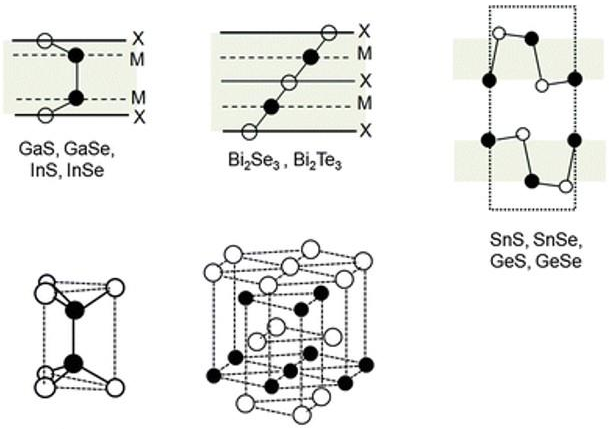

Figure 10. Single layer of metal chalcogenides exits as various polymorphs. Each layer is composed by tetra- or penta-atomic layers of metal (M) and chalcogen (X). Adapted from Ref. [82] © 2013 RSC.

If electrons are added to fill fully the *d* orbitals by changing the metal, for example moving from late TMs to bismuth ($5d^{10}6s^26p^3$ in Bi_2Se_3), the layered compound starts to have a "band inversion" and forms a topological surface state in the folded band gap (0.3 eV). This effect is triggered when the spin−orbit coupling is strong enough, as shown in Figure 11.[83] The different orbital occupation triggers a gradual evolution of electronic properties from semiconductor to band-folded topological insulators. This give us the diversity of physical and chemical properties of these of 2D layered materials.

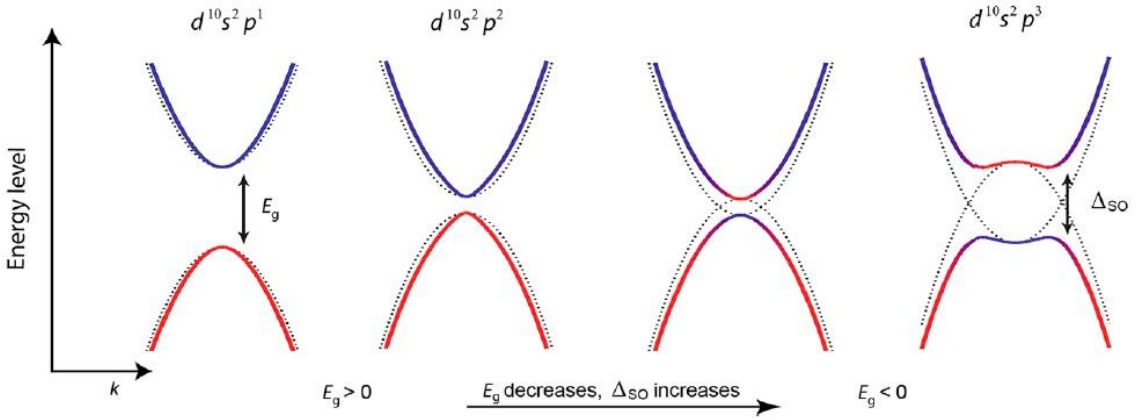

Figure 11. Band structure evolution of layered chalcogenides with group III to group V elements, with the band gap evolution from a positive value (a semiconductor) to a negative one (a topological insulator). Adapted from Ref. [83] © 2015 ACS.

For this class of materials, we decided to analyse the band structure of InSe, see the section 3.2, which has been experimentally investigated by means of ARPES. Monolayer InSe is formed by four layers, as depicted in Figure 11, where the dimer In_2 has an oxidation state of +4 and Se of -2, it belongs to the space group C_{3v}. In its bulk form, three polytypes (β, ε, γ) have been observed. They correspond to the three possible ways of stacking successive layers: the first corresponds to a rotation by π around an axis perpendicular to the plane of the layer followed by a translation parallel to the axis of rotation (the β polytype); the other two ways correspond to a translation where the horizontal components are $-(\mathbf{a}_1 + \mathbf{a}_2)/3$ in one case (ε polytype) and $(\mathbf{a}_1+\mathbf{a}_2)/3$ in the other (γ polytype), where **a** vector is the basis vectors of the hexagonal lattice.[84] As stated in the "Introduction" section, from a methodological point of view, this material represents an exception in this thesis, we decided to study vacuum exfoliated bulk crystals instead of obtaining it as a thin film. InSe bulk crystal was prepared by the vertical Bridgman−Stockbarger method,[85] we proceed to characterize the VB because a detailed investigation of some of its bulk properties was still missing in the literature, and this knowledge is pivotal to pave the way for new applications.

2D materials heterostructures

A variety of different 2D materials is nowadays available in the scientists' pockets, they range from semimetals to semiconductors, from insulators to topological insulator and they have interesting physical, chemical and PL properties. After preliminary studies on 2D materials *per se*, researchers addressed their attention to the possibility to stack or stitch together different nanosheets in order to form innovative heterostructures.

The research on 2D heterostructures began in 2010, when Dean et al. introduced the first atomically thin 2D heterostructures, composed by G placed on top of a thin *h*-BN layer[86] and demonstrated that *h*-BN can serve as an excellent 2D substrate. G roughness and charge density inhomogeneity on *h*-BN was greatly decreased compared to G on SiO_2 substrates allowing the investigation of its intrinsic transport properties.

Nowadays, the materials science of 2D heterostructures has received extensive attention and many exciting experimental results have been reported during the past few years.[87,88,89,90,91,92,93,94,95] As mentioned in the "Introduction" section, 2D heterostructures can be divided into two categories: stacked junctions formed by 2D layers place one on each other, and *in-plane* junctions where the 2D sheets are stitched together forming seamless atomic boundaries.

In-plane heterojunctions

In-plane junction refers to a system that consists of different 2D sheets bonding seamless on the same atomic plane.

To achieve *in-plane* junction bottom-up syntheses of the single components are required. In bottom-up methods, single atoms (or small group of atoms) can diffuse on a surface and arrange to form stable structures, synthesis can be stopped in any moment controlling defectivity or island size. The versatility of these methods is granted by the control of several parameters, such as temperature, reactant pressures, substrates, etc., therefore, in order to obtain 2D *in-plane* heterojunctions, it is required a deep understanding on the production of high quality 2D materials.

Due to their relatively small lattice mismatch (less than 1.7 %) and the same crystal structure, G and *h*-BN can be possibly integrated into a single atomic layer. Sheets composed by *h*-BN and G *in-plane* heterojunctions hereafter will be called *h*-BNG.

The electronic band structure and properties of *h*-BNG are expected to be different from those of pristine G and *h*-BN,[96,97,98] giving potential for the development of band gap-engineered applications in electronics and optoelectronics.[99] Spatially controlled *h*-BNG has been obtained experimentally by means of lithographic techniques, this heterojunction could find application in 2D electronic devices, such as p–n junctions, atomically thin integrated circuitry and split closed-loop resonator.[100,101]

As described earlier, high-quality G and *h*-BN can be both synthesized on metal substrates (Cu, Ni, Pt, et al.) by CVD or by decomposition of small molecules during experiments under UHV conditions. Different strategies have been employed to synthesized *h*-BNG heterostructures such as: step deposition of submonolayer coverage of G (*h*-BN) followed by the growth of the second 2D layer on the uncovered metal surfaces,[102] growth of a fully covering 2D layer followed by partial etching with hydrogen and completion with the second one,[103] simultaneous dose of precursors for G and *h*-BN.[96] In this thesis is reported an additional innovate way to obtain *h*-BNG in the section 3.1.1, the growth of this heterostructure has been attained on Pt(111) under UHV conditions by decomposition of only one molecular precursor, dimethylamine borane (DMAB).

STM has demonstrated its great power for investigating the atomic and electronic structures at the *h*-BN and G boundary.[104,105,106,107] In Figure 12c is presented an STM of a *h*-BNG layer on Ir(111), G and *h*-BN island merge with preferred zigzag type boundary. Scanning tunnelling spectroscopy (STS) allowed to investigate locally the electronic properties of G and *h*-BN as shown in Figure 12c,d by using sequential line scan dI/dV across boundary from G to *h*-BN regions. It can be clearly seen that at the location A, far from the boundary on G island, the spectrum appears to be a V-shape with the Dirac point locating at ~0 eV, which is typical of an electronically freestanding G. On *h*-BN domain the dI/dV curves at locations D, E, and F all exhibit a flat background close to zero from −0.8 to 0.8 eV, due to the insulating nature of *h*-BN. Interestingly, when the STM tip scan approaches to the boundary from G side, the V-shaped dI/dV curve becomes wider (curves B and C in Figure 12d). This remarkable decrease of G conductance close to the border of *h*-BN has not been explained well in the literature.[108] This effect underlines how complex are the physical properties at the interface between these two materials and factors such as incorporation of B and N atoms in the G lattice and C atoms in *h*-BN or small atoms dissolution into the metal selvedge,[107] cannot be excluded.

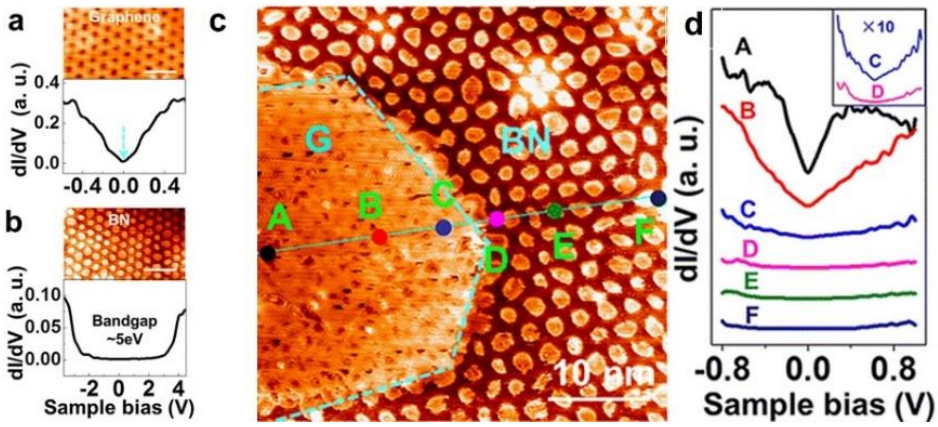

Figure 12. Electronic transition at the interface of h-BN and G. (a,b) STM images and typical dI/dV curves of G and h-BN on Ir(111), respectively (a,b: V = −0.100, −0.152 V; I = 2.432, 2.750 nA). (c,d) STM image of G h-BN heterostructure (V = −0.183 V; I = 2.134 nA) and the point-to-point dI/dV curves measured along the marked locations across the linking boundary. Scale bars: (a) 6 nm; (b) 9 nm; and (c) 10 nm. Reprinted from. Ref. [102] © 2014 ACS.

Other *in-plane* heterojunctions can be formed by stitching together different TMDs, their similar lattice structure make them ideal candidates for the construction of these kind of structures. *In-plane* TMD heterojunctions formed by $MoSe_2$–Wse_2[109,110] and MoS_2–WS_2 have been synthesized by a CVD step procedures,[111] interesting is the growth of MoS_2-WS_2 heterostructure that can be tuned from *in-plane* to stacked junction varying the synthesis temperature.[111] The border of *in-plane* MoS_2–WS_2 have been investigated by high-resolution scanning transmission electron microscopy (STEM) Z-contrast imaging. Figure 13a shows a Z–contrast image of their interface, where W atoms exhibit much higher image intensity than the Mo atoms. A series of sharp zigzag step interfaces can be identified along the overall-straight WS_2-MoS_2 junction. Careful examination of this STEM image reveals that the WS_2 and MoS_2 domains are connected seamlessly at the interface into a single 2H-TMD lattice and share the same crystal orientation. It can also be noticed the presence of some W and Mo atoms inside the MoS_2 and WS_2 lattice respectively, Figure 13b,c.

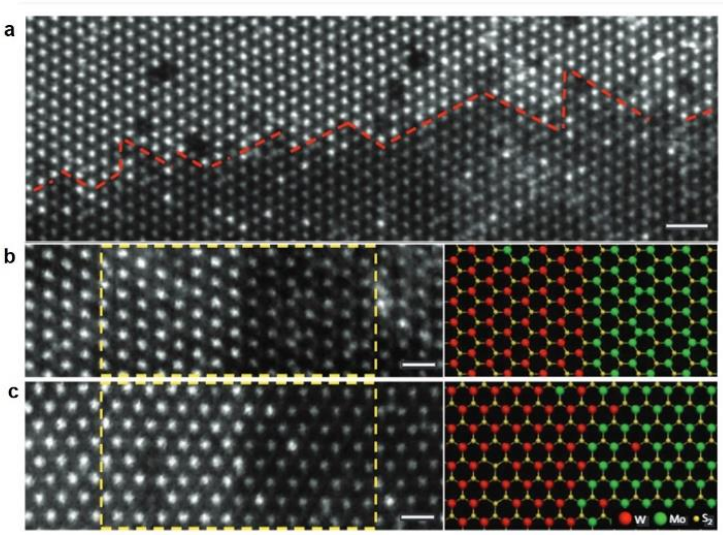

Figure 13. Atomic structure of the lateral heterojunctions between WS_2 and MoS_2 monolayers. A, Atomic-resolution Z-contrast STEM images of the in-plane interface between WS_2 and MoS_2 domains. A small roughness resulting from interfacial steps can be seen in a. The red dashed lines highlight the atomically sharp interface along the zigzag edge direction. b,c, Atomic-resolution Z-contrast images of the atomically sharp lateral interfaces along the zigzag (b) and armchair (c) directions. The atomic models on the right correspond to the structure in the highlighted regions. Scale bars: a 1 nm; b,c 0.5 nm. Adapted from Ref. [111] © 2014 NPG.

Also in the case of TMDs, spatially controlled heterojunctions have been obtained by lithography techniques, an example is reported in Ref. [112] where $MoSe_2$-MoS_2 *in-plane* junction was synthesized by controlled exposure of laser-vaporized sulphur plume.

Stacked heterojunctions

Since various methods have been proposed to produce and manipulate atomic layered 2D materials such as G, *h*-BN, TMDs, and other chalcogenides, it became possible to pick, place, and stack atomic layers of arbitrary compositions and build unique artificial architectures with desired functionalities.

A large number of vertical heterostructures including G/*h*-BN, *h*-BN/G, G/TMD, TMD/TMD stacked heterojunctions have been investigated in experiment and theory and some of them show great potential for applications in electronics, optoelectronics, etc. TMDs based stacked heterostructures are currently receiving considerable attention, the band gap variations in TMDs layers (from semimetal to semiconductors) provide different elements for multiple purpose. On the other hand, the junction composed by G stacked on *h*-BN with a suitable alignment allows a band gap opening in G due to the local breaking of the carbon sublattice symmetry,[94] thus a higher "ON/OFF" ratio can be expected in these vertical devices, compared to pristine G electronic devices.

Two different methodologies can be used to prepare such heterostructures, stack of mechanically exfoliated 2D layers or growth of 2D materials one on top of each other.

Mechanical exfoliation is the most versatile method to produce arbitrary stacked materials. The first ground-breaking study about 2D heterostructures was based on this

method. Dean et al. developed a transfer technique to obtain high-quality G/*h*-BN stacks,[90] the key idea was to use a micromanipulator to precisely aligned G close to *h*-BN flakes under optical microscope. This method has provided a strong impetus for many subsequent research investigations on the properties and applications of vertical 2D heterostructures.

An example of TMDs heterostructures obtained by this method is reported in Ref. [113]. In this work a WSe_2/MoS_2 stacked heterostructure has been studied, PL and absorption spectroscopy were used to investigate its optoelectronic properties. Due to the band offset of MoS_2 and WSe_2 (Figure 14d), optically excited excitons will relax at the MoS_2/WSe_2 interface before recombination, thus resulting in a lower PL excitonic peak energy, Figure 14c.

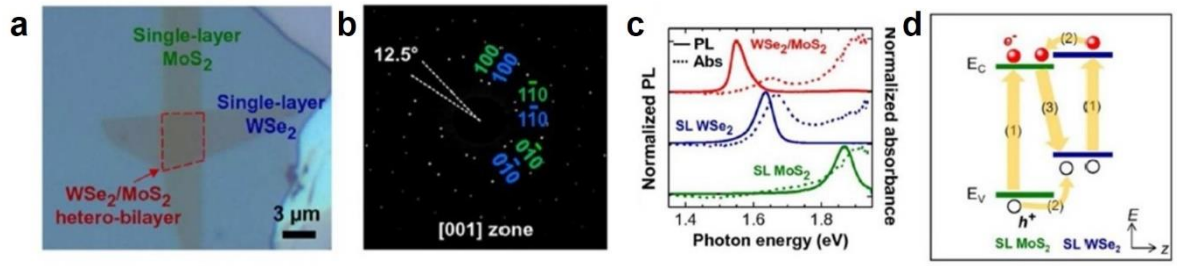

Figure 14. (a) Optical microscope image of a WSe_2/MoS_2 heterostructure on a SiO2/Si substrate. (b) The electron diffraction pattern of the heterostructure shown in (a), with the pattern of MoS_2 and WSe_2 indexed in green and blue colours, respectively. (c) Normalized PL (solid lines) and absorbance (dashed lines) spectra of monolayer WSe_2, MoS_2, and WSe_2/MoS_2 stacks. (d) Band diagram of WSe_2/MoS_2 heterostructure under photo excitation. Adapted from Ref. [113] © 2014 PNAS.

By means of sequential transfer method arbitrary 2D materials can be stack together to form innovative heterostructures, any exfoliable material can be used to form this kind of junctions, e.g. optoelectronic devices based on vertical p-n junction by stacking p-type phosphorene and n-type TMDs have been recently obtained.[114] This method can also be used to encapsulate easy oxidizable materials, e.g. phosphorene,[115] to protect them from air exposure.

Though mechanical transfer method has produced very high quality heterostructures suitable for laboratory scale research, however, several factors limit its application such as small sample size and poor output. Furthermore, vertical heterostructures fabricated by this method are usually randomly stacked, see Figure 14b, and the obtainment of selected stacking orders between different layers remains difficult. Another huge drawback is the trapping of adsorbates, such as hydrocarbons and water, between the layers during the fabrication. By careful annealing in vacuum these undesired layers can be largely reduced, but even after annealing, it should always be kept in mind the presence of a relevant contamination at the interfaces.

A way to increase the output of mechanical transfer methods maintaining its versatility is the wet transfer method. In this way 2D layers are manipulated by means of transfer techniques similar to the one used to move CVD grown G to arbitrary substrates.[116] This technique allows to efficiently stack 2D materials forming heterostructures with a variety of different orientations in a single transfer, as reported in Figure 15a. The principal drawback remains the contamination of the layer from polymer residues with addition of inevitably cracks due the transfer procedure. Using wet transfer method

MoS_2/WSe_2[117] and WS_2/MoS_2[118] heterostructures were prepared. An example is reported in Figure 15 where, using spatially localized photoemission measurements, the MoS_2/WSe_2 interlayer interactions and energy band alignment have been studied.

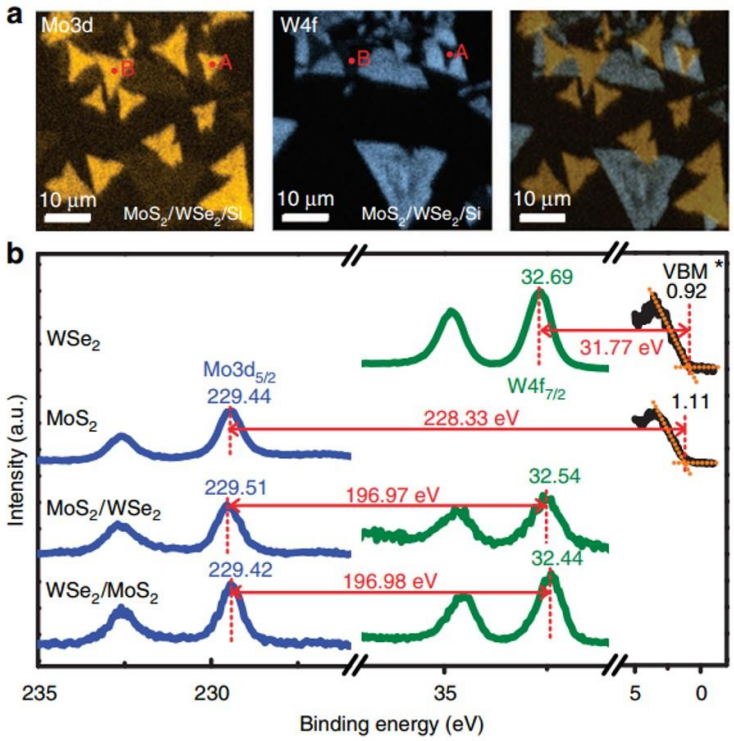

Figure 15. μ-XPS measurements on the stacked MoS_2/WSe_2 and WSe_2/MoS_2 heterostructures. (a) The Mo 3d and W 4f mappings for the same physical area. The right figure is the overlapped mapping that allows the identification of MoS_2/WSe_2 stacked areas. A and B points are the typical stacking area where the XPS are taken. (b) The spectra for the selected isolated WSe_2 and MoS_2 flakes, the stacked MoS_2/WSe_2 and WSe_2/MoS_2 heterostructure. All numbers are quoted in electron volt. There is an uncertainty of ±0.04 eV when determining the energy levels for all peaks. Reprinted from Ref. [117] © 2015 NPG.

As stated above, an alternative strategy to obtain stacked heterojunctions is the direct growth of 2D materials on top of each other via step procedures. This method allows the realization of clean heterostructures interface using as substrate the surface of a 2D material. The surface cleaning is ensured by the controlled reaction atmosphere, e.g. inert gases for CVD as well as UHV conditions for MBE, moreover, because of the absence of dangling bonds, surface defects will be significantly reduced, resulting in high-quality interfaces.

For G and *h*-BN great deal of effort has been put to stack them exploiting the non-catalytic growth of *h*-BN on G and vice versa.[119,120] A careful study of the stacked heterojunction G/h-BN/Cu(111) has been carried out by the Osterwalder's group.[121] In this study, they synthesized and investigated G/*h*-BN heterojunction *in-situ*, by means of XPD and STM they found that the two lattices are aligned in the same direction. In order to obtain this particular stacked structure other bottom-up techniques has been used such as co-segregation,[36] MBE,[122] hydrogen flame method[123], microwave[124], magnetron sputtering,[125] liquid phase method.[126]

Experimentally, TMDs vertical heterostructures have been synthesized many years ago, using the van der Waals epitaxy, which refers to the growth of layered materials

on clean surfaces even if there is a large lattice mismatch between the two layers. The resulting heterostructures are held together by weak van der Waals forces. The first layered materials produced in this way can be dated back to 1985 when Koma et al. grew ultrathin $NbSe_2$ and $MoSe_2$ on cleaved face of MoS_2 single crystals by MBE.[127]

Besides traditional ultrathin layer growth techniques, such as MBE,[80,127] one of the most promising methodology for the large scale production of TDM stacked heterojunctions is CVD. The growth of these systems by CVD is also driven by van der Waals forces that align the lattices of the 2D layers to form ordered structures. For example, the synthesis of the heterojunctions WS_2/MoS_2[111,128] was obtained by sequential sulfurization of transition metal oxides, by FFT analysis from the STEM images it has been found that the two monolayers have the same crystallographic orientation.[128]

Via bottom-up methods also G/TMDs structures can be formed. For example G/MoS_2 vertical junction has been synthesized by decomposition of $(NH_4)_2MoS_4$ on CVD G on Cu foil.[66] The clean surface of G allows a lattice-mismatched MoS_2 growth, also in this case G and MoS_2 lattices are mostly aligned because of the van der Waals epitaxy. [66] Interestingly epitaxial G grown on SiC has been identified as an ideal substrate for various van der Waals heterostructures formation. The CVD growth of MoS_2,[129] Wse_2[72,130] and *h*-BN[131] was found to be compatible with G/SiC substrate, thus leading to the formation of *h*-BN/G and TMDs/G stacked heterojunctions. Figure 16 reports an example composed by WSe_2 on epitaxial G/SiC(0001), the van der Waals epitaxy between the TMD and G is confirmed by LEED pattern that shows two hexagon lattices corresponding to an incommensurate but azimuthally oriented WSe_2 film with respect to epitaxial G.

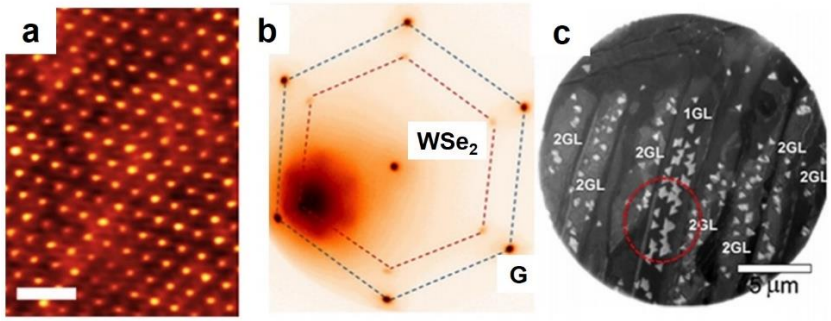

Figure 16. (a) High resolution STM demonstrates a high quality atomic structure (0.35 V, 1.5 nA, scale bar is 1 nm) and confirms the hexagonal pattern characteristic of 2H-WSe_2. LEED patterns (b) of the WSe_2 on epitaxial G confirms a close azimuthal alignment of WSe_2 and epitaxial G lattices, and LEEM imaging (c) illustrates the impact of G layer thickness on WSe_2 domain formation, where 1−2 layers of epitaxial G yield ideal surfaces for large domain WSe_2. Adapted from Ref. [130] © 2014 ACS.

In addition to the vertical heterostructures discussed above, there are also a large number of other stacked junctions that have been prepared. For example, Dang et al. reported van der Waals epitaxy between ultrathin topological insulator Bi_2Se_3 nanoplates with defined orientations on exfoliated few-layer G by a catalyst-free vapour-phase transport method.[132]

In this thesis is reported an *in-situ* growth and characterization of WS_2 monolayer on quasi-freestanding *h*-BN and WSe_2 on G in the section 3.1.2. Briefly, for WS_2/*h*-BN, *h*-BN

was obtained by decomposition of borane-ammonia complex on Ni(111) and electronically decoupled by intercalation of gold (similarly to what reported in Figure 3), thus WS_2 has been deposited by evaporation of W in sulphur atmosphere. Whereas, for WSe_2/G, G grown on Ni(111) has been decoupled by intercalation and reaction of Se atoms with the Ni substrate while WSe_2 was grown on top of G by co-evaporation of W and Se. By this method a large variety of TMDs can be synthesized changing metals or chalcogenides. We have already efficiently synthesized MoS_2, WS_2 and WSe_2 on HOPG, SiO_2 and Ni (111) (not all reported in this thesis). Moreover, by a careful coverage control, also of TMDs *in-plane* junctions can be produced.

References

1 Novoselov, K. S.; Geim, A. K.; Morozov, S. V.; Jiang, D.; Zhang, Y.; Dubonos, S. V.; Grigorieva, I. V.; Firsov, A. A. Electric field effect in atomically thin carbon films *Science* **2004**, *306*, 666.

2 Golberg, D.;Bando, Y.; Huang, Y.; Terao, T.; Mitome, M.; Tang, C. C.; Zhi, C. Y. Boron nitride nanotubes and nanosheets *ACS Nano* **2010**, *4*, 2979.

3 Pakdel, A.; Bando, Y.; Golberg, D. Nano boron nitride flatland. *Chem. Soc. Rev.* **2014**, *43*, 934.

4 Kubota, Y.; Watanabe, K.; Tsuda, O.; Taniguchi, T. Deep Ultraviolet Light-Emitting Hexagonal Boron Nitride Synthesized at Atmospheric Pressure. *Science* **2007**, *317*, 932.

5 Kim, K. K.; Hsu, A.; Jia, X.; Kim, S. M.; Shi, Y.; Hofmann, M.; Nezich, D.; Rodriguez-Nieva, J. F.; Dresselhaus, M.; Palacios, T.; Kong, J. Synthesis of monolayer hexagonal boron nitride on Cu foil using chemical vapor deposition. *Nano Lett.* **2012**, *12*, 161.

6 Yingjie Tay, R.; Griep, M. H.; Mallick, G.; Tsang, S. H.; Singh, R. S.; Tumlin, T.; Tong Teo, E. H.; Karna, S. P. Growth of large single-crystalline two-dimensional boron nitride hexagons on electropolished copper. *Nano Lett.* **2014**, *14*, 839.

7 Shi, Y.; Hamsen, C.; Jia, X.; Kang Kim, K.; Reina, A.; Hofmann, M.; Long Hsu, A.; Zhang, K.; Li, H.; Juang, Z. Y.; Dresselhaus, M. S.; Li, L. J.; Kong, J. Synthesis of few layer hexagonal boron nitride thin film by chemical vapor deposition. *Nano Lett.* **2010**, *10*, 4134.

8 Bresnehan, M. S.; Hollander, M. J.; Wetherington, M.; Wang, K.; Miyagi, T.; Pastir, G.; Snyder, D. W.; Gengler, J. J.; Voevodin, A. A.; Mitchel, W. C.; Robinson, J. A. Prospects of direct growth boron nitride films as substrates for graphene electronics. *J. Mater. Res.* **2014**, *29*, 459.

9 Zeng, H.; Zhi, C.; Zhang, Z.; Wei, Z.; Wang, X.; Guo, W.; Bando, Y.; Golberg, D. "White graphenes": boron nitride nanoribbons via boron nitride nanotube unwrapping *Nano Lett.* **2010**, *10*, 5049.

10 Chopra, N. G.; Luyken, R. J.; Cherrey, K.; Crespi, V. H.; Cohen, M. L.; Louie, S. G.; Zettl, A. Boron nitride nanotubes *Science* **1995**, *269*, 966.

11 Pokropivny, V. V.; Skorokhod, V. V.; Oleinik, G. S.; Kurdyumov, A. V.; Bartnitskaya, T. S.; Pokropivny, A. V.; Sisonyuk, A. G.; Sheichenko, D. M. Boron nitride analogs of fullerenes (the fulborenes), nanotubes, and fullerites (the fulborenites) *J. Solid State Chem.* **2000**, *154*, 214.

12 Novoselov, K. S.; Jiang, D.; Schedin, F.; Booth, T. J.; Khotkevich, V. V.; Morozov, S. V.; Geim, A. K. Two-dimensional atomic crystals *Proc. Natl. Acad. Sci. U S A.* **2005**, *102*, 10451.

13 Meyer, J. C.; Chuvilin, A.; Algara-Siller, G.; Biskupek, J.; Kaiser, U. Selective sputtering and atomic resolution imaging of atomically thin boron nitride membranes *Nano Lett.*, **2009**, *9*, 2683.

14 Pacilé, D.; Meyer, J. C.; Girit, Ç. Ö.; Zett, A. The two-dimensional phase of boron nitride: Few-atomic-layer sheets and suspended membranes *Appl. Phys. Lett.* **2008**, *92*, 133107.

15 Gorbachev, R. V.; Riaz, I.; Nair, R. R.; Jalil, R.; Britnell, L.; Belle, B. D.; Hill, E. W.; Novoselov, K. S.; Watanabe, K.; Taniguchi, T.; Geim, A. K.; Blake, P. Hunting for monolayer boron nitride: optical and raman signatures. *Small* **2011**, *7*, 465.

16 Pakdel, A.; Zhi, C. Y.; Bando Y.; Golberg, D. Low-dimensional boron nitride nanomaterials. Mater. Today **2012**, *15*, 256.

17 Li, L. H.; Chen, Y.; Behan, G.; Zhang, G. H.; Petravic M.; Glushenkov, A. M.; Large-scale mechanical peeling of boron nitride nanosheets by low-energy ball milling. J. Mater. Chem. **2011**, *21*, 11862.

[18] Chen, X. J.; Dobson, J. F.; Raston, C. L. Vortex fluidic exfoliation of graphite and boron nitride. Chem. Commun. **2012**, *48*, 3703.
[19] Han, W. Q.; Wu, L. J.; Zhu,Y. M.; Watanabe, K.; Taniguchi, T. Structure of chemically derived mono- and few-atomic-layer boron nitride sheets. Appl. Phys. Lett. **2008**, *93*, 223103.
[20] Gao, R.; Yin, L. W.; Wang, C. X.; Qi, Y. X.; Lun, N.; Zhang, L. Y.; Liu, Y. X.; Kang, L.; Wang, X. F. Raman scattering studies of electrically active impurities in in situ b-doped silicon nanowires: effects of annealing and oxidation. J. Phys. Chem. C **2009**, *113*, 15160.
[21] Nag, A.; Raidongia, K.; Hembram, K. P. S. S.; Datta, R.; Waghmare, U. V.; Rao, C. N. R. Graphene analogues of BN: novel synthesis and properties. ACS Nano **2010**, *4*, 1539.
[22] M. Basche, U.S. Pat., 3, 152, 006, 1964.
[23] Paffett, M. T.; Simonson, R. J.; Papin, P.; Paine, R. T. Borazine Adsorption and Decomposition at Pt(111) and Ru(001) Surfaces. *Surf. Sci.* **1990**, *232*, 286.
[24] Sutter, P.; Lahiri, J.; Albrect, P.; Sutter, E. Chemical vapor deposition and etching of high-quality monolayer hexagonal boron nitride films. *ACS Nano* **2011**, *5*, 7303.
[25] Auwarter, W.; Kreutz, T. J.; Greber, T.; Osterwalder, J. XPD and STM investigation of hexagonal boron nitride on Ni(111) Surf. Sci. **1999**, *429*, 229.
[26] Grad, G. B.; Blaha, P.; Schwarz, K.; Auwarter, W.; Greber, T. Density functional theory investigation of the geometric and spintronic structure of *h*-BN/Ni(111) in view of photoemission and STM experiments. Phys. Rev. B **2003**, *68*, 085404.
[27] Muntwiler, M.; Auwarter, W.; Baumberger, F.; Hoesch, M.; Greber, T.; Osterwalder, J. Determining adsorbate structures from substrate emission X-ray photoelectron diffraction. Surf. Sci. **2001**, *472*, 125.
[28] Rokuta, E.; Hasegawa, Y.; Suzuki, K.;Gamou, Y.; Oshima, C.; Nagashima, A. Phonon dispersion of an epitaxial monolayer film of hexagonal boron nitride on Ni(111). Phys. Rev. Lett. **1997**, *79*, 4609.
[29] Preobrajenski, A. B.; Vinogradov, A. S.; Mårtensson, N. Ni 3d–BN π hybridization at the h−BN/Ni(111) interface observed with core-level spectroscopies. Phys. Rev. B **2004**, *70*, 165404
[30] Preobrajenski, A. B.; Vinogradov, A. S.; Martensson, N. Monolayer of h-BN chemisorbed on Cu(111) and Ni(111): The role of the transition metal 3d states. Surf. Sci. 2005, **582**, 21.
[31] Usachov, D.; Adamchuk, V. K.; Haberer, D.; Grüneis, A. Sachdev, H.; Preobrajenski, A. B.; Laubschat, C.; Vyalikh, D. V. Quasifreestanding single-layer hexagonal boron nitride as a substrate for graphene synthesis. *Phys. Rev. B* **2010**, *82*, 075415.
[32] Ćavar, E.; Westerström, R.; Mikkelsen, A.; Lundgren, E.; Vinogradov, A. S.; Ng, M. L.; Preobrajenski, A. B.; Zakharov, A. A.; Mårtensson, N. A Single *h*-BN Layer on Pt(111). *Surf. Sci.* **2008**, *602*, 1722.
[33] Song, L.; Ci, L. J.; Lu, H.; Sorokin, P. B.; Jin, C. H.; Ni, J.; Kvashnin, A. G.; Kvashnin, D. G.; Lou, J.; Yakobson B. I.; Ajayan, P. M. Large scale growth and characterization of atomic hexagonal boron nitride layers. Nano Lett. **2010**, *10*, 3209.
[34] Gao, Y.; Ren, W. C.; Ma, T.; Liu, Z. B.; Zhang, Y.; Liu, W. B.; Ma, L. P.; Ma X. L.; Cheng, H. M. Repeated and controlled growth of monolayer, bilayer and few-layer hexagonal boron nitride on Pt foils. ACS Nano **2013**, *7*, 5199.
[35] Chatterjee, S.; Luo, Z. T.; Acerce, M.; Yates, D. M.; Johnson, A. T. C.; Sneddon, L. G. Chemical vapor deposition of boron nitride nanosheets on metallic substrates via decaborane/ammonia reactions Chem. Mater. **2011**, *23*, 4414.
[36] Zhang, C.; Zhao, S.; Jin, C.; Koh, A. L.; Zhou, Y.; Xu, W.; Li, Q.; Xiong, Q.; Peng, H.; Liu, Z. Direct growth of large-area graphene and boron nitride heterostructures by a co-segregation method. *Nat. Commun.* **2014**, *5*, 3193
[37] Xu, M.; Fujita, D.; Chen, H.; Hanagata, N. Formation of monolayer and few-layer hexagonal boron nitride nanosheets via surface segregation *Nanoscale* **2011**, *3*, 2854.
[38] Chhowalla, M.; Shin, H. S:; Eda, G.; Li, L.-J.; Loh, K. P.; Zhang, H. The chemistry of two-dimensional layered transition metal dichalcogenide nanosheets. *Nat. Chem.* **2013**, *5*, 263.
[39] Sipos, B.; Kusmartseva, A. F.; Akrap, A.; Berger, H.; Forró, L.; Tutiš, E. From Mott state to superconductivity in 1T-TaS_2. *Nature Mater.* **2008**, *7*, 960.
[40] Gordon, R. A.; Yang, D.; Crozier, E. D.; Jiang, D. T.; Frindt, R. F. Structures of exfoliated single layers of WS_2, MoS_2, and $MoSe_2$ in aqueous suspension. *Phys. Rev. B* **2002**, *65*, 125407.
[41] Kuc, A.; Zibouche, N.; Heine, T. Influene of quantum confinement on the electronic structure of the transition metal sulfide TS_2. *Phys. Rev. B* **2011**, *83*, 245213.

[42] Cao, T.; Wang, G.; Han, W.; Ye, H.; Zhu, C.; Shi, J.; Niu, Q.; Tan, P.; Wang, E.; Liu, B.; Feng, J. Valley-selective circular dichroism of monolayer molybdenum disulphide. *Nature Commun*. **2012**, *3*, 887.

[43] Zeng, H.; Dai, J.; Yao, W.; Xiao, D.; Cui, X. Valley polarization in MoS_2 monolayers by optical pumping. *Nature Nanotech.* **2012**, *7*, 490.

[44] Mak, K. F.; He, K.; Shan, J.; Heinz, T. F. Control of valley polarization in monolayer MoS_2 by optical helicity. *Nature Nanotech.* **2012**, *7*, 494.

[45] Kuc A. Low-dimensional transition-metal dichalcogenides. *Chemical Modelling: Volume 11*, **2014**, ***11***, 1.

[46] Wilson, J. A.; Yoffe, A. D. The transition metal dichalcogenides discussion and interpretation of optical, electrical and structural properties. *Adv. Phys.* **1969**, *18*, 193.

[47] Bissessur, R.; Kanatzidis, M. G.; Schindler, J. L.; Kannewurf, C. R. Encapsulation of polymers into MoS_2 and metal to insulator transition in metastable MoS_2. *J. Chem. Soc. Chem. Commun.* **1993**, 1582.

[48] Enyashin, A. N.; Yadgarov, L.; Houben, L.; Popov, I.; Weidenbach, M.; Tenne, R.; Bar-Sadan, M.; Seifert, G. New route for stabilization of 1T-WS_2 and MoS_2 phases. *J. Phys. Chem. C* **2011**, *115*, 24586.

[49] Mahler, B.; Hoepfner, V.; Liao, K.; Geoffrey, A. O. Colloidal Synthesis of 1T-WS_2 and 2H-WS_2 Nanosheets: Applications for Photocatalytic Hydrogen Evolution. *J. Am. Chem. Soc*. **2014**, *136*, 14121.

[50] Lin, Y.-C.; Dumcenco, D. O.; Huang, Y.-S.; Suenaga, K. Atomic mechanism of the semiconducting-to metallic phase transition in single-layered MoS_2. *Nat. Nanotech.* **2014**, *9*, 391.

[51] Mak, K. F.; Lee, C.; Hone, J.; Shan, J.; Heinz, T. F. Atomically thin MoS_2: A new direct-gap semiconductor. *Phys. Rev. Lett.* **2010**, *105*, 136805.

[52] Splendiani, A.; Sun, L.; Zhang, Y.; Li, T.; Kim, J.; Chim, C.-Y.; Galli, G.; Wang, F. Emerging photoluminescence in monolayer MoS_2. *Nano Lett.* **2010**, *10*, 1271.

[53] Tongay, S.; Zhou, J.; Ataca, C.; Lo, K.; Matthews, T. S.; Li, J.; Grossman, J. C.; Wu, J. Thermally driven crossover from indirect toward direct bandgap in 2D semiconductors: $MoSe_2$ versus MoS_2. *Nano Lett.* **2012**, *12*, 5576.

[54] Zhao, W.; Ghorannevis, Z.; Chu, L.; Toh, M.; Kloc, C.; Tan, P.-H.; Eda, G. Evolution of electronic structure in atomically thin sheets of WS_2 and WSe_2. *ACS Nano* **2013**, *7*, 791.

[55] Xiao, D.; Liu, G.-B.; Feng, W.; Xu, X.; Yao, W. Coupled spin and valley physics in monolayers of MoS_2 and other group-VI dichalcogenides. *Phys. Rev. Lett.* **2012**, 108, 196802.

[56] Suzuki, R.; Sakano, M.; Zhang, Y. J.; Akashi, R.; Morikawa, D.; Harasawa, A.; Yaji, K.; Kuroda, K.; Miyamoto, K.; Okuda, T.; Ishizaka, K.; Arita, R.; Iwasa, Y. Valley-dependent spin polarization in bulk MoS2 with broken inversion symmetry. *Nat. Nanotech.* **2014**, 9, 611.

[57] Riley, J. M.; Mazzola, F.; Dendzik, M.; Michiardi, M.; Takayama, T.; Bawden, F.; Granerød, C.; Leandersson, M.; Balasubramanian, T.; Hoesch, M.; Kim, T, K.; Takagi, H.; Meevasana, W.; Hofmann, Ph.; Bahramy, M. S.; Wells, J. W.; King, P. D. C. Direct observation of spin-polarized bulk bands in an inversion-symmetric semiconductor. *Nature Phys.* **2014**, *10*, 835.

[58] Wang, Q. H.; Kalantar-Zadeh, K.; Kis, A.; Coleman, J. N.; Strano, M. S. Electronics and opto-electronics of two-dimensional transition metal dichalcogenides. *Nature Nanotech.* **2012**, *7*, 699.

[59] Eda, G.; Fujita, T.; Yamaguchi, H.; Voiry, D.; Chen, M. W.; Chhowalla, M. Coherent atomic and electronic heterostructures of single-layer MoS_2. *ACS Nano* **2012**, *6*, 7311.

[60] Yin, Z. Li, H.; Li, H.; Jiang, L.; Shi, Y.; Sun, Y.; Lu, G.; Zhang, Q.; Chen, X.; Zhang, H. Single-layer MoS_2 phototransistors. *ACS Nano* **2012**, *6*, 74.

[61] Dines, M. B. Lithium intercalation via n-butyllithium of layered transition-metal dichalcogenides. *Mater. Res. Bull.* **1975**, *10*, 287.

[62] Benavente, E.; Santa Ana, M. A.; Mendizabal, F.; Gonzalez, G. Intercalation chemistry of molybdenum disulfide. *Coord. Chem. Rev.* **2002**, *224*, 87.

[63] Zhou, K.-G.; Mao, N.-N.; Wang, H.-X.; Peng, Y.; Zhang, H.-L. A mixed-solvent strategy for efficient exfoliation of inorganic graphene analogues. *Angew. Chem. Int. Ed.* **2011**, *50*, 10839.

[64] Wang, H.; Zhang, Q.; Yao, H.; Liang, Z.; Lee, H. W.; Hsu, P. C.; Zheng, G.; Cui, Y. High electrochemical selectivity of edge versus terrace sites in two-dimensional layered MoS_2 materials. *Nano Lett.* **2014**, *14*, 7138.

[65] Lee, H. S.; Min, S.-W.; Chang, Y.-G.; Park, M. K.; Nam, T.; Kim, H.; Kim, J. H.; Ryu, S.; Im, S. MoS_2 nanosheet phototransistors with thickness-modulated optical energy gap. *Nano Lett.* **2012**, *12*, 3695.

[66] Shi, Y.; Zhou, W.; Lu, A.-Y.; Fang, W.; Lee, Y.-H.; Hsu, A. L.; Kim, S. M.; Kim, K. K.; Yang, H. Y.; Li, L.-J.; Idrobo, J.-C.; Kong, J. van der Waals epitaxy of MoS_2 layers using graphene as growth templates. *Nano Lett.* **2012**, *12*, 2784.

[67] Liu, K.-K.; Zhang, W.; Lee, Y.-H.; Lin, Y.-C.; Chang, M.-T.; Su, C.-Y.; Chang, C.-S.; Li, H.; Shi, T.; Zhang, H.; Lai, C.-S.; Li, L.-J. Growth of large-area and highly crystalline MoS_2 thin layers on insulating substrates. *Nano Lett.* **2012**, *12*, 1538.

[68] Zhan, Y.; Liu, Z.; Najmaei, S.; Ajayan, P. M.; Lou, J. Large-area vapor-phase growth and characterization of MoS_2 atomic layers on a SiO_2 substrate. *Small* **2012**, *8*, 966.

[69] Lee, Y.-H.; Zhang, X.-Q.; Zhang, W.; Chang, M.-T.; Lin, C.-T.; Chang, H.D.; Yu, Y.-C.; Wang, J. T.-W.; Chang, C.-S.; Li, L.-J.; Lin, T.-W. Synthesis of large-area MoS_2 atomic layers with chemical vapor deposition. *Adv. Mater.* **2012**, *24*, 2320.

[70] Wang, X.; Gong, Y.; Shi, G.; Chow, W. L.; Keyshar, K.; Ye, G.; Vajtai, R.; Lou, J.; Liu, Z.; Ringe, E.; Tay, B. k.; Ajayan, P. M. Chemical vapor deposition growth of crystalline monolayer $MoSe_2$. *ACS Nano* **2014**, *8*, 5125.

[71] Zhang, Y.; Zhang, Y.; Ji, Q.; Ju, J.; Yuan, H.; Shi, J.; Gao, T.; Ma, D.; Liu, M.; Chen, Y.; Song, X.; Hwang, H. Y.; Cui, Y.; Liu, Z.;Controlled growth of high-quality monolayer WS_2 layers on sapphire and imaging its grain boundary. *ACS Nano* **2013**, *7*, 8963.

[72] Eichfeld, S. M.; Hossain, L.; Lin, Y.-C.; Piasecki, A. F.; Kupp, B.; Birdwell, A. G.; Burke, R. A.; Lu, N.; Peng, X.; Li, J.; Azcatl, A.; McDonnell, S.; Wallace, R. M.; Kim, M. J.; Mayer, T. S.; Redwing, J. M.; Robinson, J. A. Highly scalable, atomically thin WSe_2 grown *via* metal–organic chemical vapor deposition. *ACS Nano* **2015**, *9*, 2080.

[73] Boscher, N. D.; Blackman, C. S.; Carmalt, C. J.; Parkin, I. P.; Prieto. A. G. Atmospheric pressure chemical vapour deposition of vanadium diselenide thin films. *Appl. Surf. Sci.* **2007**, *253*, 6041.

[74] Peters, E. S.; Carmalt, C. J.; Parkin, I. P. Dual-source chemical vapour deposition of titanium sulfide thin films from tetrakisdimethylamidotitanium and sulfur precursors. *J. Mater. Chem.* **2004**, *14*, 3474.

[75] Walton, A. S.; Lauritsen, J. V.; Topsøe, H.; Besenbacher, F. MoS_2 nanoparticle morphologies in hydrodesulfurization catalysis studied by scanning tunneling microscopy. *J. Catal.* **2013**, *308*, 306.

[76] Sørensen, S. G.; Füchtbauer, H. G.; Tuxen, A. K.; Walton, A. S.; Lauritsen, J. V. Structure and electronic properties of *in situ* synthesized single-layer MoS_2 on a gold surface. *ACS Nano* **2014**, *8*, 6788.

[77] Fuchtbauer, H. G.; Tuxen, A. K.; Moses, P. G.; Topsøe, H.; Besenbacher, F.; Lauritsen, J. V. Morphology and atomic-scale structure of single-layer WS_2 nanoclusters. *Phys. Chem. Chem. Phys.* **2013**, ***15***, 15971.

[78] Cattelan, M.; Markman, B.; Lucchini, G.; Kumar Das, P.; Vobornik, I.; Robinson, J. A.; Agnoli, S.; Granozzi, G. New strategy for the growth of complex heterostructures based on different 2D materials *Chem. Mater.* **2015**, *27*, 4105.

[79] Wang, Y.; Li, L.; Yao, W.; Song, S.; Sun, J. T.; Pan, J.; Ren, X.; Li, C.; Okunishi, E.; Wang, Y.-Q.; Wang, E.; Shao, Y.; Zhang, Y. Y.; Yang, H.-T.; Schwier, E. F.; Iwasawa, H.; Shimada, K.; Taniguchi, M.; Cheng, Z.; Zhou, S.; Du, S.; Pennycook, S. J.; Pantelides, S. T.; Gao H.-J. Monolayer PtSe2, a new semiconducting transition-metal-dichalcogenide, epitaxially grown by direct selenization of Pt. *Nano Lett.*, **2015**, *15*, 4013.

[80] Yue, R.; Barton, A. T.; Zhu, H.; Azcatl, A.; Pena, L. F.; Wang, J.; Peng, X.; Lu, N.; Cheng, L.; Addou, R.; McDonnell, S.; Colombo, L.; Hsu, J. W. P. ; Kim, J.; Kim, M. J.; Wallace, R. M.; Hinkle, C. L. $HfSe_2$ thin films: 2D transition metal dichalcogenides grown by molecular beam epitaxy. *ACS Nano* **2015**, *9*, 474.

[81] Liu, H. J.; Jiao, L.; Xie, L.; Yang, F.; Chen, J. L.; Ho, W. K.; Gao, C. L.; Jia, J. F.; Cui, X. D.; Xie, M. H. Molecular-beam epitaxy of monolayer and bilayer WSe_2: A scanning tunnelling microscopy/spectroscopy study and deduction of exciton binding energy. *2D Materials* **2015**, *2*, 034004.

[82] Han, J. H.; Lee, S.; Cheon, J. Synthesis and structural transformations of colloidal 2D layered metal chalcogenide nanocrystals. *Chem. Soc. Rev.* **2013**, *42*, 2581.

[83] Yuan, H.; Wang, H.; Cui, Y. Two-dimensional layered chalcogenides: from rational synthesis to property control via orbital occupation and electron filling. *Acc. Chem. Res.*, **2015**, *48*, 81.

[84] Da Costa, P. G.; Dandrea, R. G.; Wallis, R. F.; Balkanski, M. First-principles study of the electronic structure of γ-InSe and β-InSe. *Phys. Rev. B* **1993**, *48*, 14135.

[85] Gürbulak, B.; Şata, M.; Dogan, S.; Duman, S.; Ashkhasi A.; Keskenler, E. F. Structural characterizations and optical properties of InSe and InSe:Ag semiconductors grown by Bridgman/Stockbarger technique. *Physica E* **2014**, *64*, 106.

[86] Dean, C. R.; Young, A. F.; Meric, I.; Lee, C.; Wang, L.; Sorgenfrei, S.; Watanabe, K.; Taniguchi, T.; Kim, P.; Shepard, K. L.; Hone, J. Boron nitride substrates for high-quality graphene electronics. *Nat. Nanotech.* **2010**, *5*, 722.

[87] Wang, H.; Liu, F.; Fu, W.; Fang, Z.; Zhuo, W.; Liu, Z. Two-dimensional heterostructures: fabrication, characterization, and application *Nanoscale*, **2014**, *6*, 12250.

[88] Yankowitz, M.; Xue, J.; Cormode, D.; Sanchez-Yamagishi, J. D.; Watanabe, K.; Taniguchi, T.; Jarillo-Herrero, P.; Jacquod, P.; LeRoy, B. J. Emergence of superlattice Dirac points in graphene on hexagonal boron nitride. *Nat. Phys.* **2012**, 8, 382.

[89] Dean, C. R.; Wang, L.; Maher, P.; Forsythe, C.; Ghahari, F.; Gao, Y.; Katoch, J.; Ishigami, M.; Moon, P.; Koshino, M.; Taniguchi, T.; Watanabe, K.; Shepard, K. L.; Hone, J.; Kim, P. Hofstadter's butterfly and the fractal quantum Hall effect in moiré superlattices. *Nature* **2013**, *497*, 598.

[90] Ponomarenko, L. A.; Gorbachev, R. V.; Yu, G. L.; Elias, D. C.; Jalil, R.; Patel, A. A.; Mishchenko, A.; Mayorov, A. S.; Woods, C. R.; Wallbank, J. R.; Mucha-Kruczynski, M.; Piot, B. A.; Potemski, M.; Grigorieva, I. V.; Novoselov, K. S.; Guinea, F.; Fal'ko, V. I.; Geim, A. K. Cloning of Dirac fermions in graphene superlattices. *Nature* **2013**, *497*, 594.

[91] Britnell, L.; Gorbachev, R. V.; Jalil, R.; Belle, B. D.; Schedin, F.; Mishchenko, A.; Georgiou, T.; Katsnelson, M. I.; Eaves, L.; Morozov, S. V.; Peres, N. M. R.; Leist, J.; Geim, A. K.; Novoselov, K. S.; Ponomarenko, L. A. Field-effect tunneling transistor based on vertical graphene heterostructures. *Science* **2012**, *335*, 947.

[92] Britnell, L.; Ribeiro, R. M.; Eckmann, A.; Jalil, R.; Belle, B. D.; Mishchenko, A.; Kim, Y.-J.; Gorbachev, R. V.; Georgiou, T.; Morozov, S. V.; Grigorenko, A. N.; Geim, A. K.; Casiraghi, C.; Neto, A. H. C.; Novoselov, K. S. Strong light-matter interactions in heterostructures of atomically thin films *Science* **2013**, *340*, 1311.

[93] Georgiou, T.; Jalil, R.; Belle, B. D.; Britnell, L.; Gorbachev, R. V.; Morozov, S. V.; Kim, Y.-J.; Gholinia, A.; Haigh, S. J.; Makarovsky, O.; Eaves, L.; Ponomarenko, L. A.; Geim, A. K.; Novoselov, K. S.; Mishchenko, A. Vertical field-effect transistor based on graphene-WS_2 heterostructures for flexible and transparent electronics. *Nature Nanotech.* **2013**, *8*, 100.

[94] Hunt, B.; Sanchez-Yamagishi, J. D.; Young, A. F.; Yankowitz, M.; LeRoy, B. J.; Watanabe, K.; Taniguchi, T.; Moon, P.; Koshino, M.; Jarillo-Herrero, P.; Ashoori, R. C. Massive Dirac fermions and Hofstadter butterfly in a van der Waals heterostructure *Science* **2013**, *340*,1427.

[95] Geim, A. K.; Grigorieva, I. V. Van der Waals heterostructures. *Nature* **2013**, *499*, 419.

[96] Fan, X.; Shen, Z.; Liu, A. Q.; Kuo, J.-L. Band gap opening of graphene by doping small boron nitride domains. *Nanoscale*, **2012**, *4*, 2157.

[97] Chang, C.-K.; Kataria, S.; Kuo, C.-C.; Ganguly, A.; Wang, B.-Y.; Hwang, J.-Y.; Huang, K.-J.; Yang, W.-H.; Wang, S.-B.; Chuang, C.-H.; *et al.* Band Gap Engineering of Chemical Vapor Deposited Graphene by in Situ BN Doping. *ACS Nano* **2013**, *7*, 1333.

[98] Muchharla, B.; Pathak, A.; Liu, Z.; Song, L.; Jayasekera, T.; Kar, S.; Vajtai, R.; Balicas, L.; Ajayan, P. M.; Talapatra, S.; *et al.* Tunable Electronics in Large-Area Atomic Layers of Boron–Nitrogen–Carbon. *Nano Lett.* **2013**, *13*, 3476.

[99] Fiori, G.; Betti, A.; Bruzzone, S.; Iannaccone, G. Lateral Graphene–hBCN heterostructures as a platform for fully two-dimensional transistors. *ACS Nano*, **2012**, *6*, 2642.

[100] Levendorf, M.P.; Kim, C.-J.; Brown, L.; Huang, P.Y.; Havener, R.W.; Muller, D.A.; Park, J. Graphene and boron nitride lateral heterostructures for atomically thin circuitry. *Nature* **2012**, *488*, 627.

[101] Liu, Z.; Ma, L.; Shi, G.; Zhou, W.; Gong, Y.; Lei, S.; Yang, X.; Zhang, J.; Yu, J.; Hackenberg, K. P.; Babakhani, A.; Idrobo, J.-C.; Vajtai, R.; Lou, J.; Ajayan, P. M. In-plane heterostructures of graphene and hexagonal boron nitride with controlled domain sizes. *Nat. Nanotech.*, **2013**, *8*, 119.

[102] Liu, M.; Li, Y.; Chen, P.; Sun, J.; Ma, D.; Li, Q.; Gao, T.; Gao, Y.; Cheng, Z.; Qiu, X.; Fang, Y.; Zhang, Y.; Liu, Z. Quasi-Freestanding Monolayer Heterostructure of graphene and hexagonal boron nitride on Ir(111) with a zigzag boundary. *Nano Lett.* **2014**, *14*, 6342.

[103] Liu, L.; Park, J.; Siegel, D. A.; McCarty, K. F.; Clark, K. W.; Deng, W.; Basile, L.; Idrobo, J. C.; Li, A.-P.; Gu, G. Heteroepitaxial growth of two-dimensional hexagonal boron nitride templated by graphene edges. *Science* **2014**, *343*, 163.

[104] Butler, S. Z.; Hollen, S. M.; Cao, L.; Cui, Y.; Gupta, J. A.; Gutierrez, H. R.; Heinz, T. F.; Hong, S. S.; Huang, J.; Ismach, A. F.; Johnston-Halperin, E.; Kuno, M.; Plashnitsa, V. V.; Robinson, R. D.; Ruoff, R. S.; Salahuddin, S.; Shan, J.; Shi, L.; Spencer, M. G.; Terrones, M.; Windl, W.; Goldberger, J. E. Progress, challenges, and opportunities in two-dimensional materials beyond graphene *ACS Nano*, **2013**, *7*, 2898.

[105] Rao, C.; Ramakrishna Matte, H.; Maitra, U. Graphene analogues of inorganic layered materials *Angew. Chem.*, **2013**, *52*, 13162.

[106] Xu, X.; Liang, T.; Shi, M.; Chen, H. Graphene-like two-dimensional materials *Chem. Rev.* **2013**, *113*, 3766.

[107] Sutter, P.; Cortes, R.; Lahiri, J.; Sutter, E. Interface formation in monolayer graphene-boron nitride heterostructures. *Nano Lett.* **2012**, *12*, 4869.

[108] Phark, S.; Borme, J.; Vanegas, A. L.; Corbetta, M.; Sander, D.; Kirschner, J. Scanning tunneling spectroscopy of epitaxial graphene nanoisland on Ir(111) *Nanoscale Res. Lett.* **2012**, *7*, 1.

[109] Huang, C.; Wu, S.; Sanchez, A. M.; Peters, J. J. P.; Beanland, R.; Ross, J. S.; Rivera, P.; Yao, W.; Cobden, D. H.; Xu, X. Lateral heterojunctions within monolayer MoSe2–WSe2 semiconductors. *Nat. Mater.* **2014**, *13*, 1096

[110] Zhang, X.-Q.; Lin, C.-H.; Tseng, Y.-W.; Huang, K.-H.; Lee, Y.-H. Synthesis of lateral heterostructures of semiconducting atomic layers *Nano Lett.* **2015**, *15*, 410.

[111] Gong, Y.; Lin, J.; Wang, X.; Shi, G.; Lei, S.; Lin, Z.; Zou, X.; Ye, G.; Vajtai, R.; Yakobson, B. I.; Terrones, H.; Terrones, M.; Tay, B. K.; Lou, J.; Pantelides, S. T.; Liu, Z.; Zhou, W.; Ajayan, P. M. Vertical and in-plane heterostructures from WS_2/MoS_2 monolayers. *Nat. Mater.* **2014**, *13*, 1135.

[112] Mahjouri-Samani, M.; Lin, M. W.; Wang, K.; Lupini, A. R.; Lee, J.; Basile, L.; Boulesbaa, A.; Rouleau, C. M.; Puretzky, A. A.; Ivanov, I. N.; Xiao, K.; Yoon, M.; Geohegan, D. B. Patterned arrays of lateral heterojunctions within monolayer two-dimensional semiconductors *Nat. Commun.* **2015**, *6*, 7749

[113] Fang, H.; Battaglia, C.; Carraro, C.; Nemsak, S.; Ozdol, B.; Kang, J. S.; Bechtel, H. A.; Desai, S. B.; Kronast, F.; Unal, A. A. M.; Conti, G.; Conlon, C.; Palsson, G. K.; Martin, M. C.; Minor, A. M.; Fadley, C. S.; Yablonovitch, E.; Maboudian, R.; Javey, A. Strong interlayer coupling in van der Waals heterostructures built from single-layer chalcogenides. *Proc. Natl. Acad. Sci. U S A.*, **2014**, *111*, 6198.

[114] Deng, Y.; Luo, Z.; Conrad, N. J.; Liu, H.; Gong, Y.; Najmaei, S.; Ajayan, P. M.; Lou, J.; Xu, X.; Ye, P. D. Black phosphorus–monolayer MoS_2 van der Waals heterojunction p–n diode *ACS Nano*, **2014**, *8*, 8292.

[115] Gillgren, N.; Wickramaratne, D.; Shi, Y.; Espiritu, T.; Yang, J.; Hu, J.; Wei, J.; Liu, X.; Mao, Z.; Watanabe, K.; Taniguchi, T.; Bockrath, M.; Barlas, Y.; Lake, R. K.; Lau, C. N. Gate tunable quantum oscillations in air-stable and high mobility few-layer phosphorene heterostructures *2D Mater*, **2015**, *2*, 011001.

[116] Bae, S.; Kim, H.; Lee, Y.; Xu, X.; Park, J.-S.; Zheng, Y.; Balakrishnan, J.; Lei, T.; Kim, H. R.; Song, Y. I.; Kim, Y.-J.; Kim, K. S.; Özyilmaz, B.; Ahn, J.-H.; Hong, B. H.; Iijima, S. Roll-to-roll production of 30-inch graphene films for transparent electrodes *Nat. Nanotechnol.* **2010**, *5*, 574.

[117] Chiu, M.-H.; Zhang, C.; Shiu, H.-W.; Chuu, C.-P.; Chen, C.-H.; Chang, C.-Y. S.; Chen, C.-H.; Chou, M.-Y.; Shih, C.-K.; Li, L.-J. Determination of band alignment in the single-layer MoS_2/WSe_2 heterojunction *Nat. Commun.* **2015**, *6*, 7666.

[118] Tongay, S.; Fan, W.; Kang, J.; Park, J.; Koldemir, U.; Suh, J.; Narang, D. S.; Liu, K.; Ji, J.; Li, J.; Sinclair, R.; Wu, J. Tuning interlayer coupling in large-area heterostructures with CVD grown MoS_2 and WS_2 monolayers. *Nano Lett.* **2014**, *14*, 3185.

[119] Liu, Z.; Song, L.; Zhao, S.; Huang, J.; Ma, L.; Zhang, J.; Lou, J.; Ajayan, P. M. Direct growth of graphene/hexagonal boron nitride stacked layers *Nano Lett.*, **2011**, *11*, 2032.

[120] Yan, Z.; Peng, Z.; Sun, Z.; Yao, J.; Zhu, Y.; Liu, Z.; Ajayan, P. M.; Tour, J. M. Growth of bilayer graphene on insulating substrates *ACS Nano*, **2011**, *5*, 8187.

[121] Roth, S.; Matsui, F.; Greber, T.; Osterwalder, J. Chemical vapor deposition and characterization of aligned and incommensurate graphene/hexagonal boron nitride heterostack on Cu(111) *Nano Lett.* **2013**, *13*, 2668.

[122] Garcia, J. M.; Wurstbauer, U.; Levy, A.; Pfeiffer, L. N.; Pinczuk, A.; Plaut, A. S.; Wang, L.; Dean, C. R.; Buizza, R.; van der Zande, A. M.; Hone, J.; Watanabe, K.; Taniguchi, T. Graphene growth on h-BN by molecular beam epitaxy *Solid State Commun*, **2012**, *152*, 975.

[123] Lin, T.; Wang, Y.; Bi, H.; Wan, D.; Huang, F.; Xie, X.; Jiang, M. Hydrogen flame synthesis of few-layer graphene from a solid carbon source on hexagonal boron nitride. *J. Mater. Chem.*, **2012**, *22*, 2859.

[124] Lin, T.; Liu, Z.; Zhou, M.; Bi, H.; Zhang, K.; Huang, F.; Wan, D.; Zhong, Y. Rapid microwave synthesis of graphene directly on *h*-BN with excellent heat dissipation performance *ACS Appl. Mater. Interfaces*, **2014**, *6*, 3088.

[125] Sutter, P.; Lahiri, J.; Zahl, P.; Wang, B.; Sutter, E. Scalable synthesis of uniform few-layer hexagonal boron nitride dielectric films *Nano Lett.*, **2012**, *13*, 276.

[126] Gao, G.; Gao, W.; Cannuccia, E.; Taha-Tijerina, J.; Balicas, L.; Mathkar, A.; Narayanan, T. N.; Liu, Z.; Gupta, B. K.; Peng, J.; Yin, Y.; Rubio, A.; Ajayan, P. M. Artificially stacked atomic layers: toward new van der Waals solids *Nano Lett*, 2012, **12**, 3518.

[127] Koma, A.; Sunouchi, K.; Miyajima, T. Fabrication of ultrathin heterostructures with van der Waals epitaxy *J. Vac. Sci. Technol. B* **1985**, *3*, 724.

[128] Yu, Y.; Hu, S.; Su, L.; Huang, L.; Liu, Y.; Jin, Z.; Purezky, A. A.; Geohegan, D. B.; Kim, K. W.; Zhang, Y. Equally efficient interlayer exciton relaxation and improved absorption in epitaxial and nonepitaxial MoS_2/WS_2 heterostructures *Nano Lett.*, **2015**, *15*, 486

[129] Lin, Y.-C.; Lu, N.; Perea-Lopez, N.; Li, J.; Lin, Z.; Peng, X.; Lee, C. H.; Sun, C.; Calderin, L.; Browning, P. N.; Bresnehan, M. S.; Kim, M. J.; Mayer, T. S.; Terrones, M.; Robinson, J. A. Direct Synthesis of van der Waals Solids. *ACS Nano*, **2014**, *8*, 3715.

[130] Lin, Y.-C.; Chang, C.-Y. S.; Ghosh, R. K.; Li, J.; Zhu, H.; Addou, R.; Diaconescu, B.; Ohta, T.; Peng, X.; Lu, N.; Kim, M. J.; Robinson, J. T.; Wallace, R. M.; Mayer, T. S.; Datta, S.; Li, L.-J.; Robinson, J. A. Robinson, J. A. Atomically thin heterostructures based on single-layer tungsten diselenide and graphene. *Nano. Lett.* **2014**, 14, 6936.

[131] Shin, H.-C.; Jang, Y.; Kim, T.-H.; Lee, J.-H.; Oh, D.-H.; Ahn, S. J.; Lee, J. H.; Moon, Y.; Park, J.-H.; Yoo, S. J.; Park, C.-Y.; Whang, D.; Yang, C.-W.; Ahn, J. R. Epitaxial growth of a single-crystal hybridized boron nitride and graphene layer on a wide-band gap semiconductor *J. Am. Chem. Soc.*, **2015**, *137*, 6897.

[132] Dang, W.; Peng, H.; Li, H.; Wang, P.; Liu, Z. Epitaxial heterostructures of ultrathin topological insulator nanoplate and graphene *Nano Lett.*, **2010**, *10*, 2870.

3.1. *In-situ* growth of 2D heterostructures

The following two sections present a detailed investigation of the growth 2D heterostructures synthesized by an innovative protocol completely under UHV conditions. To produce such structures we used bottom-up route that, as explained in the paragraph "2D materials heterostructures" of the previous section 3, allows the creation of both *in-plane* and stacked heterojunctions.

For the *in-plane* heterostructure we decided to use two very similar materials as G and *h*-BN, which can be stitched seamlessly because of their very similar structure forming a new hybrid structure called *h*-BNG. To synthesize this ternary atomic crystal we did not follow the usual approach in the literature that involves complex step by step procedure,[1,2,3,4,5] i.e. the growth of a fully covering G followed by hydrogen etching and *h*-BN deposition.[2]

On the contrary, we optimize a simple one-step procedure able to produce this heterostructure in a rather simple way using a single precursor.[6] The innovative procedure is explained in the section 3.1.1 where we characterize this material by using a combination of Surface Science techniques.

The investigation of stacked heterostructures is the focus of the section 3.1.2. In this case, the choice of the possible materials constituting the composite systems is wider because we were not forced to use structurally similar nanosheets that could connect seamlessly at the atomic level.

For our first heterostructure we explored the synthesis of WS_2 on *h*-BN and on gold. The synthesis has been performed by a multistep procedure,[7] the UHV conditions ensured the interface cleanness[8] and that the component materials are not oxidized by air exposure. In 3.1.2 is also presented the heterostructure composed by WSe_2 and G, which is our most recent result.

Differently from the synthesis of *h*-BNG, which required a careful choice of the precursor and of the growth conditions,[6] the synthesis of stacked heterostructures[7] is much more robust and versatile route. As an example we report to prototypical systems WS_2/*h*-BN and WSe_2/G, nevertheless from the description of the synthesis protocol it will be obvious that this method can be easily extended to arbitrary TMDs and other two dimensional nanosheets.

References

1 Liu, M.; Li, Y.; Chen, P.; Sun, J.; Ma, D.; Li, Q.; Gao, T.; Gao, Y.; Cheng, Z.; Qiu, X.; Fang, Y.; Zhang, Y.; Liu, Z. Quasi-Freestanding Monolayer Heterostructure of graphene and hexagonal boron nitride on Ir(111) with a zigzag boundary. *Nano Lett.* **2014**, *14*, 6342.

2 Liu, L.; Park, J.; Siegel, D. A.; McCarty, K. F.; Clark, K. W.; Deng, W.; Basile, L.; Idrobo, J. C.; Li, A.-P.; Gu, G. Heteroepitaxial growth of two-dimensional hexagonal boron nitride templated by graphene edges. *Science* **2014**, *343*, 163.

3 Ci, L.; Song, L.; Jin, C.; Jariwala, D.; Wu, D.; Li, Y.; Srivastava, A.; Wang, Z. F.; Storr, K.; Balicas, L.; *et al.* Atomic Layers of Hybridized Boron Nitride and Graphene Domains. *Nat. Mater.* **2010**, 9, 430–435.

[4] Muchharla, B.; Pathak, A.; Liu, Z.; Song, L.; Jayasekera, T.; Kar, S.; Vajtai, R.; Balicas, L.; Ajayan, P. M.; Talapatra, S.; *et al.* Tunable Electronics in Large-Area Atomic Layers of Boron–Nitrogen–Carbon. *Nano Lett.* **2013**, *13*, 3476.

[5] Gong, Y.; Shi, G.; Zhang, Z.; Zhou, W.; Jung, J.; Gao, W.; Ma, L.; Yang, Y.; Yang, S.; You, G.; *et al.* Direct Chemical Conversion of Graphene to Boron- and Nitrogen- and Carbon-Containing Atomic Layers. *Nat. Commun.,* **2014**, *5*, 3193.

[6] Nappini, S.; Píš, I.; Menteş, O. T.; Sala, A.; Cattelan, M.; Agnoli, S.; Bondino, F.; Magnano, E. Formation of a quasi-free-standing single layer of graphene and hexagonal boron nitride on Pt(111) by a single molecular precursor. *Adv. Funct. Mater.* DOI: 10.1002/adfm.201503591

[7] Cattelan, M.; Markman, B.; Lucchini, G.; Kumar Das, P.; Vobornik, I.; Robinson, J. A.; Agnoli, S.; Granozzi, G. New strategy for the growth of complex heterostructures based on different 2D materials *Chem. Mater.* **2015**, *27*, 4105.

[8] Haigh, S. J.; Gholinia, A.; Jalil, R.; Romani, S.; Britnell, L.; Elias, D. C.; Novoselov, K. S.; Ponomarenko, L. A.; Geim, A. K.; Gorbachev, R. Cross-sectional imaging of individual layers and buried interfaces of graphene-based heterostructures and superlattices. *Nat. Mater.* **2012**, *11*, 764.

3.1.1. Graphene and *h*-BN *in-plane* heterostructure

Introduction

In the section 3 a variety of 2D materials and heterostructures have been presented, for the *in-plane* heterostructure the one composed by *h*-BN and G has been presented as one of the most studied. As mentioned before these two materials owing to the same structure, but very different carrier mobility can find application for future electronics devices, e.g. building 2D atomic-layer circuits[1,2,3] or magnetic nanostructures at the *h*-BN/G interface,[4] tailoring the semiconducting properties of G and engineering the band gap.[5,6,7,8]

As stated above, up to now, *h*-BN stitched *in-plane* with G hybrid structures has been obtained by using CVD starting from two or three precursors[5,6,7] plasma-assisted deposition, mechanical transfer or a two-step process consisting in the growth of *h*-BN on existing G patches[9,10,11,12] or the growth of G on h-BN patches created by etching reaction.[13]

In this section it is presented a novel bottom-up approach to obtain continuous *in-plane* heterostructures combining *h*-BN and G within the same 2D sheet, called *h*-BNG, on single crystals under UHV conditions by using only one molecular precursor, dimethylamine borane (DMAB).[14] This novel growth route allows an easy and controlled preparation of a continuous almost freestanding layer with G, *h*-BN and doped G domains by dehydrogenation of DMAB on Pt(111). This method can be potentially used for band gap engineering and applications in devices. The temperature is the principal parameter to selectively grow the *h*-BNG layer in competition with defective B-C-N layers on the clean crystal surface.

The system has been investigated by high resolution core-level XPS, TPD, LEEM combined to x-ray PEEM (XPEEM) and micro LEED.

Experimental section

Sample preparation

For the preparation of the Pt(111) single crystal see "Experimental section" of the section 2.1.1.

Methods

XPS measurements were acquired at the CNR-BACH beamline at synchrotron Elettra (Trieste, Italy), by the group of Dr. F. Bondino, on *in-situ* prepared sample. The total energy resolution for XPS from core levels was set to 0.2 eV.

LEEM and XPEEM measurements were performed at the beamline Nanospectroscopy at synchrotron Elettra (Trieste, Italy), by Dr. A. Sala and Dr. O. T. Menteş, on *ex-situ* samples after an annealing at 350 °C in UHV. The LEEM, equipped with an energy filter, was used in both bright and dark-field (BF and DF) mode using the first or secondary order diffraction beam for imaging, respectively. The microscope lateral resolution approaches a few tens of nanometres; energy resolution is better than 0.3 eV. Using micro-LEED the probed area is about 2 μm in diameter.

For the details of the TPD experiments the reader is referred to the section 2.1.2. All the desorption experiments were performed dosing 12 L of CO (1.3×10^{-7} mbar for 2 minutes) at 150 K and heating using a linear temperature ramp (2.0 K/s) to 600 K.

Results and discussion

Dimethylamine borane decomposition at high temperature

In our TPD-XPS facility we have tried several growth dosing DMAB on Pt(111) at different substrate temperature, in order to fully understand the dynamic of G and *h*-BN formation on this substrate. These preliminary results have been confirmed and further analysed by the staff of CNR-BACH and Nanospectroscopy beamlines at Elettra synchrotron. In this paragraph the most interesting results for the growth at 1000 K, whereas some results of the DMAB decomposition at lower temperatures are briefly reported in another dedicated paragraph.

DMAB (Sigma Aldrich, 97.0%), purified by several cool-pump-heat cycles, was dosed (150 L, 6.65×10^{-7} mbar for 300 s) via a leak valve from a flanged glass tube kept at 41°C on the Pt substrate held at 1000 K.

In this conditions the LEED pattern (Figure 1) is characterized by the principal hexagonal Pt(111) (1×1) diffraction spots surrounded by sharp non-integer moiré satellites and an arc-shaped diffraction pattern rotated by 30° from the (1×1) Pt diffraction spots.

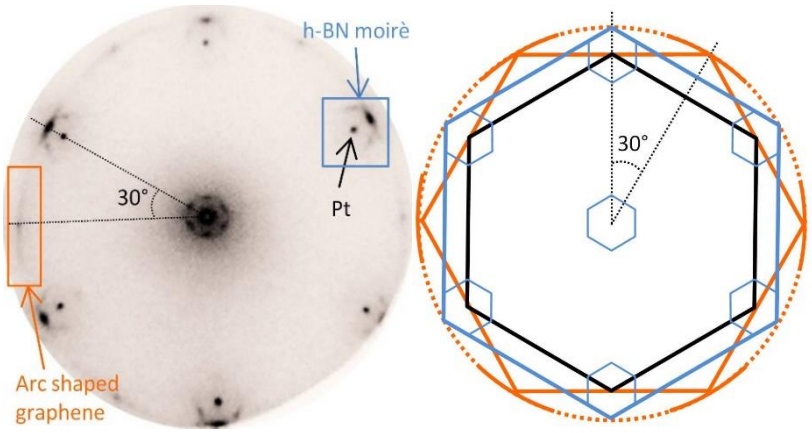

Figure 1. Left panel: LEED pattern of h-BNG layer on Pt(111) at 1000 K recorded with electron energy (E= 60 eV). h-BN moiré, G and Pt spots are identified by the corresponding labels. The distortion is due to imperfect diffraction imaging conditions in our instrument.

Right panel: scheme of the LEED pattern; black hexagon represents the first-order diffraction of Pt(111) substrate, the yellow circle is due to the first-order diffraction of graphene domains, with a preferential distribution (solid orange curves) around the 30° rotated domains (orange hexagon), the light blue hexagons represent the h-BN first-order diffraction and h-BN moiré. Reprinted from Ref. [14] © 2015 Wiley.

The moiré satellites appear as a hexagonal network of diffraction spots external to the substrate pattern and with identical orientation. The distance ratio between first order substrate reflections and external hexagonal-network spots is approximately 9:10. An analogous superstructure was also reported for *h*-BN/Pt(111) layer obtained by borazine decomposition at comparable temperature of the substrate (see Figure 4 of the section "Other 2D materials and heterostructures").[15,16] This similarity suggests

that the moiré satellites can be ascribed to the presence of long-range-ordered domains of *h*-BN aligned with the substrate lattice. The arc-shaped diffraction pattern centred at 30° from the Pt (1×1) spots is associated with the formation of G domains with different azimuthal orientations in agreement with other works reporting G growth on Pt(111) at the same temperature.[17,18]

The local order of the *in-plane h*-BNG layer grown on Pt(111) was investigated by LEEM and micro-LEED. The presence of an *in-plane* heterostructure is revealed by LEEM micrographs in BF that show a clear image contrast (see Figure 2 a and a'). The BF LEEM images (Figure 2 a and a') show darker and brighter complementary areas that identify the presence of two phases on the sample. The two regions display different electron reflectivity curves at low electron energy pointing to distinct structures. As we will show later, one area corresponds to G, whereas the other to *h*-BN.

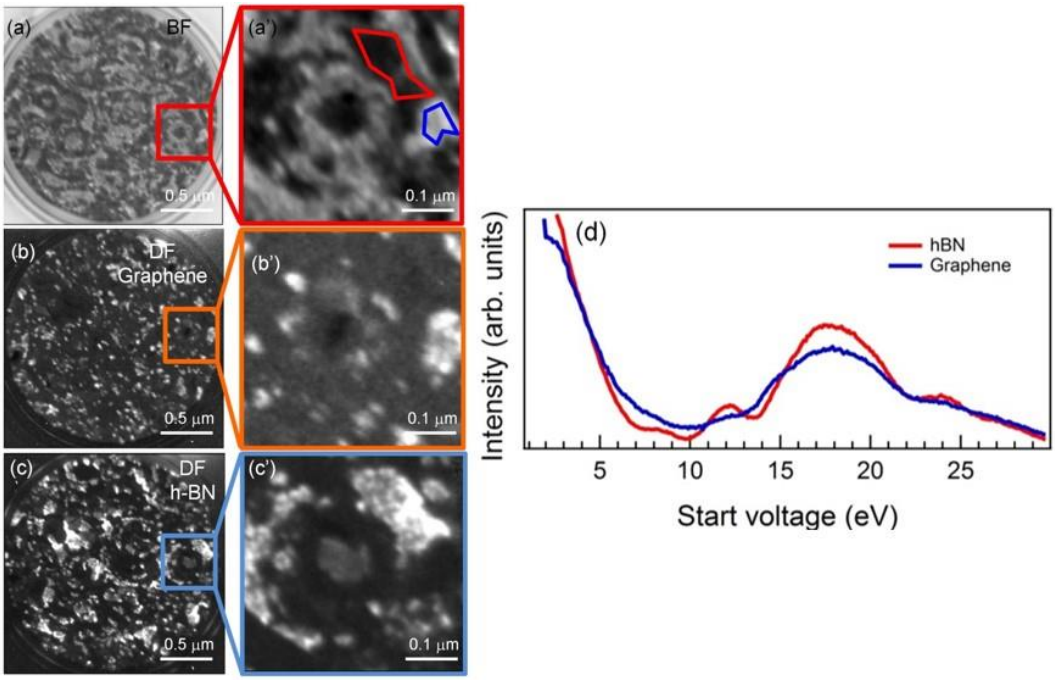

Figure 2. LEEM images of h-BNG layer on Pt(111) at 1000 K. (a) BF LEEM at V_{start} = 6 eV. The red square indicates the zoomed area (a'). (b) DF LEEM image using the graphene first-order diffraction spot of 30° rotated domains (V_{start} =35 eV). The orange square indicates the zoomed area (b'). (c) Dark Field LEEM image using the h-BN first-order diffraction (V_{start} =35 eV). The light blue square indicates the zoomed area (c'). (d) LEED (I-V) characteristics obtained from a stack of LEEM images with electron energy from 2 to 30 eV at the locations marked in (a'). Reprinted from Ref. [14] © 2015 Wiley.

DF LEEM was used to correlate the LEED pattern to real space surface structure. Representative DF images obtained using the first order of diffraction of *h*-BN and G spots are reported in Figure 2 (b, c, b',c'). In contrast to BF, DF LEEM is sensitive to the rotational alignment. DF image measured selecting the *h*-BN first-diffraction order spot show many bright irregularly shaped areas of a few hundred nm size. In the DF image taken on the centre of the G ring-like spot (at 30° from the first-order Pt diffraction spots) smaller bright regions are observed. The two DF images are only partially complementary. This is more evident by the comparison of the zoomed images Figure 2 b' and c' where the inversion of contrast is not total. This is not surprising considering that G domains have different azimuthal orientations, as it is evident from the ring-like LEED pattern. On the contrary, the BF (Figure 2a and a') and DF images on *h*-BN (Figure

2c and c') display a contrast inversion. This is a confirmation of almost identical azimuthal orientation of all the *h*-BN domains with respect to the substrate lattice as derived from the moiré satellites spots observed in the LEED pattern.

High-resolution photoemission spectra provide important indication about the *h*-BNG heterostructure formation, the strength of the interaction of this layer with the substrate and between *h*-BN and G domains. The Pt $4f_{7/2}$ and C 1s photoemission spectra were fitted with Doniach-Šunjić line shapes convoluted with Gaussian function. The other photoemission spectra were decomposed into the spectral components using Voigt functions. A Shirley type background was subtracted from Pt $4f_{7/2}$, C 1s and N 1s spectra and a linear background from the B 1s spectrum.

Both N 1s and B 1s spectra display slightly asymmetric peak shapes (Figure 3). This asymmetric peak shape has been fitted by two components, a main peak at 189.7 eV and 397.3 eV for N 1s and B 1s, respectively and a second weaker component at a BE of 190.1 eV and 397.9 eV, respectively. The presence of very similar components in B 1s and N 1s core levels was also observed in *h*-BN/Pt(111) layers and, in this case, the presence of the weak components at higher BE was assigned to a small geometrical corrugation of the *h*-BN domains produced by different interaction of the N and B atoms with the Pt(111) substrate when they are placed on different atomic sites.[19]

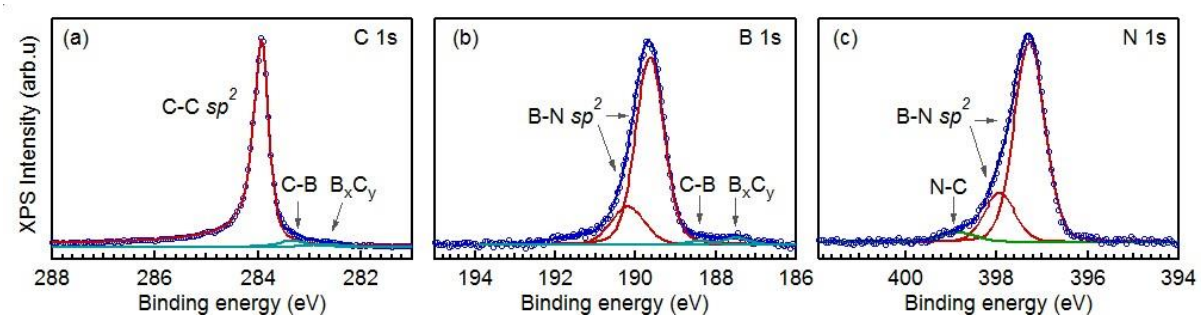

Figure 3. C 1s (a), B 1s (b), and N 1s (c) high-resolution XPS spectra of the h-BNG layer prepared on the Pt(111) substrate at a temperature of 1000 K, hv=520 eV. Reprinted from Ref. [14] © 2015 Wiley.

The N 1s spectrum exhibits also a third weak component at a BE of 398.9 eV (Figure 3c) that has been related to N-C bonds which can probably come from the *h*-BN and G boundaries or G defects. In the B 1s spectrum (Figure 3b), traces of B–C bonds can be found at lower BEs. Two weak components at 188.4 eV and 187.5 eV can be attributed to B-doping in carbon nanoparticles or G[20] or B–C bonds at the *h*–BN-G boundaries[5] and to nonstoichiometric B_xC_y boron carbide.[20,21] Corresponding B–C components in C 1s spectrum are present at 283.4 and 282.6 eV, respectively (Figure 3a). Their contribution to the whole C 1s peak is 3%. The C 1s spectrum is dominated by a sharp peak at 283.9 eV BE assigned to sp^2 hybridized C atoms in G.[22] A component in C 1s spectra related to the N–C bonds is also likely present, but it is obscured by the tail of the asymmetric Doniach-Šunjić line shape of the main peak. The components assigned to C-B and C-N bonds can be also related to the presence of heteroatoms in G and C atoms in *h*-BN.[23]

The film stoichiometric has been calculated from the area of the C, N and B photoemission lines, acquired by a conventional XPS setup, normalized by their photoemission cross section (the inelastic mean fee path of the electron can be

neglected for the 2D nature of *h*-BNG). Dosing DMAB at 1000 K the surface is covered about at 70 % of G and the remaining to *h*-BN. The *h*-BNG composition do not respect the ratio of the atoms in DMAB (C 50 %, N and B 25 %) likely because the lower absorption energy of NH_3 and BH_3 with respect to CH_3 moieties,[24] increase the probability of the formation of G with respect to *h*-BN.

By measuring the Pt 4*f* emission at high-energy resolution, information about the strength of the chemical interaction at the Pt interface with the *h*-BNG layer can be accessed. For clean metals, the lower coordination of the atoms at the surface leads to a different Pt $4f_{7/2}$ core-level BE components compared to the bulk. This can be observed in Figure 4 where the Pt $4f_{7/2}$ spectrum measured on clean Pt(111) (Figure 4a) can be deconvoluted in two components, one centred at 70.90 eV (Pt bulk atoms), a second shifted by 0.40 eV towards lower BE (Pt surface atoms), in good agreement with the literature.[25,26,27]

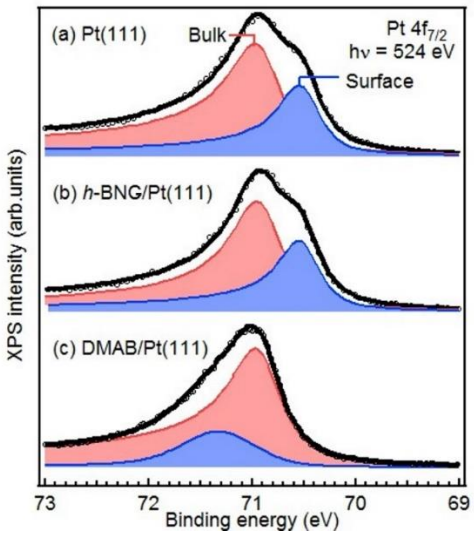

Figure 4. Pt $4f_{7/2}$ photoemission spectra of (a) the clean Pt(111) surface, (b) surface covered by the h-BNG layer, and (c) Pt surface exposed to DMAB at RT. The spectra were decomposed into components corresponding to photoemission from bulk and surface top-most platinum atoms. Reprinted from Ref. [14] © 2015 Wiley.

Upon exposure to DMAB molecules with the substrate at room temperature, the surface component is completely reduced, whereas a new peak at 71.30 eV appears (Figure 4c). The large shift of the surface component to higher BEs value implies a strong interaction of Pt with the DMAB adsorbate. On the contrary, after the formation of the *h*-BNG layer at 1000 K, the Pt $4f_{7/2}$ spectrum can be fitted well with the same peak components as in the case of clean Pt(111) surface (Figure 4b). This is indicative of a very weak interaction and suggests that the *h*-BNG layer is almost freestanding on the Pt(111) surface.

XPEEM measurements of the Pt 4*f*, C 1*s*, B 1*s* and N 1*s* core level (Figure 5a, b, c, d) confirm that the substrate is continuously covered by *h*-BN and G regions. In fact, a total inverted contrast in the XPEEM images of B 1s and N 1s images with respect to C 1*s* ones can be observed, while the image obtained with Pt $4f_{7/2}$ shows uniform intensity over the entire area.

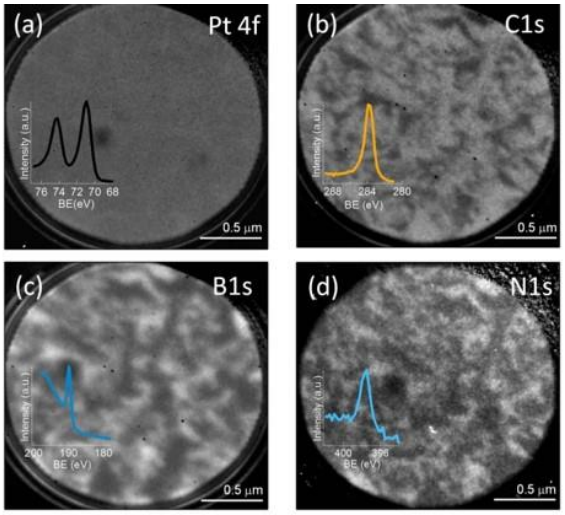

Figure 5. XPEEM images at the (a) Pt $4f_{7/2}$, (b) C1s, (c) B 1s and (d) N1s core levels. Pt 4f and B 1s were recorded using a photon energy of 260 eV, N 1s and C 1s using a photon energy of 520 eV. The inset on bottom left of each image is the core level spectrum obtained by integrating the signal on the whole field of view through a stack of XPEEM images measured at different kinetic energy of the photoemitted electrons. Adapted from Ref. [14] © 2015 Wiley.

XPEEM measurements of the Pt $4f_{7/2}$ core level (Figure 5a) indicate that, within the lateral resolution of the instrument, all the Pt surface is covered by single layer *h*-BNG, without any bi- or multi-layer domains. This conclusion is further supported by the energy-dependent low energy electron reflectivity measurements in the real space (LEED I-V data shown in Figure 2d) measured on G and *h*-BN domains separately.

The existence of a continuous layer without uncovered Pt atoms is supported by TPD measurements as done in section 2.1.2. CO desorption spectra recorded after 12 L of CO exposure at 150 K, show no CO desorption peak for *h*-BNG up to 600 K, whereas for Pt(111) there is a clear desorption peak centred at 360 K (see Figure 6). This indicates that the Pt(111) substrate is perfectly covered by the composite layer[28] and possible phase boundaries must be continuous at atomic level and do not present significant voids exposing Pt sites.

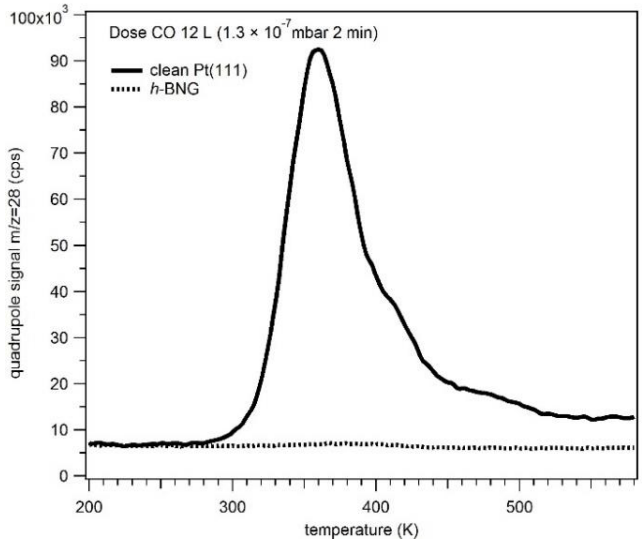

Figure 6. TPD desorption spectra of 12 L CO (1.3×10^{-7} mbar 2 min) dosed at 150 K on clean Pt(111) (solid curve) and on h-BNG (dotted curve). Reprinted from Ref. [14] © 2015 Wiley.

To demonstrate the oxidation resistance of *h*-BNG, C 1s, N 1s and B 1s core levels were acquired after exposing the layer to a partial pressure of O_2 (up to 5×10^{-6} mbar for 200 s) at different temperatures of the substrate (300 K, 500 K, 600 K) and no changes have been observed (not shown). This indicates that the *h*-BNG layer is chemically inert as G and *h*-BN *per se*.

In the literature the atomic continuity of the *h*-BN and G domains in *h*-BNG has been investigated on a local basis by STM.[9,11,12,29] An atomic scale characterization allows the identification of single dopants, i.e. N and B atoms in G and C atoms in *h*-BN, and a detailed description of the boundary between the two materials. As studied for G/Ni(111),[30] the boundaries of 2D materials can be interesting for a technologic point of view because the one dimensional defect lines, produced by the stitching of mismatched 2D sheets, have peculiar electronic features (see Figure 4 of the section 2).

As reported in the section 3 in the previous STM investigations,[9,11,12,29] *h*-BNG has been always synthesized by step procedures, i.e. the synthesis of submonolayer coverage of G (or *h*-BN) is followed by the growth of the second 2D layer. The border of the first layer acts as template for the second and the continuity of hexagonal lattice is maintained from G and *h*-BN, as a heteroepitaxy[9] in two dimensions. Because of this epitaxy, for *h*-BNG synthesized by step procedures is impossible to obtain heterointerphases with different relative alignment. Whereas, for DMAB decomposition, flakes of *h*-BN and G grow simultaneously on the surface and can stitch together forming a much more varied set of *in-plane* heterojunctions.

An example of interphase boundary is reported in Figure 7 that shows G and *h*-BN flakes with different orientation that merge in a sharp atomic boundary forming an extended defect line. Further STM measurements on this system will be undertaken in the near future.

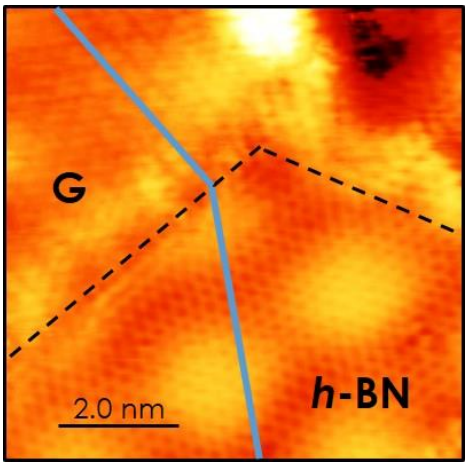

Figure 7. STM image of a sharp boundary between h-BN and G in h-BNG. (V=-0.019 mV; I=22.4 nA) The h-BN flake can be identified by the characteristic moiré (see Figure 4 of the section 3). The dashed black lines identify the island borders, the blue lines mark the lattice orientation of the two materials, at the boundary they merge with 30° of mismatch confirming LEED observations.

Dimethylamine borane decomposition at low temperature

Depositing DMAB at lower temperature, 700 K, a defective B-C-N layer is formed. The chemical composition of the layer, calculated by means of conventional XPS

measurements, is very close to the DMAB stoichiometry with a 50 % of C and 25 % of B and N. The C 1s, B 1s and N 1s photoemission lines, not reported here, are broader with respect the one reported in Figure 3 for the multiple components related to the variety of C-C, C-N, C-B and B-N bonds.

Interestingly CO-TPD do not show any difference between the growth at 1000 K and 700 K, indicating that the defective B-C-N layer is still completely covering the Pt(111) surface. A faint circular structure around the Pt(111) integer spots can be barely observed by LEED. This pattern indicates that the structure can be partially composed by a very defective graphenic layer.

The formation of a disordered structure is triggered by the low growth temperature. The nucleation density increase notably at 700 K, facilitated by the higher sticking coefficient and surface concentration of DMAB moieties at low temperatures. It can be also hypothesized that DMAB at 700 K decomposes on the surface of Pt(111), but the resulting molecular fragments have not enough energy to arrange, diffuse and reach the most stable structures, i.e. G and *h*-BN. This is also indirectly confirmed by the identical elemental composition of the layer and the precursor, which suggests that the decomposition products simply stick and polymerize on the surfaces. Annealing at 1100 K for long times (about 30 minutes) the film deposited at 700 K, does not lead to a reorganization of B-C-N layer to *h*-BNG. The disordered structure, even if is not in the most thermodynamically favoured, is still formed by strong C-C, C-N, C-B and B-N bonds, therefore, the transition from B-C-N to *h*-BNG is strongly hindered because it would involve the breaking of such bonds.

At high temperature the formation of G and *h*-BN is favoured by the lower surface concentration of the molecules, which decreases the nucleation density on the surface, and by the higher energy available for DMAB moieties to diffuse and arrange on the surface. Therefore a way to obtain B-C-N layers that range from amorphous structure to perfect *h*-BNG can be the controlled DMAB decomposition at different substrate temperatures.

Conclusions

A novel growth procedure is reported to obtain a quasi-freestanding *in-plane* layer with perfectly merging G and *h*-BN domains on Pt(111) using a single molecular precursor. LEEM measurements indicate that both G and *h*-BN domains can be as large as a few hundred nm. LEEM data, in agreement with TPD, XPS and XPEEM measurements, show that the layer fully covers the Pt substrate and there are no voids exposing Pt sites. High-resolution photoemission core level spectra prove that the h-BNG layer has a very weak interaction with the substrate and is inert to oxidation. Moreover, changing the growth temperature, the composition of the layer can be tuned from a defective B-C-N material to almost perfect G and *h*-BN *in-plane* heterostructure.

References

[1] Levendorf, M.P.; Kim, C.-J.; Brown, L.; Huang, P.Y.; Havener, R.W.; Muller, D.A.; Park, J. Graphene and boron nitride lateral heterostructures for atomically thin circuitry. *Nature* **2012**, *488*, 627.

[2] Fiori, G.; Betti, A.; Bruzzone, S.; Iannaccone, G. Lateral Graphene–hBCN heterostructures as a platform for fully two-dimensional transistors. *ACS Nano*, **2012**, 6, 2642.

[3] Liu, Z.; Ma, L.; Shi, G.; Zhou, W.; Gong, Y.; Lei, S.; Yang, X.; Zhang, J.; Yu, J.; Hackenberg, K. P.; Babakhani, A.; Idrobo, J.-C.; Vajtai, R.; Lou, J.; Ajayan, P. M. In-plane heterostructures of graphene and hexagonal boron nitride with controlled domain sizes. *Nat. Nanotech.*, **2013**, *8*, 119.

[4] Haldar, S.; Srivastava, P.; Eriksson, O.; Sen, P.; Sanyal, B. Designing Fe Nanostructures at Graphene/h-BN Interfaces. *J. Phys. Chem. C* **2013**, *117*, 21763.

[5] Ci, L.; Song, L.; Jin, C.; Jariwala, D.; Wu, D.; Li, Y.; Srivastava, A.; Wang, Z. F.; Storr, K.; Balicas, L.; *et al.* Atomic Layers of Hybridized Boron Nitride and Graphene Domains. *Nat. Mater.* **2010**, *9*, 430–435.

[6] Muchharla, B.; Pathak, A.; Liu, Z.; Song, L.; Jayasekera, T.; Kar, S.; Vajtai, R.; Balicas, L.; Ajayan, P. M.; Talapatra, S.; *et al.* Tunable Electronics in Large-Area Atomic Layers of Boron–Nitrogen–Carbon. *Nano Lett.* **2013**, *13*, 3476.

[7] Gong, Y.; Shi, G.; Zhang, Z.; Zhou, W.; Jung, J.; Gao, W.; Ma, L.; Yang, Y.; Yang, S.; You, G.; *et al.* Direct Chemical Conversion of Graphene to Boron- and Nitrogen- and Carbon-Containing Atomic Layers. *Nat. Commun.,* **2014**, *5*, 3193.

[8] Chang, C.-K.; Kataria, S.; Kuo, C.-C.; Ganguly, A.; Wang, B.-Y.; Hwang, J.-Y.; Huang, K.-J.; Yang, W.-H.; Wang, S.-B.; Chuang, C.-H.; *et al.* Band Gap Engineering of Chemical Vapor Deposited Graphene by in Situ BN Doping. *ACS Nano* **2013**, *7*, 1333.

[9] Liu, L.; Park, J.; Siegel, D. A.; McCarty, K. F.; Clark, K. W.; Deng, W.; Basile, L.; Idrobo, J. C.; Li, A.-P.; Gu, G. Heteroepitaxial growth of two-dimensional hexagonal boron nitride templated by graphene edges. *Science* **2014**, *343*, 163.

[10] Sutter, P.; Cortes, R.; Lahiri, J.; Sutter, E. Interface Formation in Monolayer Graphene-Boron Nitride Heterostructures. *Nano Lett.* **2012**, *12*, 4869.

[11] Lu, J.; Gomes, L. C.; Nunes, R. W.; Castro Neto, A. H.; Loh, K. P. Lattice relaxation at the interface of two-dimensional crystals: graphene and hexagonal boron-nitride. *Nano Lett.* **2014**, *14*, 5133.

[12] Liu, M.; Li, Y.; Chen, P.; Sun, J.; Ma, D.; Li, Q.; Gao, T.; Gao, Y.; Cheng, Z.; Qiu, X.; Fang, Y.; Zhang, Y.; Liu, Z. Quasi-freestanding monolayer heterostructure of graphene and hexagonal boron nitride on Ir(111) with a zigzag boundary. *Nano Lett.* **2014**, *14*, 6342.

[13] Gao, T.; Song, X.; Du, H.; Nie, Y.; Chen, Y.; Ji, Q.; Sun, J.; Yang, Y.; Zhang, Y.; Liu, Z. Temperature-triggered chemical switching growth of in-plane and vertically stacked graphene-boron nitride heterostructures. *Nat. Commun.* **2015**, *6*, 6835.

[14] Nappini, S.; Píš, I.; Menteş, T. O.; Sala, A.; Cattelan, M.; Agnoli, S.; Bondino, F.; Magnano, E. Formation of a quasi-free-standing single layer of graphene and hexagonal boron nitride on Pt(111) by a single molecular precursor. *Advanced Functional Materials. Accepted*

[15] Paffett, M. T.; Simonson, R. J.; Papin, P.; Paine, R. T. Borazine adsorption and decomposition at Pt(111) and Ru(001) Surfaces. *Surf. Sci.* **1990**, *232*, 286.

[16] Preobrajenski, A. B.; Vinogradov, A. S.; Ng, M. L.; Ćavar, E.; Westerström, R.; Mikkelsen, A.; Lundgren, E.; Mårtensson, N. Influence of Chemical Interaction at the Lattice-Mismatched h−BN/Rh(111) and h−BN/Pt(111) Interfaces on the Overlayer Morphology. *Phys. Rev. B* **2007**, *75*, 245412.

[17] Sutter, P.; Sadowski, J. T.; Sutter, E. Graphene on Pt(111): Growth and Substrate Interaction. *Phys. Rev. B* **2009**, *80*, 245411.

[18] Gao, M.; Pan, Y.; Huang, L.; Hu, H.; Zhang, L. Z.; Guo, H. M.; Du, S. X.; Gao, H.-J. Epitaxial growth and structural property of graphene on Pt(111) *Appl. Phys. Lett.* **2011**, *98*, 033101

[19] Ćavar, E.; Westerström, R.; Mikkelsen, A.; Lundgren, E.; Vinogradov, A. S.; Ng, M. L.; Preobrajenski, A. B.; Zakharov, A. A.; Mårtensson, N. A Single *h*-BN Layer on Pt(111). *Surf. Sci.* **2008**, *602*, 1722.

[20] Cattelan, M.; Agnoli, S.; Favaro, M.; Garoli, D.; Romanato, F., Meneghetti, M.; Barinvon, A,; Dudin, P.; Granozzi, G. Microscopic view on a chemical vapor deposition route to boron-doped graphene nanostructures. *Chem. Mater.* **2013**, *25*, 1490.

[21] Gebhardt, J.; Koch, R. J.; Zhao, W.; Höfert, O.; Gotterbarm, K.; Mammadov, S.; Papp, C.; Görling, A.; Steinrück, H.-P-; Seyller, Th. Growth and electronic structure of boron-doped graphene, *Phys. Rev. B.* **2013**, *87*, 155437.

[22] Cattelan, M.; Peng, G. W.; Cavaliere, E.; Artiglia, L.; Barinov, A.; Roling, L. T.; Favaro, M.; Píš, I.; Nappini, S.; Magnano, E.; Bondino, F.; Gavioli, L.; Agnoli, S.; Mavrikakis, M.; Granozzi, G. The nature of the Fe–graphene interface at the nanometer level. *Nanoscale* **2015**, *7*, 2450.

[23] Sutter, P.; Cortes, R.; Lahiri, J.; Sutter, E. Interface formation in monolayer graphene-boron nitride heterostructures. *Nano Lett.* **2012**, *12*, 4869.

[24] Ford, D. C.; Xu, Y.; Mavrikakis, M. Atomic and molecular adsorption on Pt(111). *Surf. Sci.* **2005**, *587*, 159.

[25] Bianchettin, L.; Baraldi, A.; Gironcoli, S. de; Vesselli, E.; Lizzit, S.; Petaccia, L.; Comelli, G.; Rosei, R. Core level shifts of undercoordinated Pt atoms. *J. Chem. Phys.* **2008**, *128*, 114706.

[26] Ng, M. L.; Balog, R.; Hornekær, L.; Preobrajenski, A. B.; Vinogradov, N. A.; Mårtensson, N.; Schulte, K. Controlling Hydrogenation of Graphene on Transition Metals. *J. Phys. Chem. C* **2010**, *114*, 18559.

[27] Rajasekaran, S.; Kaya, S.; Anniyev, T.; Ogasawara, H.; Nilsson, A. Probing Substrate Effects in the Carbon-Projected Band Structure of Graphene on Pt(111) through Resonant Inelastic X-Ray Scattering. *Phys. Rev. B* **2012**, *85*, 045419.

[28] Cattelan, M.; Cavaliere, E.; Artiglia, L.; Gavioli, L.; Agnoli, S.; Granozzi, G. The dynamics of Fe intercalation on pure and nitrogen doped graphene grown on Pt(111) probed by CO adsorption, *Surf. Sci.* **2015**, *634*, 49.

[29] Gao, Y.; Zhang, Y.; Chen, P.; Li, Y.; Liu, M.; Gao, T.; Ma, D.; Chen, Y.; Cheng, Z.; Qiu, X.; Duan, W.; Liu, Z. Toward single-layer uniform hexagonal boron nitride–graphene patchworks with zigzag linking edges. *Nano Lett.* **2013**, *13*, 3439.

[30] Lahiri, J.; Lin, Y.; Bozkurt, P.; Oleynik, I. I.; Batzill, M. An extended defect in graphene as a metallic wire. *Nat. Nanotechnol.* **2010**, *5*, 326.

3.1.2. Growth and characterization of stacked heterostructures

Introduction

In the section 3 an introduction of several 2D materials and their heterostructure has been presented. In this section a new route to synthesize 2D stacked heterojunctions is reported.

As already mentioned, monolayer systems of *h*-BN and TMDs offer interesting optical and electronic properties that differ from their bulk counterparts.[1,2,3,4] Monolayer semiconducting TMDs are attractive candidates for future optoelectronics, including flexible electronics,[1,5,6] and even spintronics.[7] Additionally, MoS_2 and WS_2 are already widely used in catalytic applications including hydrotreating, hydrocracking,[8] and HER.[9,10] On the other hand, *h*-BN exhibits a bandgap of 5.97 eV[11] making it an attractive candidate for solar blind detectors, UV lasers, and low-k dielectric materials for 2D devices,[12,13,14,15] and when coupled with magnetic metal substrates can exhibit ferrimagnetism.[16]

Beyond the synthesis and characterization of the 2D material *per se* now the researchers turned their attention on the 2D heterojunctions, where monolayers of different 2D materials are stacked vertically layer-by-layer, or stitched together seamlessly *in-plane* to form lateral heterojunctions. Many physical properties (e.g. electrical, optoelectronic and PL properties) have been investigated in such van der Waals heterostructures, and devices with improved performances have been realized.[4,17,18,19,20,21]

For example, monolayer TMD heterostructures artificially stacked by mechanical transfer techniques,[4] i.e. WS_2/MoS_2[22,23] and WSe_2/MoS_2,[24] exhibit interlayer coupling that enables electron-hole recombination between layers allowing to modify their overall optoelectronic properties. By placing *h*-BN layers in between TMD layers, this electronic coupling can be modulated.[24] However, the fabrication of 2D heterostructures with clean and sharp interfaces, essential for preserving their intrinsic properties, remains an unmatched technological challenge.

Mechanical transfer methods have major drawbacks: the stacking orientation cannot be precisely controlled, the interface between layers can be easily contaminated,[25] and the presence of metal or polymer residues in contact with the 2D layers modifies their pristine properties[26,27] and the characteristics of the desired heterojunctions.[5] However, there are only a few reports of directly grown 2D heterostructures with TMDs,[28,29,30] indicating that a concerted effort is needed for developing direct growth methods of these structures.[31] For G/TMDs an ideal substrate has been found in G epitaxially grown on SiC, on the contrary for single layer WS_2 has been obtained by CVD on transferred *h*-BN flakes.[32] The production method of 2D heterostructures is a crucial factor for their future scale-up and implementation into industrial applications. As a result, CVD and MBE[33,34,35] techniques may be considered industrial standards for building advanced device structures. These bottom-up techniques allow a precise control of the orientation of the layers by the van der Waals epitaxy even if there is a relevant lattice mismatch.

MoS_2 has been widely investigated,[36] whereas other TMDs such as WS_2 and WSe_2 have received less attention. TMDs monolayer can adopt two polymorphs: the 1T (octahedral) and the 2H (trigonal prismatic) phases,[37] (see Figure 5b,c in the section 3). The former is metallic and metastable, whereas the latter is semiconducting and thermodynamically favoured. Because of its instability, the 1T phase can be irreversibly converted into the 2H polymorph by annealing at 300-400 °C.[9] The 1T phase can be formed from bulk 2H crystals by intercalating alkali metals,[9] or by irradiation with high-energy electrons, as in TEM.[37] The 1T-WS_2 metallic phase is important because its conductive properties can boost the activity for HER, achieving performance comparable to commercial platinum catalysts.[9] Thus, recent research has focused on direct deposition and stabilization of the metastable metallic phase. Because of the disadvantages of the alkali metal intercalation (partial damage of the layer by strain and reactions to form Li_2S[38]), some recently proposed methods include colloidal synthesis[39] and stabilization via donor doping.[40]

This section is principally focused on the synthesis of single layer WS_2 on quasi-freestanding *h*-BN and Au/Ni(111), and comprises an analysis of the transformation from amorphous WS_2 to 2H-WS_2.[41] A final section is dedicated to our most recent results on the growth of 2H-WSe_2/G heterostructure.

The syntheses were carried out under UHV conditions in order to study the pristine properties and to create stacked heterojunctions without air contamination/oxidation or any presence of residues due to transfer procedures.[25] Samples were examined by XPS, to determine the surface composition, ultraviolet photoemission spectroscopy (UPS), to study the VB structure, LEED, to determine the degree of the long-range order and epitaxy, and *ex-situ* by Raman spectroscopy, to confirm the presence of the 2H-phase.

For our first heterostructure growth study we focused our efforts on WS_2 formation on different substrates. We found that its structure is "tuneable" since it depends strongly on the synthesis temperature. For WS_2 films grown at low temperatures, we find that XPS data are compatible with the presence of 1T-WS_2, which subsequently transforms into 2H-WS_2 at temperatures comparable to those reported for 1T→2H phase transition;[9] however, Raman spectroscopy, LEED and VB data indicate the presence of a disordered structure formed by both amorphous and 2H-WS_2 phases at low temperatures. The reported data suggest that the XPS signal attributed to the 1T phase in previous reports,[9,39,42] may be due to the presence of amorphous WS_2.

We have performed a photoemission study on a system compatible with a previous scanning STM investigation where the growth of few-nanometre wide single layer WS_2 islands on Au(111) was observed.[43] The deposition of WS_2 at low temperature leads to a disordered structure, while thermal treatment triggers the formation of ordered 2H-WS_2. Recently, an ARPES, STM and LEED study on WS_2/Au(111) confirmed our findings.[44] Another work[45] presented a VB study of bulk and single layer 2H-WS_2 supported on HOPG. This demonstrates that highly controlled single layer films of WS_2 can be grown under UHV conditions on several substrates by carefully controlling the growth procedure, however, a complete photoemission study from core level to VB, of the evolution from disordered to ordered WS_2 on a different substrates it was missing in the literature.

For WSe_2 we took advantage of the great knowledge acquired with our precedent studies on WS_2, and we focused principally on the realization of 2H-WSe_2 epitaxy on G. A very recent study on WSe_2 on HOPG confirmed the quality of our growth procedure, the authors used synthesis conditions very similar to ours.[46]

Experimental details

Materials preparation

To synthesize the 2D heterostructures, a Ni(111) single crystal substrate was chosen because it allows a facile growth of high quality *h*-BN and G layers under UHV conditions. Moreover, the resulting layers can be electronically decoupled by intercalating gold underneath,[47,48] as reported in Figure 5 of the section 2 and Figure 3 of section 3.

The Ni(111) single crystal was prepared as reported in the "sample preparation" paragraph in the section 2.2.

Hexagonal boron nitride monolayers were synthesized by dosing 2×10^{-7} mbar of borane-ammonia complex (NH_3-BH_3) on the Ni(111) at 700°C. The precursor was placed in a flanged glass tube, heated at 80 °C and dosed via a leak valve. In order to intercalate gold underneath *h*-BN, few layers of Au (about 6 ML) were deposited using electron-beam evaporation on the *h*-BN/Ni(111) surface, while annealing the crystal at 400 °C.

G has been grown on Ni(111) following the procedure reported in the "graphene growth" paragraph in the section 2.2.

Tungsten sulphide layers were obtained by evaporating W in an atmosphere of 2×10^{-8} mbar of sulphur vapour, while heating the sample at 120 °C and post treated at 400 °C to achieve the semiconducting trigonal prismatic phase (2H).[40] It is also possible to obtain directly 2H-WS_2 by depositing W in the presence of S vapour while annealing the crystal at 400°C. Sulphur vapours were obtained by placing elemental sulphur in a glass vial connected to the main preparation chamber *via* a gate valve. The introduced sulphur is likely consisting of S_6 or S_8 clusters.[49] The use of sulphur, instead of H_2S[43] has been chosen for the safety of the operator, since H_2S is a highly toxic and flammable gas, and because of the low pressure necessary to fully sulfurize W layers deposited at rate of about 0.1 ML/min. This is probably due to the higher oxidation number of the sulphur chains with respect to the already reduced H_2S; the sulfurization reaction of metallic W is facilitated by this redox reaction.

Both tungsten and gold evaporation rates were calibrated using angle resolved XPS measurements according to the method reported in Ref. [50]. A crosscheck of the amount of deposited material has also been carried out by XPS after film preparation.

Tungsten diseleneide layers were obtained is very similar way, but the lower vapour pressure of Se with respect to S makes necessary to use an additional evaporator for the chalcogenide source. This device is an evaporator formed by a graphite crucible filled by selenium powder resistively heated at 120 °C by a tungsten spiral. Also selenium as sulphur is likely present in the gas phase as clusters of various dimensions and not as single atoms.[51]

Methods

All XPS photoemission lines were acquired with a conventional Al K_α source with PE=20 eV; the BE scale was calibrated by normalizing the Au $4f_{7/2}$ BE position to 84.0 eV. Photoemission lines were separated into single chemically shifted components (after Shirley or linear background subtraction) using symmetrical Voigt functions with a FWHM of 1.35 eV.

For WS_2 the VB spectra were acquired using a standard Helium discharge source with PE=2eV for He I and PE=10eV for He II, spectra were acquired in the Γ direction of the Brillouin zone (i.e. normal emission) with an analyser angular acceptance of 3°. ARPES measurements were carried out at the APE beamline at synchrotron Elettra (Trieste, Italy) with 40 eV photons, PE=10 eV and an overall energy resolution of 20 meV. The electron analyser angular resolution was better than 0.2°.

For WSe_2, after optimization of our lab scale equipment, we had the possibility to carry out ARPES measurements also with conventional UPS source.

Ex-situ Raman spectra were acquired with a ThermoFisher DXR Raman microscope using a 532 nm laser (1 mW), focused on the sample with a 50× objective (Olympus) obtaining a spot size of about 1 μm.

Result and discussion

WS_2 stacked heterostructures

We have investigated, in a systematic way, the different types of interfaces that arise by growing WS_2 on *h*-BN and Au, with the aim of understanding possible effects originating from variations in the electronic coupling with the substrate. Hexagonal boron nitride is a large band gap semiconductor whereas Au is a metal. Following a strict reductionist approach, we have studied in detail the following heterostructures *h*-BN/Ni(111), *h*-BN/Au/Ni(111), WS_2/Au/Ni(111) and finally WS_2/*h*-BN/Au/Ni(111). In this context, *h*-BN and gold represent the prototypical atomic thin insulating layer and "3D" metal contact, respectively. In the following, the results of each different interface will be reported separately.

Growth of h-BN/Ni(111) and h-BN/Au/Ni(111)

The Ni(111) catalyst has been chosen for the ability to grow high quality epitaxial *h*-BN film, as mentioned in the paragraph "hexagonal boron nitride" of the section 3. As explained in the experimental section, *h*-BN layers on clean Ni(111) were obtained by dehydrogenation of the borane-ammonia complex.

Under UHV condition the *h*-BN deposition is self-limiting to 1 ML and is characterized by a (1×1) structure with respect to the Ni(111) surface (as visible in Figure 1a); a deposition time of 10 minutes was used to insure complete coverage. The insulating *h*-BN is tightly chemically bound to Ni substrate,[16] but can be decoupled by intercalating gold in order to reach a quasi-freestanding state[47]. In order to do so, few layers (about 6 ML) of Au were deposited on the *h*-BN/Ni(111) surface, while annealing the crystal at 400°C. The LEED patterns of *h*-BN/Ni(111) and *h*-BN/Au/Ni(111) are reported in Figure 1.a. In the sample intercalated by Au, multiple diffraction spots with six-fold symmetry can be observed around the integer reflections indicating the

formation of an ordered (9×9) moiré superstructure between the unstrained *h*-BN and the Au(111) surface. The effect of gold intercalation can also be seen in the N 1*s* and B 1*s* photoemission lines (Figure 1.b), that are shifted to lower BEs, and also in VB spectra (Figure 1.c), where the *h*-BN π band moves from 9.9 eV to 8.2 eV, whereas the σ band shifts from 5.8 eV to about 4 eV, in agreement with Ref. [47] (see Figure 3 of the section 3). These electronic changes are related to the elimination of the chemisorption bonds between *h*-BN and Ni atoms and to the strain associated with the (1×1) epitaxy on Ni(111), in favour of relaxed structure of *h*-BN on the Au thin films.

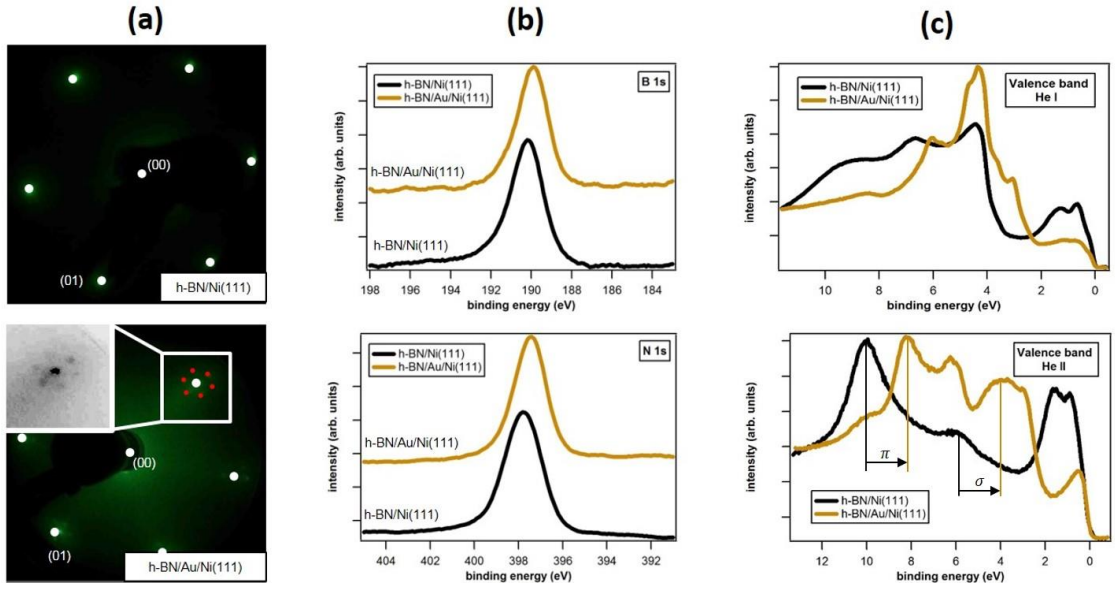

Figure 1. (a) LEED images, acquired at 70 eV, of h-BN/Ni(111) (1×1) reconstruction, h-BN/Au/Ni(111) a (9×9), the inset shows a magnified view of six-fold h-BN diffraction spots around one of the substrate integer diffraction beams. (b) Photoemission from B 1s and N 1s core levels and (c) VB photoemission spectra acquired with He I and He II source of h-BN/Ni(111) and h-BN/Au/Ni(111). Adapted from Ref. [41] © 2015 ACS.

Growth of WS_2/Au/Ni(111)

Monolayer WS_2 was grown on Au/Ni(111) at 120°C and then annealed at 200°C, 300°C and 400°C; the effects of the thermal treatment on the W 4*f* photoemission lines is reported in Figure 2. The elemental composition of the deposited layer was determined by considering the integrated intensity of S 2*p* and W 4*f* photoemission peaks and using as an internal reference, an *ex-situ* bulk sample of stoichiometric WS_2. It was found that the WS_2/Au/Ni(111) system composition, when deposited at 120°C, was $WS_{2.9}$. The annealing process decreased the S/W ratio to $WS_{2.5}$. The WS_{2+x} stoichiometry can be explained by the presence of nanometric domains, whose edges are S terminated, and by S adsorption on the substrate surface.[43] As the sample is annealed, the area of the WS_2 islands increases, while reducing the amount of edges.[10,43] Moreover, the annealing process desorbs adventitious S that was deposited due to residual sulphur background. This residual sulphur atmosphere has been also indirectly observed leaving the sample overnight in pressure $<10^{-9}$ mbar after the growth of WS_2, this minimal exposure led to an increase the quantity of sulphur on the sample. Therefore, all the analysis at different temperatures reported here have been acquired in the same day to avoid the strong influence of the chamber background pressure.

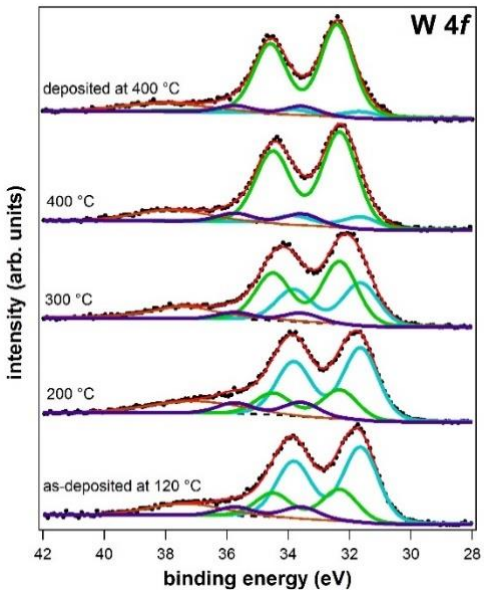

Figure 2. W 4f photoemission spectra of WS_2/Au/Ni(111): as-deposited at 120 °C and subsequently annealed at 200, 300 and 400 °C, or directly deposited at 400°C. Measured data, Shirley background and total fit are represented with black dots, dashed black line and solid red line, respectively. Photoemission lines for amorphous WS_2, 2H-WS_2, WS_3 and W $5p_{3/2}$ are shown with blue, green, purple and brown solid lines, respectively. Reprinted from Ref. [41] © 2015 ACS.

No LEED pattern was observed after the deposition of WS_2 at 120°C, while, after post treatment at 400 °C faint hexagonal diffraction spots were visible. To obtain a better diffraction pattern, WS_2 can be deposited directly on Au/Ni(111) at 400°C. In this way, the W atoms have higher mobility and therefore can attain a more ordered and energetically stable structure. The corresponding LEED pattern is reported in Figure 3a, and shows six elongated spots forming a hexagonal cell corresponding to an incommensurate 2H-WS_2 film, whereas the substrate diffraction spots are heavily attenuated indicating that a fully covering monolayer film has formed.[45] The diffraction spots are about 10° wide, (see the inset in Figure 3.a) indicating the presence of several rotational domains characterized by a small angle misalignment between the lattices of substrate and overlayer, similarly to what is reported for the WS_2/HOPG system.[45] For low WS_2 coverage, several S/Au(111) reconstructions are detectable, as well.[52,53]

The presence of 2H-WS_2, after annealing at 400°C, was confirmed by *ex-situ* Raman spectra reported in Figure 3.b. Three principal peaks are visible: the first one at 176 cm^{-1} corresponds to the longitudinal acoustic mode (LA(M)), the second one at 354 cm^{-1} originates from the overlap of the second order mode 2LA(M) and the $E_{2g}(\Gamma)$, whereas the third one at 417 cm^{-1} corresponds to the first order $A_{1g}(\Gamma)$. Moreover, the intensity ratio of the peaks at 354 and 417 cm^{-1} confirms the presence of predominantly single layer 2H-WS_2.[2] Because of the low temperature growth, the characteristic peaks of 2H-WS_2 are still well recognizable, but their FWHM is larger than in the annealed sample confirming a quite disordered structure. In the as-prepared samples, no features at lower wavenumbers corresponding to 1T-WS_2 have been detected.[9] Because of the clearly distinguishable Raman features of 2H-WS_2, we suggest the presence of a mixed phase where small seed crystals of 2H-WS_2 coexist with amorphous WS_2. As the sample is annealed, the amorphous areas can rearrange and grow off the already formed 2H seed crystals.

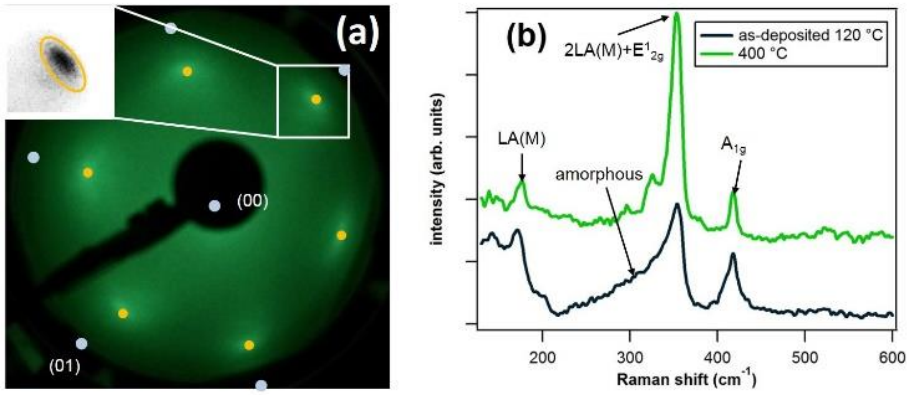

Figure 3. (a) LEED image acquired at 60 eV of WS_2/Au/Ni(111) deposited at 400 °C, inset showing a magnified view of a typical WS_2 diffraction spot; the white circles indicate calculated positions of Ni(111) diffraction spots. (b) Raman spectra of WS_2/Au/Ni(111) acquired with an excitation wavelength of 532 nm, before and after annealing at 400 °C. Reprinted from Ref. [41] © 2015 ACS.

Typically, W 4*f* photoemission line is exploited to understand which polymorph of WS_2 has been obtained, and its evolution with the annealing temperature is used to characterize the structural changes.[9,39,42] Additionally, TEM,[9] x-ray diffraction,[39] or Raman spectroscopy are used to confirm the octahedral environment for W, but these techniques cannot exclude *a priori* the presence of a disordered part into the layer. For our experiments W 4*f* photoemission spectra can be separated into three single components, two related to WS_2, and the third to WS_3. The W $5p_{3/2}$ XPS line is found in the same spectral region of the W 4*f* photoemission line, which results in a broad component in the higher BE tail of the W 4*f* photoemission line (see brown component in Figure 2); the BEs for each component W $4f_{7/2}$ lines are reported in Table 1. Comparing the LEED and Raman data (Figure 3) and the XPS literature data, we assigned the lower BE WS_2 component to an amorphous phase and the higher BE one to the 2H-WS_2 phase. The W 4*f* photoemission line of a WS_2 layer deposited directly at 400°C and separated into chemically shifted components, shows a predominant peak at 32.3 eV, which accounts for 88 % of the whole photoemission spectrum. In Figure 4 the percentage of composition for each component of the W 4*f* photoemission line as a function of annealing temperature is reported (dots with the same colour code reported in Figure 2).

Table 1 BEs (eV) for the different components of the W $4f_{7/2}$ photoemission lines for WS_2/Au/Ni(111) and WS_2/h-BN/Au/Ni(111).

	Amorphous WS_2[54]	**2H-WS_2[9]**	**WS_3[55]**
WS_2/Au/Ni(111)	31.6	32.3	33.6
WS_2/*h*-BN/Au/Ni(111)	31.7	32.4	33.6

As mentioned in the introduction, the layer deposited at low temperature exhibits W4*f* BEs comparable with the values expected for the 1T-WS_2 phase.[9,39,42] However, due to the lack of order detected by LEED and to the Raman data (see Figure 3), the XPS data are better interpreted as evidence of an amorphous WS_2 layer. It is well clear from Figure 4 that thermal treatment transforms the amorphous WS_2 layer into the 2H-WS_2 phase. The presence of a component related to WS_3 in XPS data, which remains

constant with annealing temperature (Figure 4), can be explained as non-stoichiometric, sulphur-rich WS_{2+x} species formed at the edges of WS_2 islands. In Raman spectra, amorphous WS_3 species, which are characterized by a spectral fingerprint at 460 and 520 cm^{-1},[56] were not detected suggesting that WS_3 is not a reaction intermediated of the formation of 2H-WS_2, as it is in the sulfurization of WO_3 to WS_2[56], or the decomposition of $(NH_4)_2WS_4$.[57]

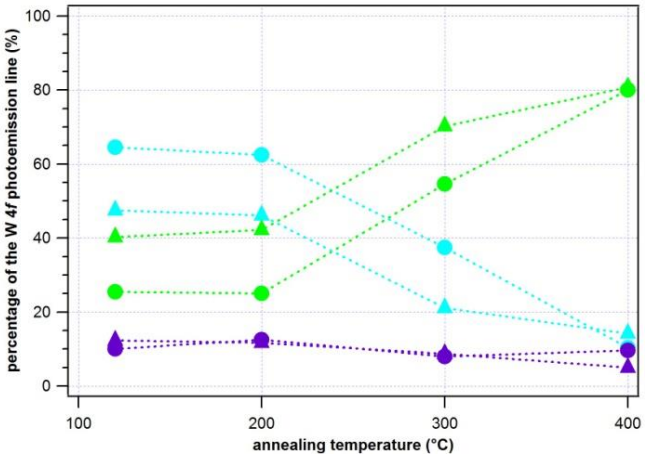

Figure 4. Percentage composition of amorphous WS_2, 2H-WS_2 and WS_3 on the W 4f photoemission lines for WS_2/Au/Ni(111) (circles) and WS_2/h-BN/Au/Ni(111) (triangles). The colour code is the same as that in Figure 2. Reprinted from Ref. [41] © 2015 ACS.

In the VB UPS data of the sample deposited at 120°C (Figure 5), we can observe a strong attenuation of the substrate bands due to the presence of a fully covering WS_2 single layer film and the appearance of new broad features at about 1.3, 4.4, and 6.9 eV. After annealing at 300-400 °C these peaks become sharper and shift slightly their BE positions to 1.7, 3.9 and 7.4 eV, respectively and a new state appears at 2.8 eV. All of these features can be named according to the symmetry driven combinations between W 5*d* and S 3*p* orbitals, as mentioned in the section 3 for monolayer 2H-TMDs the space group is D_{3h}, see Figure 6. The symmetry combination in monolayer 2H-WS_2 can combine into four bands with different symmetry i.e. Γ_1^+, Γ_2^-,Γ_3^-. In 2H-WS_2 and more generally in most TMDs, there is a pronounced hybridization between the chalcogenide *p* and the metal *d* orbitals.[58,59] The electronic states that characterize the VBM, stem from the hybridization between p_z ($\Gamma_1^+$and Γ_2^-) and d_{z^2} states.[60] Moreover, the d_{xy} and $d_{x^2-y^2}$ metal orbitals mix with the Γ_3^+ state, whereas the d_{xz} and d_{yz} interact with the Γ_3^-.[44] As in a previous work,[44] the transition involving Γ_3^+ is difficult to discern because of the low photoionization cross section.

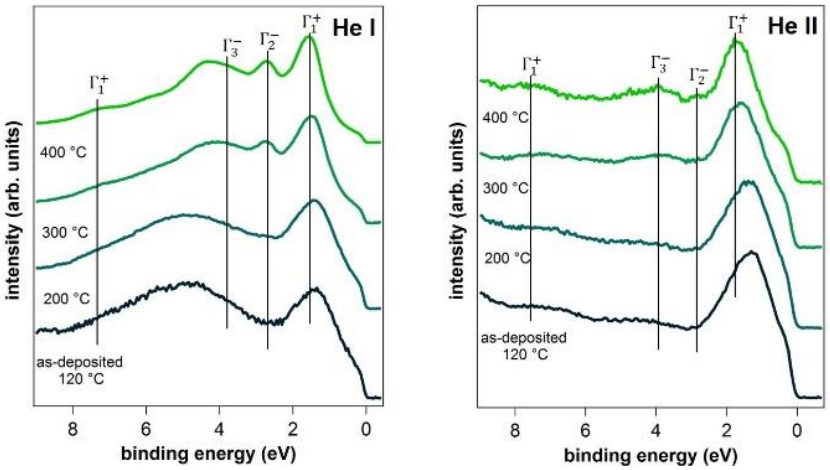

Figure 5. VB photoemission spectra of WS_2/Au/Ni(111) as-deposited at 120 °C and subsequently annealed at higher temperature under UHV conditions, acquired with He I (hv=21.2 eV), and He II (hv=40.8 eV). The features were linked to symmetry of S p orbitals based on Ref. [44]. Reprinted from Ref. [41] © 2015 ACS.

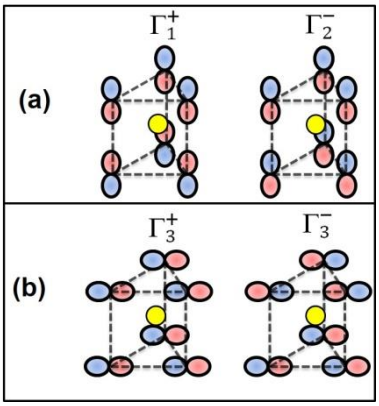

Figure 6. Symmetry combinations of (a) p_z and (b) p_x/p_y sulphur orbitals in a monolayer 2H-WS_2 unit cell with symmetry labels used for the irreducible representations of the space group D_{3h}. Reprinted from Ref. [41] © 2015 ACS.

Growth of WS_2/h-BN/Au/Ni(111)

In order to grow single layer WS_2 on a quasi-freestanding, ultrathin insulator, WS_2 was grown on *h*-BN decoupled from Ni(111) by few Au layers (WS_2/*h*-BN/Au/Ni(111)).

WS_2 was grown at 120°C and then annealed at 200°C, 300°C, and 400°C. For this system, the low temperature deposition of WS_2 has been also used to avoid the sulphur intercalation underneath *h*-BN, see the discussion in the following paragraph.

The growth of coherent and ordered interfaces in the WS_2/*h*-BN/Au/Ni(111) system is difficult because the *h*-BN layer must be of high quality in order to serve as a good epitaxial substrate for the growth of an ordered WS_2 layer, as reported for WS_2/HOPG.[44] In the best conditions, as shown in Figure 7.a, the experimental LEED pattern of this heterostructure presents six incommensurate, but azimuthally oriented spots with the spacing expected for 2H-WS_2,[32] which is qualitatively similar to the WS_2/Au/Ni(111) system reported in Figure 3.a. This LEED pattern demonstrates the presence of van der Waals epitaxy. Unfortunately, the low image quality makes any precise unit cell estimation unreliable, thus preventing the determination of possible strain or layer

relaxation. Also in this case, no LEED pattern was observed for WS_2 grown at 120°C, further confirming the presence of a prevalently amorphous structure.

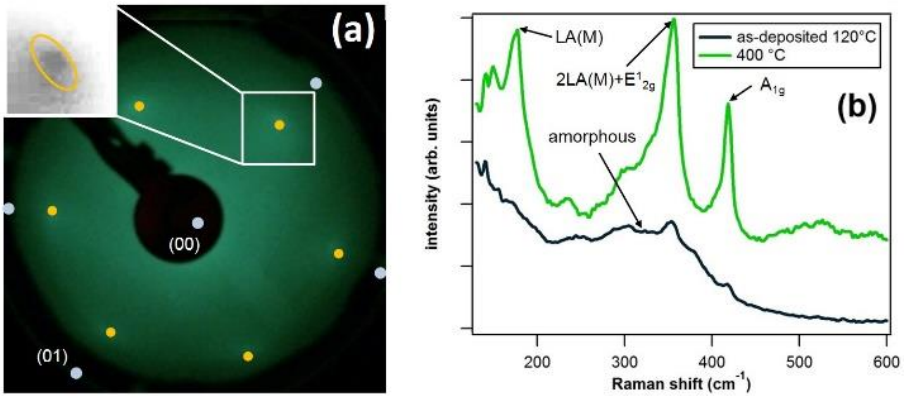

Figure 7. (a) LEED image acquired at 60 eV of WS_2/h-BN/Au/Ni(111) after annealing, the inset reports a magnified view of a WS_2 diffraction spot, white circles indicate calculated positions of Ni(111) diffraction spots. (b) Raman spectra of WS_2/h-BN/Au/Ni(111) acquired with an excitation wavelength of 532 nm, before and after annealing at 400 °C. Reprinted from Ref. [41] © 2015 ACS.

Comparing the Raman spectra of WS_2/Au/Ni(111) and WS_2/h-BN/Au/Ni(111), Figure 3 and Figure 7, the features for the as-prepared samples indicate a more disordered layer in the case of WS_2/*h*-BN/Au/Ni(111). After annealing, the peaks have a higher FWHM with respect to those of the WS_2/Au/Ni(111) system. As in the case of WS_2/Au, because of the presence of 2H features in Raman spectra, it is likely that 2H-WS_2 nanometric domains form at low temperature and serve as seeds during annealing. Therefore, combined evidence from LEED and Raman spectroscopy (Figure 3 vs Figure 7) shows that Au has a higher templating effect than *h*-BN for the growth of 2H-WS_2. This can be explained by assuming that the interaction between the WS_2 and h-BN is very weak, whereas the interaction with Au is stronger. This is in agreement with previous experiments on the growth of MoS_2 on Au(111) and HOPG: while in the case of Au(111) the interaction with the substrate is stronger and a clear epitaxial relationship is observed, in the case of HOPG disorder is enhanced.[61,62]

Also in this case the disappearance of the diffraction spots of the substrate in the LEED pattern and the intensity ratio between the bands at 354 and 417 cm^{-1} less than one[2] indicate the presence of single layer WS_2.

XPS data indicates (Figure 8) a similar trend in phase structure for WS_2/h-BN/Au/Ni(111) compared to WS_2/Au/Ni(111) the fraction of the 2H-phase increases with increasing annealing temperature (Figure 4). Interestingly, for the WS_2/h-BN/Au/Ni(111) system, the WS_3 photoemission signals decrease with annealing temperature. Indeed, dosing sulphur in our conditions (2×10^{-8} mbar at 400 °C for 15 min) on Au (≈6 ML)/Ni(111) results in various stable superstructures.[52,53] We speculate that WS_3 is abundant at the edges of the WS_2 nanoparticles. Therefore, because of the lower affinity for S to bind to *h*-BN, the formation of a non-stoichiometric, sulphur-rich WS_{2+x} is less favourable with respect to Au.

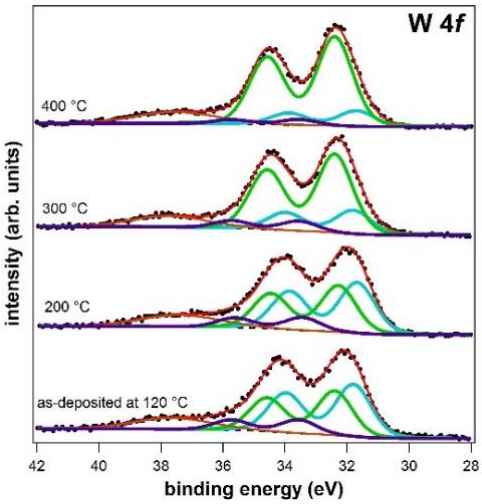

Figure 8. W 4f photoemission spectra of WS_2/h-BN/Au/Ni(111) as-deposited at 120 °C and subsequently annealed at 200, 300 and 400 °C. Measured data, Shirley background and total fit are represented with black dots, dashed black line and solid red line, respectively. Photoemission lines of amorphous WS_2, 2H-WS_2, WS_3, W $5p_{3/2}$ are shown with blue, green, purple and brown solid lines, respectively. Reprinted from Ref. [41] © 2015 ACS.

Interestingly, the W 4*f* photoemission spectra corresponding to amorphous and 2H-WS_2 are shifted of 0.1 eV to higher BEs with respect the WS_2/Au/Ni(111), while maintaining their separation of 0.7 eV, indicating a slightly different electronic coupling, see Figure 8. Additionally, the VB UPS data of the monolayer WS_2/h-BN/Au/Ni(111) (Figure 9), show features very similar to those reported for WS_2/Au/Ni(111) (Figure 5). The spectra are mostly dominated by the presence of the outermost layer of WS_2 as expected for a fully covering single layer films; however they show a barely visible additional state at ~4.35 eV related to the σ band of quasi-freestanding *h*-BN (see Figure 1.c).[47,48] Even when WS_2 is placed on an insulator, there is no large energy shift of its bands with respect to WS_2/Au. This can be explained by the absence of strong interlayer coupling between WS_2 and both Au and *h*-BN.[22,23,24]

Similar to WS_2/Au/Ni(111), annealing at high temperature leads to a transition from broad spectral features to sharper ones, which is correlated with Raman spectroscopy (Figure 7), indicating a transition from predominantly amorphous to single layer 2H-WS_2. For the as-deposited layer, Raman spectra show a broad band centred at ~300 cm^{-1}, but there are still small peaks present in the position of 2H-WS_2. For the as-deposited sample of WS_2/Au/Ni(111) there are no clear Raman features of 1T-WS_2 or of WS_3, which suggests a growth mechanism similar to that on the Au/Ni(111) substrate.

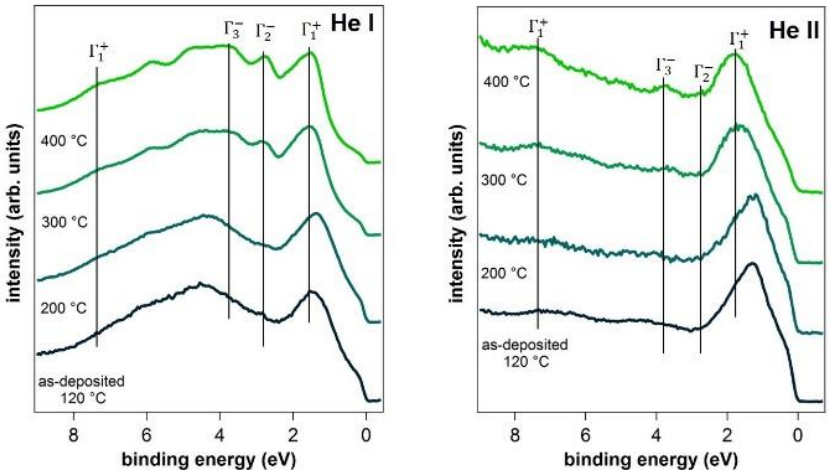

Figure 9. VB spectra of WS_2/h-BN/Au/Ni(111) as-deposited at 120 °C and subsequently annealed at higher temperature under UHV conditions, acquired with He I (hv=21.2 eV), and He II (hv=40.8 eV). The features were linked to symmetry of S p orbitals based on Ref. [44]. Reprinted from Ref. [41] © 2015 ACS.

Recently, ARPES revealed the opening of mini-gap in graphene π orbitals with the out-of-plane states of the TMDs when placed on MoS_2 single crystal.[63] We investigated by ARPES with variable-polarization synchrotron radiation *in situ* grown WS_2/*h*-BN heterostructure, in order to identify the band character of our stacked materials, and the presence of possible modifications induced by interfacial interactions. The VB spectra of 1 ML of WS_2 deposited on *h*-BN/Au/Ni(111) along Γ–M direction with two perpendicular linear polarizations (Figure 10a,b). Since the angle of light incidence on the sample surface is 45°, linear horizontal polarization vector can be decomposed in two components in and out of the surface plane, while the linear vertical polarization is mainly in the surface plane and along the dispersion direction. We identify three main band structure features at 1.5, 2.8 and 4 eV at the Γ point. Notably, the absence of a band (Γ_4^-) at ~1 eV is a distinctive electronic feature of single layer WS_2.[44]

The first band at 1.5 eV originates from the hybridization of W $5d_{z^2}$ and Γ_1^+ S $3p_z$ orbitals, (see Figure 6) and is particularly emphasized with horizontal polarization (Figure 10.a out of surface plane). The second band, at 2.8 eV, can be observed with horizontally polarized radiation and comes from symmetrically different p_z, orbitals (Γ_2^-). The third feature visible in Figure 10.a, derives from the Γ_3^- states mixed with W d_{xz} and d_{yz} orbitals. These states generate two distinct bands that cross each other in the Γ point at a BE of 4 eV. The use of linearly polarized radiation in the surface plane (Figure 10.b) suppresses the band at 1.5 eV, whereas the band at 2.8 eV becomes almost undetectable. On the contrary, the bands that are a result of the hybridization of p_x and p_y orbitals, Γ_3^- , become highly emphasized.[44]

Comparing the VBM in the Γ point of WS_2/*h*-BN with recently high resolution ARPES data acquired on *in-situ* grown WS_2/Au(111)[44] there is a shift of about 0.1 eV at high BEs of the band structure for WS_2/*h*-BN. This confirm the W 4*f* shift (see Table 1) to higher BEs of WS_2/Au vs WS_2/*h*-BN, whereas probably UPS measurements (Figure 5 and Figure 9) are not sufficiently accurate to visualize this shift.

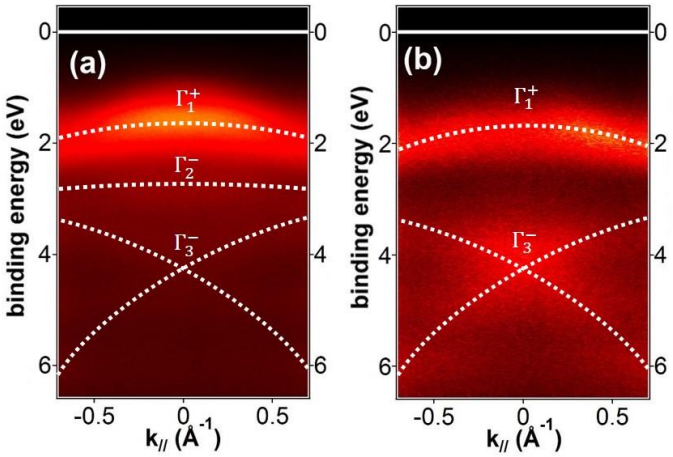

Figure 10. ARPES spectra obtained with synchrotron light at 40 eV with (a) linear horizontal polarization and (b) linear vertical polarization. The features were linked to the symmetry of S 3p orbitals based on Ref. [44]. Reprinted from Ref. [41] © 2015 ACS.

It is interesting to observe that the energy separation between the bands at the Γ point is the same as that observed for UHV exfoliated WS_2 single crystal or epitaxial WS_2 films grown in situ on HOPG under UHV conditions.[45] This indicates the good quality of our films: operating under UHV conditions allows eliminating any source of contamination and preparing films with low defect concentration, which therefore are very prone to any electronic interaction.

WSe_2 heterostructure

Similar to what we have done with WS_2 heterostructures we have investigated, in a systematic way, the different types of interfaces that arise from growing WSe_2 on G. Following a strict reductionist approach, we have studied in detail the following structures $NiSe_x$/Ni(111), G/Ni(111), G/$NiSe_x$/Ni(111) and WSe_2/G/$NiSe_x$/Ni(111).

Growth of $NiSe_x$/Ni(111), graphene/Ni(111) and graphene/$NiSe_x$/Ni(111)

Nickel selenide layers can be formed exposing the bare Ni(111) surface to Se while annealing the crystal at 500°C. The LEED pattern, Figure 11a, of this surface has a peculiar "star-like" structure that we related not to a simple surface reconstruction of a Se overlayer on Ni(111)[64] but to a faced structure probably caused by the migration of Se atoms inside the selvedge of the Ni(111) substrate, hereafter this layer will be called $NiSe_x$. We reached such conclusion because the $NiSe_x$ LEED structure has features that do not follow the typical behaviour of the LEED pattern of 2D reconstruction that increasing/reducing the electron energy reduce/increase the visible pattern on the LEED screen.

G has been grown on Ni(111) by decomposition of C_2H_4. As mentioned in the paragraph "graphene on Ni(111)" of the section 2, on this surface the G grows adopting a 1x1 epitaxial structure, and therefore Figure 11b, shows a simple (1×1) pattern. When selenium is evaporated on G/Ni(111) while keeping the crystal at 500 °C, it can quickly intercalate underneath G. This phenomenon is visible by LEED, Figure 11c, where a faint $NiSe_x$ reconstruction is visible underneath the (1×1) G pattern.

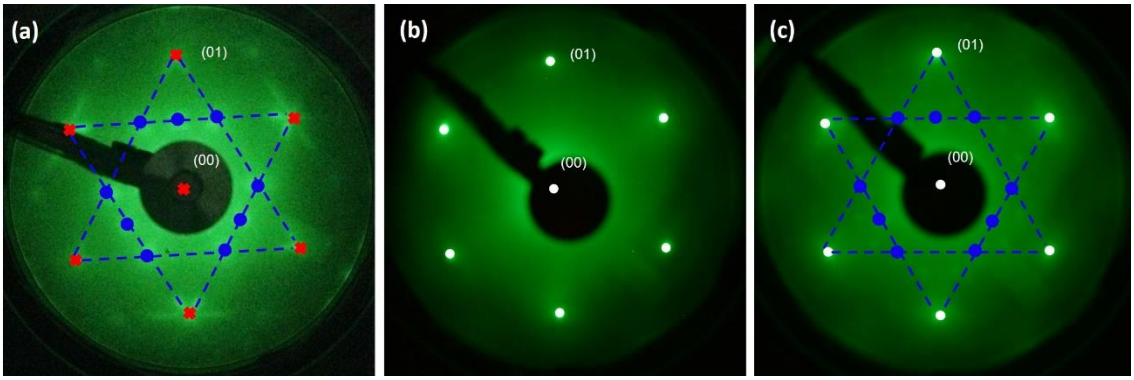

Figure 11. LEED images acquired at 120 eV (a) $NiSe_x$/Ni(111), (b) G/Ni(111), (c) G/$NiSe_x$/Ni(111) red crosses, white spots, blue circles and dashed lines indicate positions of Ni(111) diffraction spots, G diffraction spots, and $NiSe_x$ reconstruction.

Another proof of the Se intercalation underneath G/Ni(111) comes from photoemission from core level and VB photoemission, Figure 14, similarly to what is observed in Figure 1b,c for intercalation of *h*-BN/Au/Ni(1111) or accordingly to Figure 5 of the section 2 for G/Au(1 ML)/Ni(111). The C 1s photoemission line before and after the formation of $NiSe_x$ has been deconvoluted into single chemically shifted components, see Figure 14a. The G/Ni(111) has been fitted as done in Figure 2a in the section 2.2 considering the different possible G configuration and a small components of Ni carbide,[65,66,67] see also paragraph "graphene on Ni(111)" in the section 2. After $NiSe_x$ formation the C 1s photoemission line changes drastically, it shifts of about 0.7 eV to lower BE and it can be fitted with a single Doniach-Šunjić components. The G/$NiSe_x$ has a BE of about 284.05 eV comparable to the value observed in G/Pt(111)[68] and reported in the section 2.1.1 indicating a quasi-freestanding electronic structure. Selenium reduced drastically the charge transfer between Ni and G as found for oxygen on Fe NPs[68] on G/Pt(111).

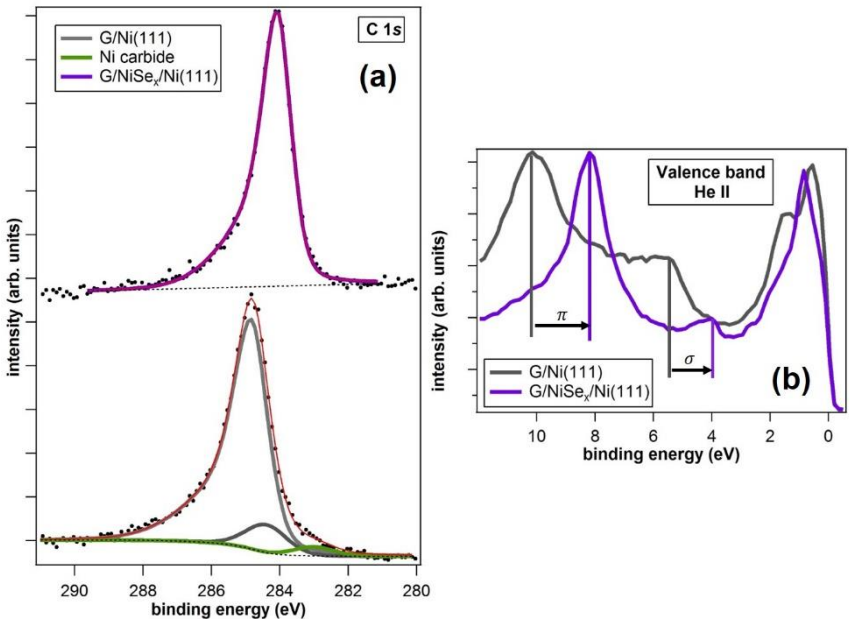

Figure 12. (a) Photoemission from C 1s core levels of G/Ni(111) and G/$NiSe_x$/Ni(111). Measured data, background, total fit and single peak are represented with black dots, dashed black line, solid red line. (b) VB photoemission spectra acquired with He II source (hv=40.8 eV) of G/Ni(111) and G/$NiSe_x$/Ni(111).

By means of UPS at Γ point it is possible to detect that after the Se intercalation the G π band shift to lower BE of about 2 eV and the σ band of 1.5 eV, see Figure 14b. Unfortunately, up to now, we cannot estimated the doping at G K point (white line in Figure 14a) for technical reasons. At the G K point the doping can be easily estimated by the Dirac point position with respect to the Fermi energy (as done in the section 2.3). The observed shift are similar to what can be found for G/Au/Ni(111)[48] further confirming that G has a quasi-freestanding structure on $NiSe_x$, further investigation of $G/NiSe_x$ band structure will be undertaken.

Growth of $WSe_2/G/NiSe_x/Ni(111)$

For the heterostructure composed by WSe_2 our aim was to synthesize directly the 2H-WSe_2 phase, for this reason W and Se has been deposited simultaneously on G/Ni(111) while maintaining the crystal at 500 °C, Se evaporator was calibrated to be in strongly excess of chalcogenide atoms. During the W and Se co-deposition, W atoms are blocked on the surface by Se atoms and WSe_2 islands can nucleate on top of G, while part of the chalcogenide atoms can pass through G and form $NiSe_x$.

As done for WS_2 the presence of WSe_2 was confirmed by LEED and Raman spectroscopy, see Figure 13. The coverage has been kept lower than 1 ML, to distinguish by LEED the (1×1) reconstruction of G, and to analyse simultaneously the band structure of G and WSe_2. The decoupling of G from the Ni substrate operated by $NiSe_x$ is difficult to detect by LEED because the $NiSe_x$ pattern is strongly attenuated by the WSe_2 and G layers, but was confirmed by C 1s BE and UPS.

The LEED pattern, Figure 13b, of this heterostructure presents six incommensurate, but azimuthally oriented spots with the spacing expected for 2H-WSe_2,[30] which is qualitatively similar to for WS_2 systems reported above, this LEED pattern demonstrates the presence of van der Waals epitaxy. The 2H-WSe_2 are quite elongated indicating that the 2D layers are not perfectly aligned.

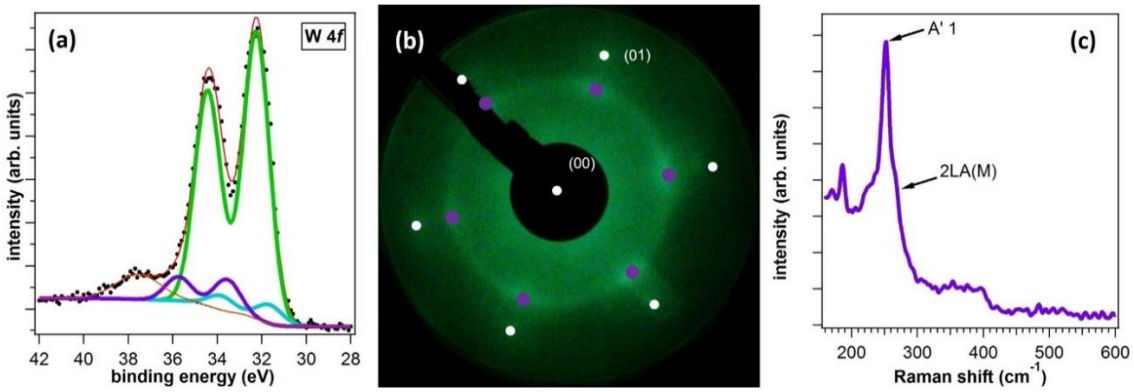

Figure 13. (a) W 4f photoemission spectra of $WSe_2/G/NiSe_x/Ni(111)$ directly deposited at 400°C. Measured data, Shirley background and total fit are represented with black dots, dashed black line and solid red line, respectively. Photoemission lines for amorphous WSe_2, 2H-WSe_2, WSe_3 and W $5p_{3/2}$ are shown with blue, green, purple and brown solid lines, respectively. (b) LEED image acquired at 110 eV of WSe_2(0.5 ML)/G/Se/Ni(111) white and purple circles indicate the position of G and WSe_2 spots respectively. (c) Raman spectrum of $WS_2/NiSe_x/Ni(111)$ acquired with an excitation wavelength of 532 nm.

The Raman spectrum, Figure 13c, presents a peak at 250 cm^{-1} (A'1) with a shoulder at 260 cm^{-1} (2LA(M)), which are characteristic of WSe_2, the absence of a mode at 310

cm^{-1} indicates that the coverage was below 1 ML.[69] The other peaks at 160 and 176 cm^{-1} are probably related to $NiSe_x$.

The W 4*f* photoemission line, Figure 13a, has been deconvoluted into single chemically shifted components. Similarly to what we have studied for WS_2 (see discuss above, Figure 2 and Figure 8), three components can be identified and related to amorphous WSe_2 (31.7 eV), 2H-WSe_2 (32.3 eV) and WSe_3 (33.6 eV) structures. The biggest part of the signal (85%) is provided by 2H-WSe_2 but we want further decrease the components related to amorphous WSe_2 and WSe_3 by optimization of the growth conditions.

As observed before for WS_2/Au and WS_2/*h*-BN the W $4f_{7/2}$ photoemission line shifts to higher BE when the material is placed on insulating substrate, see Table 1; in this case the of 2H-WSe_2 photoemission line is at about 32.3 eV confirming that the TMDs has been grown on a semimetallic substrate, i.e. G.

The ARPES acquisition in the Γ→K direction is reported in Figure 14a. From the VB map the 2H-WSe_2 band structure is well visible. Owing the same symmetry of 2H-WS_2 the VB features can be linked to Se *p* orbitals symmetry, see Figure 6. At the Γ point are distinguishable three features at 1.4, 2.2 and 2.7 eV, that are related to Γ_1^+, Γ_2^-,Γ_3^- band respectively. Other bands linkable to Γ_3^+ and Γ_1^- at about 4 and 8 eV are overlapping with G σ and π decoupled bands, see Figure 12b.

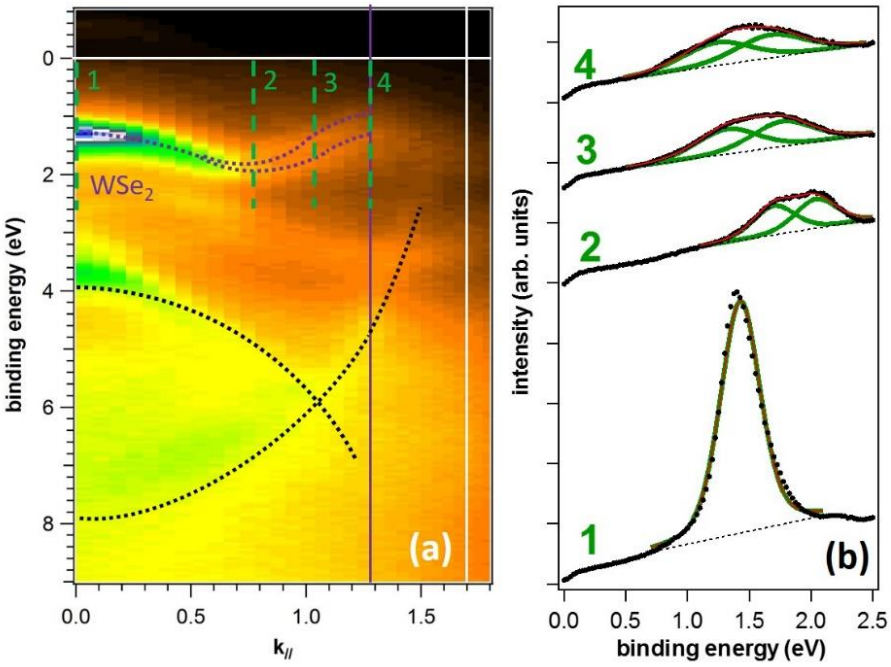

Figure 14. (a) ARPES spectra acquired with He I (hv=21.2 eV) of WSe_2(0.5 ML)/G/Se/Ni(111), white and purple solid lines indicate the position of G and WSe_2 K point respectively. Black and purple dashed lines indicates the band structure of G and WSe_2 bands respectively, green dashed lines indicate where the single spectra in (b) where acquired. (b) Spectra of the WSe_2 top VB. The spectra were fitted with symmetrical Voigt function after subtraction of a linear background. Measured data, background, total fit and single peak are represented with black dots, dashed black line, solid red line and solid green line respectively

Some single spectra, focused on the Γ_1^+ band formed by the hybridization of W $5d_{z^2}$ and Γ_1^+ Se $4p_z$ orbitals, have been acquired to underline the features of WSe_2 band structure at four different k space vectors, Figure 14b. Monolayer WSe_2 band structure

has been studied theoretically[70] and experimentally by μ-ARPES.[71,72] The Γ_1^+ band is degenerate at the Γ point and appears as a single band. However, moving in the Γ to K direction it splits in two spin polarized components that at the K point result to be separated by about 0.5 eV.[71] Moreover the VBM is at the K point, whereas for two layers or more is at Γ point. All these features have been confirmed by our UPS measurements and by fitting the WSe_2 features. At the Γ point (curve 1, Figure 14b) only a features is visible centred at 1.43 eV, moving to the WSe_2 K point (curve 2) two bands with the same area are visible with a split of 0.3 eV, for curves 3 and 4 (the latter is on the WSe_2 K point) the two bands have a separation of 0.4 eV. Moreover, the VBM in K (curve 4) is 0.2 eV higher than the one on Γ point confirming the monolayer nature of WSe_2. The curves became broader moving away from the Γ point probably because of the presence of different azimuthally rotated domains as indicated also by the WSe_2 enlarged spots in LEED pattern, Figure 13a.

As stated above G bands at Γ point overlap with some WSe_2 features so it is difficult to judge exactly the position of its band at that symmetry point. However C 1s photoemission line is very similar to G/$NiSe_x$ reported in Figure 12a, and the band position moving close to the K point (black dashed line in Figure 14a) is similar to what observed for quasi-freestanding G,[48] therefore we can safely state that G has a quasi-freestanding electronic structure.

This result, even if preliminary, confirms that we reached a quite complex (WSe_2/G/$NiSe_x$/Ni(111)) heterostructure of good quality. Notably all the synthesis protocol has been carried out under UHV conditions allowing a systematic investigation of the subsequent changes in the systems. This represent the starting point for improve the syntheses to obtain better controlled morphology (enlargement of the grain and better orientation with respect to the substrate).

Conclusions

In this section we described the growth of a WS_2 monolayer on gold and on quasi-freestanding *h*-BN and a WSe_2 monolayer on G. These systems were characterized by using XPS, UPS, Raman spectroscopy and LEED. The latter indicates the van der Waals epitaxy between TMD films and the substrates.

For WS_2, photoemission VB measurements reveal the absence of interlayer coupling, so that WS_2 supported either on insulating *h*-BN or metal Au presents the same electronic structure. This outcome is not unexpected considering the high chemical perfection and absence of any possible contaminants in systems grown under UHV conditions. These results suggest that Au is a perfect candidate for the preparation of metal contacts, whereas *h*-BN can be used as an ideal substrate to support monolayer WS_2 with the aim of keeping intact its intrinsic properties such as PL.[73] The WS_2 film deposited at low temperature on both substrates, shows a W 4*f* photoemission line centred at BE very close to the values reported in the literature for 1T-WS_2.[9,39,42] However, our data indicate that similar spectra can be obtained on amorphous WS_2 that can be converted to crystalline 2H-WS_2 after annealing at 300-400°C. Therefore, these findings suggest that amorphous WS_2 could be erroneously identified as 1T-WS_2 on the basis of the simple XPS fingerprint. This must be taken in account when XPS measurements are used as quantitative technique to estimate the 1T/2H ratio in WS_2 based materials.

The other heterostructure presented, i.e. WSe_2/G, it is our most recent result. For this artificially stacked material, we exploited our knowledge acquired with WS_2/*h*-BN to assemble a material with such good quality of interface that allows us to sample, with our lab scale equipment, its spin resolved VB structure.

We demonstrated our method for growing heterostructures under UHV conditions represents a quite general strategy to synthesize and study the pristine properties of other artificially stacked materials. For example, tungsten can be replaced by other transition metals, i.e. Mo or Ni, and other chalcogenides can be evaporated as well, so that a full gamut of TMDs can be easily obtained. This method provides an alternative and more reliable route with respect to *ex-situ* CVD synthesis or mechanical transfer method, for the fundamental study of the authentic properties of complex heterostructures.

References

1 Chhowalla, M.; Suk Shin, H.; Eda, G.; Li, L. J.; Loh, K. P.; Zhang, H. The chemistry of two-dimensional layered transition metal dichalcogenide sheets. *Nat. Chem.* **2013**, *5*, 263.

2 Berkdemir, A.; Gutiérrez, H. R.; Botello-Méndez, A. R.; Perea-López, N.; Elías, A. L.; Chia, C. I.; Wang, B.; Crespi, V. H.; López-Urías, F.; Charlier, J. C.; Terrones, H.; Terrones, M. Identification of few layers of WS_2 using Raman spectroscopy. *Sci. Rep.* **2013**, *3*, 1755.

3 Mak, K. F.; Lee, C.; Hone, J.; Shan, J.; Heinz, T. F. Atomically thin MoS_2: A new direct-gap semiconductor. *Phys. Rev. Lett.* **2010**, *105*, 136905.

4 Geim, A. K.; Grigorieva, I. V. Van der Waals heterostructures. *Nature* **2013**, *499*, 419.

5 Xu, X.; Yao, W.; Xiao, D.; Heinz, T. F. Spin and pseudospins in layered transition metal dichalcogenides. *Nature Phys.* **2014**, 10, 343.

6 Janisch, C.; Wang, Y.; Ma, D.; Mehta, N.; Elías, A. L.; Perea-López, N.; Terrones, M.; Crespi, V.; Liu, Z. Extraordinary Second Harmonic Generation in tungsten disulfide monolayers. *Sci. Rep.* **2014**, *4*, 5530.

7 Riley, J. M.; Mazzola, F.; Dendzik, M.; Michiardi, M.; Takayama, T.; Bawden, F.; Granerød, C.; Leandersson, M.; Balasubramanian, T.; Hoesch, M.; Kim, T, K.; Takagi, H.; Meevasana, W.; Hofmann, Ph.; Bahramy, M. S.; Wells, J. W.; King, P. D. C. Direct observation of spin-polarized bulk bands in an inversion-symmetric semiconductor. *Nature Phys.* **2014**, *10*, 835.

8 Thakur, D. S.; Delmon, B. The role of group VIII metal promoter in MoS_2 and WS_2 hydrotreating catalysts: I. ESR studies of CoMo, NiMo, and NiW catalysts. *J. Catal.* **1985**, *91*, 308.

9 Voiry, D.; Yamaguchi, H.; Li, J.; Silvia, R.; Alves, D. C. B.; Fujita, T.; Chen, M.; Asefa, T.; Shenoy, V.; Eda, G.; Chowalla, M. Enhanced Catalytic Activity in Strained Chemically Exfoliated WS_2 Nanosheets for Hydrogen Evolution. *Nat. Mater.* **2013**, *12*, 850.

10 Jaramillo, T. F.; Jørgensen, K. P.; Bonde, J.; Nielsen, J. H.; Horch, S. Identification of active edge sites for electrochemical H_2 evolution from MoS_2 nanocatalysts. *Science* **2007**, *317*, 100.

11 Kubota, Y.; Watanabe, K.; Tsuda, O.; Taniguchi, T. Deep Ultraviolet Light-Emitting Hexagonal Boron Nitride Synthesized at Atmospheric Pressure. *Science* **2007**, *317*, 932.

12 Kim, K. K.; Hsu, A.; Jia, X.; Kim, S. M.; Shi, Y.; Hofmann, M.; Nezich, D.; Rodriguez-Nieva, J. F.; Dresselhaus, M.; Palacios, T.; Kong, J. Synthesis of monolayer hexagonal boron nitride on Cu foil using chemical vapor deposition. *Nano Lett.* **2012**, *12*, 161.

13 Yingjie Tay, R.; Griep, M. H.; Mallick, G.; Tsang, S. H.; Singh, R. S.; Tumlin, T.; Tong Teo, E. H.; Karna, S. P. Growth of large single-crystalline two-dimensional boron nitride hexagons on electropolished copper. *Nano Lett.* **2014**, *14*, 839.

14 Shi, Y.; Hamsen, C.; Jia, X.; Kang Kim, K.; Reina, A.; Hofmann, M.; Long Hsu, A.; Zhang, K.; Li, H.; Juang, Z. Y.; Dresselhaus, M. S.; Li, L. J.; Kong, J. Synthesis of few layer hexagonal boron nitride thin film by chemical vapor deposition. *Nano Lett.* **2010**, *10*, 4134.

15 Bresnehan, M. S.; Hollander, M. J.; Wetherington, M.; Wang, K.; Miyagi, T.; Pastir, G.; Snyder, D. W.; Gengler, J. J.; Voevodin, A. A.; Mitchel, W. C.; Robinson, J. A. Prospects of direct growth boron nitride films as substrates for graphene electronics. *J. Mater. Res.* **2014**, *29*, 459.

[16] Joshi, N.; Ghosh, P. Substrate-induced changes in the magnetic and electronic properties of hexagonal boron nitride. *Phys. Rev. B* **2013**, *87*, 235440.

[17] Britnell, L.; Gorbachev, R. V.; Jalil, R.; Belle, B. D.; Schedin, F.; Mishchenko, A.; Georgiou, T.; Katsnelson, M. I.; Eaves, L.; Morozov, S. V.; Peres, N. M. R.; Leist, J.; Geim, A. K.; Novoselov, K. S.; Ponomarenko, L. A. Field-effect tunneling transistor based on vertical graphene heterostructures. *Science* **2012**, *335*, 947.

[18] Gannett, W.; Regan, W.; Watanabe, K.; Taniguchi, T.; Crommie, M. F.; Zettl, A. Boron nitride substrates for high mobility chemical vapor deposited graphene. *Appl. Phys. Lett.* **2011**, *98*, 242105.

[19] Georgiou, T.; Jalil, R.; Belle, B. D.; Britnell, L.; Gorbachev, R. V.; Morozov, S. V.; Kim, Y.-J.; Gholinia, A.; Haigh, S. J.; Makarovsky, O.; Eaves, L.; Ponomarenko, L. A.; Geim, A. K.; Novoselov, K. S.; Mishchenko, A. Vertical field-effect transistor based on graphene-WS_2 heterostructures for flexible and transparent electronics. *Nature Nanotech.* **2013**, *8*, 100.

[20] Yu, W. J.; Liu, Y.; Zhou, H.; Yin, A.; Li, Z.; Huang, Y.; Duan, X. Highly efficient gate-tunable photocurrent generation in vertical heterostructures of layered materials. *Nat. Nanotech.* **2013**, *8*, 952.

[21] Lee, C.; Hong, J.; Whangbo, M.-H.; Shim, J. H. Enhancing the Thermoelectric Properties of Layered Transition-Metal Dichalcogenides 2H-MQ_2 (M = Mo, W; Q = S, Se, Te) by Layer Mixing: Density Functional Investigation. *Chem. Mater.* **2013**, *25*, 3745.

[22] Tongay, S.; Fan, W.; Kang, J.; Park, J.; Koldemir, U.; Suh, J.; Narang, D. S.; Liu, K.; Ji, J.; Li, J.; Sinclair, R.; Wu, J. Tuning Interlayer Coupling in Large-Area Heterostructures with CVD Grown MoS_2 and WS_2 Monolayers. *Nano Lett.* **2014**, *14*, 3185.

[23] Yuan, J.; Najmaei, S.; Zhang, Z.; Zhang, J.; Lei, S.; Ajayan, P. M.; Yakobson, B. I.; Lou, J. Photoluminescence quenching and charge transfer in artificial heterostacks of monolayer transition metal dichalcogenides and few-layer black phosphorus. *ACS Nano*, **2015**, *9*, 555.

[24] Fang, H.; Battaglia, C.; Carraro, C.; Nemsak, S.; Ozdol, B.; Kang, J. S.; Bechtel, H. A.; Desai, S. B.; Kronast, F.; Unal, A. A. M.; Conti, G.; Conlon, C.; Palsson, G. K.; Martin, M. C.; Minor, A. M.; Fadley, C. S.; Yablonovitch, E.; Maboudian, R.; Javey, A. Strong interlayer coupling in van der Waals heterostructures built from single-layer chalcogenides. *Proc. Natl. Acad. Sci. U S A.*, **2014**, *111*, 6198.

[25] Haigh, S. J.; Gholinia, A.; Jalil, R.; Romani, S.; Britnell, L.; Elias, D. C.; Novoselov, K. S.; Ponomarenko, L. A.; Geim, A. K.; Gorbachev, R. Cross-sectional imaging of individual layers and buried interfaces of graphene-based heterostructures and superlattices. *Nat. Mater.* **2012**, *11*, 764.

[27] Ambrosi, A.; Pumera, M. The CVD graphene transfer procedure introduces metallic impurities which alter the graphene electrochemical properties. *Nanoscale* **2014**, *6*, 472.

[28] Lin, Y.-C.; Lu, C.-C. L.; Yeh, C.-H.; Jin, C.; Suenaga, K.; Chiu, P.-W. Atomic mechanism of the semiconducting-to metallic phase transition in single-layered MoS_2. *Nano Lett.* **2012**, *12*, 414.

[28] Lin, Y.-C.; Lu, N.; Perea-Lopez, N.; Li, J.; Lin, Z.; Peng, X.; Lee, C. H.; Sun, C.; Calderin, L.; Browning, P. N.; Bresnehan, M. S.; Kim, M. J.; Mayer, T. S.; Terrones, M.; Robinson, J. A. Direct Synthesis of van der Waals Solids. *ACS Nano*, **2014**, *8*, 3715.

[29] Lin, Y.-C.; Chang, C.-Y. S.; Ghosh, R. K.; Li, J.; Zhu, H.; Addou, R.; Diaconescu, B.; Ohta, T.; Peng, X.; Lu, N.; Kim, M. J.; Robinson, J. T.; Wallace, R. M.; Mayer, T. S.; Datta, S.; Li, L.-J.; Robinson, J. A. Robinson, J. A. Atomically thin heterostructures based on single-layer tungsten diselenide and graphene. *Nano. Lett.* **2014**, 14, 6936.

[30] Eichfeld, S. M.; Hossain, L.; Yu-Chuan, L.; Piasecki, A.; Kupp, B.; Birdwell, A. G.; Burke, R. A.; Liu, N.; Li, J.; Azcati, A.; McDonnell, S.; Wallace, R. M.; Kim, M. J.; Mayer, T. S.; Redwing, J. M.; Robinson, J. A. Highly scalable, atomically thin WSe_2 grown via metal-organic chemical vapor deposition *ACS Nano* **2015**, *9*, 2080.

[31] Shi, Y.; Zhou, W.; Lu, A.-Y.; Fang, W.; Lee, Y.-H.; Hsu, A. L.; Kim, S. M.; Kim, K. K.; Yang, H. Y.; Li, L.-J.; Idrobo, J.-C.; Kong, J. van der Waals Epitaxy of MoS_2 Layers Using Graphene As Growth Templates. *Nano Lett.* **2012**, *12*, 2784.

[32] Okada, M.; Sawazaki, T.; Watanabe, K.; Taniguch, T.; Hibino, H.; Shinohara, H.; Kitaura, R. Direct Chemical Vapor Deposition Growth of WS_2 Atomic Layers on Hexagonal Boron Nitride. *ACS Nano* **2014**, *8*, 8273.

[33] Yue, R.; Barton, A. T.; Zhu, H.; Azcatl, A.; Pena, L. F.; Wang, J.; Peng, X.; Lu, N.; Cheng, L.; Addou, R.; McDonnell, S.; Colombo, L.; Hsu, J. W. P. ; Kim, J.; Kim, M. J.; Wallace, R. M.; Hinkle, C.

L. $HfSe_2$ thin films: 2D transition metal dichalcogenides grown by molecular beam epitaxy. *ACS Nano* **2015**, *9*, 474.

[34] Liu, H. J.; Jiao, L.; Xie, L.; Yang, F.; Chen, J. L.; Ho, W. K.; Gao, C. L.; Jia, J. F.; Cui, X. D.; Xie, M. H. Molecular-beam epitaxy of monolayer and bilayer WSe_2: A scanning tunnelling microscopy/spectroscopy study and deduction of exciton binding energy. *2D Materials* **2015**, *2*, 034004.

[35] Koma, A.; Sunouchi, K.; Miyajima, T. Fabrication of ultrathin heterostructures with van der Waals epitaxy *J. Vac. Sci. Technol. B* **1985**, *3*, 724.

[36] Ganatra, R.; Zhang, Q. Few-Layer MoS_2: A Promising Layered Semiconductor. *ACS Nano* **2014**, *8*, 4074.

[37] Lin, Y.-C.; Dumcenco, D. O.; Huang, Y.-S.; Suenaga, K. Atomic mechanism of the semiconducting-to metallic phase transition in single-layered MoS_2. *Nat. Nanotech.* **2014**, *9*, 391.

[38] Wang, H.; Zhang, Q.; Yao, H.; Liang, Z.; Lee, H. W.; Hsu, P. C.; Zheng, G.; Cui, Y. High electrochemical selectivity of edge versus terrace sites in two-dimensional layered MoS_2 materials. *Nano Lett.* **2014**, *14*, 7138.

[39] Mahler, B.; Hoepfner, V.; Liao, K.; Geoffrey, A. O. Colloidal Synthesis of 1T-WS_2 and 2H-WS_2 Nanosheets: Applications for Photocatalytic Hydrogen Evolution. *J. Am. Chem. Soc.* **2014**, *136*, 14121.

[40] Enyashin, A. N.; Yadgarov, L.; Houben, L.; Popov, I.; Weidenbach, M.; Tenne, R.; Bar-Sadan, M.; Seifert, G. New Route for Stabilization of 1T-WS_2 and MoS_2 Phases. *J. Phys. Chem. C* **2011**, *115*, 24586.

[41] Cattelan, M.; Markman, B.; Lucchini, G.; Kumar Das, P.; Vobornik, I.; Robinson, J. A.; Agnoli, S.; Granozzi, G. New strategy for the growth of complex heterostructures based on different 2D materials. *Chem. Mater.* **2015**, *27*, 4105.

[42] Eng, A. Y. S.; Ambrosi, A.; Sofer, Z.; Simek, P.; Pumera, M. Electrochemistry of Transition Metal Dichalcogenides: Strong Dependence on the Metal-to-Chalcogen Composition and Exfoliation Method. *ACS Nano* **2014**, *8*, 12185.

[43] Fuchtbauer, H. G.; Tuxen, A. K.; Moses, P. G.; Topsøe, H.; Besenbacher, F.; Lauritsen, J. V. Morphology and atomic-scale structure of single-layer WS_2 nanoclusters. *Phys. Chem. Chem. Phys.* **2013**, ***15***, 15971.

[44] Dendzik, M.; Michiardi, M.; Sanders, C.; Bianchi, M.; Miwa, J. A.; Grønborg, S. S.; Lauritsen, J. V.; Hofmann, P. Growth and electronic structure of epitaxial single-layer WS_2 on Au(111). arXiv:1509.05133v1

[45] Klein, A.; Tiefenbacher, S.; Eyert, V.; Pettenkofer, C.; Jaegermann, W. Electronic band structure of single-crystal and single-layer WS_2: Influence of interlayer van der Waals interactions. *Phys. Rev. B* **2001**, *64*, 205416.

[46] Liu, H. J.; Jiao, L.; Xie, L.; Yang, F.; Chen, J. L.; Ho, W. K.; Gao, C. L.; Jia, J. F.; Cui, X. D.; Xie, M. H. Molecular-beam epitaxy of monolayer and bilayer WSe_2: A scanning tunneling microscopy/spectroscopy study and deduction of exciton binding energy. DOI: 10.1088/2053-1583/2/3/034004

[47] Usachov, D.; Adamchuk, V. K.; Haberer, D.; Grüneis, A. Sachdev, H.; Preobrajenski, A. B.; Laubschat, C.; Vyalikh, D. V. Quasifreestanding single-layer hexagonal boron nitride as a substrate for graphene synthesis. *Phys. Rev. B* **2010**, *82*, 075415.

[48] Varykhalov, A.; Sánchez-Barriga, J.; Shikin, A. M.; Biswas, C.; Vescovo, E.; Rybkin, A.; Marchenko, D.; Rader, O. Electronic and magnetic properties of quasifreestanding graphene on Ni. *Phys. Rev. Lett.* **2008**, *101*, 157601.

[49] Berkowitz, J.; Marquardt, J. R. Equilibrium Composition of Sulphur Vapor *J. Chem. Phys.* **1963**, *39*, 275.

[50] Fadley, C. S. Angle-resolved x-ray photoelectron spectroscopy. *Prog. Surf. Sci.* **1984**, *16*, 275.

[51] Minaev, V. S.; Timoshenkov, S. P.; Kalugin, V. V. Structural and phase transformations in condensed selenium. *J. Optoelectron. Adv. M.* **2005**, *7*, 1717.

[52] McGuirk, G. M.; Shin, H.; Caragiu, M.; Ash, S.; Bandyopadhyay, P. K.; Prince, R. H.; Diehl, R. D. Au(111) surface structures induced by adsorption: LEED I(E) analysis of (1 × 1) and (5 × 5) Au(111)-S phases. *Surf. Sci.* **2013**, *610*, 42.

[53] Lay, M. D.; Varazo, K.; Stickney, J. L. Formation of sulfur atomic layers on gold from aqueous solutions of sulfide and thiosulfate: Studies using EC-STM, UHV-EC, and TLEC. *Langmuir* **2003**, *19*, 8416.

[54] Zabinski, J. S.; Donley, M. S.; Prasad, S. V. Synthesis and characterization of tungsten disulphide films grown by pulsed-laser deposition. *J. Mater. Sci.* **1994**, *29*, 4834.

[55] Khudorozhko, G. F.; Asanov, I. P.; Mazalov, L. N.; Kravtsova E. A.; Parygina, G. K.; Fedorov, V. E.; Mironov, J. V. The study of electronic structure of molybdenum and tungsten trisulfides and their lithium intercalates by x-ray electron and x-ray emission and absorption spectroscopy. *J. Electron Spectrosc. Relat. Phenom.* **1994**, *68*, 199.

[56] Payen, E.; Kasztelan, S.; Grimblot, J.; Bonnelle, J. P. Study of the sulphurization of WO_3/ γ-Al_2O_3 catalysts by in situ laser raman spectroscopy. *Catal. Today* **1988**, *4*, 57.

[57] Walton, R. I.; Hibble, S. J. A combined *in situ* X-ray absorption spectroscopy and X-ray diffraction study of the thermal decomposition of ammonium tetrathiotungstate. *J. Mater. Chem.* **1999**, 9, 1347.

[58] Bromley, R. A.; Murray, R. B.; Yoffe, A. D. The band structures of some transition metal dichalcogenides. III. Group VIA: trigonal prism materials. *J. Phys. C: Solid State Phys.* ***1972,*** *5*, 759.

[59] Mattheiss, L. F. Band structures of transition-metal-dichalcogenide layer compounds. *Phys. Rev. B* **1973**, *8*, 3719.

[60] Coehoorn, R.; Haas, C.; Dijkstra, J.; Flipse, C. J. F.; de Groot, R. A.; Wold, A. Electronic structure of $MoSe_2$, MoS_2, and WSe_2. I. Band-structure calculations and photoelectron spectroscopy. *Phys. Rev. B* **1987**, *35*, 6195.

[61] Kibsgaard, J.; Lauritsen, J. V.; Clausen, B. S.; Topsøe, H.; Besenbacher, F. Cluster-support interactions and morphology of MoS_2 nanoclusters in a graphite-supported hydrotreating model catalyst. *J. Am.Chem. Soc.* **2006**, *128*, 13950.

[62] Walton, A. S.; Lauritsen, J. V.; Topsøe, H.; Besenbacher, F. MoS_2 nanoparticle morphologies in hydrodesulfurization catalysis studied by scanning tunneling microscopy. *J. Catal.* **2013**, *308*, 306.

[63] Coy Diaz, H.; Avila, J.; Chen, C.; Addou, R.; Asensio, M. C.; Batzill, M. Artificially Stacked Atomic Layers: Toward New van der Waals Solids. *Nano Lett.* **2015**, *15*, 1135.

[64] Capehart, T. W.; Rhodin, T. N. Bonding geometry and electronic structure of the chalcogens on Ni(111). *J. Vac. Sci. Technol.* **1979**, *16*, 594.

[65] Zhao, W.; Kozlov, S. M.; Höfert, O.; Gotterbarm, K.; Lorenz, M. P. A.; Viñes, F.; Papp, C.; Görling, A.; Steinrück, A.-P. Graphene on Ni(111): coexistence of different surface structures. *J. Phys. Chem. Lett.* **2011**, *2*, 759.

[66] Lahiri, J.; Lin, Y.; Bozkurt, P.; Oleynik, I. I.; Batzill, M. An extended defect in graphene as a metallic wire. *Nat. Nanotechnol.* **2010**, *5*, 326.

[67] Bianchini, F.; Patera, L. L.; Peressi, M.; Africh, C.; Comelli, G. Atomic scale identification of coexisting graphene structures on Ni(111). *J. Phys. Chem. Lett.* **2014**, *5*, 467.

[68] Cattelan, M.; Peng, G. W.; Cavaliere, E.; Artiglia, L.; Barinov, A.; Roling, L. T.; Favaro, M.; Píš, I.; Nappini, S.; Magnano, E.; Bondino, F.; Gavioli, L.; Agnoli, S.; Mavrikakis, M.; Granozzi, G. The nature of the Fe–graphene interface at the nanometer level. *Nanoscale* **2015**, *7*, 2450.

[69] Terrones, H.; Del Corro, E.; Feng, S.; Poumirol, J. M.; Rhodes, D.; Smirnov, D.; Pradhan, N. R.; Lin, A.; Nguyen, M. A. T.; Elías, A. L.; Mallouk, T. E.; Balicas, L.; Pimenta, M. A.; Terrones, M. New first order raman-active modes in few layered transition metal dichalcogenides. Sci. *Rep.* **2014**, *4*, 4215.

[70] Terrones, H.; López-Urías, F.; Terrones, M. Novel hetero-layered materials with tunable direct band gaps by sandwiching different metal disulfides and diselenides. Sci. *Rep.* **2013**, *3*, 1549.

[71] Le, D.; Barinov, A.; Preciado, E.; Isarraraz, M.; Tanabe, I.; Komesu, T.; Troha, C.; Bartels, L.; Rahman, T. S.; Dowben, P. A. Spin–orbit coupling in the band structure of monolayer WSe_2. *J. Phys.: Condens. Matter* **2015**, *27*, 182201.

[72] Riley, J. M.; Mazzola, F.; Dendzik, M.; Michiardi, M.; Takayama, T.; Bawden, F.; Granerød, C.; Leandersson, M.; Balasubramanian, T.; Hoesch, M.; Kim, T, K.; Takagi, H.; Meevasana, W.; Hofmann, Ph.; Bahramy, M. S.; Wells, J. W.; King, P. D. C. Direct observation of spin-polarized bulk bands in an inversion-symmetric semiconductor. *Nature Phys.* **2014**, *10*, 835.

[73] Gutiérrez, H. R.; Perea-López, N.; Elías, A. L.; Berkdemir, A.; Wang, B.; Lv, R.; López-Urías, F.; Crespi, V. H.; Terrones, H.; Terrones, M. Extraordinary Room-Temperature Photoluminescence in Triangular WS_2 Monolayers. *Nano Lett.* **2012**, *13*, 3447

3.2. Indium selenide

Introduction

G had a ground-breaking impact on science and technology.[1] However, the absence of a band gap in G, although beneficial for applications requiring frequency-independent absorption,[2] prevents the effective switching of its conductivity in any electronic device and the achievement of a high ON-OFF ratio.[3] Large dark current dominates the non-zero bias operation in G-based devices.[4,5] Finite and direct bandgaps are required for a wealth of applications,[3] including transparent optoelectronic, photovoltaic and photodetector devices.

Nature offers a manifold of layered materials "beyond graphene",[6] including metals, semimetals, insulators and semiconductors with direct and indirect band gaps ranging from ultraviolet to infrared through the visible range.

The production of novel 2D materials,[6] such as transition-metal dichalcogenides (e.g. MoS_2[7]) or atomically thin elemental materials, (e.g. silicene,[8] germanene[9] and phosphorene[10,11]) promises a revolutionary step-change. Such innovative 2D sheet-like materials could combine flexibility[12,13] with electronic properties[14] that G cannot match.

The impossibility of exfoliating silicene and germanene complicates their potential use in technology.[15] In principle, black phosphorus could be a more suitable material for optoelectronics since it is a van der Waals solid with a semiconducting direct band gap,[11,16] which can be exfoliated in phosphorene layers. However, black phosphorus flakes are found to chemically degrade upon exposure to ambient conditions.[17,18] The ambient degradation causes large increases in threshold voltage after 6 h in atmosphere, followed by a 10^3 decrease in field-effect transistors current ON/OFF ratio and mobility.[17,18,19,20] Black phosphorus also increases of over 200% in volume due to water absorption over several days.[19]

A suitable solution could be provided by InSe, which is a layered semiconductor made of stacked layers of Se−In−In-Se atoms with van der Waals bonding between quadruple layers, see Figure 11 in the section 3. In its bulk form, three polytypes (β, ε, γ) have been observed. They correspond to the three possible ways of stacking successive layers: the first corresponds to a rotation by π around an axis perpendicular to the plane of the layer followed by a translation parallel to the axis of rotation (the β polytype). The other two ways correspond to a translation where the horizontal components are $-(\mathbf{a}_1 + \mathbf{a}_2)/3$ in one case (ε polytype), and $(\mathbf{a}_1+\mathbf{a}_2)/3$ in the other (γ polytype), where $\mathbf{a}$ vector is the basis vectors of the hexagonal lattice.[21] At RT β-InSe is a direct bandgap (1.26 eV) semiconductor with valence band maximum (VBM) at Γ point,[22,21] γ-InSe have a similar band gap, but the VBM is in the Z point, i.e., at the Brillouin zone edge going in a direction perpendicular to the layers.[21,23] Whereas, the literature is controversial, an experimental work indicates that ε-InSe shows an indirect band gap of 1.4 eV,[24] whereas a theoretical paper foresees a direct band gap similar to β-InSe.[25]

Many recent works have reported the superb performance of InSe-based optoelectronic devices.[24,26,27,28] InSe-based field effect transistors have high carrier mobility.[26,27,29,30,31] In the bulk form, the electron mobility of InSe is near 10^3 $cm^2/(V\ s)$ at RT[31] making it another promising candidate for next-generation high-performance 2D semiconductor devices.[26,27,31] Together with potential optoelectronic applications, InSe offers also intriguing prospects for strain engineering,[32] nonlinear optics,[33] and photovoltaics.[34] While an abundant number of theoretical investigations on band structure properties is available,[21,35,36,37,38] only a few experimental works exist.[38,39,40,]

Although pristine, free-standing G is chemically inert,[41] other 2D materials such as graphane,[42] silicene,[43] germanane,[44] and phosphorene[17,18,19,20] possess lower chemical stability. The reduced chemical stability of these 2D materials is related to the energetics needed to maintain stable bonding configurations, which is notably affected by structural puckering.[43] The environmental degradation of these materials strongly hinders their application capabilities. Environmental stability would favour the fast-track implementation of 2D materials in optoelectronic devices. For this reason, the reactivity of InSe toward ambient gases and the effect of surface chemical reactions on device-relevant electronic properties constitute crucial issue for establishing whether InSe-based technology is suitable.

In this section we exploit our knowledge on the study of the electronic and chemical properties of 2D materials in order to prove that InSe can be a strong candidate for future ultrathin electronical devices. In the following the electronic structure of InSe was sampled by high resolution ARPES, to test its chemically reactivity to ambient gases the band structure was studied also after dosing of O_2 and H_2O and after air exposure. The understanding of the chemical properties of InSe surface has been completed by TPD and XPS experiments.

Experimental section

As mentioned in the "Introduction" section the β-InSe represents an exception in this thesis because instead of growing and analysing the material *in-situ* we decided to study its properties starting from vacuum exfoliated bulk materials.

Growth of single-crystal InSe

Single crystalline ingot of β-InSe was grown from melt by the vertical Bridgman−Stockbarger method, by E. F. Keskenler's group.[22] In and Se starting elements of a high purity grade (not less than 99.999%) were sealed in quartz ampoule, which was annealed at 950 °C under a vacuum of 10^{-6} mbar for 15 hours in a furnace. The temperature of the quartz ampoule was decreased to RT in 24 hours. The crucible was then suspended in the middle of the vertical furnace with two zone designed. The temperature of the furnace was increased to 950 °C and maintained at this temperature for 40 hours and then decreased to 750 °C. Temperature was kept at 750°C for 15 hours. The temperature of the lower zone of furnace was reduced to 250 °C at a rate of 1.54 °C/h. Both the furnace zones were cooled to 250 °C in 75 hours. The solidified ingot was cooled to RT in 50 hours. The grown InSe samples are 10 mm in diameter and about 60 mm in length. Samples were cleaved into perpendicular planes parallel to the (001) surface with a razor.

Methods

The band structure mapping of InSe was performed using a photon energy of 74 eV at the Spectromicroscopy beamline at synchrotron Elettra (Trieste, Italy), for details see method paragraph of section 2.1.1. The measurements were acquired at about 110 K, the estimated total energy resolution at this temperature is ≈50 meV.

For TPD experiments the sample was glued on a tantalum frame by a UHV compatible oxide adhesive (Ceramabond 569 Aremco), for other details see the methods paragraph of section 2.1.2.

XPS measurements were carried out with conventional non-monochromatic Al K_α source with PE=20 eV; the BE scale was calibrated by normalizing the Au $4f_{7/2}$ BE position to 84.0 eV.

Results and Discussion

The experimental band structure of freshly exfoliated β-InSe was probed by means of ARPES. The experimentally measured valence band cuts along the high-symmetry lines,[40] evident from the ARPES isokinetic energy maps in Figure 1b, of the first Brillouin zone are reported in Figure 1c.

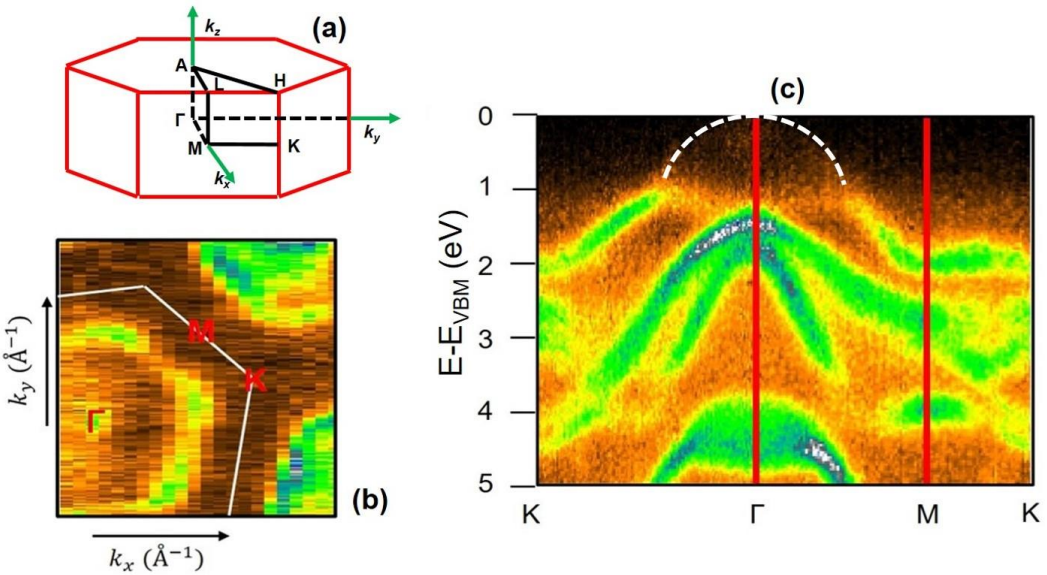

Figure 1. (a) Representation of the Brillouin zone of β-InSe. (b) Constant energy map at 1 eV below the VBM. (c) Experimental band structure along the high-symmetry directions. The energy scale was set to zero at VBM.

The high-resolution ARPES measurements reported here show much more precisely the β-InSe band positions and shapes with respect to other data measured for this crystal before.[38] It is possible to distinguish very well the band that forms the VBM in Γ (as expected for β-InSe[21]), that previously was not well-underlined[38] probably because of the low photoemission intensity. The VBM has a dominant p_z component of selenium and indium, whereas the states that cross the Γ point at about 1.6 and 4.4 eV are related to *p* state of selenium mixed with *x y* state of In.[37] Around the Γ point a parabola can fit the band that form the VBM, and the effective mass of the holes can be calculated by the second derivative with respect to energy, Figure 2, at 110 K it resulted to be about 4.0 ± 0.3 m_e.

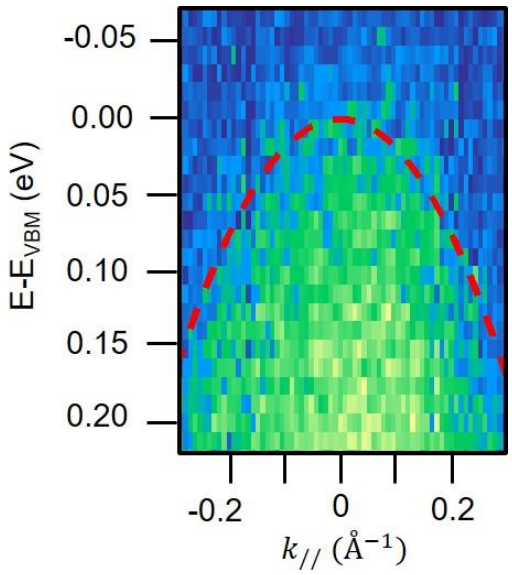

Figure 2. VBM at Γ point of as-exfoliated InSe. Red dashed line is for the parabola used for the fitting.

In order to study the InSe chemical robustness, the vacuum exfoliated crystal was exposed to >10^4 L of H_2O, O_2 and to air (10 min) at RT. Figure 3 shows the modification of the band structure. Exposure to O_2 and H_2O under UHV conditions does not induce any shift of the electronic bands of pristine InSe. On the contrary, in the case of air exposure a small p-doping of 130 meV, i.e. rigid shift of the bands towards low binding energies, is visible. Furthermore, for the air exposed sample, an overall decrease of the photoemission signal has been observed.

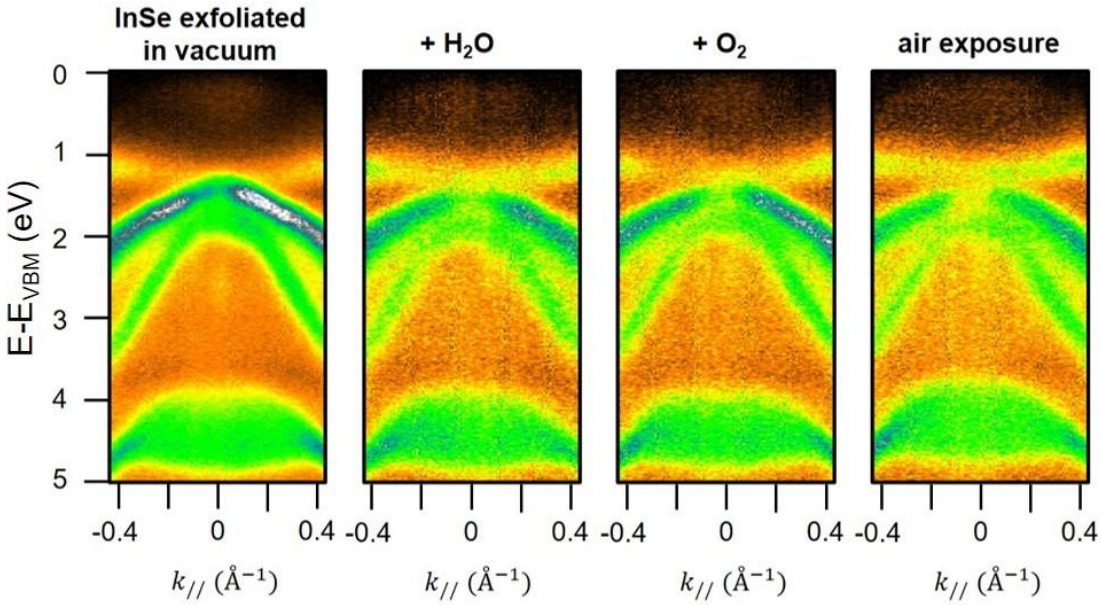

Figure 3. InSe band structure close to the Γ point, from the left to the right, as-exfoliated in vacuum, after water dosing, after oxygen dosing, and after air exposure. The energy scale was set to zero at as-exfoliated sample VBM.

The ARPES signal reduction after air exposure can be related to a small hydrocarbon contamination coming from the environment that attenuated the outgoing photoelectrons. The 130 meV p-doping maybe can be also associated with

hydrocarbon species, similar to what observed for other 2D layers with polymer residues,[45] or to the oxidation of surface defects, which require relative high pressure to be formed.[46]

In order to understand the desorption temperature of the species present in air, TPD measurements of water, molecular oxygen and carbon monoxide were performed. The molecules were dosed at 160 K and the desorption heating ramp was set to 2 K/sec. No desorption species were visible after dosing O_2 and CO. Whereas for the desorption spectra of water, only one desorption at 177 K related to ice, i.e. physisorbed water multilayer, was visible [47] (Figure 4). To simulate the air conditions other experiments dosing the same molecules at about 10^6 L (at 10^{-4} mbar) at RT, as done in the section 2.2 led to the same results, no desorption for O_2, CO and H_2O at temperature above RT.

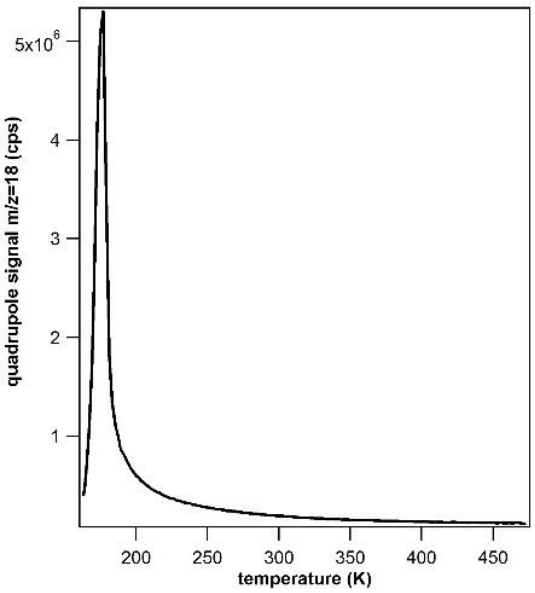

Figure 4. TPD of 100 L H_2O ($1.33 \cdot 10^{-6}$ mbar per 100 sec) dosed at 160 K on InSe, heating ramp 2/s.

The absence of desorption peaks of H_2O and O_2 at temperature above RT explains why no doping from the dosed molecules was visible using ARPES.

Conventional XPS measurements of In 3*d* and Se 3*d* photoemission lines, Figure 5, present the maximum of the In $3d_{5/2}$ at 444.6 eV and Se $3d_{5/2}$ at 53.4 eV of BEs with a FWHM of about 1 eV, which are values compatible with pristine InSe.[48] Before and after the exposure to water and O_2 no changes in the core-levels were observed, confirming a good oxidation resistance.

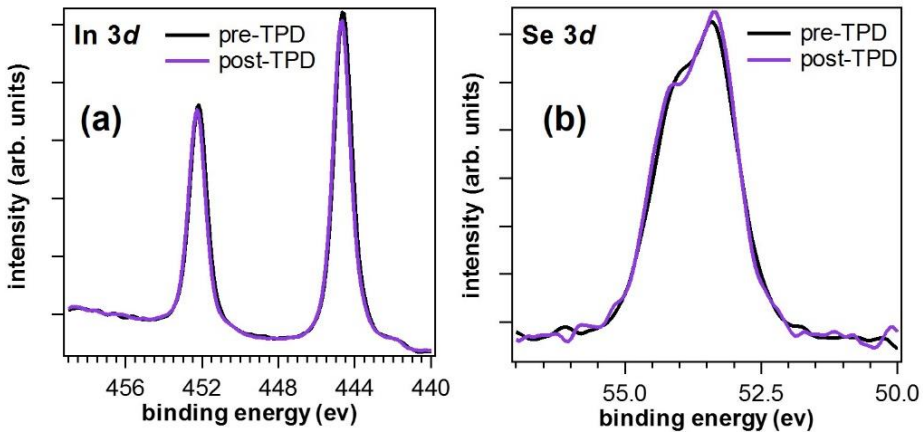

Figure 5. (a) In 3d and (b) Se 3d photoemission lines of InSe pre and post TPD of O_2 and H_2O.

The inertness of the basal plane of this material can be explained by the surface terminated by Se atoms[48] that do not allow oxidizing agents to chemically bond with the second layer, i.e. In atoms, producing a bulk oxidation.[48]

Conclusions

In this section the electronic properties of a β-InSe have been investigated with an unprecedented precision by ARPES. In order to apply this material in real application we tested its chemical reactivity at RT exposing the as-cleaved surface to O_2 and H_2O and to air. The Se terminated surface protects efficiently the indium atoms from oxidation and the air exposure led only a small rigid upshift in energy of the band structure and a reduction of the photoemission intensity, both phenomena have been related to small hydrocarbon adsorption from the environment.

These results indicate that the InSe is a good candidate for future 2D electronic devices because of its robust chemistry that preserves its electronic structure in air.

References

1 Katsnelson, M. I. Graphene: carbon in two dimensions. *Mater. Today* **2007**, *10*, 20.

2 Mak, K. F.; Sfeir, M. Y.; Wu, Y.; Lui, C. H.; Misewich, J. A.; Heinz, T. F. Measurement of the Optical Conductivity of Graphene, *Phys. Rev. Lett.* **2008**, *101*, 196405.

3 Novoselov, K. Graphene: Mind the gap. *Nat. Mater.* **2007**, *6*, 720.

4 Gan, X.; Shiue, R.-J.; Gao, Y.; Meric, I.; Heinz, T. F.; Shepard, K.; Hone, J.; Assefa, S.; Englund, D. Chip-integrated ultrafast graphene photodetector with high responsivity. *Nat. Photon.* **2013**, *7*, 883.

5 Koppens, F. H. L. ; Mueller, T.; Avouris, P.; Ferrari, A. C.; Vitiello, M. S.; Polini, M. Photodetectors based on graphene, other two-dimensional materials and hybrid systems. *Nat. Nanotechnol.* **2014**, *9*, 780.

6 Miro, P.; Audiffred, M.; Heine, T. An atlas of two-dimensional materials, *Chem. Soc. Rev.* **2014**, *43*, 6537.

7 Sangwan, V. K.; Jariwala, D.; Kim, I. S.; Chen, K.-S.; Marks, T. J.; Lauhon, L. J.; Hersam, M. C. Gate-tunable memristive phenomena mediated by grain boundaries in single-layer MoS_2. *Nat. Nanotech.* **2015**, *10*, 403.

8 Tao, L.; Cinquanta, E.; Chiappe, D.; Grazianetti, C.; Fanciulli, M.; Dubey, M.; Molle, A.; Akinwande, D. Silicene field-effect transistors operating at room temperature, *Nat. Nanotech.* **2015**, *10*, 227.

9 Derivaz, M.; Dentel, D.; Stephan, R.; Hanf, M.-C.; Mehdaoui, A.; Sonnet, P.; Pirri, C. Continuous Germanene Layer on Al(111). *Nano Lett.* **2015**, *15*, 2510.

[10] Liu, H.; Neal, A. T.;Zhu, Z.; Luo, Z.; Xu, X.; Tománek, D.; Ye, P. D. Phosphorene: an unexplored 2D semiconductor with a high hole mobility. *ACS Nano* **2014**, *8*, 4033.

[11] Viti, L.; Hu, J.; Coquillat, D.; Knap, E.; Tredicucci, W.; Politano, A.; Vitiello, M. S. Black phosphorus terahertz photodetectors. *Adv. Mater.* **2015**, *27*, 5567.

[12] Zhu, W.; Yogeesh, M. N.; Yang, S.; Aldave, S. H.; Kim, J.-S.; Sonde, S.; Tao, L.; Lu, N.; Akinwande, D. Flexible black phosphorus ambipolar transistors, circuits and AM demodulator, *Nano Lett.* **2015**, *15*, 1883.

[13] Akinwande, D.; Petrone, N.; Hone, J. Two-dimensional flexible nanoelectronics. *Nat. Commun.* **2014**, *5*, 5678.

[14] Wang, G.; Pandey, R.; Karna, S. Phosphorene oxide: stability and electronic properties of a novel 2D material. *Nanoscale* **2014**, *7*, 524.

[15] Kara, A.; Enriquez, H.; Seitsonen, A. P.; Lew Yan Voon, L. C.; Vizzini, S.; Aufray, B.; Oughaddou, H. A review on silicene — New candidate for electronics. *Surf. Sci. Rep.* **2012**, *67*, 1.

[16] Liu, H.; Du, Y.; Deng, Y.; Ye, P. D. Semiconducting black phosphorus: synthesis, transport properties and electronic applications, *Chem. Soc. Rev.* **2015**, *44*, 2732.

[17] Edmonds, M. T.; Tadich, A.; Carvalho, A.; Ziletti, A.; O'Donnell, K. M.; Koenig, S. P.; Coker, D. F.; Özyilmaz, B.; Neto, A. H. C.; Fuhrer, M. S. Creating a stable oxide at the surface of black phosphorus, *ACS Appl. Mater. Interfaces*, **2015**, *7*, 14557.

[18] Wood, J. D.; Wells, S. A.; Jariwala, D.; Chen, K.-S.; Cho, E.; Sangwan, V. K.; Liu, X.; Lauhon, L. J.; Marks, T. J.; Hersam, M. C: Effective passivation of exfoliated black phosphorus transistors against ambient degradation. *Nano Lett.* **2014**, *14*, 6964.

[19] Joshua, O. I.; Gary, A. S.; Herre, S. J. v. d. Z.; Andres, C.-G.; Environmental instability of few-layer black phosphorus. *2D Materials* **2015**, *2*, 011002.

[20] Wang, Z.; Islam, A.; Yang, R.; Zheng, X.; Feng, P. X.-L. Environmental, thermal, and electrical susceptibility of black phosphorus field effect transistors, *J. Vac. Sci. Technol., B* **2015**, *33*, 052202.

[21] da Costa, P. G.; Dandrea, R. G.; Wallis, R. F.; Balkanski, M. First-principles study of the electronic structure of γ-InSe and β-InSe. *Phys. Rev. B* **1993**, *48*, 14135.

[22] Gürbulak, B.; Şata, M.; Dogan, S.; Duman, S.; Ashkhasi A.; Keskenler, E. F. Structural characterizations and optical properties of InSe and InSe:Ag semiconductors grown by Bridgman/Stockbarger technique. *Physica E* **2014**, *64*, 106.

[23] Sánchez-Royo, J. F.; Muñoz-Matutano, G.; Brotons-Gisbert, M.; Martínez-Pastor, J. P.; Segura, A.; Cantarero, A.; Mata, R.; Canet-Ferrer, J.; Tobias, G.; Canadell, E.; Marqués-Hueso, J.; Gerardot, B. D. Electronic structure, optical properties, and lattice dynamics in atomically thin indium selenide flakes. *Nano Res.* **2014**, *7*, 1556.

[24] Lei, S.; Ge, L.; Najmaei, S.; George, A.; Kappera, R.; Lou,J.; Chhowalla, M.; Yamaguchi, H.; Gupta, G.; Vajtai, R.; Mohite, A. D.; Ajayan, P. M. Evolution of the electronic band structure and efficient photo-detection in atomic layers of InSe. *ACS Nano*, **2014**, *8*, 1263.

[25] Kharkhail, L. Y.; Glukhov, K. E.; Sxnajder, M. Peculiarities of chemical bonding in crystals of the In-Se system. *Acta. Phys. Pol. A* **2014**, *126*,1146.

[26] Mudd, G. V., Svatek, S. A.; Hague, L.; Makarovsky, O.; Kudrynskyi, Z. R.; Mellor, C. J.; Beton, P. H.; Eaves, L.; Novoselov, K. S.; Kovalyuk, Z. D.; Vdovin, E. E.; Marsden, A. J.; Wilson, N. R.; Patanè, A. High broad-band photoresponsivity of mechanically formed InSe–Graphene van der Waals heterostructures. *Adv. Mater.* **2015**, *27*, 3760.

[27] Lei, S.; Wen, F.;Ge, L.; Najmaei, S.; George, A.; Gong, Y.; Gao, W.; Jin, Z.; Li, B.; Lou, J.; Kono, J.; Vajtai, R.; Ajayan, P.; Halas, N. J. An atomically layered InSe avalanche photodetector, *Nano Lett.* **2015**, *15*, 3048.

[28] Darwish, A. A. A. Photoinduced effect in nanostructured InSe thin films for photonic applications. *Opt. Commun.* **2014**, *310*, 104.

[29] Sucharitakul, S.; Goble, N. J.; Kumar, U. R.; Sankar, R.; Bogorad, Z. A.; Chou, F.-C.; Chen, Y.-T.; Gao, X. P. A. Intrinsic electron mobility exceeding 10^3 $cm^2/(V\ s)$ in multilayer InSe FETs, *Nano Lett.* **2015**, *15*, 3815.

[30] Chen, Z.; Biscaras, J.; Shukla, A. A high performance graphene/few-layer InSe photo-detector, *Nanoscale* **2015**, *7*, 5981.

[31] Tamalampudi, S. R.; Lu, Y. Y.; Kumar, R.; Sankar, U. R.; Liao, C. D.; Moorthy, K.; Cheng, C. H.; Chou, F. C.; Chen, Y. T. High performance and bendable few-layered InSe photodetectors with broad spectral response. *Nano Lett.* **2014**, *14*, 2800.

[32] Yandong, M.; Ying, D.; Lin, T.; Chengwang, N.; Baibiao, H. Engineering a topological phase transition in β-InSe via strain. *New J. Phys.* **2013**, *15*, 073008.

[33] Kyazym-zade, A. G.; Salmanov, V. M.; Guseinov, A. G.; Gasanova, L. G.; Mamedov, R. M. Optical nonlinearities in GaSe and InSe crystals upon laser excitation. *Optics and Spectroscopy* **2014**, *116*, 595.

[34] Feng, W.; Zheng, W.; Chen, X.; Liu, G.; Cao, W.; Hu, P. Solid-state reaction synthesis of a InSe/$CuInSe_2$ lateral p–n heterojunction and application in high performance optoelectronic devices. *Chem. Mater.* **2015**, *27*, 983.

[35] Debbichi, L.; Eriksson, O.; Lebègue, S. Two-dimensional indium selenides compounds: an ab ınitio study. *J. Phys. Chem. Lett.* **2015**, *6*, 3098.

[36] Srivastava, A.; Chandiramouli, R. Band structure and transport studies on impurity substituted InSe nanosheet - A first-principles investigation, *Superlattices Microstruct.* **2015**, *79*,135.

[37] Camara, M. O. D.; Mauge, A.; Devos, I. Electronic structure of the layer compounds GaSe and InSe in a tight-binding approach. *Phys. Rev. B* **2002**, *65*,1252061.

[38] Larsen, P. K.; Chiang, S.; Smith, N. V. Determination of the valence band structure of InSe by angle-resolved photoemission using synchrotron radiation. *Phys. Rev. B* **1977**, *15*, 3200.

[39] Manjón, F. J.; Segura, A.; Muñoz-Sanjosé, V.; Tobías, G.; Ordejón, P.; Canadell, E. Band structure of indium selenide investigated by intrinsic photoluminescence under high pressure. *Phys. Rev. B* **2004**, *70*, 125201.

[40] Amokrane, A.; Proix, F.; El Monkad, S.; Cricenti, A.; Barchesi, C.; Eddrief, M.; Amimer, K.; Sébenne, C. A. Band structure of an epitaxial thin film of InSe determined by angle-resolved ultraviolet photoelectron spectroscopy *J. Phys. Condens. Matter* **1999**, *11*, 4303.

[41] Qi, J. S.; Huang, J. Y.; Feng, J.; Shi, D. N.; Li, J. The possibility of chemically inert, graphene-based all-carbon electronic devices with 0.8 eV gap. *ACS Nano* **2011**, *5*, 3475.

[42] Elias, D. C.; Nair, R. R.; Mohiuddin, T. M. G.; Morozov, S. V.; Blake, P.; Halsall, M. P.; Ferrari, A. C.; Boukhvalov, D. W.; Katsnelson, M. I.; Geim, A. K.; Novoselov, K. S. Control of graphene's properties by reversible hydrogenation: evidence for graphane. *Science*, **2009**, *323*, 610.

[43] Molle, A.; Grazianetti, C.; Chiappe, D.; Cinquanta, E.; Cianci, E.; Tallarida, G.; Fanciulli, M. Hindering the oxidation of silicene with non-reactive encapsulation. *Adv. Funct. Mater.* **2013**, *23*, 4340.

[44] Bianco, E.; Butler, S.; Jiang, S.; Restrepo, O. D.; Windl, W.; Goldberger, J. E. Stability and exfoliation of germanane: a germanium graphane analogue. *ACS Nano* **2013**, *7*, 4414.

[45] Pirkle, A.; Chan, J.; Venugopal, A.; Hinojos, D.; Magnuson, C. W.; McDonnell, S.; Colombo, L.; Vogel, E. M.; Ruoff, R. S.; Wallace, R. M. The effect of chemical residues on the physical and electrical properties of chemical vapor deposited graphene transferred to SiO_2 Appl. Phys. Lett. **2011**, 99, 122108

[46] Balitskii, O. A.; Lutsiv, R. V.; Savchyn, V. P.; Stakhira, J. M. Thermal oxidation of cleft surface of InSe single crystal. *Mat. Sci. Eng. N-solid* **1988**, *56*, 5.

[47] Mayer, T.; Klein, A.; Lang, O.; Pettenkofer, C.; Jaegermann, W. H_20 adsorption on the layered chalcogenide semiconductors WSe_2, InSe and GaSe. *Surf. Sci.* **1992**, *269*, 909.

[48] Miyake, I.; Tanpo, T.; Tatsuyama, C. XPS Study on the Oxidation of InSe Jpn. J. Appl. Phys. **1984**, *23*, 172.

4. Conclusion

In this thesis work we tried to investigate some fundamental phenomena that are emerging in the field of 2D materials.

In particular, we focused our attention on the electronic and chemical effects that are inherent in the interfaces, and represent the most distinctive features of 2D materials. As a matter of fact, the pure bidimensional nature of these systems implies that interfacial interactions impact as a whole the materials, producing massive effects on their physical-chemical properties.

In order to tackle this investigation, we had to develop adequate synthesis procedures and therefore, to acquire a clear understanding of the growth of these nanosystems.

Taking the cue from this basic need, we worked on different fronts. In section 3.1.2 we have optimized a quite robust and versatile method for the preparation under UHV conditions of TMDs supported on other 2D nanosheets such as G or *h*-BN. This method is indeed quite simple and is based on a modified version of MBE applied to the growth of van der Waals materials. By the direct co-evaporation of transition metals and chalcogenides is possible to obtain in a quite reliable way specific TMDs with specific structure and composition. By a careful control of the growth temperature and flux rate of different precursors it is possible to obtain monolayer thick films epitaxially oriented with respect to the substrate. This method does not allow obtaining films with large crystallinity such as mechanical exfoliation or CVD, however has the advantage of avoiding any air exposure or the presence of contaminants induced by transfer methods that could induce modifications in the materials. Moreover, it allows the *in-situ* growth of very highly complex stacked heterostructures using step-by-step growth and directly studying the electronic properties of the obtained materials.

In our chase for novel 2D materials heterostructures, we also developed in 3.1.1 a novel growth procedure to synthesize in one step G and *h*-BN *in-plane* heterostructure. After an extended scrutiny of several different synthesis methods and precursors we have identified in the pyrolytic decomposition of one only molecule, dimethylammino borane, the perfect preparation methods. Actually the catalytic decomposition of DMAB on the Pt(111) surface allows the combined formation of hybrid layers of *h*-BN and G.

The *in-situ* 2D material growth has been coupled with intercalation of metals in order to be able to modify efficiently the electronic properties of the resulting heterojunctions. The interaction with metals can lead to electronic decoupling or hybridizations in 2D systems and therefore different band alignment at the interface that can be useful to tune the physicochemical properties of these novel nanosystems and also to trigger totally new functionalities.

Intercalation has been exploited to study the G properties in contact with different metals in the section 2.1.1. In this context, a low interacting substrate, i.e. Pt(111), has been used to grow G with a quasi-freestanding electronic structure and then Fe thin films deposited by PVD, has been brought in contact with G. In this way the electronic

and magnetic properties of G have been drastically changed (the DIrac cones are spin polarized and not degenerate anymore) as well as the magnetic properties of Fe. The system composed by 1 Fe monolayer intercalated underneath G, i.e. G/Fe (1 ML)/Pt(111), has been proposed as an ideal testing ground for expanding the fundamental knowledge on G interfacial physics but also as a practical material for the development for future G spintronic devices.

The sections 2.1.2 and 2.2 have been dedicated to the study of the chemical properties of G. However, also in this case we focused our attention on an interfacial phenomenon that is the study of the reaction beneath the cover of G. The chemical activity of confined spaces is an interesting field that emerged almost twenty years ago in together with the study of nanotubes, which now is gaining more and more interesting since G could allow its exploitation on a large scale. In the section 2.2 our attention has been focused on the hydrogen production obtained by the water dissociation reaction that can happen at the interface between G and Ni(111). By combining several techniques we were able to obtain a rather precise description of the mechanism that explain such unexpected chemical activity.

This thesis clearly outlines the very special nature of the G/metal interfaces, therefore a natural line of investigation has been devoted to the preparation and characterization of different heterointerfaces. A good angle for this study was offered by single crystal of Pt_3Ni, which is the combination of a noble and an easily oxidizable transition metal. The section 2.3 has been focused on the growth of the G and multilayer G on this unconventional substrate. It has been found that the 1 ML Pt-skin that forms the outmost layer of the crystal is enough to induce a quasi-freestanding electronic structure similar to the G/Pt(111) system, on the other hand by exposing this system to oxygen an nickel oxide skin directly in contact with G can be formed. Growth mode and electronic properties of these systems have been investigated, whereas the study of their interfacial chemistry is still to be tackled.

Graphenic substrate can be used as support for catalysts, as done in the section 2.1.2, where TPD has been used to study Fe NPs supported on top of G and N-G. In that section CO-TPD has been exploited for the first time to analyse the intercalation rate of Fe underneath of graphenic layers.

In this thesis we are reporting also some initial work on one of the most innovative layered material that are currently studied: indium selenide. In section 3.2 we exploited both our knowledge on the study of the electronic and chemical properties of 2D materials providing a complete investigation of its electronic properties and chemical stability, which is fundamental for practical applications. Indeed, we proved that InSe could challenge the most promising 2D material for electronics, such as phosphorene, for its intrinsic chemical robustness.

List of acronyms and abbreviations

2D	Two-dimensional
3D	Three-dimensional
ARPES	Angle resolved photoemission spectroscopy
bcc	Body centred cubic
BE	Binding energy
BF	Bright-field
BN	Boron nitride
CMG	Chemically modified graphene
CVD	Chemical vapour deposition
DF	Dark-field
DFT	Density functional theory
DMAB	Dimethylamino borane
EELS	Electron energy loss spectroscopy
fcc	Face centred cubic
FFT	Fast Fourier transformation
FWHM	Full width at half maximum
G	Graphene
GI	Grazing incidence
GO	Graphene oxide
***h*-BN**	Hexagonal boron nitride
***h*-BNG**	See the section 3.1.1
HOPG	Highly ordered pyrolytic graphite
HREELS	High-resolution electron energy loss spectroscopy
L	Langmuir
LEED	Low energy electron diffraction
LEEM	Low energy electron microscopy
MBE	Molecular beam epitaxy
ML	Monolayer
N-G	Nitrogen doped graphene
NI	Normal incidence
NEXAFS	Near edge x-ray absorption fine structure
NPs	Nanoparticles
ORR	Oxygen reduction reaction
PE	Pass energy
PEEM	Photoemission electron microscopy
PL	Photoluminescence
PVD	Physical vapour deposition
RT	Room temperature
STEM	Scanning transmission electron microscopy
STM	Scanning tunneling microscopy
STS	Scanning tunneling spectroscopy
TEM	Transmission electron microscopy
TMD	Transition metal dichalcogenide
TPD	Temperature programmed desorption
UHV	Ultra-high vacuum
UPS	Ultraviolet photoemission spectroscopy
VB	Valence band

VBM	Valence band maximum
XMCD	X-ray magnetic circular dichroism
XPD	X-ray photoelectron diffraction
XPEEM	X-ray photoemission electron microscopy
XPS	X-ray photoemission spectroscopy

Acknowledgement

Ringrazio la mia famiglia che mi ha supportato durante tutto il mio lungo periodo di studio, senza di loro non avrei potuto far niente di tutto ciò.

In particolare voglio ringraziare i miei genitori che hanno fatto di tutto per sostenermi e agevolarmi il più possibile e Nicole che spero un giorno scriva anche lei una tesi di dottorato.

L'esperienza, gli articoli, le abilità che ho acquisito in questi anni sono merito del mio supervisore Prof. Stefano Agnoli. Oltre essere il capo è anche un amico.

Ringrazio il Prof. Gaetano Granozzi, che mi ha sempre dato sostegno e guidato in questi anni, e il Prof. Gian Andrea Rizzi per i suoi utili consigli.

Poi nel gruppo di Surface Science and Catalysis group devo ringraziare tante persone. Quelle con cui ho stretto più amicizia e mi hanno formato negli anni sono Dr. Luca Artiglia, Dr. Marco Favaro, Dr.ssa Laura Calvillo e Dott. Francesco Carraro.

Ringrazio tutti quelli che hanno dato un contribuito a questa tesi. I laureandi futuri e passati, in particolare Giacomo Lucchini, Brian Markman e Roberto Sant. Il Dr. Politano e il Dr. Nguyen e i beamline scientists di Elettra, in particolare il personale di Spectromicroscopy, di BACH e di APE.

Colgo anche l'occasione per scusarmi con i miei amici storici per la mia quasi completa assenza in questi anni, li ringrazio per aver capito la mia scelta e per essere sempre lì pronti a darmi una mano quando ne ho bisogno.